

**Design of An Improved Miniature Ion Neutral Mass  
Spectrometer for NASA Applications**

*Final  
Report  
OUT  
204987*

**Final Report**

Period of Performance January 12, 1995 – July 11, 1997.

**Contract No: NAS5 – 32823**

**Issued by:**

NASA/Goddard Space Flight Center  
Engineering Procurement Office  
Greenbelt, MD 20771.

**Contractor**

Princeton Electronic Systems  
P.O. Box 8627  
Princeton, NJ 08543-8627  
609-275-6500

**Principal Investigator**

Viji Swaminathan, Ph.D.

# Design of An Improved Miniature Ion Neutral Mass Spectrometer for NASA Applications

## Contents

1. Background	1
The Ion Neutral Mass Spectrometer Instrument	1
INMS Operation	3
Technical Objectives	5
The BEAM3D Ion Optics Program	6
2. The Open Source	7
The Three Dimensional Model	8
Open Source Simulations	13
Transmission Analysis	14
Angular Response of the Open Source	19
Sensitivity Analysis	25
3. The Quadrupole Deflector	28
The Three Dimensional Model	28
Software Modification	29
Quadrupole Deflector Simulations	32
Sensitivity Analysis	
Sensitivity to Changes in Deflector Geometry	38
Misalignments of the Deflector Rods	39
Voltage Sensitivities	46
4. The Exit Lens	60
The Three Dimensional Model	60
Ion Optics of the INMS	66
Neutral Beams	70
Comparison with Experiment	72
Comparison with the Engineering Model	72
Comparison with the Flight Instrument	89
Comparisons in Ion Mode	93
5. The Mass Analyzer	96
6. Miniaturization of the Instrument	99
Reduction in Dimensions	99
Reduction in Weight	101
7. The Portable Gas-Chromatograph Mass Spectrometer	106
8. Phase III Plan	119
Appendix	

# 1. BACKGROUND

Mass spectrometers have been widely used by the National Aeronautical and Space Administration (NASA) for investigation of the planetary atmospheres. Mass spectrometers, specially designed for use in space, have been used to measure the composition and density variations of ions and neutral species around planets. The Ion Neutral Mass Spectrometer (INMS) to be used aboard the Cassini Orbiter on its mission to Saturn is designed to measure the *in-situ* composition and density variations of low energy positive ions and neutral species in the upper atmosphere of Titan. It will also measure the *in-situ* composition of low energy positive ions and neutrals in the atmospheres and plasma environments of the icy satellites, rings and the inner magnetosphere of Saturn where densities are measurable.

Princeton Electronic Systems (PES) undertook the project to provide NASA with accurate simulations of the Ion-Neutral Mass Spectrometer (INMS) with a view to design and develop a lower weight, compact quadrupole mass spectrometer to be used in NASA's future space missions. For this purpose, PES utilized the advanced three-dimensional charged particle trajectory beam simulation software called BEAM3D available at the David Sarnoff Research Center (Sarnoff). The capability of the software for mass spectrometer applications was demonstrated in Phase I of this project. For part of the simulations involving the quadrupole mass analyzer, another ion optic software called SIMION was used. SIMION, developed at the Idaho National Engineering Laboratory by David Dahl, has been used by a number of researchers in the field of mass spectrometry.

## The Ion Neutral Mass Spectrometer Instrument

The Ion Neutral Mass Spectrometer (INMS) instrument sensor was designed, built, tested and characterized at NASA/Goddard Space Flight Center (GSFC, Greenbelt, Maryland). It is a modification of the Neutral Gas and Ion Mass Spectrometer (NGIMS) instrument designed for the Comet Rendezvous Asteroid Flyby Mission (CRAF) and has a heritage of similar instruments designed by GSFC for upper atmosphere measurement missions such as Atmosphere Explorer, Dynamics Explorer, Pioneer Venus and Galileo Probe Mass Spectrometer.

The INMS instrument and its operation have been described in detail by Kasprzak et al. (Kasprzak et al., *Cassini Orbiter Ion and Neutral Mass Spectrometer*, Proc.SPIE - Cassini Huygens: A Mission to the Saturnian Systems, Vol. 2803, Denver CO, pp. 129-140, 1996.). The INMS sensor, shown in Figure 1, consists of two separate inlets for measurement of ambient ions and neutral particles, the electrostatic quadrupole deflector (switching lens), the quadrupole mass analyzer and a dual detector system. The two ion sources help detect a wide range of species during a Titan flyby. The "closed source" inlet is used to measure surface non-reactive neutral gases such as N<sub>2</sub> and CH<sub>4</sub>. A velocity ram enhancement as a result of the spacecraft's motion increases the detection range for these species. The geometry provides an accurate means of measuring ambient density for species that are not surface reactive. An "open source" inlet is used for measuring surface reactive neutral gases such as N and HCN, utilizing the spacecraft's motion to form a neutral beam which is subsequently ionized, with no surface interaction. The neutrals are ionized by impact of electrons from a filament. The entrance ion collimator also serves as a trap for electrons and ions that could cause spurious ionization of neutral species. With the filament off, the ion collimator system is also used for direct sampling and measurement of surface reactive ambient thermal and suprathermal ions. The ions, ambient or created by electron impact ionization, are focused into an electrostatic quadrupole deflector or switching lens. The switching lens multiplexes ions from either the closed or open source into a single radio frequency quadrupole mass analyzer, which separates the ions according to their mass-to-charge ratio. The ions are detected by two secondary electron multipliers operating in

pulse counting mode to cover the dynamic range required. Appendix A gives some of the instrument parameters.

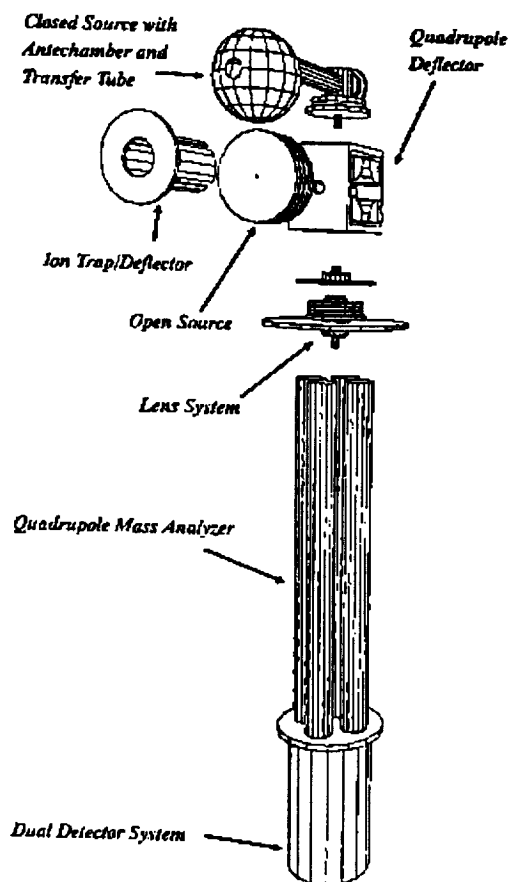
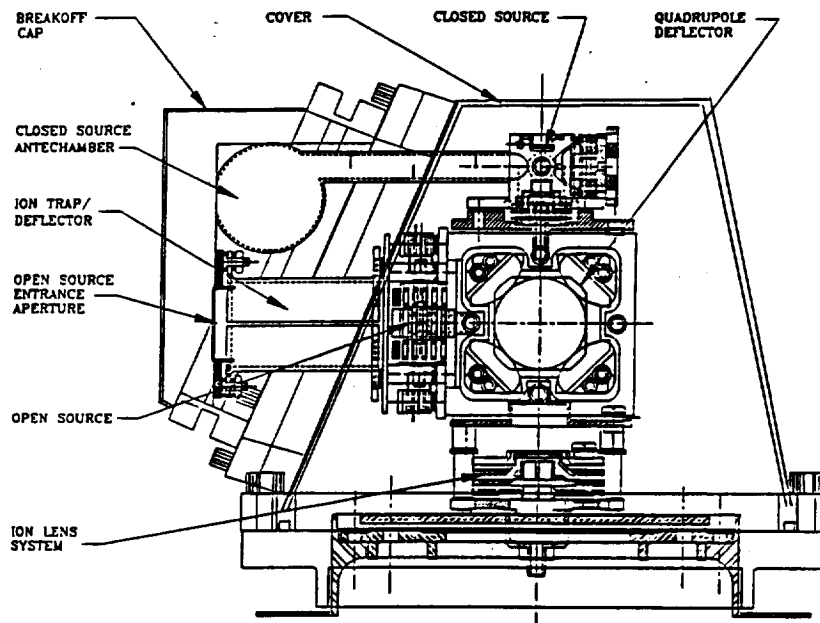


Figure 1: The INMS sensor.

The complete layout of the INMS sensor, electronics and other elements is shown in Figure 2. They are packaged in the form of a box. The entrance apertures are contained in a single plate covered by a metal-ceramic breakoff hat that is pyrotechnically activated. During cruise, the breakoff hat is protected by thermal shielding. The INMS instrument is mounted on the Fields and Particle Platform (FPP), with the normal to both the open and closed source INMS orifices pointing in the spacecraft -X direction. The fields of response of the two gas inlets are different. The geometric field of view of the open source is limited to about 8° cone half angle, which limits the angular response of neutral and ions measured in this inlet. The closed source has a much wider field of response, approximately 2° steradians. Venting of the ion sources occurs at right angles to the -X axis. This is to lower the ion source and analyzer pressures (increasing the ion mean free path) during a Titan pass when the spacecraft ram approximately along the -X direction. The electronics are mounted on boards parallel to the FPP platform. The sensor is made mainly of titanium and the electronics box of aluminum to be strong, yet lightweight. The box forms an electrostatic shield for the instrument as well as providing micrometeoroid and high-energy particle protection. The entrance apertures of the sensor protrude beyond the edge of the FPP platform and the spacecraft multilayer insulation. This is to prevent gas contamination from the spacecraft and provide maximum field of view.



**Figure 2:** The layout of the INMS sensor, electronics and other elements.  
(Courtesy, NASA)

The main electronic subsystems of the INMS instrument (developed by the Space Physics Laboratory at the University of Michigan) include a dedicated instrument microprocessor, spacecraft interface circuits, analog modules, and interfaces between the CPU and the analog modules. Major analog modules are circuits to regulate the emission of electron and ion guns, fixed voltage and programmable power supplies to set the potentials on the lenses, RF/DC supplies for the mass analyzer, high voltage supplies for the detectors and pulse counting circuits.

The mass spectrometer is constructed of titanium and is free of organic materials. The sensor and ion sources are maintained under a vacuum to keep them clean until ambient neutral atmosphere measurements can be made. They are opened to the external environment by the ejection of the pyrotechnically activated breakoff hat after Saturn Orbit Insertion.

### **INMS Operation**

The closed source (Figure 1) which measures neutral gases consists of a spherical antechamber with an entrance orifice for the ambient gas flux. The chamber is connected to the entrance of the ionization region by a long cylindrical tube. Ionization of the gas flux is achieved by the use of a collimated electron beam from two redundant electron gun assemblies. The ions formed are focused into the quadrupole switching lens by a series of cylindrical electrostatic lenses. The incoming gas makes many collisions with the antechamber surfaces and thermally accommodates to the wall temperatures. A ram enhancement is achieved by limiting the gas conductance from the antechamber into the ion source while maintaining a high particle flux into the entrance aperture.

The entrance aperture of the open source leads to a cylindrical antechamber consisting of four plates in four equally spaced segments. This ion trap/collimator is used to focus ambient ions into an exit aperture while the instrument is operating in the "ion mode" and to trap ions while operating in "neutral mode". There are four electrostatic lenses in the open source, which focus the ions into a quadrupole deflector or switching lens. All the electrostatic lenses of the open sources and the switching lens, with the exception of the entrance plate are programmable. This allows optimization of the lens system to measure both ions and neutrals following the

spacecraft equivalent of energy. In neutral mode, they can be programmed to discriminate gas particles that have thermally accommodated to the ion source walls from the direct beaming component at spacecraft energies. In ion mode, they can be used to steer the incoming ions to perform a coarse energy scan. Optimal sampling in the open source occurs when the instrument ram direction aligns with the axis of the open source and the ion trap/deflector.

The electron guns have filaments (0.0076 cm, 97% tungsten-3% Rhenium) in a coiled configuration, which are heated to provide an electron beam that is collimated and focused by electrostatic lenses. Two electron impact ionization energies are provided: 70 and 25 eV. The electron emission is 40  $\mu$ a.

The quadrupole deflector or the switching lens consists of four circular rod sectors mounted in a cube assembly to provide a nearly hyperbolic electrostatic field for a 90° deflection. This electrostatic device allows the closed source and the open source to be sequentially switched into the common entrance lens system of the quadrupole mass analyzer. Since the deflector voltages are programmable, the instrument can be configured to measure the energy distributions of incoming ions with energies from -1 eV to over 100 eV. The energy resolution of the deflector  $\Delta E/E$  is 0.3 for a 0.3 cm entrance and exit aperture diameters. The switching lens potentials can be scanned to provide an estimate of the ion and neutral energy distribution up to about 150 volts since the potential on each rod can range from 0 to -300 volts. Doubly charged species require a different potential on the rod segments than do singly charged species.

The quadrupole mass analyzer consists of four precision ground hyperbolic rods mounted in a mechanical assembly. The rod spacing parameter,  $r_0$ , is 0.58 cm and the rod length is 10 cm. The quadrupole rods are excited by Radio Frequency (RF) and Direct Current (DC) electric fields, which are varied between adjacent rod pairs while opposite rod pairs are kept at the same potential. The dynamic electrostatic field thus created within the quadrupole region controls the transmitted mass (mass/charge ratio), the resolution, and the transmission efficiency. Mass scan is controlled by varying the potential amplitude,  $V_{ac}$ , to satisfy the relationship  $M = 0.55 V_{ac}/f^2$  where  $V_{ac}$  is in volts,  $f$  is the RF frequency in megahertz, and  $M$  is in atomic mass units (amu). The nominal mass range for the INMS is 1-8 amu and 12-99 amu using two separate frequencies. The frequency,  $f$ , is counted and is used to compensate for drift. The resolution is controlled over each mass range by programming the  $V_{dc}/V_{ac}$  ratio to maintain the resolving power as defined by a crosstalk criterion appropriate for that mass range. The resulting flat-topped peaks allow a mass scan mode in which each mass is monitored by a single step to achieve the lowest detection limit in a specified period. Another operating mode reduces  $V_{dc}$  to zero and creates a high pass filter giving the sum of all masses greater than a specified value. Mass scans are controlled by a microprocessor to allow for a range of microfrequencies.

Two secondary electron multipliers operating in a pulse counting mode detect the ions exiting the quadrupole. The multipliers differ in signal detection level by about a factor of 2000. The upper count rate of each detector system is about 10 MHz, limited by the product of the multiplier pulse width and gain bandwidth of the pulse amplifier counter system. Ion counts above this value can be measured directly as an analog current. The dynamic range of the two detector system is  $\sim 10^8$ .

To make valid ion and neutral density measurements, the spacecraft velocity vector plus any atmosphere or ionosphere drift velocity must be within the field of response of the appropriate source of the INMS. During Titan flybys the spacecraft can operate either in Radar Mode with the radar tracking local nadir or in INMS Mode with the spacecraft velocity vector tracking the INMS axis. In Radar Mode the INMS angle of attack ranges from 0° to 8° within 2.4 minutes of closest approach at a spacecraft speed of 6 km/sec. The altitude change is 60 km over a spacecraft track length of 870 km.

## Technical Objectives

While the INMS is the result of many improvements of the mass spectrometer models that have been used in NASA's space missions, NASA continues its attempts to improve the performance and reduce the size and weight of the mass spectrometer for its future missions. The trend towards smaller payload points to the need for small low weight, low power and compact sensors. Princeton Electronic Systems, in collaboration with the David Sarnoff Research Center (Sarnoff), undertook the project to provide NASA with accurate simulations of the ion optics of the INMS and to develop designs with lower size and weight. The goal would be achieved through the following major tasks:

- Simulate accurately the ion optics of the INMS sensor from the entrance aperture to the quadrupole mass analyzer and compare results of transmission analyses with experimental data provided by NASA. This would help in validating the model and also to assess improvements in performance and size of redesigned models.
- Carry out simulations varying the configuration of the electrodes and also the potentials to optimize the geometry of the open source for maximum collection efficiency and angular acceptance.
- Carry out simulations of the quadrupole deflector or the switching lens. Simulations with reduced disk separations would determine the limits on these reductions beyond which the performance is degraded and aid in the construction of a smaller deflector.
- Carry out simulations varying the configuration of the exit lens electrodes (ionlens system) for maximum transmission. Some electrodes could be reduced in size or completely eliminated to reduce overall size and weight of the sensor.
- Carry out sensitivity analysis to identify electrodes that need to be rigid and can be used as support structures. Also identify electrodes whose shape or size could be altered to reduce overall size and weight and increase performance. This would involve simulations with reduced component dimensions to identify limits on these reductions beyond which the performance is degraded beyond specified values and regained by design.
- Simulate the mass analyzer. Simulations with smaller quadrupole lengths would help in the construction of a more compact sensor. Simulations of the assembly of the exit lens system and the mass analyzer and a study of peak shapes would identify means of improving performance.
- Identify materials that are good candidates for lighter weight components. This would involve an investigation of lighter weight materials and their suitability for mass spectrometer applications.

With the experience gained from the project, PES also undertook, with limited funds, to build a field portable Gas Chromatograph Mass Spectrometer based on the small GC-MS technology developed by Lawrence Livermore National Laboratory and the bench top GC-MS developed by the Hewlett-packard Company.

## **The BEAM3D Ion Optics Program**

The INMS was modeled in three dimensions and simulations carried out using BEAM3D, an ion optics simulation software developed at Sarnoff over a period of thirty years and \$75 million investment for the design of high performance electron guns and magnetic deflection systems for color television picture tube industry. Today, this proprietary software is heavily used by Sarnoff to design commercial TV tubes for Thomson and high performance displays and other electron beam systems for commercial customers and the US Government. BEAM3D currently runs on Sun<sup>TM</sup> workstations.

BEAM3D is fully three-dimensional and enables parametric modeling of complex and coexistent electrostatic and magnetic structures. The program relies on input files created by the user or obtained from the BEAM3D library. Tasks are invoked by typing commands at the operating system level. A workstation or a terminal supporting graphics is used to view current density plots and slit profiles, electron trajectories superposed on device drawings, phase space diagrams, etc.

BEAM3D models 3D static electric and magnetic fields. Parametric models for electrostatic parts facilitate studies involving part geometry changes without requiring the user to create a separate model for each case. BEAM3D models steady state electron beams. The space charge limited emission from a flat thermionic cathode is computed using a self-consistent calculation based on Langmuir diode cells. General user-specified current distributions are also supported. The beam propagation takes into account the magnetic and electrostatic focusing and deflection effects produced by the components in the device as well as the mutual repulsion of the beam electrons.

BEAM3D provides a flexible method for defining the device and its operating conditions. Symbolic names for reference planes within each part allow for the assembly of one component relative to another. These names are also used to specify beam output planes relative to part features such as the main lens. Symbols can also be used for operating parameters, facilitating electrical interconnections between parts. Automatic methods set operating parameters to values implied by performance objectives.

The BEAM3D program was used to simulate NASA's Ion Neutral Mass Spectrometer in three dimensions. Minor enhancements (described in a later section) to the software were made to simulate the ion optics of the INMS system. All simulations were carried out at Sarnoff using a Sun Sparc workstation.

During the first six months of the project, models of the open source, the quadrupole deflector and the exit-lens system were created based on a set of drawings received from NASA at the beginning of the project. Initial models were generated with the all the major geometrical characteristics of the parts, ignoring detailed geometry. These models underwent minor and some major changes as more detailed geometry became available and we gained better understanding of the construction and operation of the INMS. Minor changes were again introduced during the fourth quarter when NASA sent geometrical parameters from the most recent engineering model of the INMS. The refinement of the models also involved finer discretizations for better accuracy. As refinement progressed, many calculations were repeated to ensure that the analyses corresponded to the latest models. While efforts were made to model INMS as accurately as possible, minor discrepancies in parameters exist. However, these do not affect the trajectory simulations or the results of transmission analyses.

Detailed geometrical parameters obtained from NASA's drawings and those from the BEAM3D model are given in Appendix B. The models have been divided into several smaller sections in order to indicate all the detailed parameters clearly.

## 2. The Open Source

The open source is the part of the mass spectrometer first encountered by ions and neutrals from the atmosphere during satellite motion. Figure 1 shows the open source design of the INMS. The open source consists of two collimating entrance apertures through which ions and neutrals are swept in by satellite motion. The entrance aperture of the open source leads to a cylindrical antechamber consisting of four plates in four equally spaced segments. This ion trap/collimator is used to focus ambient ions into an exit aperture while the instrument is operating in the "ion mode" and to trap ions while operating in "neutral mode". There are four electrostatic lenses in the open source, which focus the ions into a quadrupole deflector or switching lens. All the electrostatic lenses of the open source and the switching lens, with the exception of the entrance plate are programmable. This allows optimization of the lens system to measure both ions and neutrals following the spacecraft equivalent of energy. In neutral mode, they can be programmed to discriminate gas particles that have thermally accommodated to the ion source walls from the direct beaming component at spacecraft energies. In ion mode, they can be used to steer the incoming ions to perform a coarse energy scan. Optimal sampling in the open source occurs when the instrument ram direction aligns with the axis of the open source and the ion trap/deflector.

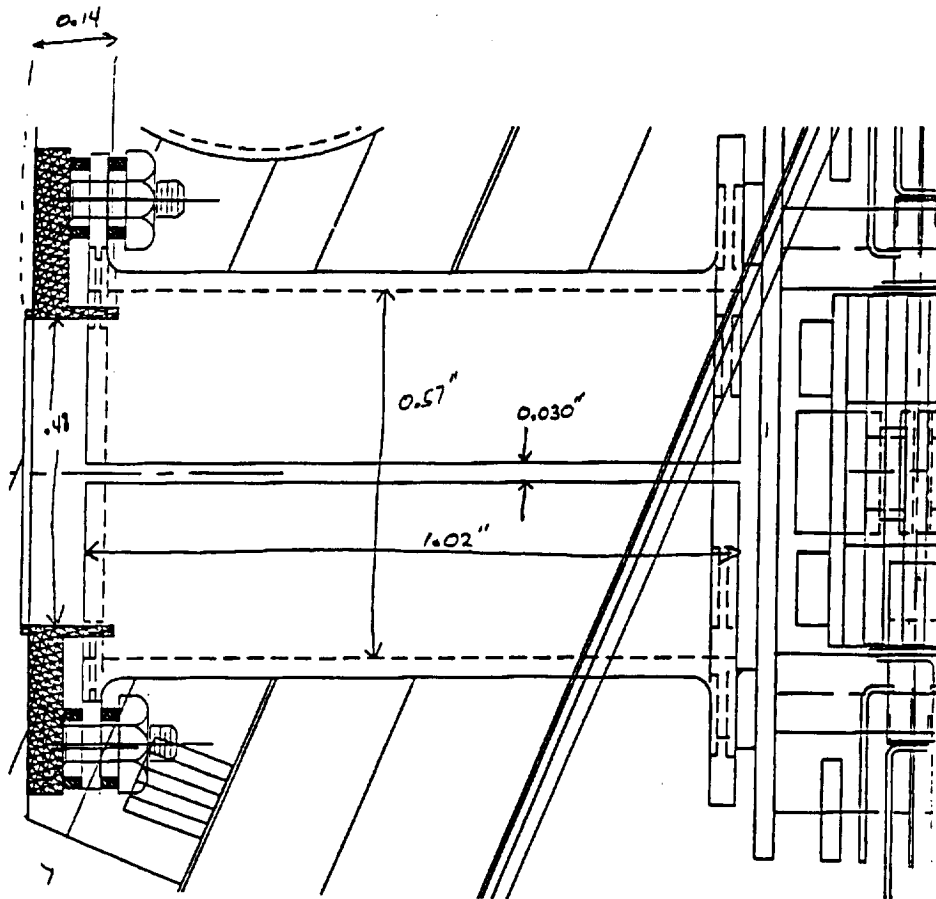
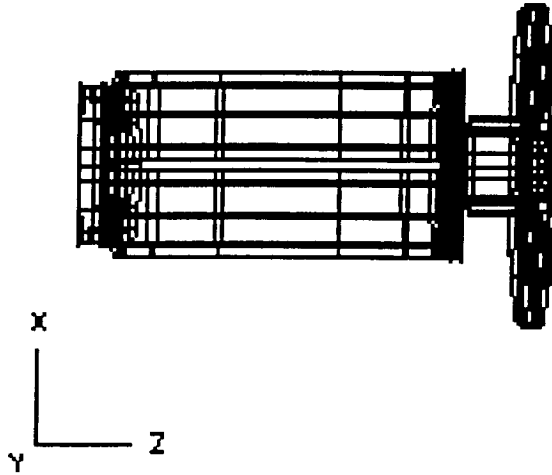


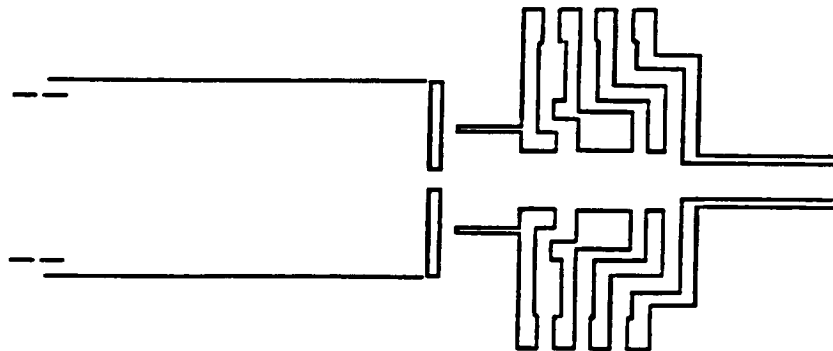
Figure 1: The Open source of the INMS (Courtesy, NASA)

## The Three-Dimensional Model

Figure 2 shows the BEAM3D model of the open source in three dimensions and in cross section.



(a)



(b)

**Figure 2:** (a) The three-dimensional model of the open source and (b) its cross-section.

### The Ion Trap/Collimator

The ion trap/collimator is a cylindrical antechamber consisting of four plates in four equally spaced segments. The cylinder has an inner diameter of 0.57" and a gap of 0.03" between segments. As mentioned earlier, this ion trap/collimator is used to focus ambient ions into an exit aperture while the instrument is operating in the "ion mode" and to trap ions while operating in "neutral mode". Figure 3 shows the segmented cylinder in different orientations. The voltages on the four plates are programmable. An average potential on all four segments focuses the ions on the aperture plate while a potential difference applied between opposite pairs of segments deflects ions towards the aperture. The ion trap can be configured in two ways differing in the orientations of the segments, one obtained by a 45° rotation of the other.

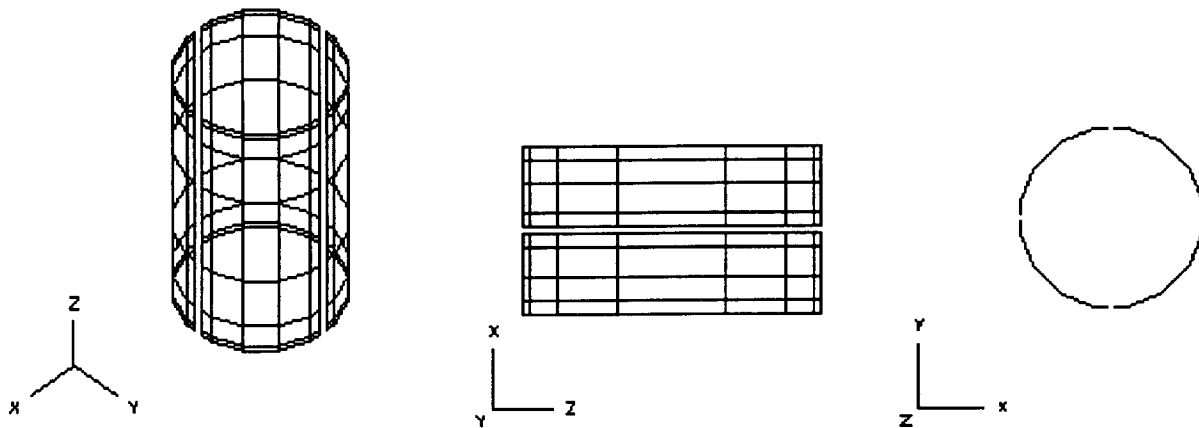


Figure 3: The Ion Trap/Collimator in different orientations.

### The Aperture Plate

The aperture plate (Figure 4) is a thin plate at the end of the ion trap/collimator, which focuses ions through a small aperture of diameter 0.02". The voltage on this plate is programmable from 0 to -300 volts.

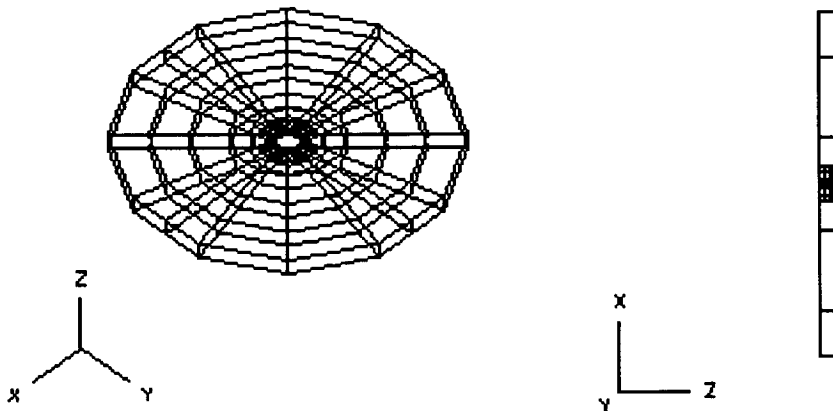


Figure 4: Beam3D model of the aperture plate at the end of the ion trap/collimator.

## The Electrostatic Lenses of The Open Source

There are four electrostatic lenses in the open source. The geometry of the four lenses with the aperture plate is shown in Figure 5. The beam3D model of the same is shown in Figure 6.

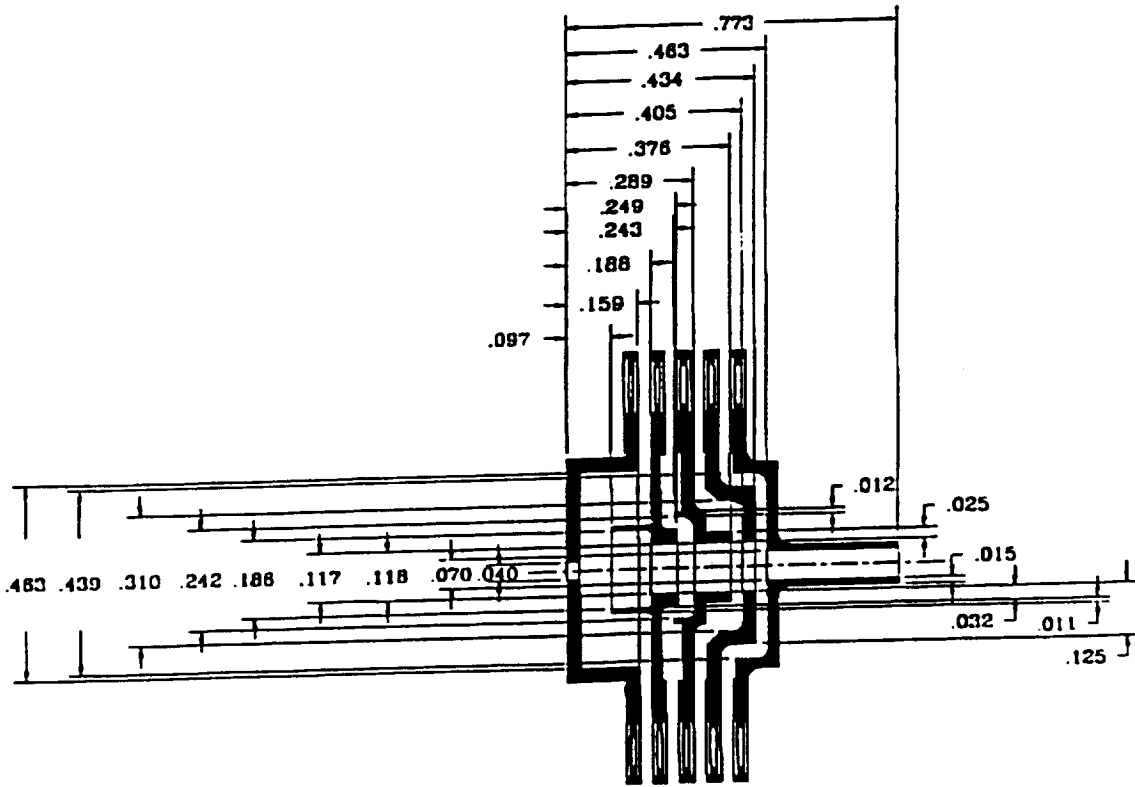


Figure 5: Geometry of the electrostatic lenses of the open source.

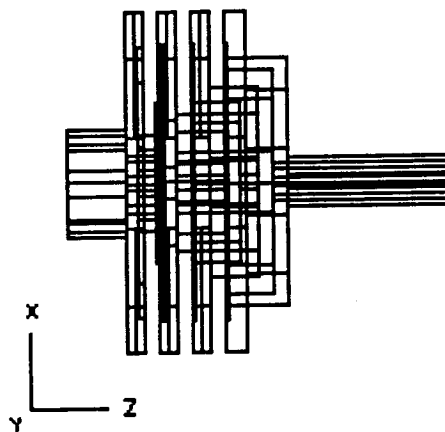
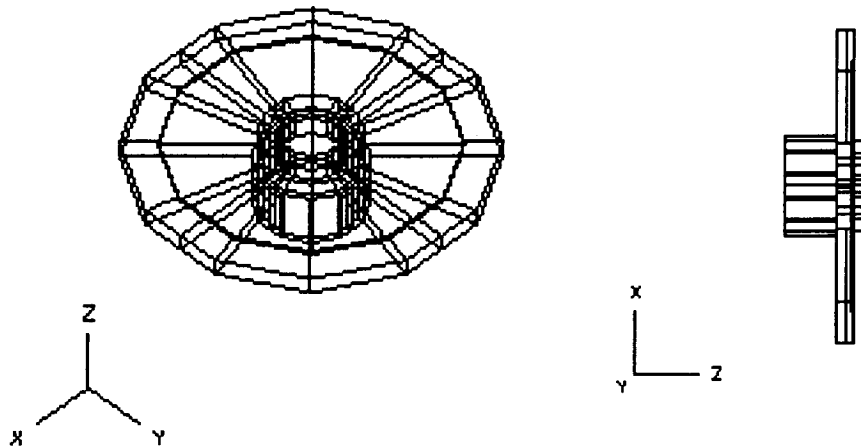


Figure 6: BEAM3D model of the electrostatic lenses of the open source.

**Lens 1:** Shown in Figure 7, this is the entrance electrode of the ionization chamber where neutrals are ionized. The cylindrical part has a thickness of 0.022", with an aperture of diameter 0.118", separated from the aperture plate by 0.03".



**Figure 7:** BEAM3D model of Lens 1 of the open source.

**Lens 2:** Lens 2 (shown in Figure 8) is the second electrode of the chamber where neutrals are ionized - Neutrals are ionized in this chamber by an electron beam, not shown in the figure. Ions with sufficient initial energy pass on to the last electrodes and other parts of the mass spectrometer, while those with reduced energy are reflected back. This is a cylinder of thickness 0.022", with an aperture of diameter 0.118", separated from the entrance electrode by 0.03".

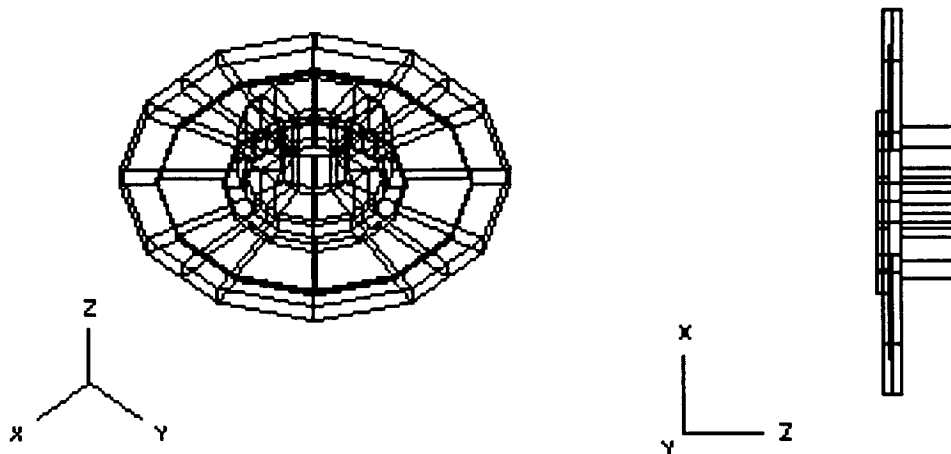


**Figure 8:** BEAM3D model of Lens 2 of the open source.

**Lens 3:** This is the focus electrode of the decelerating lens, also called the repeller electrode (Figure 9). This collimates the ions for the quadrupole deflector. This is a cylinder of thickness 0.022", with an aperture of diameter 0.118", separated from the chamber electrode by 0.03".

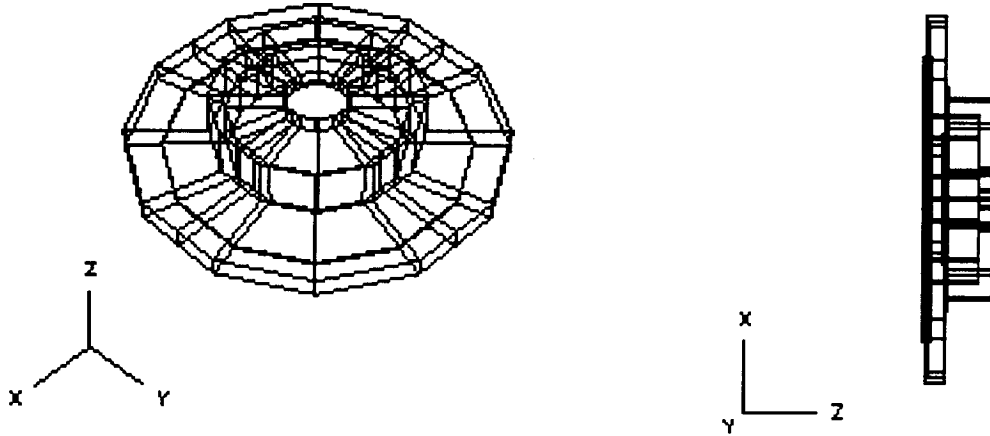


**Figure 9:** BEAM3D model of Lens 3 of the open source.

**Lens 4:** This electrode, called the extractor electrode, is the second part of the decelerating lens (Figure 10) - Ions exit from here into the quadrupole deflector. This has a thickness of 0.022", with an aperture of diameter 0.070", separated from the focus electrode by 0.03".

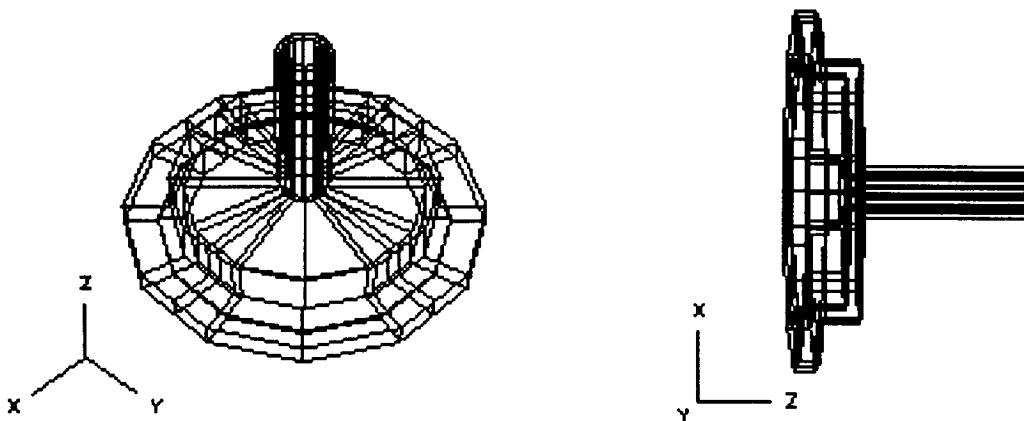


**Figure 10:** BEAM3D model of Lens 4 of the open source.

## Open Source Simulations

When the INMS operates in the open source mode, the relative motion of the spacecraft with respect to the ambient atmosphere is used to discriminate between fast and slow moving ionized neutral particles when the ion source is approximately pointed in the direction of motion. The geometry allows ambient gas to enter the ionization region directly and permits measurements of chemically active species. The angular response is limited by the geometric field of view to a cone of about  $8^\circ$  half angle.

- Simulations of the open source were carried out to
1. To analyze transmission through the open source and to optimize transmission by varying voltages on different electrodes of the open source.
  2. To study the angular response of the open source in the ion mode for ions of masses ranging from 1 to 99 amu.
  3. To determine transmission sensitivity to voltages and geometrical parameters of the electrodes.
  4. To analyze transmission of neutral species.

To analyze transmission through the open source, some simulations were carried out with two different models. These two models correspond to two possible orientations of the ion trap in the INMS. Figure 11 shows the perspective end views of the segmented cylinder in two orientations. The actual dimensions of the inner and outer arcs are the same, the inner arc being away from the observer. In 11a, the  $yz$  and  $xz$  planes intersect the gaps between the segments while in 11b, they bisect the segments. The orientation in 11b is obtained by a rotation of the structure in 11a by  $45^\circ$ . The  $z$ -axis coincides with the axis of the source. The satellite motion is in the  $xz$  plane.

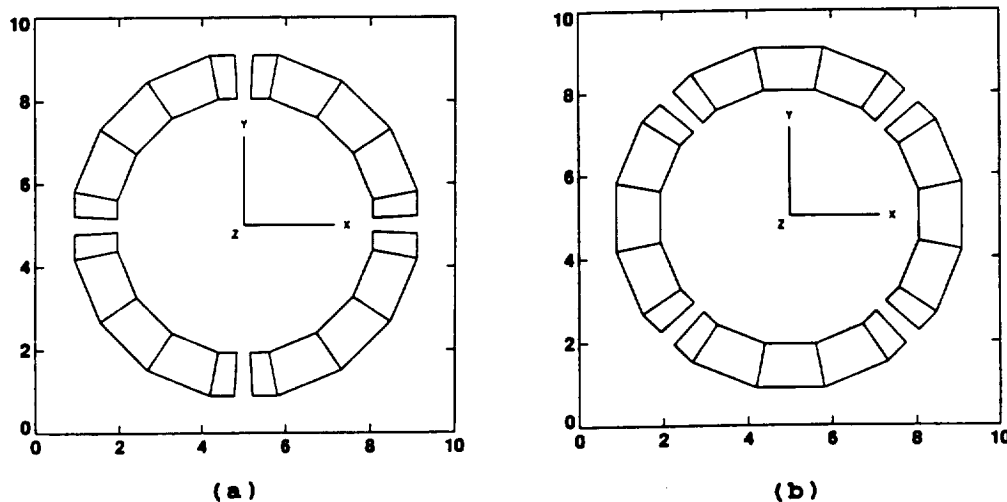


**Figure 11:** Perspective end views of the ion trap/collimator in two orientations. The actual dimensions of the inner and outer arcs are the same, the inner arc being away from the observer. In 11a, the  $yz$  and  $xz$  planes intersect the gaps between the segments while in 11b, they bisect the segments. The orientation in 11b is obtained by a rotation of the structure in 11a by  $45^\circ$ . The  $z$ -axis coincides with the axis of the source. The satellite motion is in the  $xz$  plane.

## Transmission Analysis

To analyze transmission through the open source, preliminary simulations were first carried out to compare the results of BEAM3D calculations with those provided by NASA. For these calculations, the model used was a simpler version, ignoring some of the geometrical detail (some errors in this model were discovered at a later stage and corrected in the final model). Since no experimentally measured results of transmission through the open source were available, BEAM3D calculations were compared with those obtained under identical conditions using another ion-optic simulation software called SIMION, provided by NASA. Transmission was calculated as a function of the voltage on the aperture plate.

Figure 12 shows the outline of the preliminary, simple open source model in xz plane with trajectories of ions entering parallel to the axis of the device. The ion flux is simulated as a beam current with uniform current density over the entrance aperture. The beam contains more than a thousand trajectories of which only a fraction is shown in the figure.

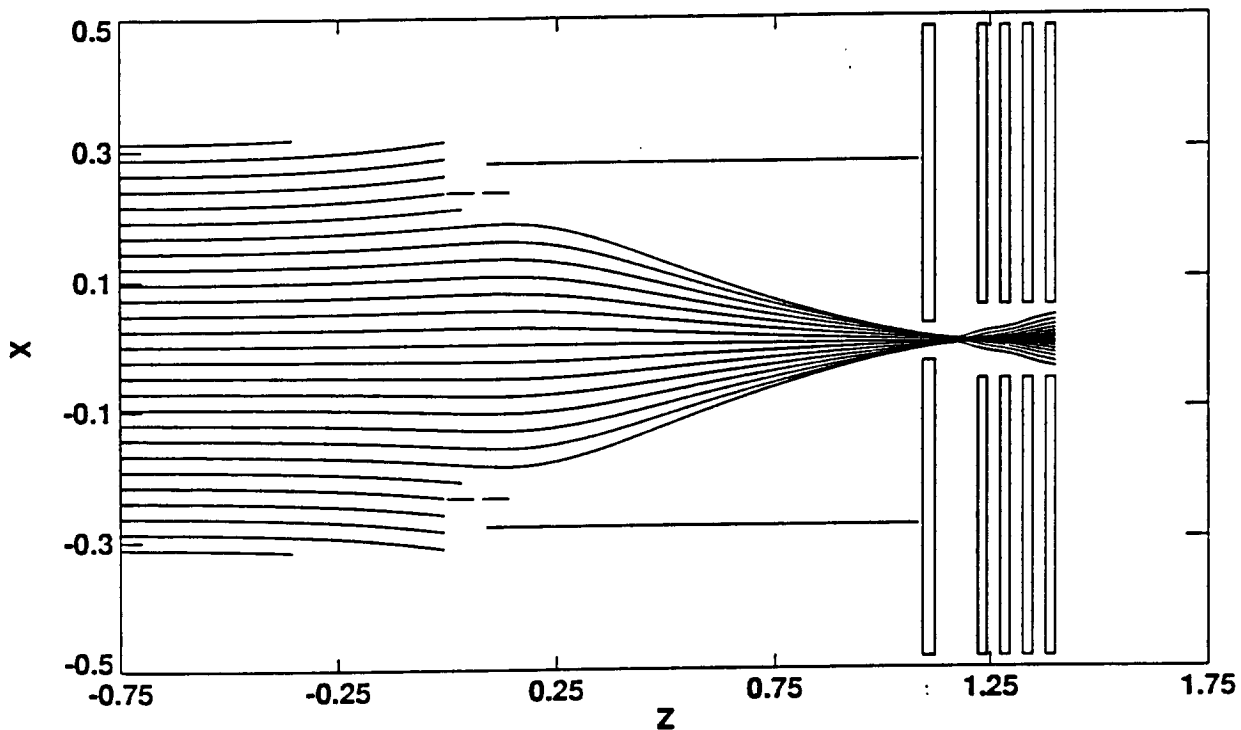


**Figure 12:** Outline of the model of the open source with trajectories of ions entering parallel to the axis of the device.

For ions entering parallel to the axis of the device, transmission was calculated as the ratio of the residual current at the exit to the current at the entrance of the open source. The entrance electrodes, the ion collimator/deflector plates, open source lenses 1 and 2 were all maintained at 0 Volts; the repeller electrode (Lens 3) and the extractor electrode (Lens 4) were held at 20 and 50 Volts respectively. Transmission was calculated as a function of the voltage on the aperture plate. Figure 13a shows the results for 1, 28, and 75 amu ions, (assuming the velocity of the spacecraft to be 6 km/sec, the equivalent energies are 0.187, 5.224, and 13.993 respectively) with no thermal energy spread. Figure 13b shows SIMION calculations for the same cases, showing good agreement between the two calculations for voltages at which maximum transmission occurs. For the four cases, maximum transmission occurs at aperture voltages of -4.2, -200, -600 Volts. In the above simulations, monoenergetic ions were used, ignoring the effect of thermal variation.

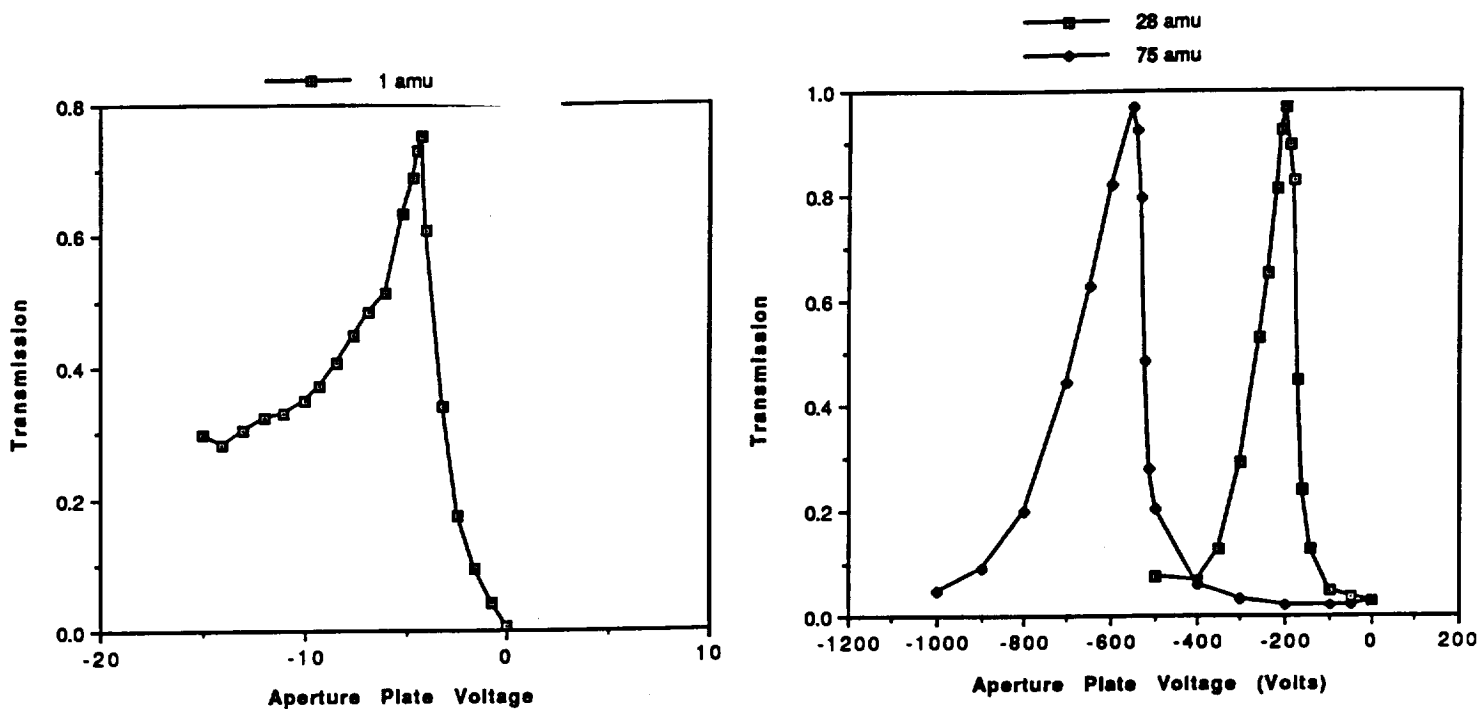


Figure 13a: Open source transmission of 1,28 and 75 amu ions as a function of voltage on the aperture plate calculated using the BEAM3D model.

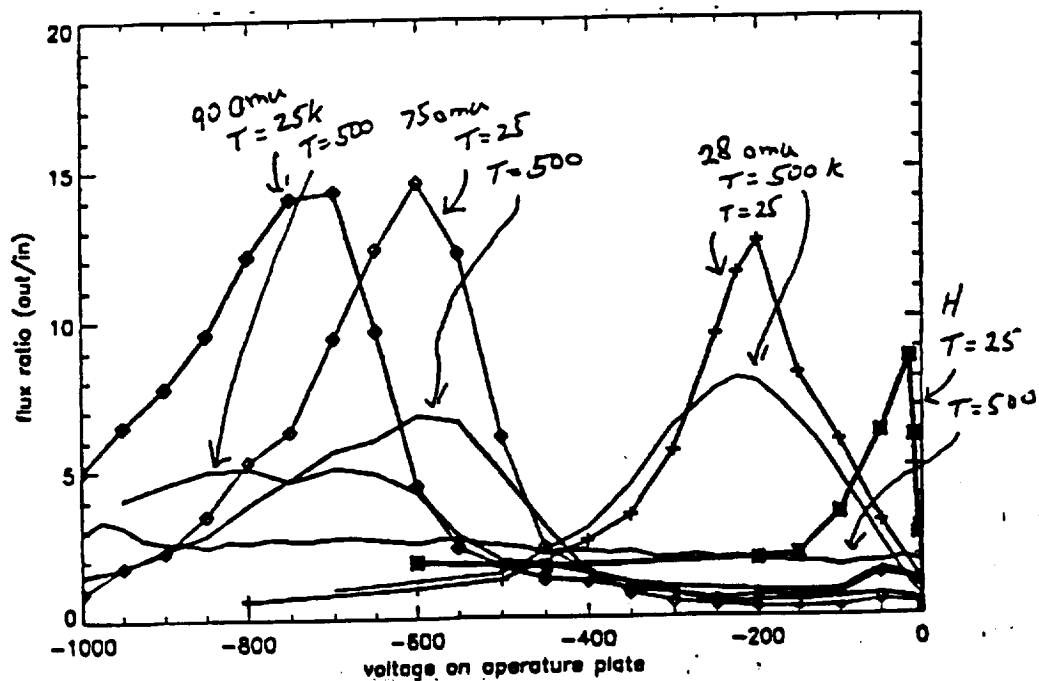
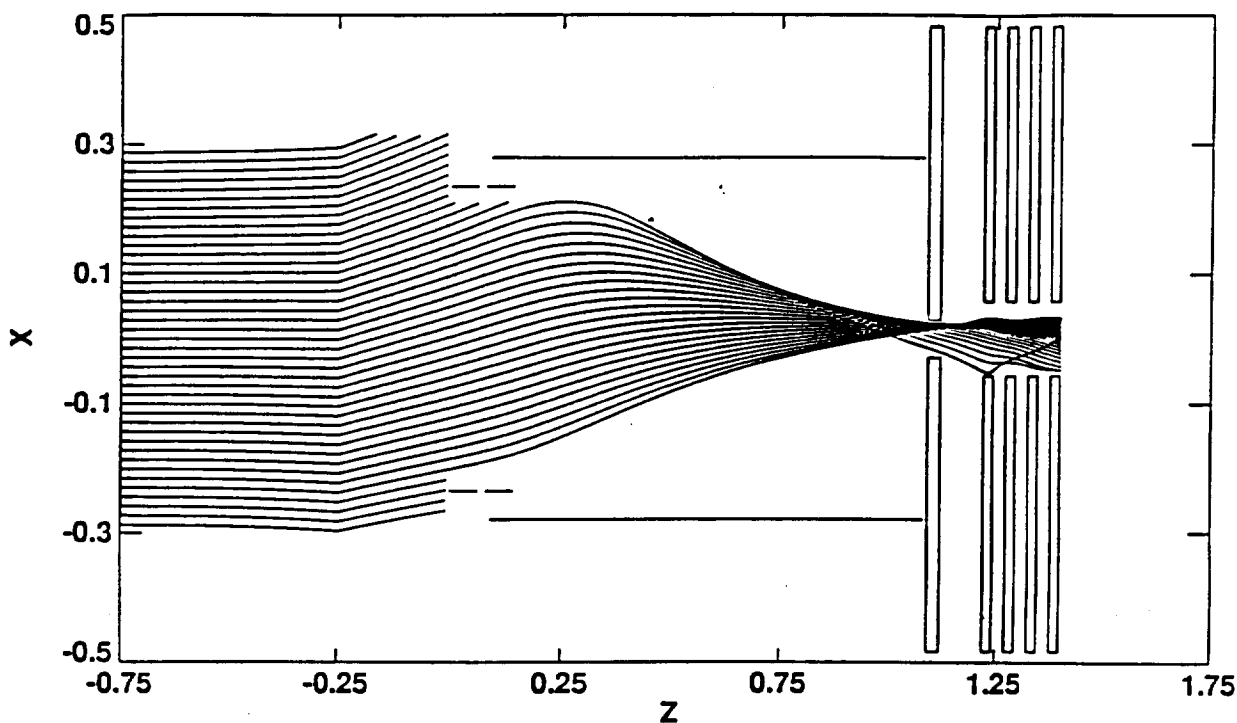


Figure 13b: INMS ion transmission as a function of voltage on the aperture plate using SIMION.

Of more interest is the case where ions enter the open source of the mass spectrometer at an angle as it occurs during satellite motion. Figure 14a shows the  $xz$ -plane trajectories of ions entering the open source at an angle. The off-axis beam is simulated by artificially deflecting the beam prior to entering the open source. As the direction of motion of the satellite changes continuously, ions enter the open source in different directions. With increasing angle of attack (the angle in the  $xz$  plane of Figure 14a between the direction of satellite motion and the axis of the device), more and more ions are lost due to impact with the sides of the ion trap resulting in a rapid decline in transmission. However, considerable improvement in transmission can be achieved by applying appropriate potentials to the ion trap to deflect the ions and focus them towards the aperture. Further, potentials on the lenses can be varied to maximize their transmission efficiency as demonstrated by the following simulations with ions with an initial energy of 3 eV.

As mentioned earlier, with increasing angle of incidence, more and more ions are lost by impact with the ion trap segments and the aperture plate. Deflecting potentials can be applied to the ion trap segments to direct the ions towards the aperture. The average potential on all four segments focuses the ions to the aperture in the aperture plate. The potential difference between the upper and lower segments deflects the ion focus to coincide with the aperture. The upper(lower) segments in Figure 11a are the pairs of segments above(below) the  $yz$  plane; they are the single segments intersecting the  $xz$  plane in Figure 11b. A potential difference between adjacent segments, with opposite segments at the same potential, forms a quadrupole lens that adjusts for astigmatism in the focus. Without it, ions in the  $xz$  and  $yz$  planes may focus behind or in front of the aperture. Fig 14b shows  $yz$ -plane trajectories for the same case. It should be noted that the symmetry exhibited by these trajectories is due to the symmetry in the orientation of the segments.



**Figure 14a.**  $xz$ -Plane trajectories of ions entering the open source at an angle, with deflecting potentials on the ion trap segments to focus them towards the aperture.

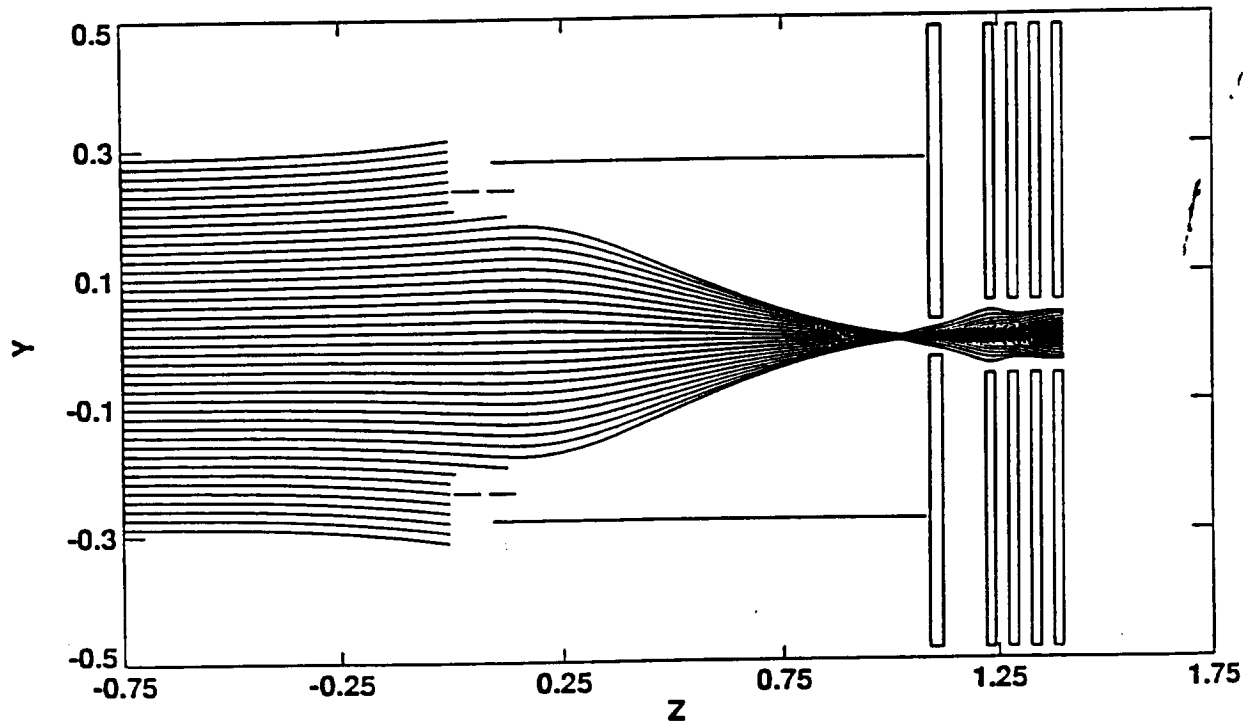


**Figure 14b.**  $yz$ -Plane trajectories of ions entering the open source at an angle, with deflecting potentials on the ion trap segments to focus them towards the aperture.

A detailed analysis of transmission as a function of the voltages on the four segments of the ion trap was done. For the model with the ion trap in the  $0^\circ$  orientation (Fig 11a), simulations were carried out in the following steps:

- With all four segments at the same voltage, trajectories were simulated with varying voltages on the ion trap to find the best focus voltage.
- The two upper segments were then separated from the two lower segments and assigned different potentials so that the structure essentially functioned as a deflector of the ions entering the ion trap at an angle. Ion trajectories in both  $xy$  and  $yz$  planes were simulated to analyze the results of these potentials on focusing. Keeping the angle of incidence constant, voltages were varied to achieve focusing in both the planes as close to the ion trap aperture as possible to achieve maximum transmission through the ion trap.
- Small quadrupole voltages were then applied to the four segments to bring the focus planes closer.
- The above simulations were repeated for various angles of incidence up to  $20^\circ$ .

Figure 15 shows the variation of transmission as a function of the deflection voltage (voltage difference between the two pairs of segments) for an angle of incidence of  $13.6^\circ$ . For this angle, highest transmission is obtained for a voltage difference of about 1.35V. A similar analysis was conducted for different angles of incidence. Figure 16 shows the voltage difference at maximum transmission as a function of the angle of incidence, showing a linear dependence. Maximum transmission is obtained for a voltage difference of approximately 0.105 volts/degree of the incident angle.

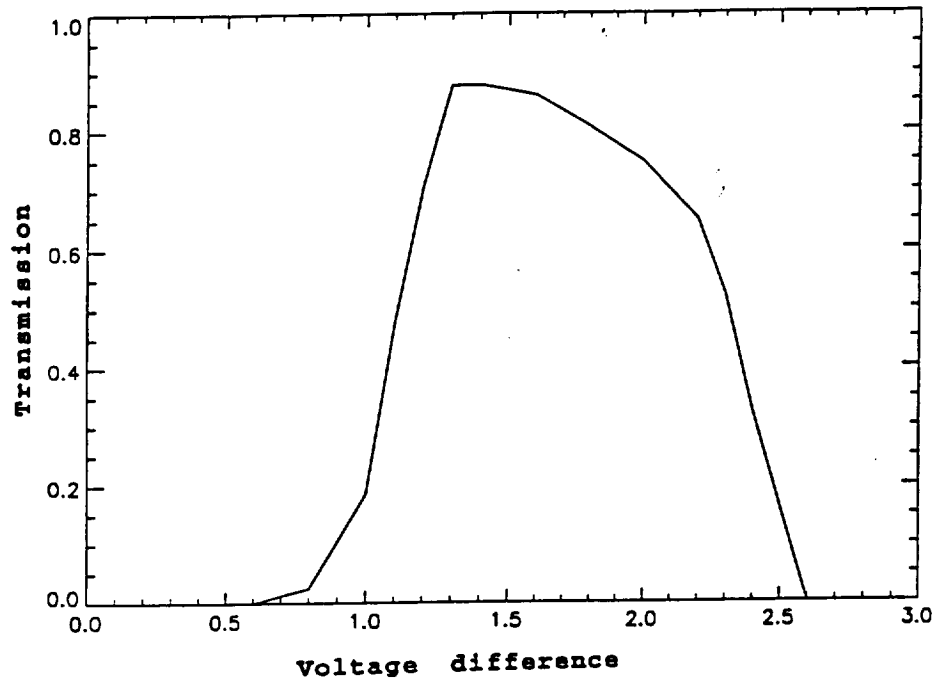


**Figure 15:** Variation of transmission with deflection voltage for 3 eV ions at an angle of attack of 13.6°.

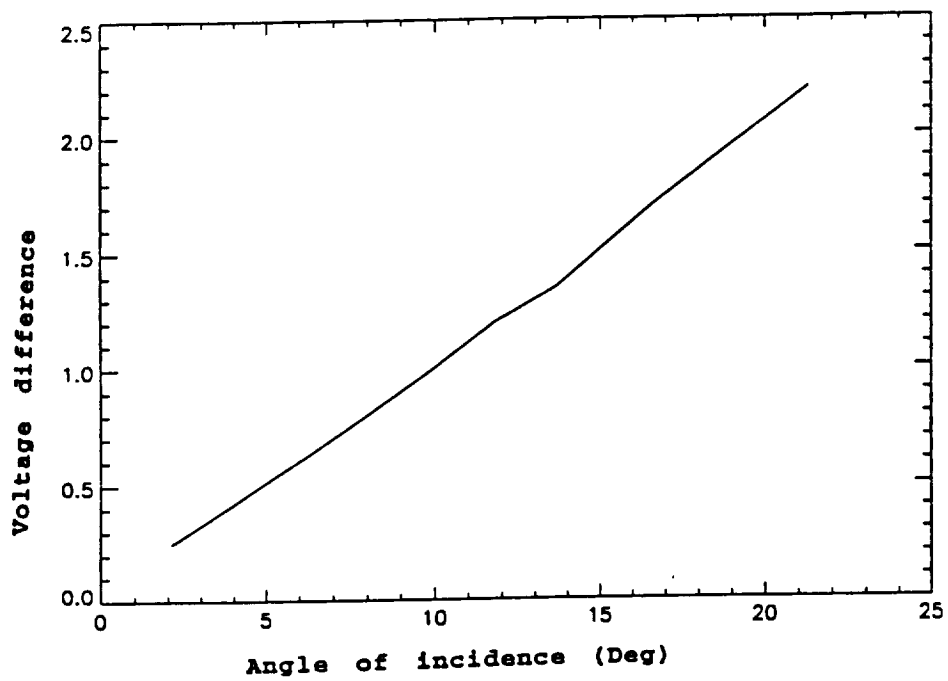


**Figure 16:** Variation of voltage difference at maximum transmission with angle of incidence.

The analysis was repeated with the ion trap rotated through  $45^\circ$  as in Figure 11b. In this case, voltages on one pair of segments that intersect the yz plane were kept constant while the voltage difference on the pair that intersects the xz plane was varied to get maximum transmission. Small quadrupole voltages were then applied to study their effect on transmission. The analysis showed that

- Transmission was improved from 0 to 90% by the use of deflection voltages.
- Application of quadrupole voltages did not improve transmission significantly for either orientation of the ion trap. The transmission did not show sensitivity to small quadrupole voltages. Application of larger quadrupole voltages resulted in a reduction of transmission.
- No appreciable differences in transmission were observed for the two orientations of the ion trap. Further simulations were carried out with only the model with the ion trap orientation shown in 11a.

### Simulations with the Detailed model

As mentioned earlier, the above simulations were carried out with a simple model, ignoring details of the geometry. As more details of the geometry became available, the open source was modeled in detail to conform to the latest drawings and improvements were made. The improved model is shown in cross section in Figure 17. Some of the analyses including the angular response of the open source described earlier were repeated with the new model and are reported here. In these simulations for ions of masses 1, 28, 75 and 99 amu, the voltage on the aperture plate was maintained within the INMS operating limits of -300 volts to +300 volts.

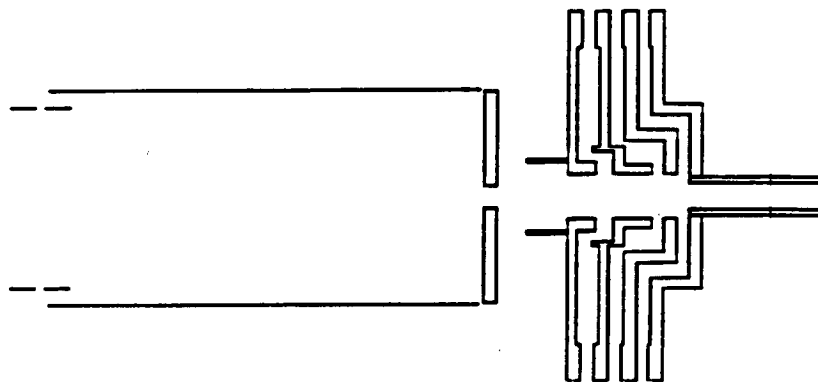


Figure 17: Detailed model of the open source in cross-section.

With the new model, transmission calculations were done with the following parameters: For a satellite velocity of 6 km/sec and ions of masses 1 amu and 28 amu (energies 0.187 and 5.22 eV respectively), the voltage on the aperture plate was optimized for optimum transmission keeping the voltage on all the ion trap segments zero. This however is not possible for the higher masses of 75 and 99 amu ions (energies 13.992 and 18.871 eV respectively), if the aperture voltage has to be maintained within the INMS operating limits of -300 volts to +300 volts. In these cases therefore, keeping the voltage on the aperture plate at the maximum allowed voltage of -300 volts, voltage on the ion trap segments (same on all four) was optimized for maximum transmission. The parameters used in the simulations are as follows:

Mass (amu)	Aperture plate voltage (Volts)	Ion trap voltage (Volts)
1	0	-4.8
28	0	-200
75	-4	-300
99	-10.5	-300

The voltages on the four electrodes of the open source (starting from the one closest to the aperture plate) were -10, -5, -20, and -50 volts respectively.

Keeping the voltage at these values, the angle of attack was varied and transmission at the exit of the open source calculated. Figure 18 shows the variation of transmission with angle for the four cases. As observed earlier, losses in the entrance lens increase with ion energy.

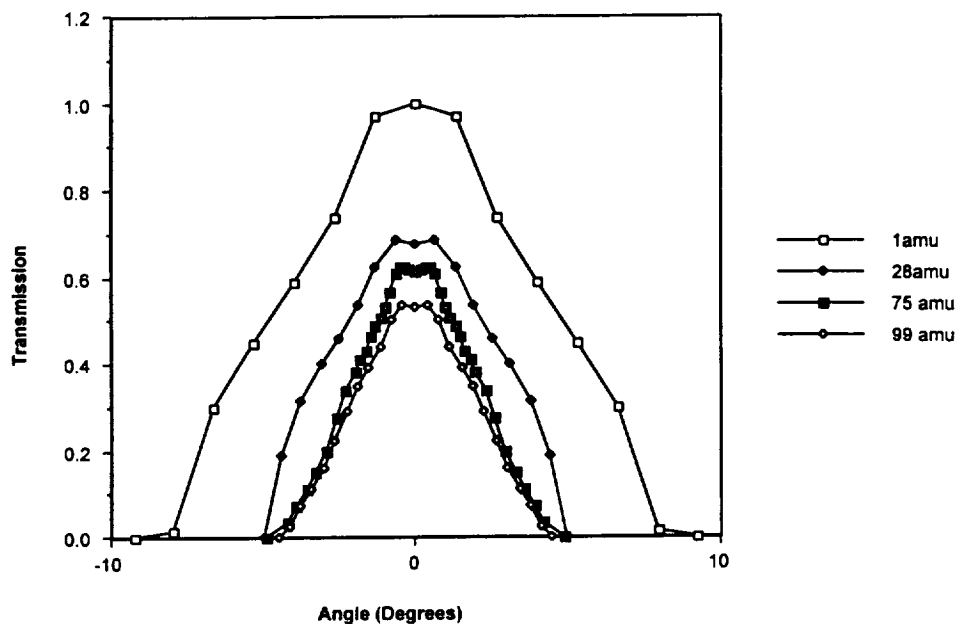


**Figure 18:** Variation of transmission at the exit of the open source with the angle of attack when transmission is optimized at zero angle of attack..

At selected angles, deflecting voltages were applied to the ion trap segments symmetrically about the ion trap voltages (i.e.,  $+dv$  on two of the segments and  $-dv$  on the other two) to maximize the transmission. Figure 19 gives the deflecting voltage (voltage difference between pairs of ion trap segments) for maximum transmission as a function of angle and shows an approximately linear variation. From the curves for 1, 28 and 75 amu ions, it is observed that the deflecting voltage needed for maximum transmission per degree of angle increases with increasing energy. The reason for departure from this trend for 99 amu ions is not clear.

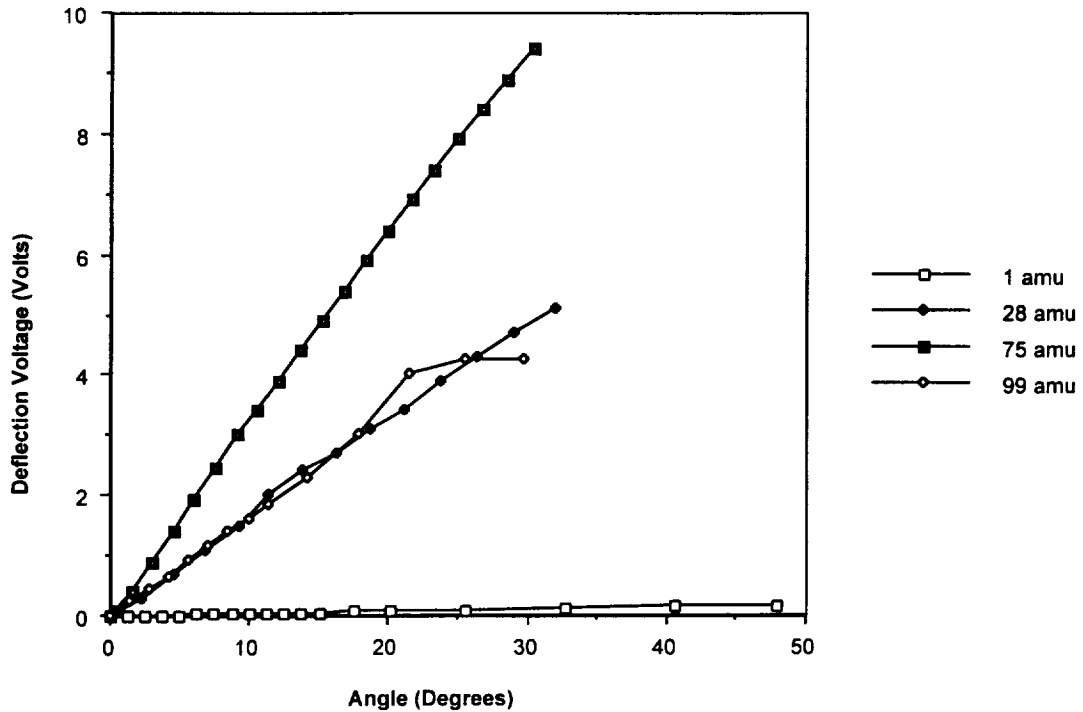


**Figure 19:** Variation of deflecting voltage on the ion trap required for maximum transmission with angle for ions with masses of 1, 28, 75 and 99 amu.

Figure 20 gives the maximum transmission achievable at these angles by the application of deflecting voltage. Comparing the curves with those in Figure 18, one can see the advantage of programming voltages on the 4-segment cylinder plate to increase the angular response of the open source of the INMS in the ion mode beyond the geometric view cone. When the transmission is maximized only at 0° angle of attack, the half width half maximum (HWHM) points for 1, 28, 75 and 99 amu ions are at 4.8°, 3.5°, 2.4° and 2.4° respectively. By applying the deflecting voltage on the ion trap segments at different angles to optimize transmission, HWHM for the four cases increase to 14.5°, 20.5°, 19.0° and 19.0° respectively. This increase in response beyond the geometric view cone is important for increasing the altitude range of coverage for thermal ions. Transmission data for these cases are given in Tables 1 and 2.

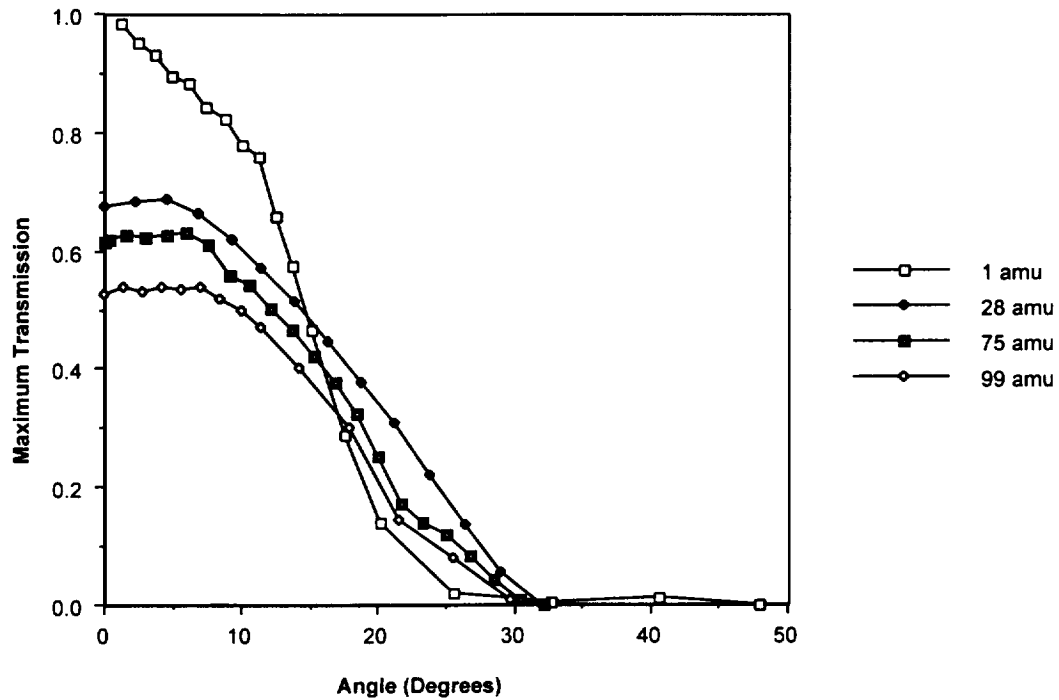


**Figure 20:** Variation of maximum transmission achievable with application of deflection voltage on the ion trap with angle.

**Table 1****Variation of Transmission with Angle**

1 amu		28 amu		75 amu		99 amu	
Angle(Deg)	Transmission	Angle(Deg)	Transmission	Angle(Deg)	Transmission	Angle(Deg)	Transmission
0.000	1.000	0.000	0.673	0.000	0.613	0.000	0.528
1.320	0.971	0.600	0.684	0.180	0.617	0.403	0.535
2.640	0.736	1.300	0.622	0.338	0.621	0.780	0.503
3.960	0.587	1.900	0.537	0.500	0.624	1.150	0.440
5.290	0.446	2.500	0.458	0.660	0.606	1.520	0.388
6.620	0.298	3.100	0.398	0.820	0.565	1.900	0.348
7.940	0.016	3.800	0.315	0.985	0.531	2.270	0.290
9.250	0.000	4.400	0.186	1.147	0.505	2.650	0.224
		5.000	0.000	1.309	0.485	3.020	0.160
				1.470	0.461	3.394	0.113
				1.630	0.428	3.770	0.073
				1.794	0.409	4.145	0.025
				1.954	0.382	4.500	0.000
				2.280	0.335		
				2.606	0.277		
				2.930	0.200		
				3.253	0.148		
				3.574	0.109		
				3.900	0.070		
				4.230	0.033		
				4.870	0.000		

**Table 2**

**Deflection voltage on the ion trap needed to maximize transmission at different angles and the maximum transmission achievable with the deflecting voltages.**

<b>1 amu</b>			<b>28 amu</b>			<b>75 amu</b>			<b>99 amu</b>		
Angle (Deg)	Deflection Voltage	Maximum Transmission	Angle (Deg)	Deflection Voltage	Maximum Transmission	Angle (Deg)	Deflection Voltage	Maximum Transmission	Angle (Deg)	Deflection Voltage	Maximum Transmission
1.230	0.005	0.983	0.000	0.000	0.673	0.000	0.000	0.613	0.000	0.000	0.528
2.470	0.010	0.952	2.300	0.300	0.682	0.310	0.100	0.620	1.420	0.250	0.537
3.700	0.015	0.930	4.600	0.700	0.688	1.530	0.400	0.626	2.840	0.425	0.530
4.940	0.020	0.897	6.900	1.100	0.662	3.020	0.900	0.626	4.240	0.650	0.538
6.180	0.025	0.884	9.200	1.500	0.617	4.520	1.400	0.626	5.630	0.925	0.534
7.420	0.030	0.843	11.400	2.000	0.572	6.000	1.940	0.630	7.040	1.150	0.537
8.670	0.035	0.822	13.800	2.400	0.514	7.510	2.440	0.609	8.440	1.400	0.517
9.920	0.040	0.781	16.200	2.700	0.447	9.010	3.000	0.559	9.880	1.600	0.496
11.170	0.045	0.760	18.700	3.100	0.379	10.550	3.400	0.541	11.290	1.850	0.468
12.430	0.050	0.658	21.200	3.400	0.308	12.080	3.900	0.503	14.190	2.300	0.401
13.710	0.055	0.573	23.700	3.900	0.222	13.640	4.400	0.464	17.830	3.000	0.300
14.980	0.060	0.465	26.400	4.300	0.137	15.200	4.900	0.421	21.430	4.000	0.145
17.550	0.070	0.290	29.100	4.700	0.058	16.770	5.400	0.377	25.470	4.250	0.081
20.170	0.080	0.142	32.000	5.100	0.000	18.370	5.900	0.327	29.780	4.250	0.009
25.570	0.100	0.021				19.990	6.400	0.252			
32.730	0.125	0.004				21.630	6.900	0.172			
40.600	0.150	0.012				23.310	7.400	0.141			
47.900	0.175	0.000				25.010	7.900	0.119			
						26.740	8.400	0.084			
						28.510	8.880	0.043			
						30.350	9.400	0.007			
						32.200		0.000			

## Sensitivity Analysis

With the detailed geometry of the open source lenses, simulations were done to determine the sensitivity of ion transmission to some of the geometrical parameters of the open source, particularly those of the repeller and extractor electrodes. This would be of help in deciding how the open source can be redesigned to reduce the size or improve ion transmission. For the extractor electrode, the radius of the aperture and the length of the cylindrical part were changed in small increments with respect to the INMS geometry. Simulations were done with the changed geometrical parameters, keeping the voltages at the same values as in the previous simulations. Figure 21 gives the variation of transmission of ions of mass 28 amu at two different angles of incidence, when the inner radius of the extractor electrode aperture is varied about the INMS value of 0.053" (corresponding to 0.0 along the abscissa in fig 23). With ions entering parallel to the axis of the device, transmission falls rapidly with reducing radius. However, it reaches a plateau starting at a value slightly below the INMS value. With ions entering at an angle of 4.5°, transmission falls to zero when the radius is decreased to about 0.038" and increases considerably with increasing radius.

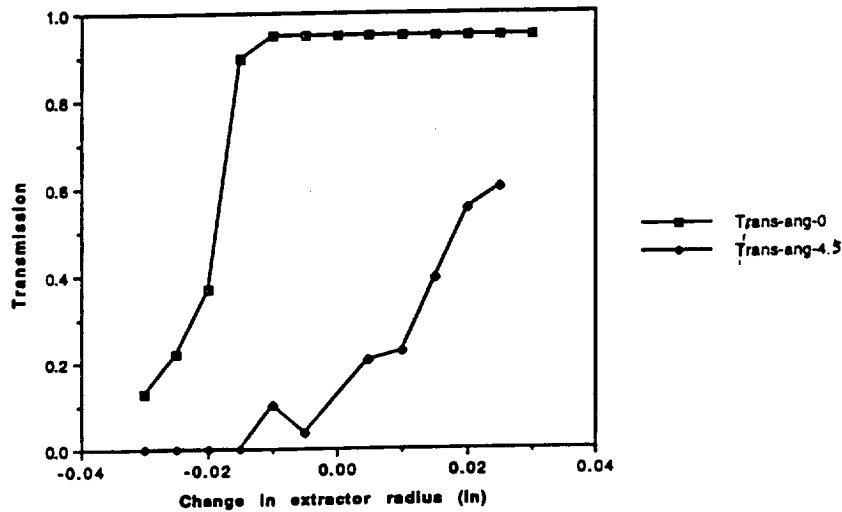


Figure 21: Transmission as a function of the variation in the radius of the extractor electrode.

Figure 22 shows the variation of transmission of 28 amu ions with the inner radius of the repeller electrode aperture about the INMS value of 0.087". There is no significant variation in the transmission indicating very low sensitivity.

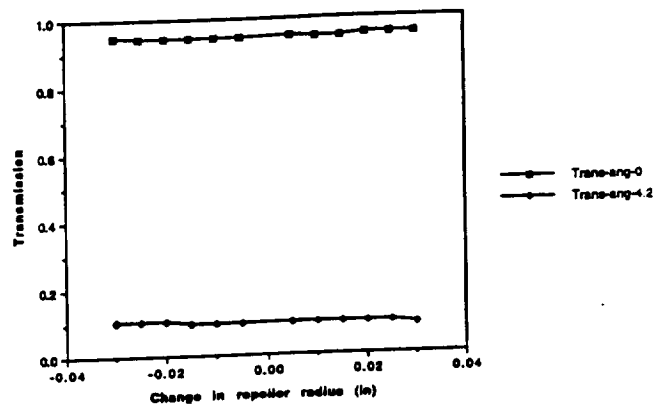
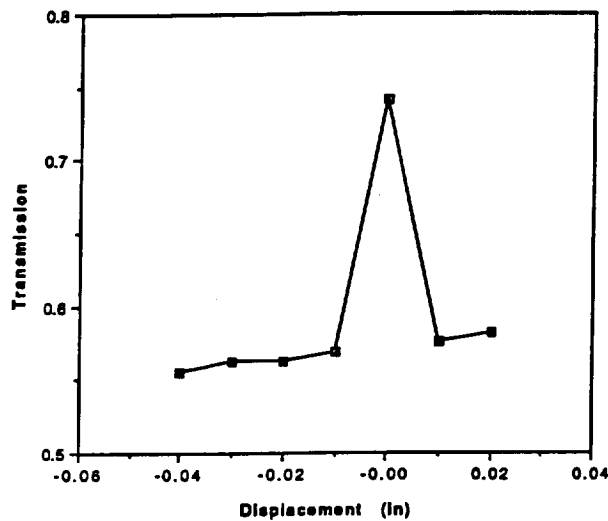


Figure 22: Transmission as a function of the variation in the radius of the repeller electrode.

The sensitivity of transmission to the spacing between the repeller and extractor electrodes was also studied by moving either of the repeller and extractor electrodes. Figure 23 shows the ion transmission as a function of the displacement (or the change in the spacing between the two electrodes). The analysis was done at a small angle of incidence of  $2.8^\circ$ .

The length of the cylindrical part of the extractor electrode plays an important role in determining the transmission. Figure 24 shows the variation of transmission at some selected angles when the length of the cylinder is varied about the INMS value of  $0.495''$ . As is to be expected, there is no significant change in transmission at low angles. There is a significant loss in transmission at higher angles.



**Figure 23:** Ion transmission as a function of the change in the spacing between the repeller and extractor electrodes.

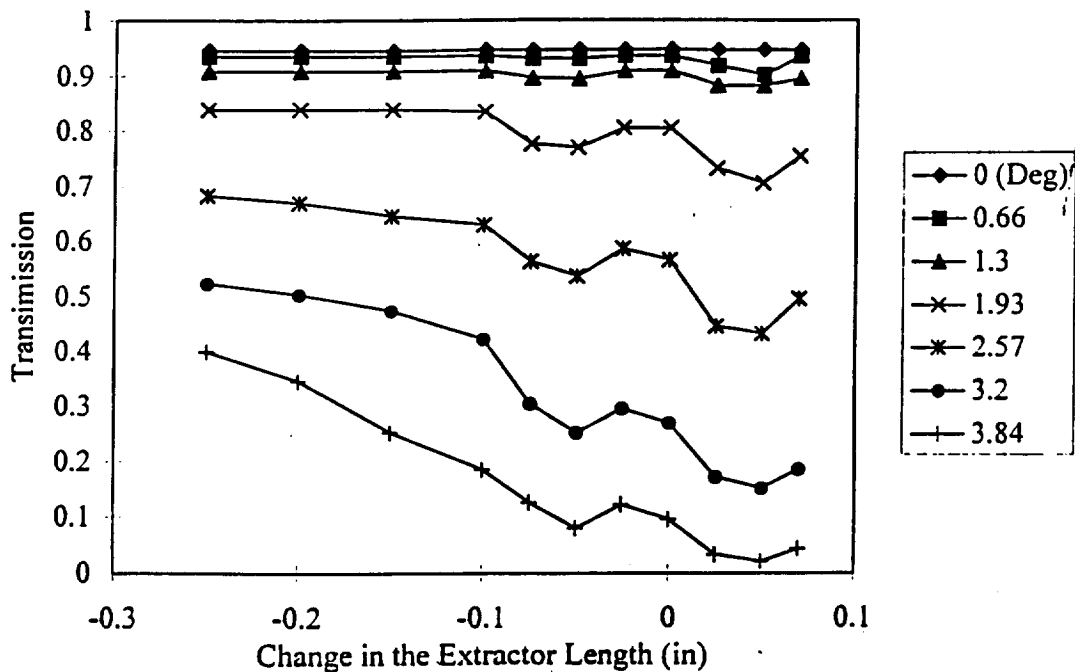


**Figure 24:** Ion transmission as a function of the change in length of the cylindrical part of the extractor.

### **Optimization using the simplex algorithm**

The simplex algorithm was used to optimize ion transmission through the open source. Two simple cases were tried for the 28 amu ions entering parallel to the axis of the device. The aperture plate voltage was maintained at the maximum transmission value of 200 Volts. In the first case, keeping all other voltages at zero, the voltages on the repeller and extractor plates were varied starting from 20 Volts and 50 Volts respectively. Transmission converged (the voltages not changing by more than 0.5 Volts) with the voltages at 23.8 Volts and 46.4 Volts, the transmission changing from 0.947 to 0.967. In the second case, the voltage on the second electrode (the entrance electrode of the ionization chamber) was also allowed to vary, starting from a value of 0 Volts. The voltages on the three electrodes (the entrance electrode, the repeller and the extractor) at convergence were 0.2 Volts, 22.5 Volts and 48.7 Volts respectively. The transmission changed from 0.947 to 0.954.

### 3. The Quadrupole Deflector

The quadrupole deflector or the switching lens of the INMS accepts ions from both the closed source and the open source. It uses four circular rod sectors mounted in a cube assembly to provide a nearly hyperbolic electrostatic field for a 90° deflection. This device is used to multiplex ions from either the closed source or the open source into the common entrance lens system of the quadrupole mass analyzer. The potential on each rod of the switching lens can range from 0 to -300 volts. The potentials can be scanned to provide an estimate of the ion and neutral energy distribution up to about 150 volts.

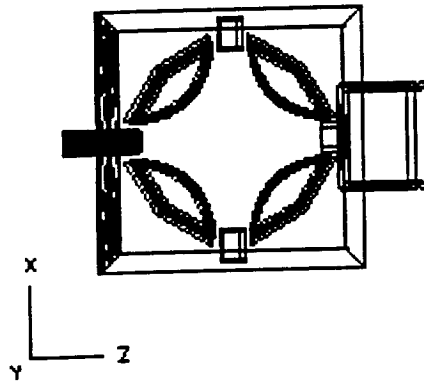


**Figure 1:** BEAM3D Model of the Quadrupole Deflector. Also included are the parts of the last lens of the open source on the left and the first lens of the exit lens on the right.

The initial three-dimensional BEAM3D model of the quadrupole deflector is shown in Figure 1. It consists of five independent grids. The four deflector plates of length 1.07" each are modeled as sections of a hyperbolic cylinder with endcaps. Independent potentials can be placed on each hyperbolic section. A rectangular shield box surrounds the quadrupole plates. There are four cylindrical apertures in the shield box to allow for entrance and exit of the ions. Figure 2 gives the coordinate dimensions of the hyperbolic sections and the formula used to generate the hyperbola. The three-dimensional view of the hyperbolic sections is shown in Figure 3.

COORDINATE DIMENSIONS

Y ±0.00010	X ±0.00010	Y ±0.00010	X ±0.00010
0.000000	0.250000	0.120000	0.277308
0.005000	0.250050	0.125000	0.279508
0.010000	0.250200	0.130000	0.281780
0.015000	0.250450	0.135000	0.284121
0.020000	0.250799	0.140000	0.286531
0.025000	0.251247	0.145000	0.289007
0.030000	0.251794	0.150000	0.291548
0.035000	0.252438	0.155000	0.294151
0.040000	0.253180	0.160000	0.296816
0.045000	0.254018	0.165000	0.299541
0.050000	0.254951	0.170000	0.302324
0.055000	0.255979	0.175000	0.305164
0.060000	0.257099	0.180000	0.308058
0.065000	0.258312	0.185000	0.311006
0.070000	0.259615	0.190000	0.314006
0.075000	0.261008	0.195000	0.317057
0.080000	0.262488	0.200000	0.320156
0.085000	0.264055	0.205000	0.323303
0.090000	0.265707	0.210000	0.326497
0.095000	0.267442	0.215000	0.329735
0.100000	0.269258	0.220000	0.333017
0.105000	0.271155	0.225000	0.336341
0.110000	0.273130	0.230000	0.339706
0.115000	0.275182	0.231224	0.340536

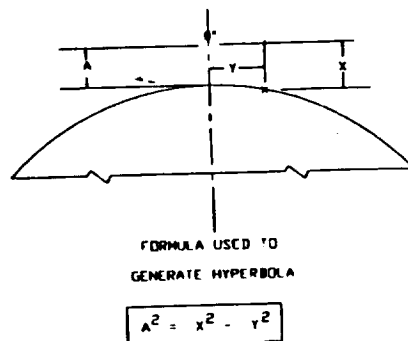


**Figure 2:** Coordinate dimensions and the formula used to generate the hyperbolic sections of the quadrupole deflector.

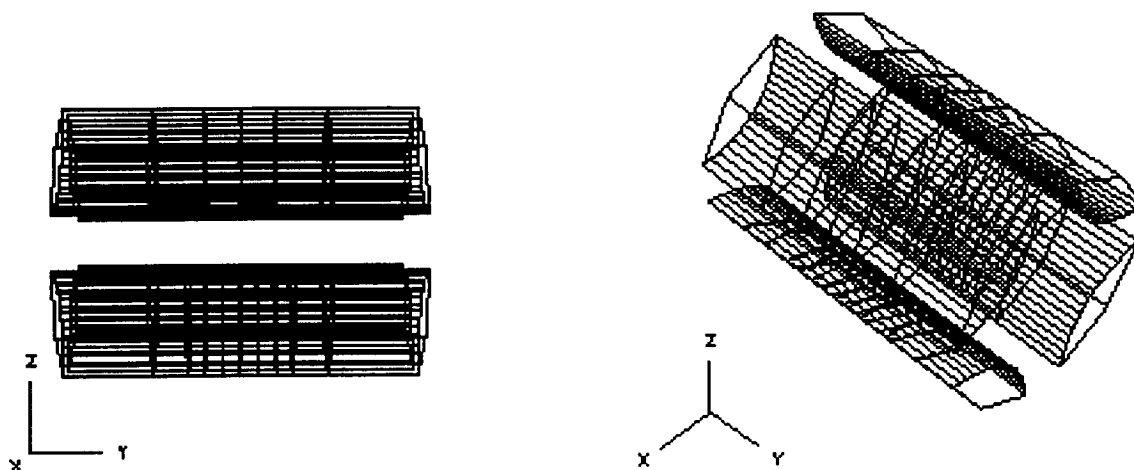


**Figure 3:** Views of the hyperbolic sections of the quadrupole deflector.

### Software Modification

Simulation of ion trajectories through the quadrupole deflector involves propagating a beam that turns through  $90^\circ$ . For example, a particle initially moving in the  $z$  direction could exit the quadrupole deflector traveling parallel to the  $x$ -axis, with no forward motion in  $z$ . This situation violates one of the assumptions built into the BEAM3D simulator used for the mass spectrometer design calculation. To use BEAM3D effectively, it is necessary to change to a new, rotated coordinate system at some point in the trajectory. The new  $z$ -axis can be aligned with the old  $x$ -axis, so that the particle moves forward in the new system. To accomplish the required change of coordinates, a procedure was developed employing a rotated model of the deflecting part along with a special transformation to construct the beam in the rotated frame. The approach was tested on a simple example for accuracy of results.

The BEAM3D software used in the Mass Spectrometer design project was originally developed for CRT design. For CRT designs, one can assume a mono-energetic, steady state beam that always advances in the  $z$  direction. These assumptions permit a reduction in the number of equations that must be solved, from six functions of time:

$$x(t), y(t), z(t), p_x(t), p_y(t), p_z(t)$$

to four functions of  $z$ :

$$x(z), y(z), p_x(z), p_y(z)$$

where  $t(z)$  is of no interest and  $E(z)$  is constant. The change to  $z$  as the independent variable is also convenient for space-charge force estimation, which requires a description of the beam at the same location (i.e.  $z$  value) rather than at the same time.

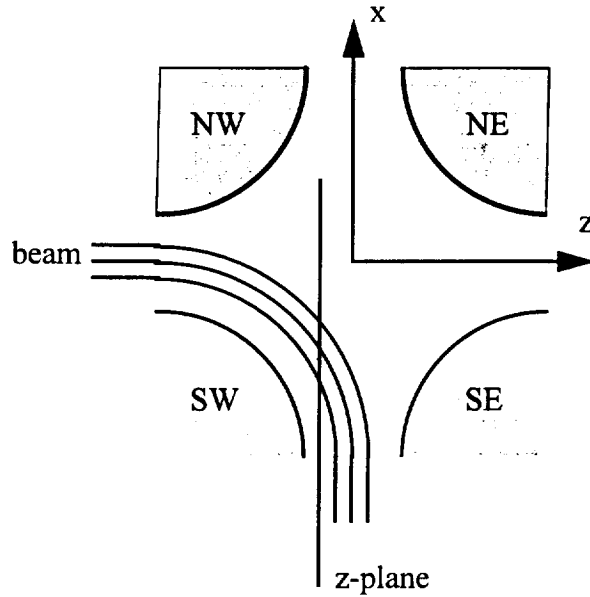


**Figure 4** - Schematic representation of a beam deflected through 90 degrees.

The use of  $z$  as the independent variable and the representation of the beam in constant  $z$ -planes become a problem when the beam is deflected through an angle approaching  $90^\circ$ . As illustrated in Figure 4, the transverse beam cross section elongates as the deflection angle increases, with a singularity at  $90^\circ$ . To avoid this problem, the deflected beam is stopped on a plane of constant  $x$ , and then restarted in a new, rotated coordinate system as illustrated in Figure 5. In the initial coordinate system, the intersection of each trajectory with the plane  $a$ - $a'$  is saved, and the beam is propagated far enough in  $z$  so that all trajectories have crossed the constant  $x$  plane. The intersection points are then used to start a beam on a constant  $z$ -plane in the new "tilde" coordinate system.

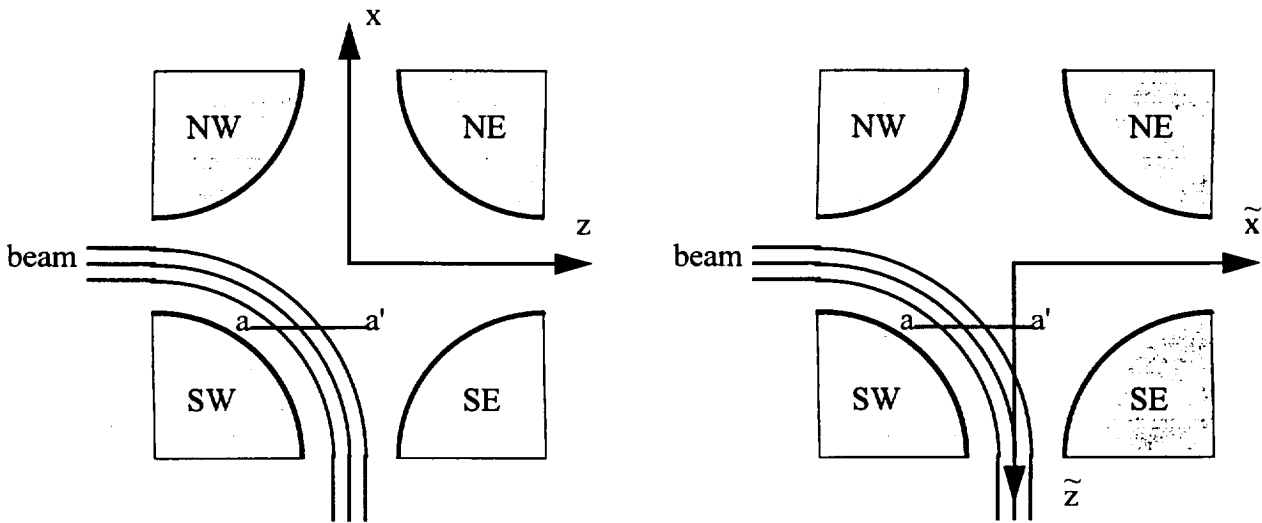


**Figure 5** - Introduction of a rotated coordinate system.

Lining up the  $z$  and  $\tilde{z}$  axes gives Figure 6 which corresponds to the output expected from a BEAM3D simulation using the two coordinate systems. Figure 4 shows the left half of the quadrupole deflector superimposed with a rotated version of the bottom half of the deflector. Figure 5 shows actual BEAM3D output from an example calculation. The trajectory segments between the vertical lines near  $Z = 200$  and  $Z = 450$  are an artifact of the trajectory plotting program. With the above modifications, trajectories could now be simulated through the quadrupole deflector.

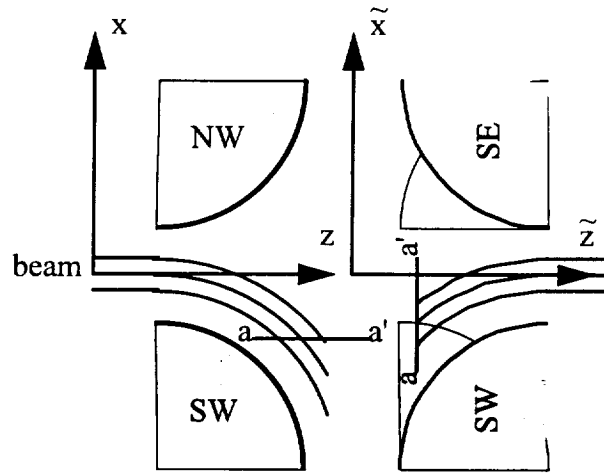


**Figure 6** - Composite diagram combining the original and rotated coordinate system.

## Quadrupole Deflector Simulations

Preliminary simulations of the quadrupole deflector were carried out using an ion beam of 25 eV, with opposite pairs of quadrupole rods at 0 and -100 Volts.

An example of a simulation in which trajectories of ions are bent by 90° is shown in Figure 7. The figure shows the edges of the deflector rods, the enclosing box and the entrance and exit apertures in cross section. The diagram is a superposition of two views of half the deflector as in Figure 6. The left half shows the rods near the entrance and the right half shows the rods near the exit. Thus the lower rods are two views of the same rod. This rod is at -100 Volts while the other two rods as well as the enclosing box are at ground. The incident ion flux, at left, has an energy of 25 eV. The trajectories are recorded on the horizontal plane at  $X = -0.070$ ". This data is transferred to the vertical plane at  $Z = 0.070$ " where the simulation is resumed. The trajectory segments between the planes at  $X = -0.070$ " and  $Z = -0.100$ " are repeated following the resumption at  $Z = 0.070$ ". The line segments between  $Z = -0.100$ " and  $0.070$ " are artifacts of the plotting routine.

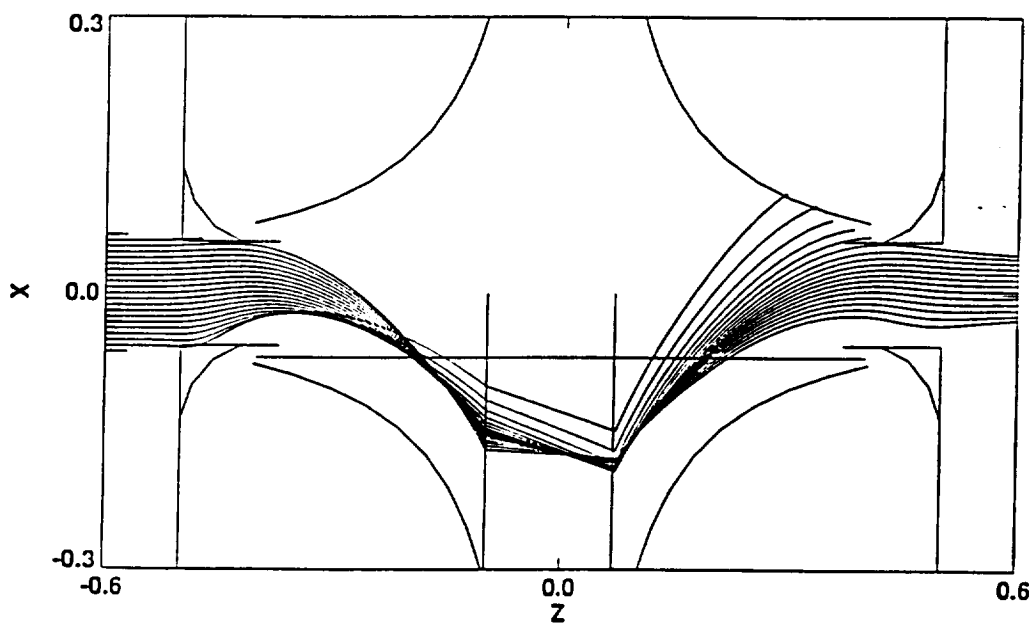


**Figure 7.** Selected trajectories in the quadrupole deflector near the transmission maximum. Edges of the deflector rods are shown, as is the enclosing box, with apertures for the beam, shown in cross-section at the entrance and exit. Actually this is a superposition of two views of half the deflector, as in Fig. 6. The left half shows the rods near the entrance and the right half shows the rods near the exit. Thus the lower rods are two views of the same rod. This rod is at -100 Volts and the other two rods shown are at ground. The enclosing box is at ground. The incident ion flux, at the left, has an energy of 25 eV. The trajectories are recorded on the horizontal plane at  $X = -0.070$ ". This data is transferred to the vertical plane at  $Z = 0.070$ " where the simulation is resumed. The trajectory segments between the planes at  $X = -0.070$ " and  $Z = -0.100$ " are repeated following the resumption at  $Z = 0.070$ ". The line segments between  $Z = -0.100$ " and  $0.070$ " are artifacts of the plotting routine.

This initial model of the quadrupole deflector was improved over the period of the project as the model was adjusted to simulate the hardware more closely and refined. In particular, the supporting box was partially removed and the deflector back surface, exposed by this removal, was included in the simulation. Several changes in the internal structure of the model were made. The endplates, not apparent in the original specifications, were added. The importance of the thickness of the entrance and exit cylinders was identified, and these thicknesses were added to the model. Extraneous structures in the specifications were removed from the model. Figure 8 shows XZ cross section of the improved model with nomenclature adopted to identify the hyperbolic rods. The ion beam enters the deflector at left and exits at the bottom (compare with Figure 7). The rod nearest to the beam is called the proximal rod. The adjacent rods are called distal rods. The distal rod nearest to the beam is called the entrance distal rod and the one nearest the exit is called the exit distal rod.

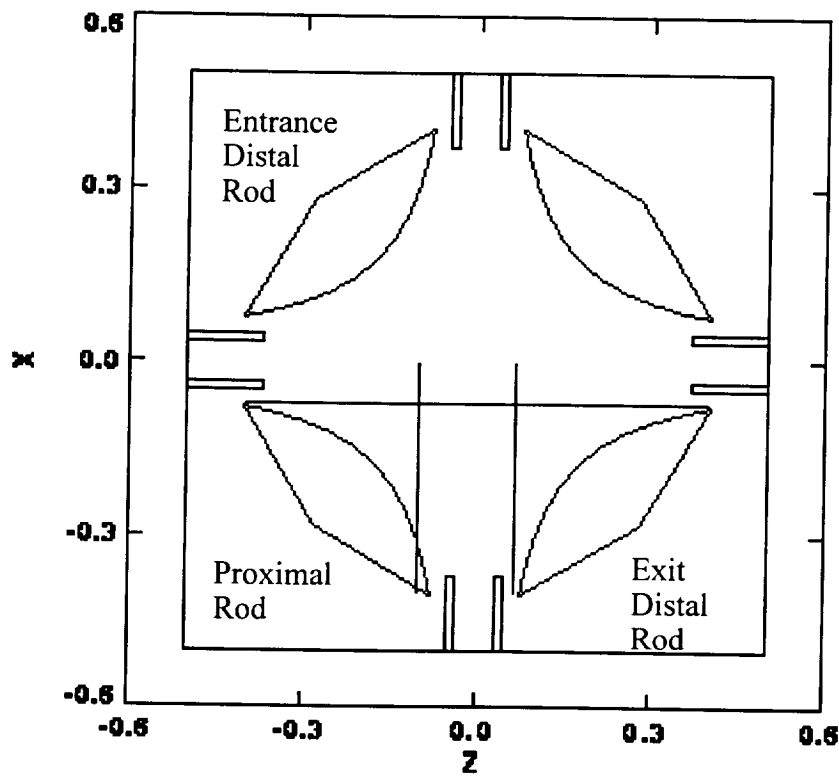


**Figure 8.** Sketch of the quadrupole deflector. In this XZ cross-section the four hyperbolic deflector rods extend above and below the plane of the sketch. Cylinders, shown in axial cross-section between the rods, surround the ion beam at its entrance and exit. Ions enter at the left with specified kinetic energy and exit at the bottom. The rod nearest the beam is called the proximal rod. The adjacent rods are called distal rods.

Figures 9 and 10 show two cross-sections of the model with selected trajectories of an ion beam transmitted through the deflector. Figures 9 and 10 show details of the ion trajectory distribution at the exit of the deflector.

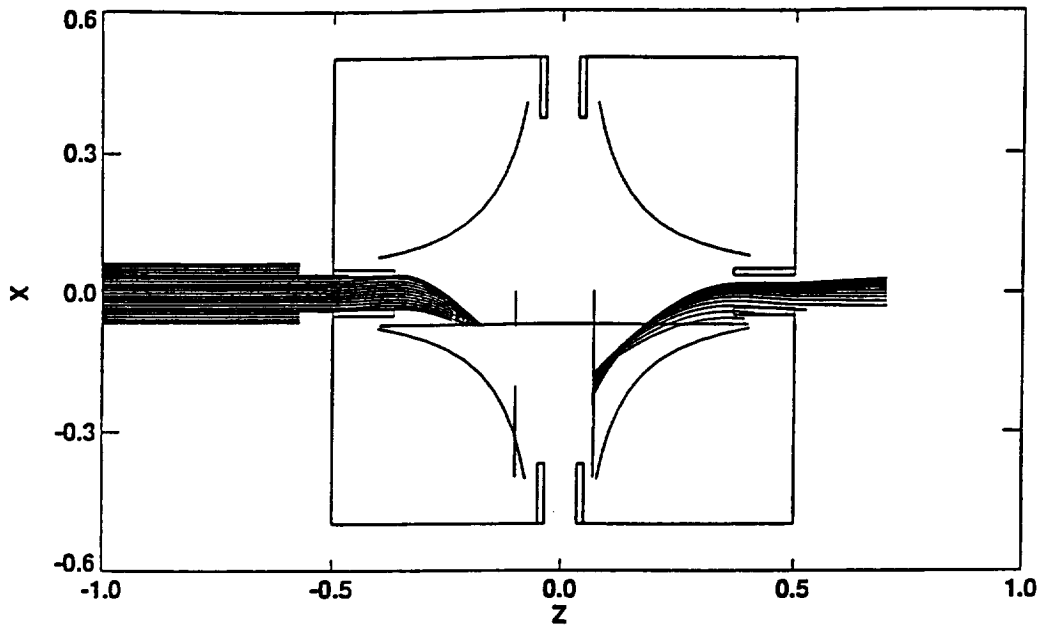


Figure 9. Selected trajectories in the quadrupole deflector near the transmission maximum. Edges of the deflector rods are shown, as is the enclosing box, with cylinders for the beam, shown in cross-section at the entrance and exit. Actually this is a superposition of two views of half the deflector. (The trajectories up to the horizontal line at  $X = -0.07$ " are calculated with positive voltage on the rods in the first and third quadrants. They are continued from the vertical line at  $Z = +0.07$ " with positive voltage on the rods in the second and fourth quadrants.) The enclosing box is at ground. The incident ion flux, at the left, has an energy of 5 eV.

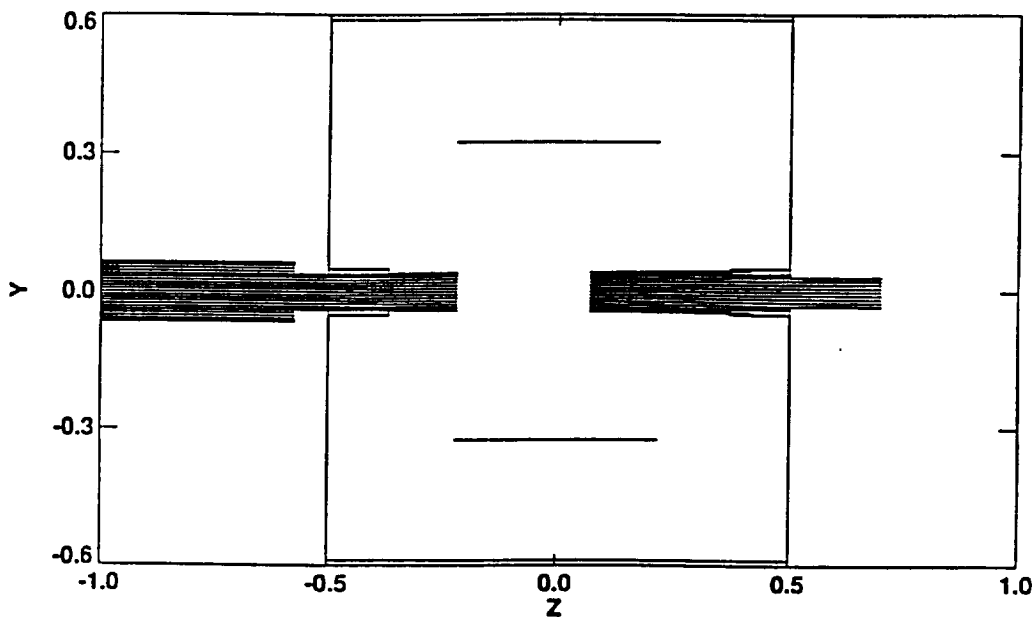
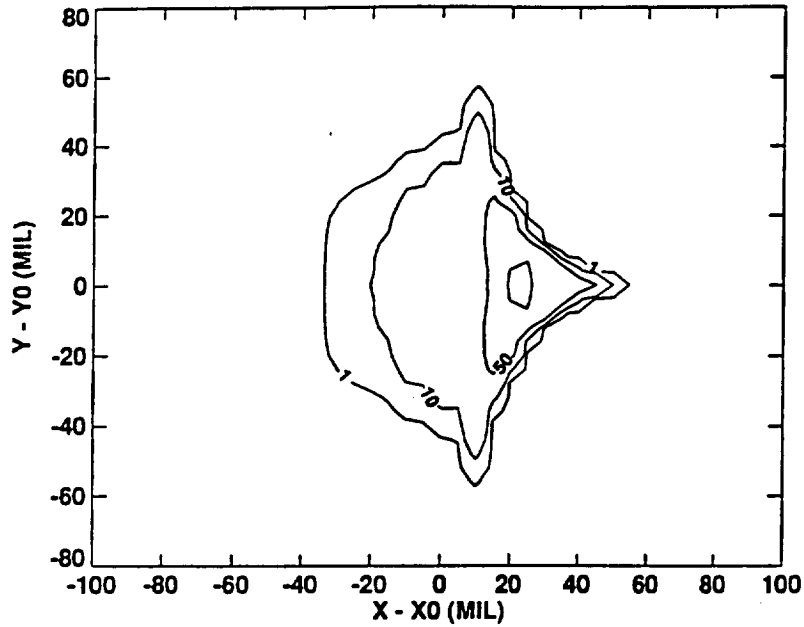
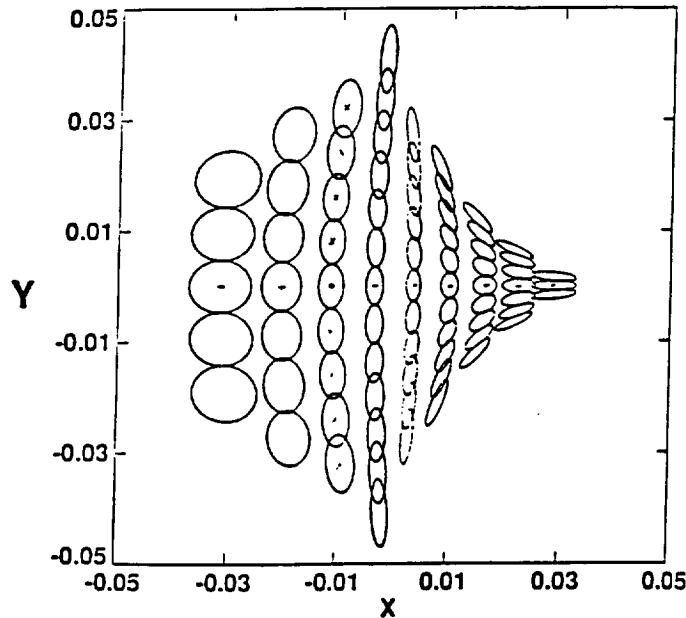


Figure 10. Selected trajectories in the quadrupole deflector near the transmission maximum. Complementing Fig. 9, which shows trajectories in the plane intersecting the deflector rods, this figure shows trajectories in the symmetry plane of the ion beam. The central trajectory of Figs. 9 and 10 is the same. The deflector rods are not shown, as they do not intersect this plane. The lines at  $Y = \pm 0.325$ " are endplates. The enclosing box is shown, with cylinders for the beam, shown in cross-section at the entrance and exit. As in Fig. 9, this is a superposition of two views of half the deflector. The enclosing box is at ground. The incident ion flux, at the left, has an energy of 5 eV.



**Figure 11.** A contour plot of the ion-current density at the exit of the deflector ( $Z = 0.7''$  in Figs. 9 and 10). Contours at 1, 10, and 50% of peak intensity are shown. The contour is centered at  $X = -0.0114''$ . The density distribution is noisy above the 50% level, leading to the valley inside the 50% contour.



**Figure 12.** A plot of the trajectories from which Fig. 10 was computed. A trajectory is at the center of each ellipse. (The size of the ellipse measures the transverse thermal energy.) The ellipses containing a '+' are those shown in Fig. 9 at  $Z = 0.7''$  and those containing a 'X' are those shown in Fig. 10. The units are inches. From 373 trajectories at  $Z = -1.00''$ , 121 enter the deflector at  $Z = -0.50''$ , and 75 continue to  $Z = 0.70''$ .

### Ion transmission through the quadrupole deflector

Preliminary simulations were carried out to analyze ion transmission (ratio of the ion fluxes at the exit and entrance of the deflector) through the quadrupole deflector for selected energy values. Figures 13 and 14 show selected trajectories in the deflector for ion energies of 20 eV and 40 eV. Figure 15 shows the variation in deflector transmission with ion energy. In these simulations, the deflector voltages were set symmetrically about zero. The proximal rod and the rod opposite were held at +50 Volts while the distal rods were held at -50 Volts or  $\Delta V = 50$  Volts. The entrance and exit cylinders were maintained at ground potential.

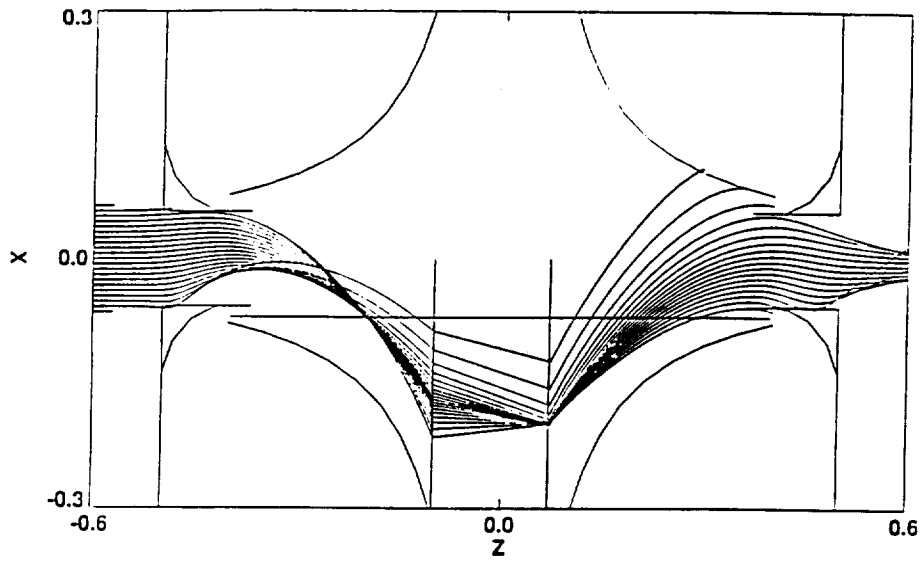


Figure 13. Selected trajectories in the quadrupole deflector at an ion energy of 20 eV.

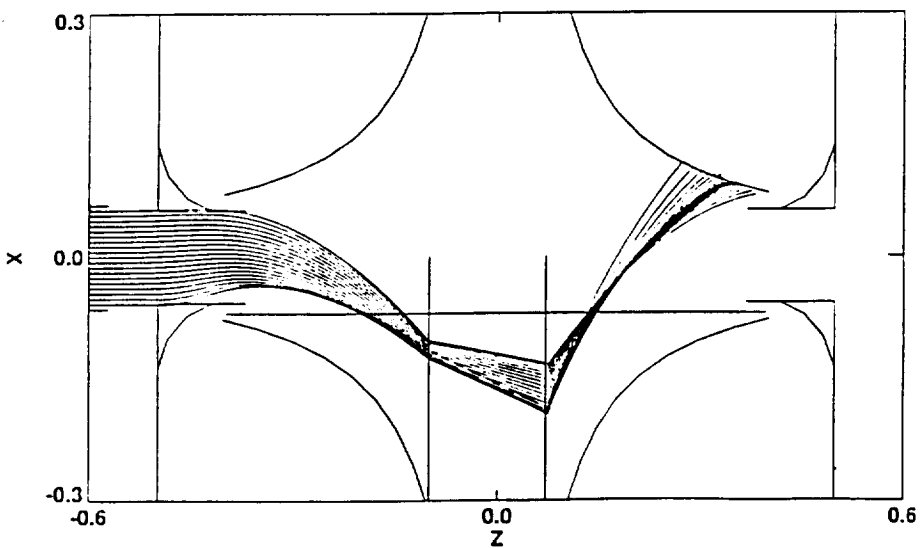


Figure. 14. Selected trajectories in the quadrupole deflector at an ion energy of 40 eV.

Hyperbolic Rods at 0 and 100 Volts  
Box at 50 Volts  
Solid Cylinders

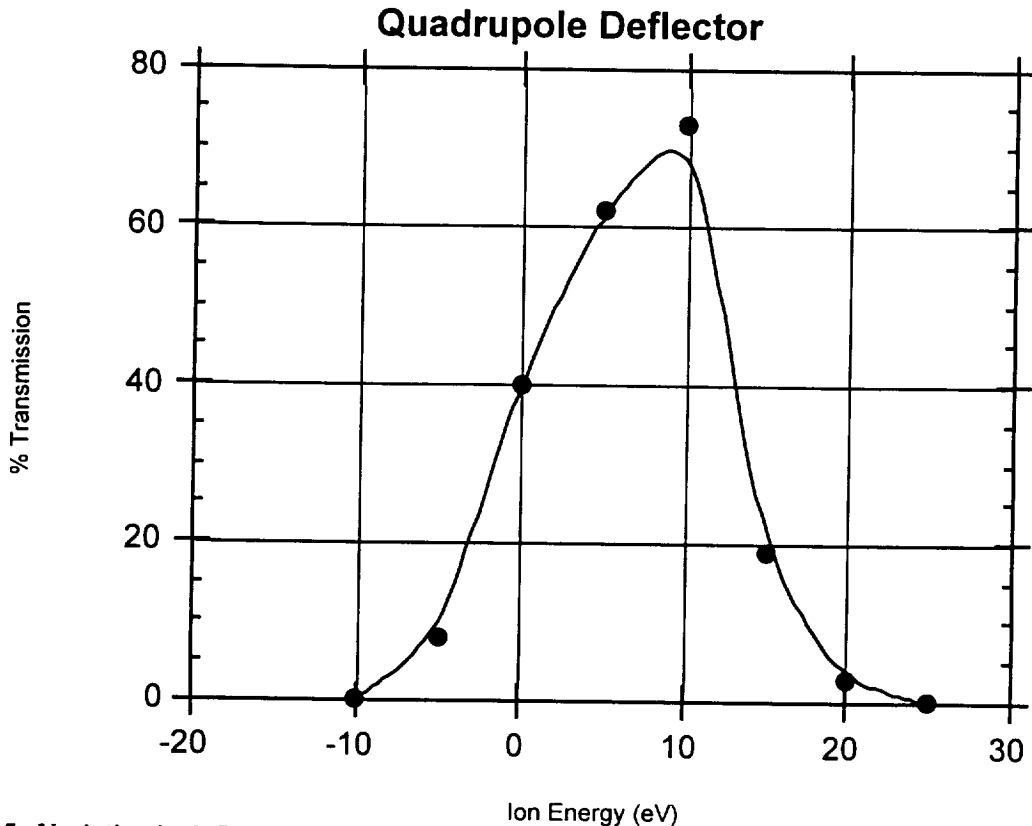


Fig. 15. Variation in deflector transmission with ion energy for  $DV = 50$  Volts. The transmission, the ratio of the ion fluxes at the exit and entrance of the deflector, is plotted versus the ion energy. The ion energy is measured relative to the potential on the box.

The results qualitatively agree with obtained by Mahaffy and Lai (Mahaffy and Lai, *J. Vac. Sci. Tech.* 1990, A8, 3244). The quadrupole introduces a crossover in the beam near the mid-deflector region. The crossover is displaced with ion energy, lying nearer to the entrance at lower energies (see Fig 13) and nearer to the exit at higher energies (Fig 14). However, there is a disparity in the positions of the transmission peaks.

## Sensitivity Analysis

### Sensitivity to changes in deflector geometry

Simulations were carried out to analyze the sensitivities of the transmission peak and energy variations in the hyperbolic focus, the separation of the endcaps, and the interior/exterior diameters and lengths of the entrance and exit cylinders. The results are shown in Table 1. The geometric parameters are named in the first column, the nominal values are in the second column, and the changes are in the third column of Table 1. Calculated changes in the transmission peak, its ion energy, and the curve width at 50% of peak are listed in the fourth, fifth, and last columns respectively. The first data row shows the absolute values of the calculations for the nominal deflector. The next two rows show the results of changes in the

**Table 1**

**Deflector Sensitivities**

Parameter	Value Peak (Inch)	Change Position (Inch)	Transmission Width %	Ion Energy (eV)	Energy (eV)	
Nominal		—		78.0	54.7	13.21
Hyperbolic 'A'	.250	-.001		-1.5	+0.44	+0.15
Disk Separation	.650	-.02		+0.1	+0.05	-0.03
Entr. Cyl. Diam.	.070	+.002		-0.6	+0.26	+0.14
Entr. Cyl. Thick.	.015	+.0025		+1.1	-0.07	-0.01
Entr. Cyl. Length	.130	+.005		+1.1	-0.85	+0.14
Exit Cyl. Diam.	.070	+.002		+0.1	-0.01	-0.20
Exit Cyl. Thick.	.015	+.0025		-1.6	-0.71	-0.24
Exit Cyl. Length	.130	+.005		-1.7	-0.60	-0.24
Vert. Misalignment of Proximal Deflector Rod	0	.010		+5.3	+1.58	-0.41

hyperbolic focus and end-plate separation. (The end plates are not seen in Figure 7.) The next three rows show the results of changes in the entrance cylinder parameters. The entrance cylinder outline appears at the left of Figure 7, where it encloses the incident trajectories. The

three subsequent rows show the results of similar changes in the exit cylinder at the right of Figure 7. The last calculation was done for a misalignment of the deflector nearest the beam. It is at the lower left of Figure 7 when the incident trajectories are calculated and at the lower right when the exit trajectories are calculated. This deflector is displaced toward the entrance cylinder. These sensitivity calculations were done to demonstrate use of the software. The small changes were consistently calculated by fitting lines and parabolas to data points at a prescribed set of ion energies. For more accurate sensitivities, several changes of each parameter should be made to confirm that the calculated changes are linear in the parameter change. The sensitivities are the slopes of these lines.

The results in Table 1 show a significant improvement in ion transmission when the deflector rods are misaligned. Confirmation of these results by further analysis would indicate that an asymmetric structure for the quadrupole deflector could be a better design.

### **Misalignments of the quadrupole deflector rods**

To verify the results obtained with the preliminary deflector simulations, transmission changes with misalignments of several of the quadrupole deflector rods were calculated to study two types of sensitivities: (1) transmission-sensitivity, which is defined as the change in maximum transmission per unit misalignment of the rods and (2) energy-sensitivity, which is defined as the change in the ion energy (at which maximum transmission occurs) per unit misalignment of the rods. Simulations were done with misalignments in both proximal and distal rods of the deflector. In all the simulations, the proximal rod and the rod opposite were held at +50 Volts while the distal rods were held at -50 Volts. The entrance and exit cylinders were maintained at ground potential.

For a perfectly constructed deflector with no misalignments, the maximum transmission and the energy at which it occurs are 0.78 and 54.7 eV respectively. The sensitivities (slopes of the variation of these quantities with misalignments) taken from Table 1 are 0.0053/mil and 0.16 eV/mil of vertical misalignment of the proximal deflector rod. These values were confirmed, and they are within the ranges of values obtained in this study. The largest sensitivity for the transmission maximum occurs for X-misalignment of the entrance distal rod and the largest sensitivity of the energy of maximum transmission occurs for Z-misalignments of the exit distal rod.

For normal misalignment distributions, such as shown in Fig. 16, the probability distributions for the maximum transmission and for its energy can be calculated. They are shown in Figs. 17 and 18. For misalignments taken randomly from a distribution with a 5-mil standard deviation, the standard deviation of the distribution for maximum transmission is 0.08, meaning there is a 68% probability that a quadrupole deflector constructed with misalignments from the distribution in Fig. 16 will have maximum transmission between 0.70 and 0.86. The standard deviation of the distribution for the energy of maximum transmission is 2 eV, meaning there is a 68% probability that a quadrupole deflector constructed with misalignments from the distribution in Fig. 16 will have an energy of maximum transmission between 52.7 and 56.7 eV. The selection of a 5-mil standard deviation is arbitrary.

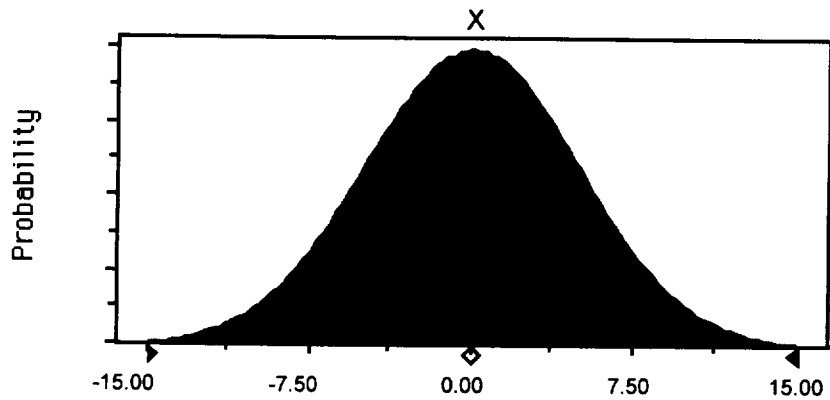


**Figure 16.** Distributions of rod misalignments for a standard deviation of 5 mils. The misalignment of each rod in each direction is selected randomly from distributions like this one.

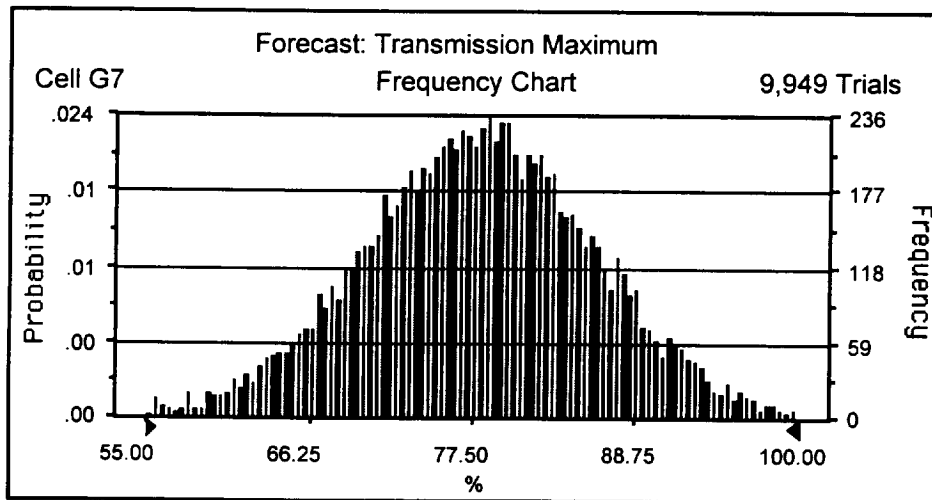


**Figure 17.** Probability distribution for the maximum fractional transmission of a deflector made with misalignments from distributions like that shown in Fig. 16. The mean is 0.78; the transmission of the perfectly constructed deflector, and the standard deviation is 8%. Therefore, there is a 68% probability that a quadrupole deflector constructed with misalignments from these distributions will have maximum transmission between 0.70 and 0.86. Higher transmissions than 0.78 are possible because the sensitivities are linear in the misalignments. 51 transmission values lay outside the range of this histogram.

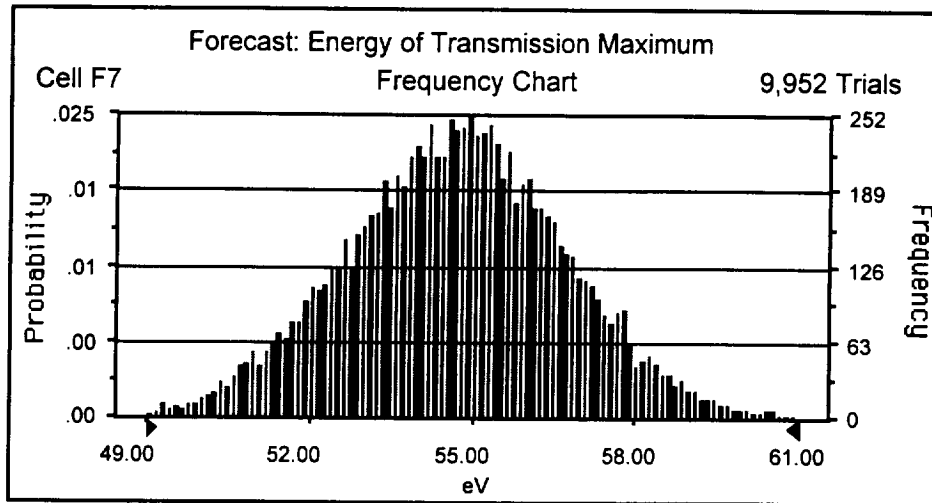


**Figure 18.** Probability distribution for the kinetic energy of the maximum transmission of a deflector made with misalignments from distributions like that shown in Fig. 16. The mean is 54.7 eV and the standard deviation is 2 eV. Therefore, there is a 68% probability that a quadrupole deflector constructed with misalignments from these distributions will have energy of maximum transmission between 52.7 and 56.7 eV. 48 transmission energies lay outside the range of this histogram.

Transmission calculations for selected misalignments were performed as described in the Fourth Quarterly Report. That is, for each misalignment of each rod, ion-beam simulations of the transmission were done for a chosen set of incident energies. A parabola was fitted to these data to find the maximum transmission and the energy at which it occurs. This procedure was developed to assure that small changes in misalignment give small changes in the simulations, i. e., to assure continuity.

For misalignment of the proximal rod, the values of the maximum transmission and the energy at which it occurs are plotted in Figs. 19 and 20. The lines are fitted to the calculations, and their slopes are the sensitivities. These sensitivities, and the others calculated, are listed in Table 2. The sensitivities for X-misalignment of the exit distal rod are small, and so those for Z-misalignment of the entrance distal rod are expected to be small. The sensitivities due to misalignment of the fourth rod, unnamed, are also expected to be small.

**Table 2.** Misalignment Sensitivities.

Rod	Displacement	Sensitivity		% / mil
		Energy	Transmission	
Proximal	X	0.135	eV/mil	0.39
Proximal	Z	0.160		0.45
Distal Entrance	X	-0.074		1.31
Distal Exit	Z	-0.350		-0.71
Distal Exit	X	0.090		0.07

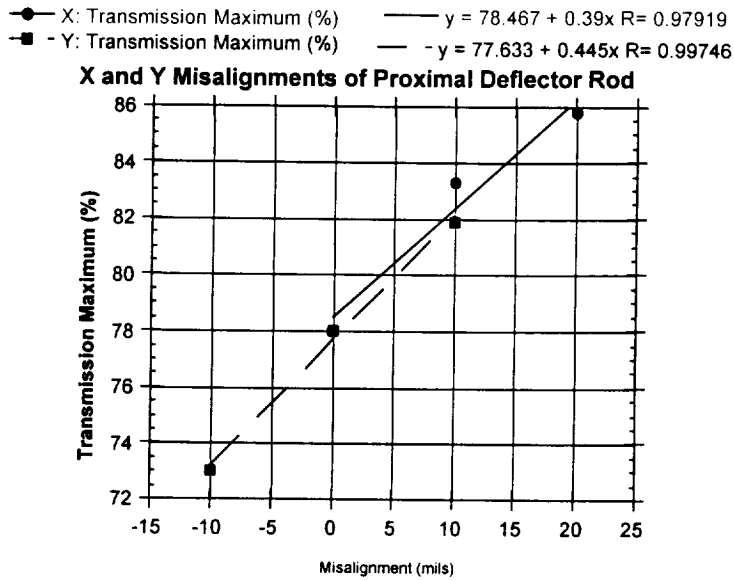


**Figure 19.** Calculation of the sensitivities of maximum transmission fraction with X and Z misalignments of the proximal deflector rod. Calculated data is shown by the solid dots, and the slopes of lines fitted to this data are the sensitivities.

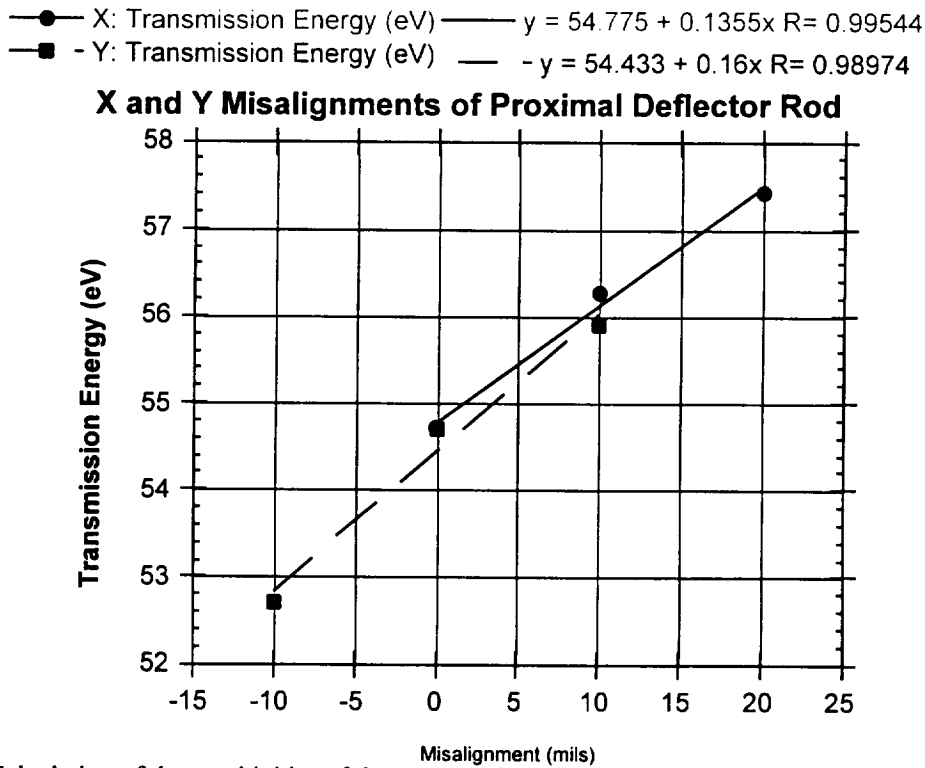


**Figure 20.** Calculation of the sensitivities of the energy of maximum transmission with X and Z misalignments of the proximal deflector rod. Calculated data are shown by the solid dots, and the slopes of lines fitted to this data are the sensitivities.

The changes associated with a group of misalignments add linearly. That is, for a set of misalignments,  $M_i$ , and a set of sensitivities  $S_i$  from Table 2, the performance  $P$  of the deflector is  $P = P_0 + \sum M_i S_i$ , where  $P_0$  is the performance of the perfectly constructed deflector. Maximum transmission is a performance, as is its energy. To find the probability distributions of performance, shown in Figs. 16 and 17, Monte Carlo calculations were done for 10,000 random misalignment sets  $M_i$ . Most of the 10,000 values of the performance were allocated into 100 bins of equal performance range. The histograms obtained by plotting bin population versus bin value are shown in Figs. 16 and 17. Add-on software for EXCEL, called Crystal Ball and marketed by Decisioneering, was used do these operations.

To illustrate the changes associated with a group of misalignments add linearly, and to explore the range beyond which the linear approximation is inadequate, a specific misalignment set was chosen; 5 mils of +X and +Z misalignment of the proximal rod, 2 mils of +X misalignment of the entrance distal rod, and 3 mils of -Z misalignment of the exit distal rod. The signs of these choices were made to maximize the change in the maximum transmission, and the magnitudes were chosen to make the contributions of each misalignment nearly equal. From Table 2 this misalignment set increases the maximum transmission by 8.95 percentage points and the energy at which it occurs by 2.17 eV. Calculations done for this misalignment set and for multiples of it are shown in Figs. 21 and 22. Lines with slopes defined by the values from Table 2 are also shown. The calculations do follow these lines for small multiples, and they depart as the multiples get larger.

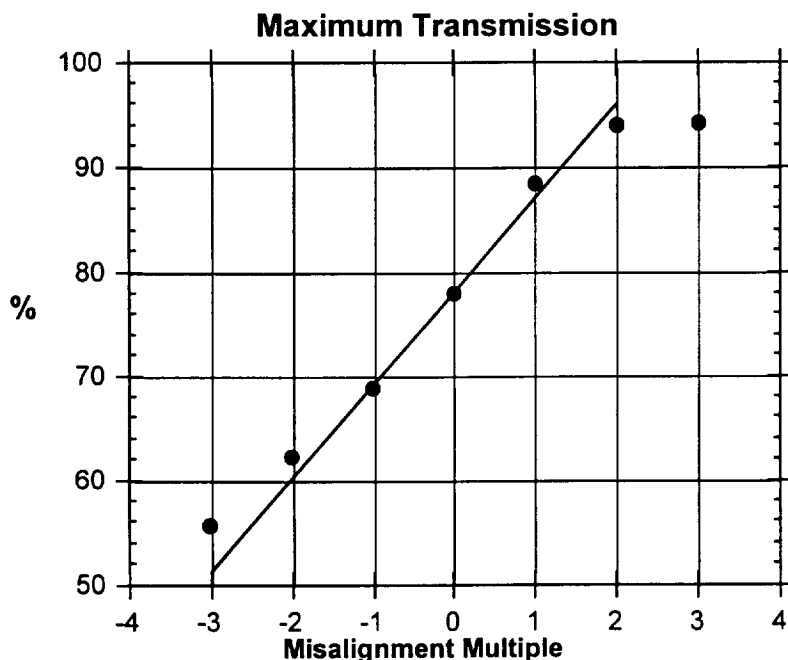


**Figure 21.** Calculations of the maximum transmission for multiples of the misalignment set described below are shown by the solid dots. The misalignment set is 5 mils of +X and +Z misalignment of the proximal rod, 2 mils of +X misalignment of the entrance distal rod, and 3 mils of -Z misalignment of the exit distal rod. Calculations were done for integer multiples of this set. The line is obtained from the sensitivities in Table 2. The concurrence of the line and the calculations for small multiples confirms the quality of the linear approximation in combining many misalignments. The departure at large multiples illustrates the breakdown of the linear approximation for large misalignments.

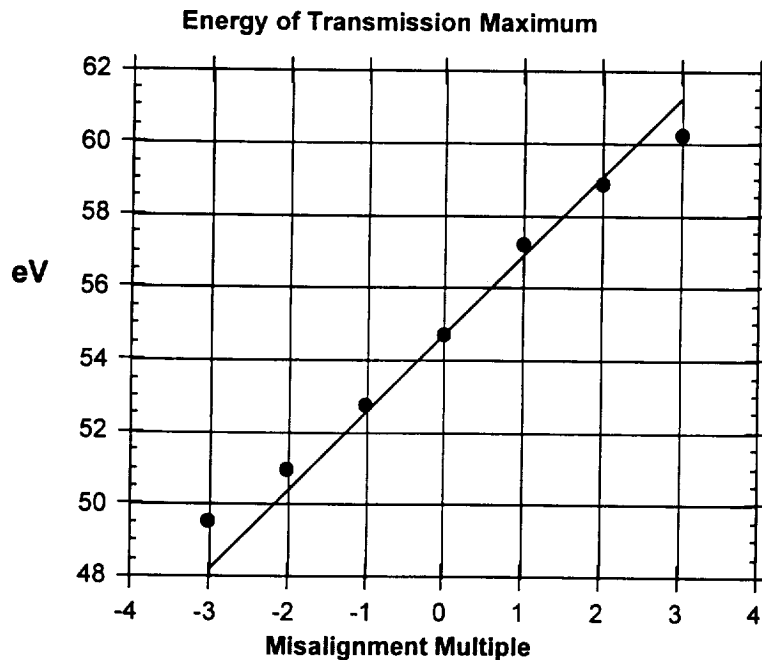


**Figure 22.** Calculations of the energy of maximum transmission for multiples of the misalignment set described below are shown by the solid dots. The misalignment set is 5 mils of +X and +Z misalignment of the proximal rod, 2 mils of +X misalignment of the entrance distal rod, and 3 mils of -Z misalignment of the exit distal rod. Calculations were done for integer multiples of this set. The line is obtained from the sensitivities in Table 2. Again, the concurrence of the line and the calculations for small multiples confirms the quality of the linear approximation in combining many misalignments.

Trajectories in the XZ plane of the deflector, shown in Figs. 23 and 24, clearly show the differences in transmission. The calculations for Fig. 23 are done for triple the misalignment set defined in the preceding paragraph, and they are done at the energy of maximum transmission. The ions are well collimated as they enter the exit cylinder, so few are lost. The calculations for Fig. 24 are done for the negative triple of the misalignment set at its energy of maximum transmission. The ions are much more poorly collimated at the exit cylinder, and many do not enter it. The beam is clearly broadened during deflection.

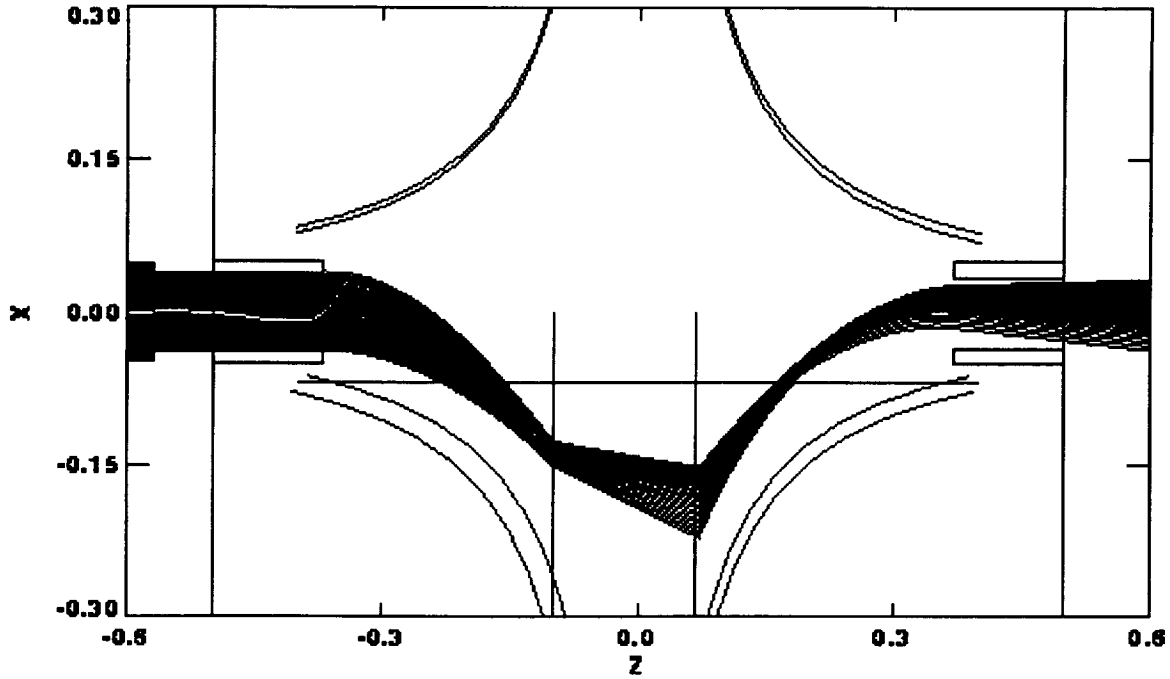


**Figure 23.** Selected ion trajectories calculated for triple the misalignment set described in the caption of Fig. 21. All the selected ions are transmitted through the deflector. Trajectories of 34 of the 866 ions entering the deflector are shown. 95% of the 866 ions entering the deflector are transmitted. The ions enter at left and cross the horizontal plane shown by a line in the deflector. The values on the horizontal plane are transferred to the vertical plane shown by the vertical line at larger  $Z$ . The calculation is continued to the exit of the deflector. The region between these two planes is redundant and irrelevant. The outlines are overlaid from the entrance and exit calculations, and misalignment introduces a separation of these curves.

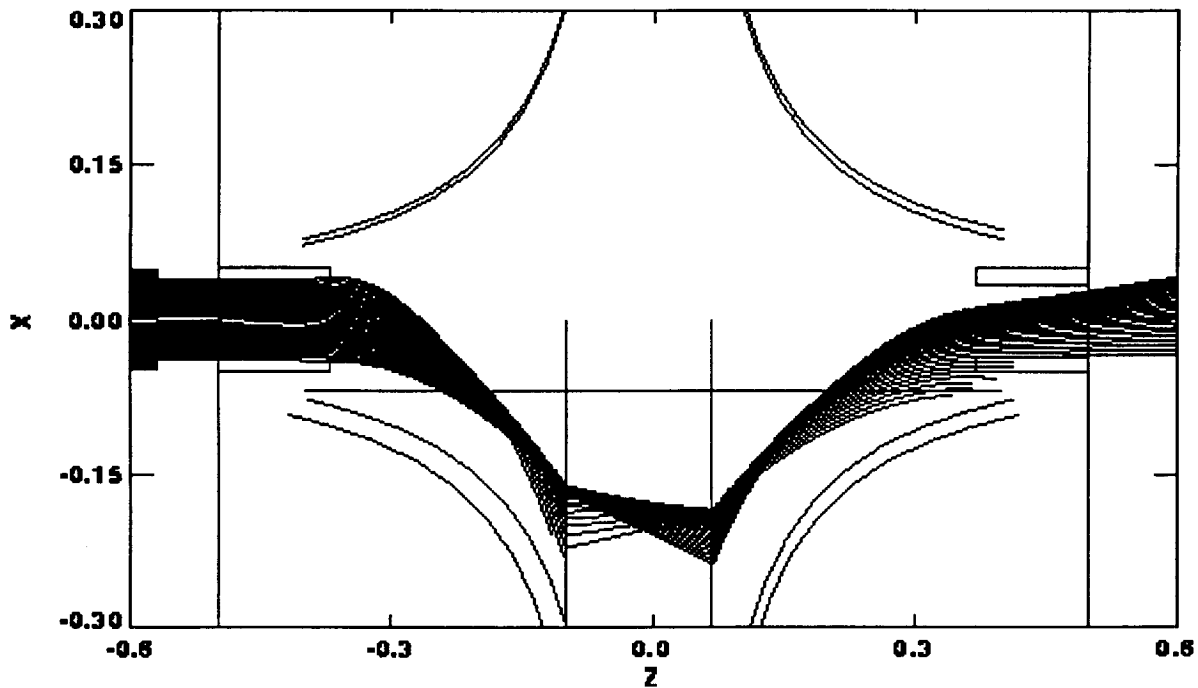


**Figure 24.** Selected ion trajectories calculated for the negative triple of the misalignment set described in the caption of Fig. 21. This diagram is similar to Fig. 23. Here, however, many of the selected ions are not transmitted through the deflector. Only 55% of the 866 ions entering the deflector are transmitted.

These simulations of the misaligned deflector suggest that increased transmission may be possible with a geometrically asymmetrical deflector. Indeed, if the transmission can be made nearly complete, there is an opportunity to design a deflector with much lower sensitivities of transmission to misalignments.

### Voltages on the Quadrupole Deflector Electrodes

A study was also conducted of the changes in transmission with voltage variations on the rods and the other deflector. These changes are easily checked in a laboratory setting, as the voltage on a rod is easily adjusted.

Transmission changes with the voltage of each of the quadrupole deflector were calculated to study two types of sensitivities: (1) transmission-sensitivity, which is defined as the change in maximum transmission per volt applied to the rod and (2) energy-sensitivity, which is defined as the change in the ion energy (at which maximum transmission occurs) per volt applied to the rod. Simulations were done for voltage variations on all four rods, on the entrance and exit cylinders, and on the endplates. In all the simulations, the proximal rod and the rod opposite were held at -50 Volts while the distal rods were held at +50 Volts. The entrance and exit cylinders and the endplates were maintained at ground potential.

The maximum transmission and the energy at which it occurs are 78.0% and 54.7 eV respectively. Transmission calculations were performed for selected voltage variations. That is, for each voltage of each rod, ion-beam simulations of the transmission were done for a chosen set of incident energies. A parabola was fitted to these data to find the maximum transmission and the energy at which it occurs. This procedure was developed to assure that small changes in voltage give small changes in the simulations, i. e., to assure continuity.

### Sensitivities

For voltage variations of the distal entrance rod, the values of the maximum transmission and the energy at which it occurs are plotted in Figures 25 and 26. The lines are fitted to the calculations for small voltage changes, and their slopes are the sensitivities. These sensitivities, and the others calculated, are listed in Table 3. The signs of the rod sensitivities correspond to increases in the magnitude of the voltage. The sum over all four rods of the sensitivities for the energy of maximum transmission energy is near 1 eV/Volt, for the energy should increase by 1 eV when the magnitudes of all the rod voltages are increased by 1 Volt. The sum over all four rods of the sensitivities for the maximum transmission is near zero, for the maximum transmission should not change when the magnitudes of all the rod voltages are increased equally. The signs of the cylinder and endplate sensitivities correspond to the signs of the voltage.

**Table 3. Voltage Sensitivities.**

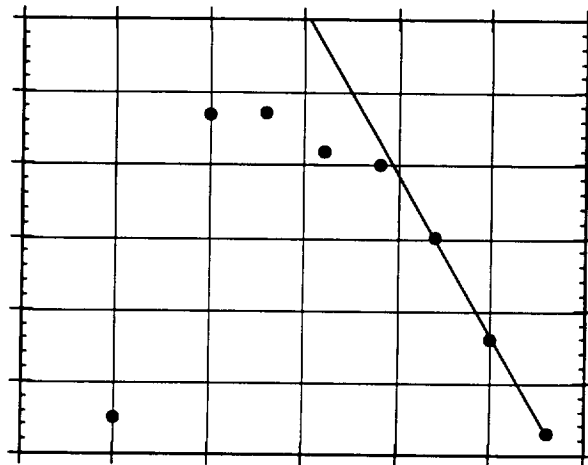
Rod	Nominal Setting	Sensitivity	
		Energy	Transmission
Proximal	-50 Volts	0.37 eV/Volt	1.4 %/Volt
Distal Entrance	+50	0.03	-2.3
Distal Exit	+50	0.50	0.7
Opposite Proximal	-50	-0.10	0.0
Entrance Cylinder	0	0.11	1.7
Exit Cylinder	0	0.20	0.3
Endplates	0	0.15	0.5

## Transmission Improvement

### Distal Entrance Rod

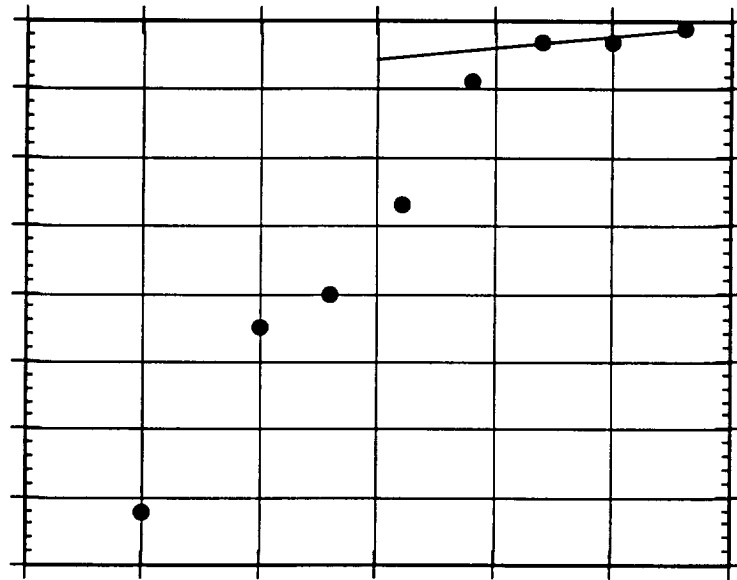
The largest sensitivity for transmission occurs for voltages on the distal entrance rod. Reduction in the voltage magnitude increases the transmission. This could be a simple operational adjustment to maximize the ion transmission. Calculations of the maximum transmission for several reduced voltages are shown in Fig. 25 to illustrate the increase in maximum transmission. There is, of course, a voltage on the distal entrance rod for which the maximum transmission is largest; it is near 35 Volts.

The energy of the maximum transmission is seen from Table 3 to be insensitive to changes in the distal entrance rod voltage. As this voltage is adjusted for largest maximum transmission, however, the transmission energy drops, as shown in Fig. 26. The sensitivity to voltage change is increased to about 0.3 eV/Volt.



25 Distal Entrance Rod Voltage 50

**Figure 25.** Calculations of the maximum transmission for voltage-magnitude changes on the distal entrance rod are shown by the solid dots. The line is obtained from the transmissions nearest the nominal voltage, +50 Volts. The slope appears in Table 3. The departure at large voltage changes is expected because the transmission cannot exceed 100%.



25 Distal Entrance Rod Voltage 50

**Figure 26.** Calculations of the energy of maximum transmission for voltage-magnitude changes on the distal entrance rod are shown by the solid dots. The line is obtained from the energies nearest the nominal voltage, +50 Volts. The slope appears in Table 3. When the deflector is operated with lower voltages on the distal entrance rod, these calculations show the sensitivity of the energy to voltage changes is increased.

### Entrance Cylinder

A large sensitivity for transmission also occurs for voltages on the entrance cylinder. Transmission increases with voltage. Calculations of the maximum transmission for some increased voltages are shown in Fig. 27 to illustrate the increase in maximum transmission, similar to that shown in Fig. 25. Again, there is a voltage on the entrance rod for which the maximum transmission is largest; it is near 25 Volts.

The energy of the maximum transmission is plotted in Fig. 28. It grows nearly linearly with increases of the voltage on the entrance rod throughout the range of calculations.

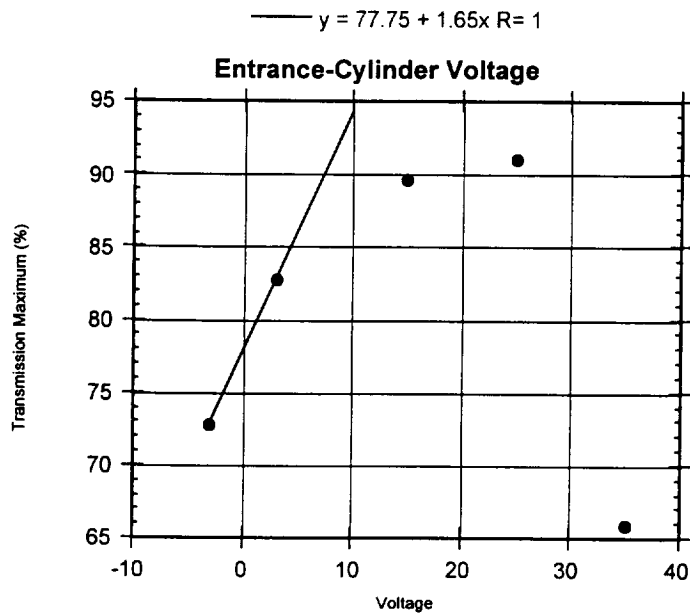


**Figure 27.** Calculations of the maximum transmission for voltage changes on the entrance cylinder are shown by the solid dots. The line is obtained from the transmissions nearest the nominal voltage, which is zero. The slope appears in Table 3. The departure at large voltage changes is expected because the transmission cannot exceed 100%.

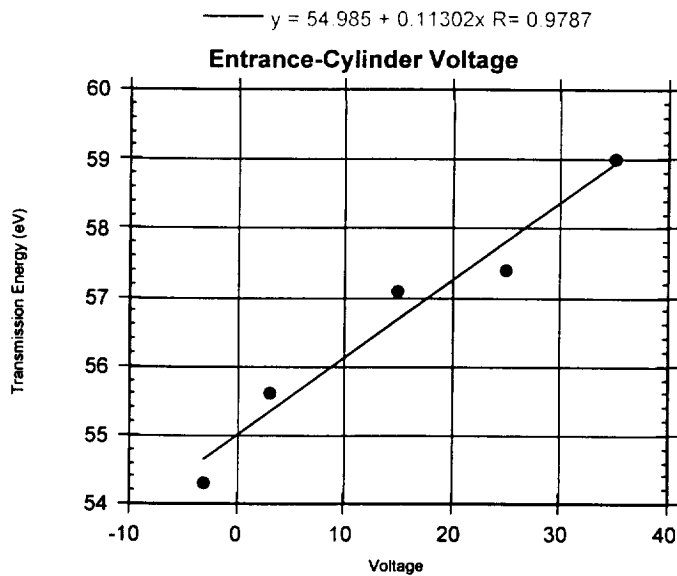


**Figure 28.** Calculations of the energy of maximum transmission for voltage changes on the entrance cylinder are shown by the solid dots. The line is obtained from all the energies as the variations near the origin do not exceed the noise in the calculations. The slope appears in Table 3.

## Endplates

The sensitivity for transmission to voltages on the endplates is small, but positive. Calculations of the maximum transmission for several voltages on the endplates, shown in Fig. 29, show it grows with apparent limit! However, the growth is small for endplate voltages above 50 Volts. The energy of the maximum transmission is plotted in Fig. 30. The sensitivity is near 0.15 eV/Volt over a large range.

Increases of the endplate voltage cause the quadrupole deflector to behave like an electron lens, especially in the YZ plane. Figure 31 shows trajectories calculated for an energy near the transmission maximum when 200 Volts are applied to the endplates. The ions are focused in the exit cylinder. Figure 32 shows a similar plot when there is no added voltage on the endplates. There is no focusing.

There is also some focusing in the XZ plane. Figure 33 shows ion trajectories in this plane when 200 Volts are applied to the endplates and Fig. 34 shows similar trajectories when there is no added endplate voltage. There is a focus in both figures. Without the added voltage, in Fig. 34, the focus is near the middle of the deflector, and it has aberration. With the added focus, in Fig. 33, it is shifted toward the exit cylinder and the aberrations are reduced.

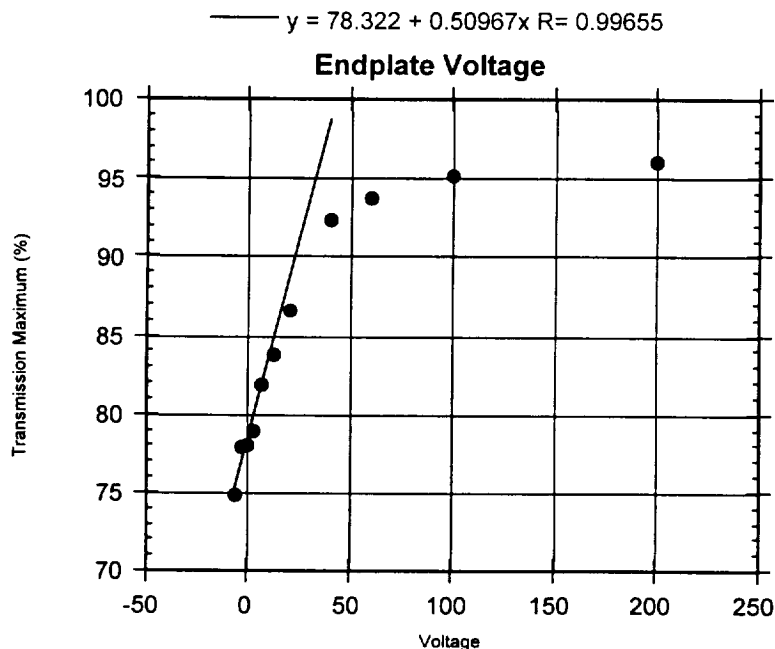


**Figure 29.** Calculations of the maximum transmission for voltage changes on the endplates are shown by the solid dots. The line is obtained from the transmissions nearest the nominal voltage, which is zero. The slope appears in Table 1. While the departure at large voltage changes is expected because the transmission cannot exceed 100%, the transmission asymptotically approaches 100% instead of dropping sharply as the endplate voltage grows.

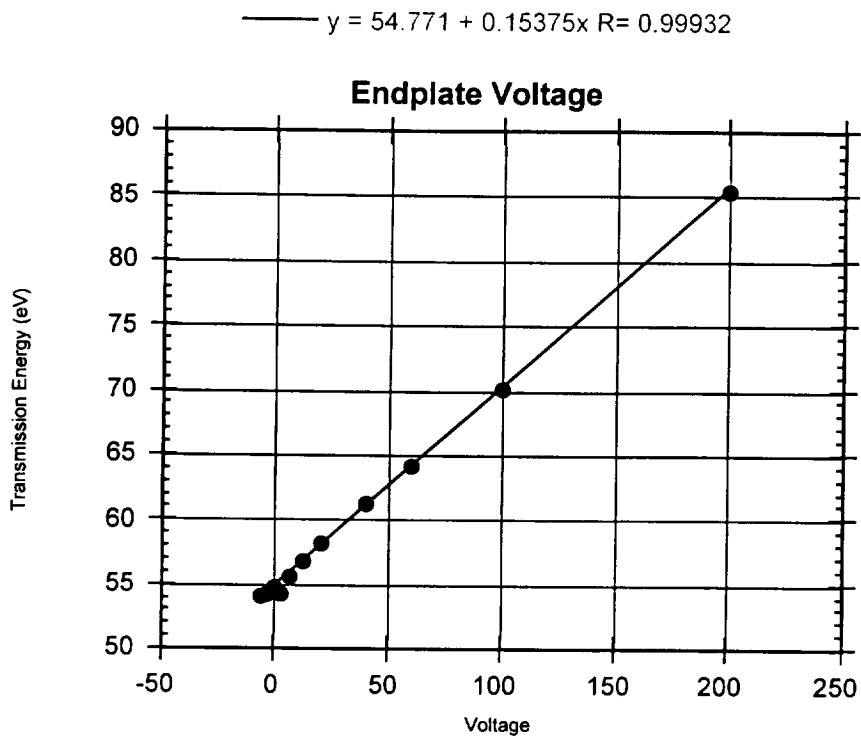


**Figure 30.** Calculations of the energy of maximum transmission for voltage changes on the endplates are shown by the solid dots. The line is obtained from all the energies as the variations near the origin do not exceed the noise in the calculations. The slope appears in Table 3.

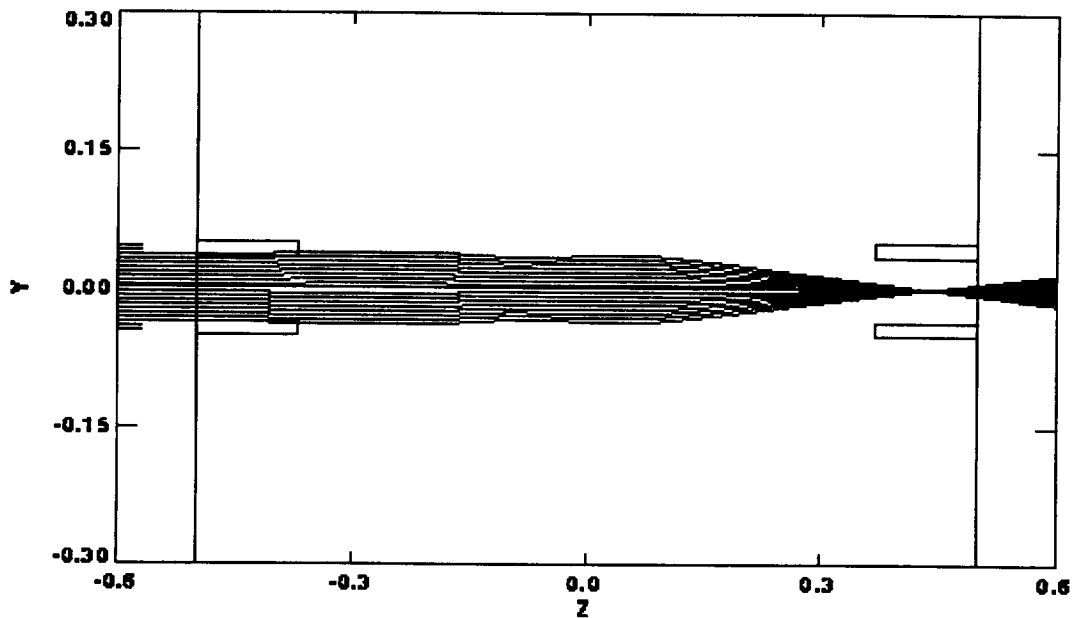


**Figure 31.** Selected 86 eV ion trajectories calculated for 200 Volts applied to the endplates. The selected ions lie in the ZY plane and are initially parallel to the Z-axis. All the selected ions are transmitted through the deflector. The ions enter the deflector at left and exit at right. The central region is redundant and irrelevant, as it connects the two ends of the deflector. The voltage on the endplates focuses the ions in the ZY plane.

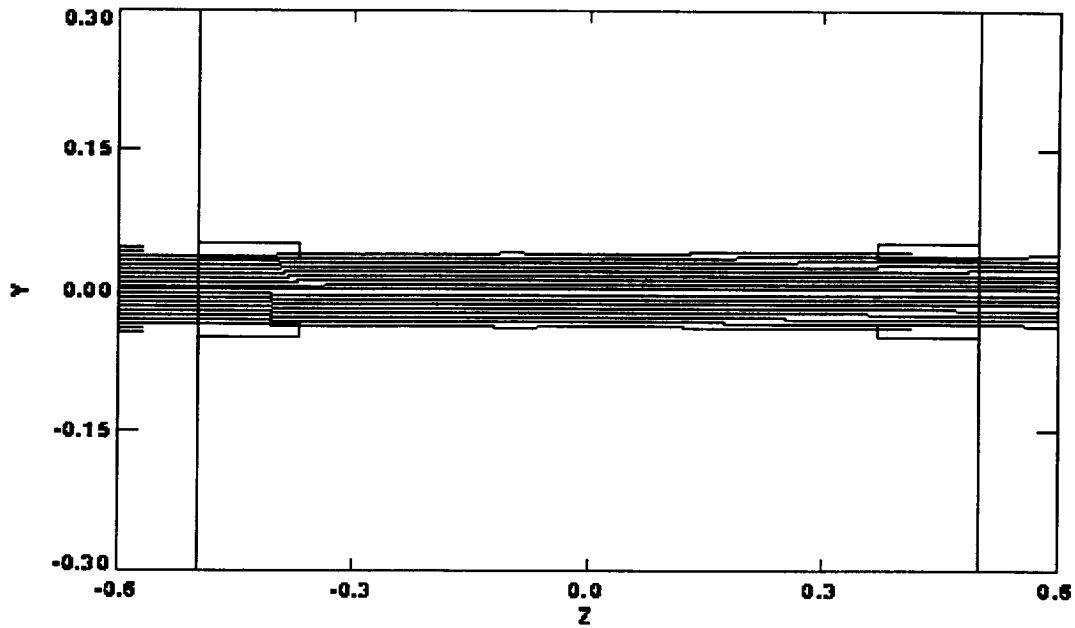


**Figure 32.** Selected 54 eV ion trajectories calculated for 0 Volts applied to the endplates. The selected ions lie in the ZY plane and are initially parallel to the Z-axis, as in Fig. 31. With the endplates at ground the ions are unfocused in the ZY plane.

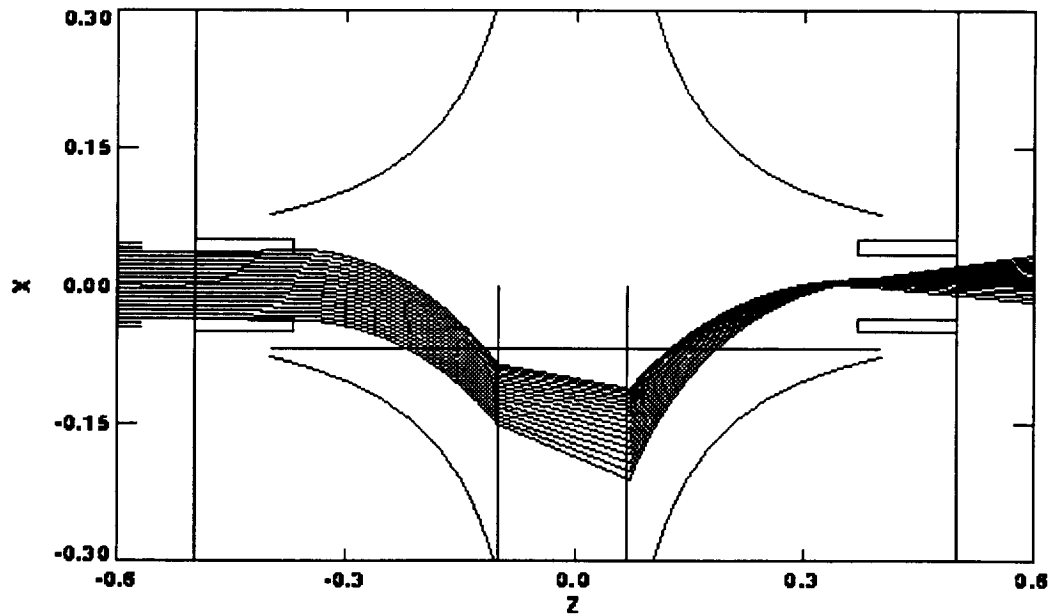


**Figure 33.** Selected 86 eV ion trajectories calculated for 200 Volts applied to the endplates. The selected ions lie in the ZX plane and are initially parallel to the Z-axis. All the selected ions are transmitted through the deflector. The ions enter at left and cross the horizontal plane shown by a line in the deflector. The values on the horizontal plane are transferred to the vertical plane shown by the vertical line at larger Z. The calculation is continued to the exit of the deflector. The region between these two planes is redundant and irrelevant. The ions are brought to a sharp focus near the exit cylinder.

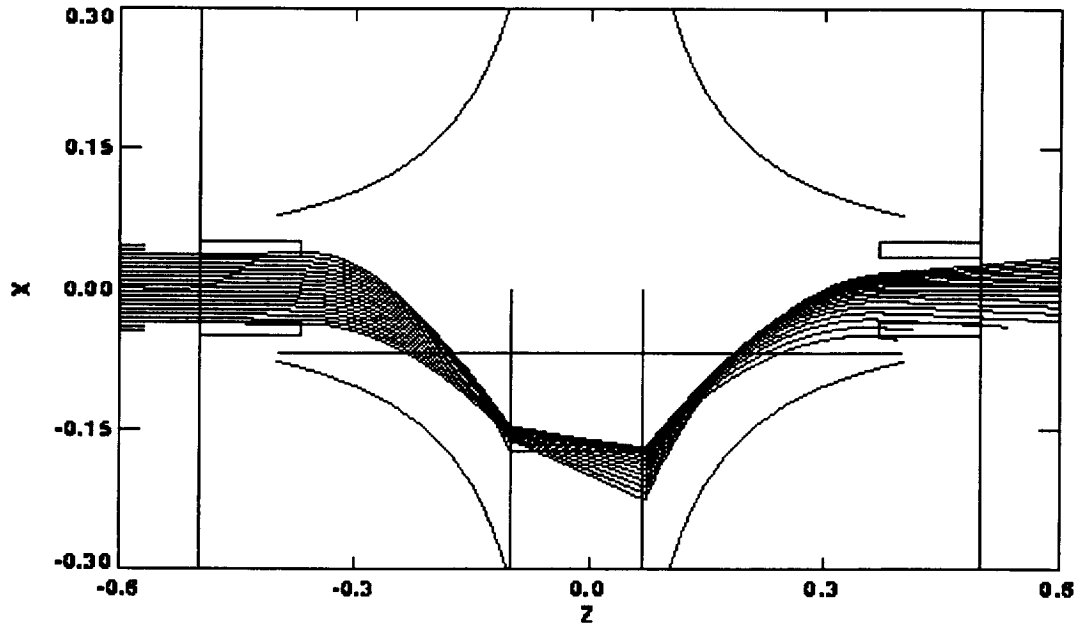


**Figure 34.** Selected 54 eV ion trajectories calculated for 0 Volts applied to the endplates. The selected ions lie in the ZX plane and are initially parallel to the Z-axis, as in Fig. 10. The ions are brought to an aberrated focus in the mid-deflection region. (The focus is aberrated because the trajectories do not have a common intersection point.)

## Applications

These sensitivity calculations were done for a separate model of the quadrupole deflector. They should apply to the quadrupole deflector in the INMS. To verify they do, calculations were done for the deflector in a model of the INMS being used to calculate transmissions of ions in various mass ranges and various angles of attack.

### Endplates

Figures 35 and 36 show selected ion trajectories in the ZY plane of the deflector region, analogous to Figs. 31 and 32. The endplates are at zero volts in Fig. 35 and at 100 Volts in Fig. 36. With 100 Volts on the endplates, more ions are focused into the exit cylinder and the deflector transmission is raised from 82 to 89%. The focusing that leads to this 33% reduction of the ion loss in the deflector is illustrated by the ion-density distributions just prior to the exit cylinder of the deflector, shown in Figs. 37 and 38. Figure 37 shows the distribution with the endplates grounded, and Fig. 38 shows it with the endplates at 100 Volts. The distribution is more confined, especially in the Y direction, in Fig. 38.

### Entrance Cylinder and Distal Entrance Rod

The ion-density distribution of the INMS at the entrance of the exit lens in Fig. 37 at least 4 disjoint peaks. The two on the X-axis are separated by more than 40 mils. Since the exit lens, even when optimized, can be expected to focus only one of these peaks onto the entrance of the mass spectrometer, the ion current in the other peaks is lost. To better illustrate these two peaks, the current density along the X-axis is plotted in Fig. 39.

When the entrance-cylinder voltage is reduced from 50 to 25 volts, these two peaks become closer together, being only 30 mils apart. and one of the peaks increases by nearly 50%,

as shown in Fig. 40. When the distal entrance rod voltage is reduced from 50 to 25 volts, these two peaks again come closer together, being only 20 mils apart and both peaks increase, one by more than a factor two, as shown in Fig. 41. When both these changes are made together these two peaks come yet closer together, being only 10 mils apart, as shown in Fig. 42. The peaks nearly coalesce and the peak height is more than doubled.

The ion-density distribution, analogous to Fig. 37, is shown in Fig. 43. A single 50% contour replaces the four separate contours of Fig. 37. The current contained in the region is increased by about an order of magnitude.

The multi-mode current distribution shown in Figs. 37-42 is present in the ion beam before it enters the deflector, as shown in Fig. 44. About 60% of the ion current lies in the outer edges of the distribution; very little is in the central peak. Analysis of the momenta of the current in the other edges shows it is converging to a focus in the deflector. When focused, it forms the center of the distribution shown in Fig. 37, and makes it a multi-moded distribution. The entrance lens should be redesigned to put more current into the central portion of the beam, i. e., to make Fig. 44 a single mode. One redesign example is reduction of the voltage on the entrance lens, leading to the distribution shown in Fig. 40.

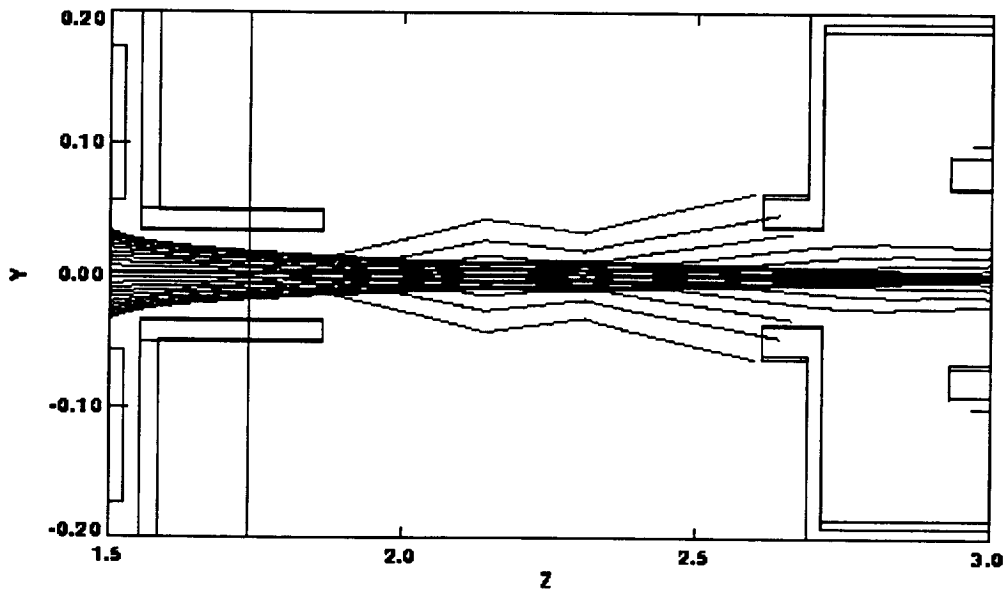


**Figure 35.** Selected ion trajectories in the INMS deflector calculated for 0 Volts applied to the endplates. The selected ions lie in the ZY plane and are initially parallel to the Z-axis. The ions enter the deflector at left and exit at right. The straight lines from  $Z = 2.13''$  to  $2.31''$  are irrelevant artifacts of modeling the deflector region. Portions of the trajectories before  $Z = 2.13''$  and after  $Z = 2.31''$  are redundant, also artifacts of modeling the deflector region. These calculations were done for 28 amu ions at zero angle of attack. The voltages on the open-source electrodes (the last two which are shown) are 0, 10, 10, and 50 Volts, and 200 Volts is placed on the aperture plate. Pairs of quadrupole deflector rods (which lie above and below the plane shown) are at zero and 100 Volts (50 -50 and 50 +50) and the voltage on the exit-lens electrodes (the first two of which are shown) are 50, 229, 771, 18 and 500 Volts.

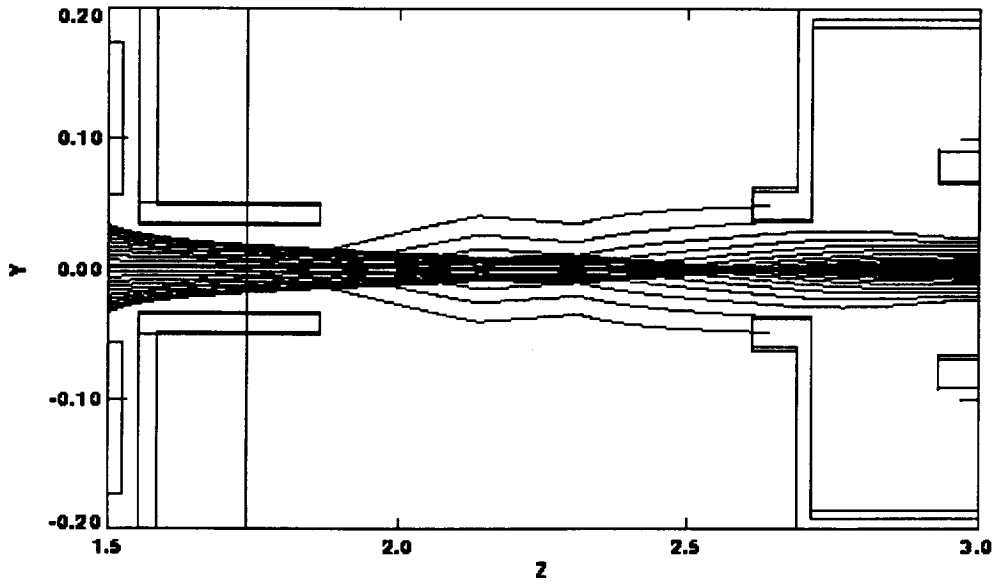


**Figure 36.** Selected ion trajectories in the INMS deflector calculated for 100 Volts applied to the endplates. The conditions are similar to Fig. 35. Pairs of quadrupole deflector rods (which lie above and below the plane shown) are at 14 and 86 Volts (50 -36 and 50 +36).

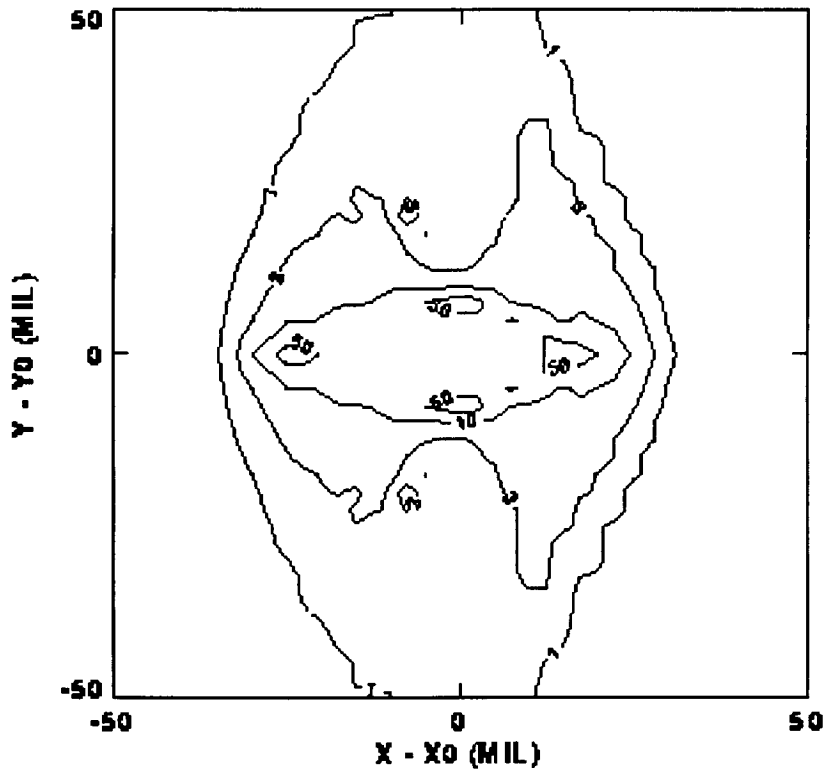


**Figure 37.** Ion-density distribution at the entrance of the exit cylinder calculated for 0 Volts applied to the endplates. This XY plane is at  $Z = 2.61$ " in Fig. 35. Contours at 1, 3, 10 and 50% of peak ion density are shown. The exit cylinder interior diameter is 75 mils; so much of the 1 and 3% contours do not enter the exit cylinder.

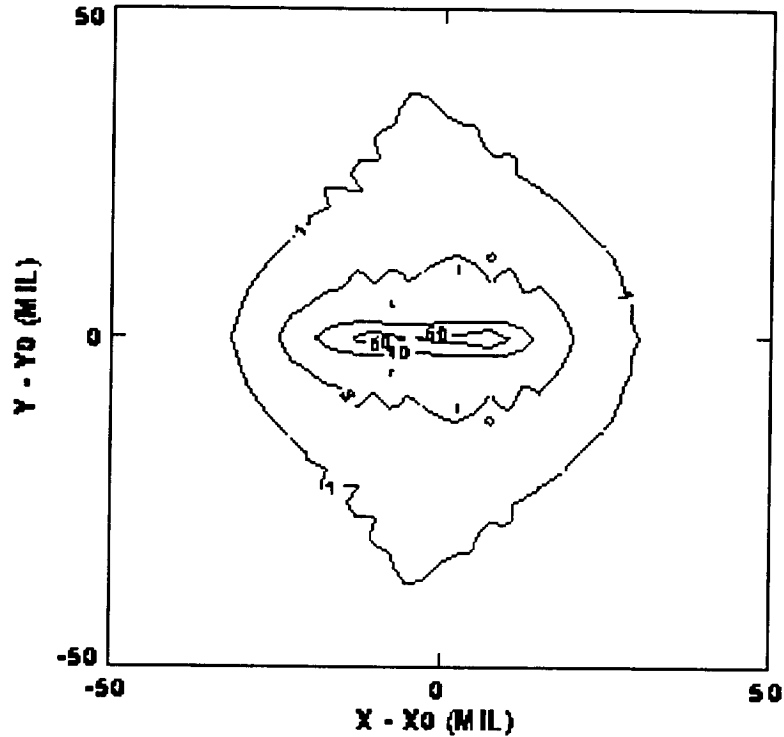


**Figure 38.** Ion-density distribution at the entrance of the exit cylinder calculated for 100 Volts applied to the endplates. This XY plane is at  $Z = 2.61$ " in Fig. 36. Contours at 1, 3, 10 and 50% of peak ion density are shown, as in Fig. 37. The exit cylinder interior diameter is 75 mils, so nearly all the ions enter the cylinder.

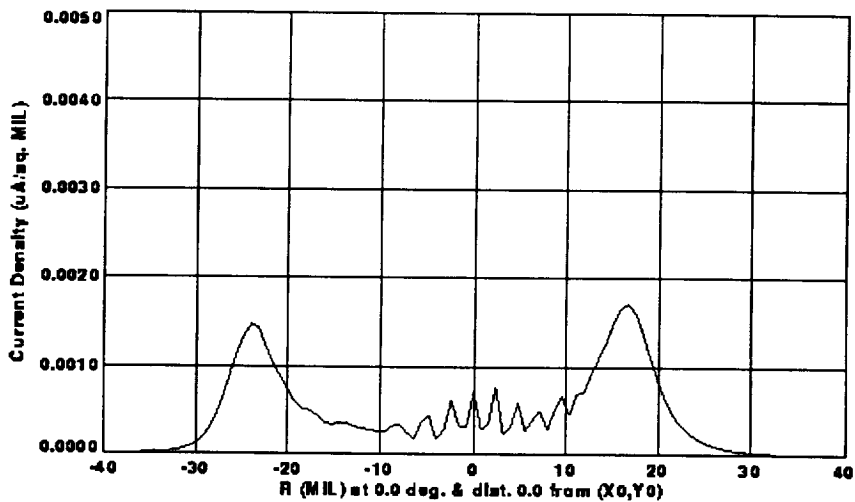


**Figure 39.** Ion-density along the X-axis ( $Y=0$ ) of Fig. 37. The two 50% contours of Fig. 37 on this axis appear as the two peaks in this figure. They are separated by about 40 mils. The intersections of the 10, 3, and 1% contours of Fig. 37 with this axis are in the tails of this distribution. The current contained in one of the large peaks is about 0.02 mA ( $0.001 \text{ mA/mil}^2$  over a 5 mil diameter area), which is about 4% of the current in the entire distribution.

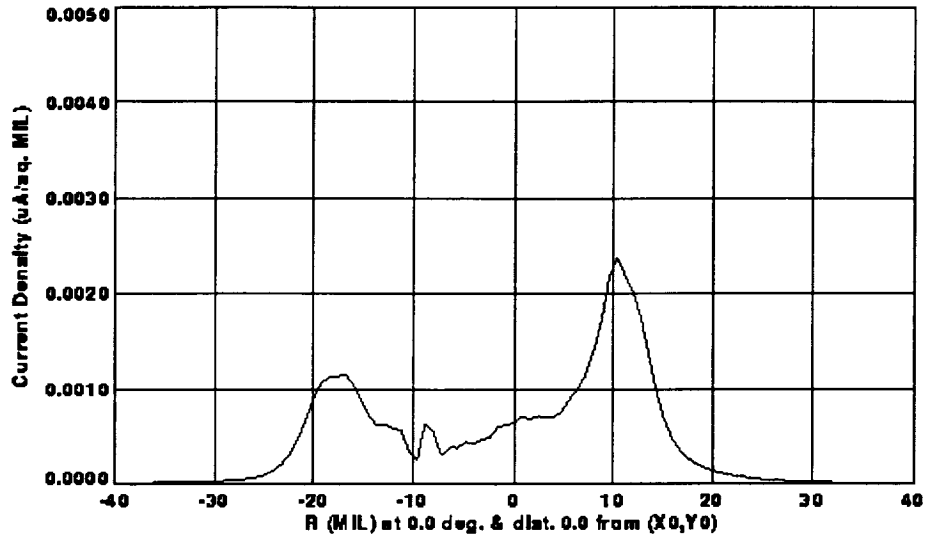


**Figure 40.** Ion-density along the X-axis, analogous to Fig. 39, calculated for a reduction in the voltage on the entrance cylinder from 50 to 25 volts. This reduction upsets the collimation of the beam, so the voltage on the preceding two electrodes had to raised from 10 volts. Thus, the voltages on the open-source electrodes are 0, 20, 50, and 25 Volts (see the caption of Fig. 35). The voltage magnitudes on the deflector rods were decreased from 50 to 45 Volts to properly deflect the beam. The peaks are closer together and the current in one peak is more intense.

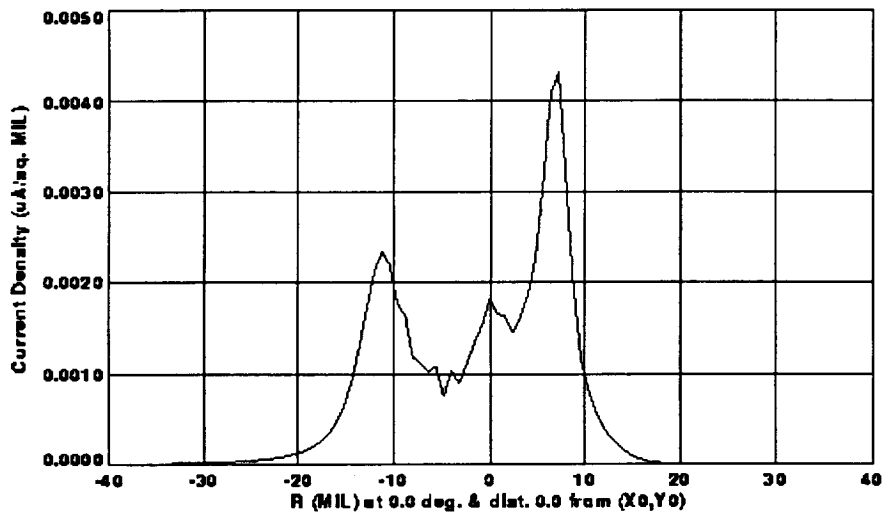


**Figure 41.** Ion-density along the X-axis, analogous to Fig. 39, calculated for a 25-Volt reduction in the voltage on the distal entrance rod. The voltage on this rod is 35 Volts and the voltage magnitudes on the other deflector rods are 60 Volts to properly deflect the beam. The peaks are closer together and the current in both peaks is more intense.

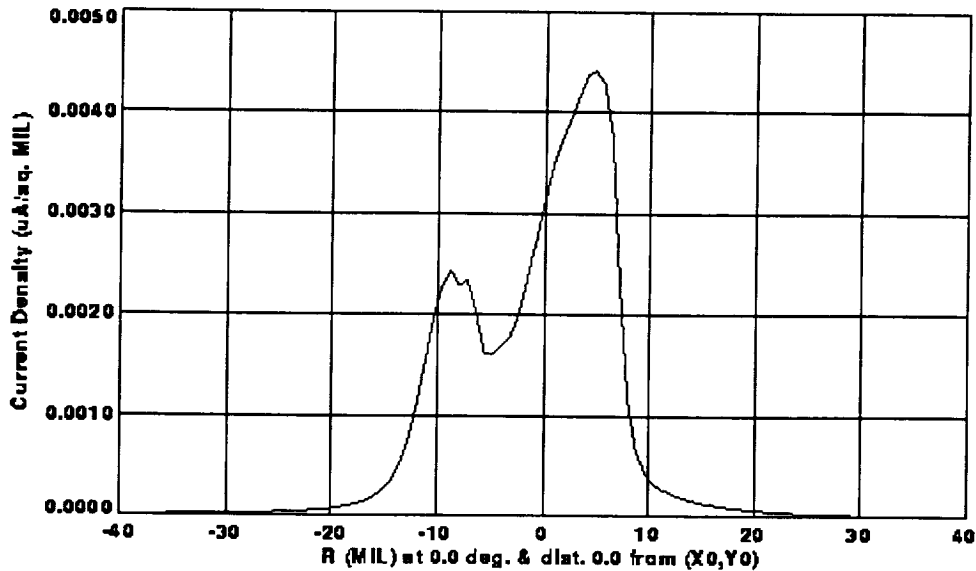


**Figure 42.** Ion-density along the X-axis, analogous to Fig. 16, calculated with both the changes used to generate Figs. 40 and 41. The voltages on the open-source electrodes are 0, 20, 50, and 25 Volts. The voltage on the distal entrance rod is 33 Volts, and the voltage magnitudes on the other deflector rods are 58 Volts to properly deflect the beam. The peaks are yet closer together and larger. The current contained in the larger peak is about 0.2 mA (0.003 mA/mil<sup>2</sup> over a 10 mil diameter area), which is about 40% of the current in the entire distribution.

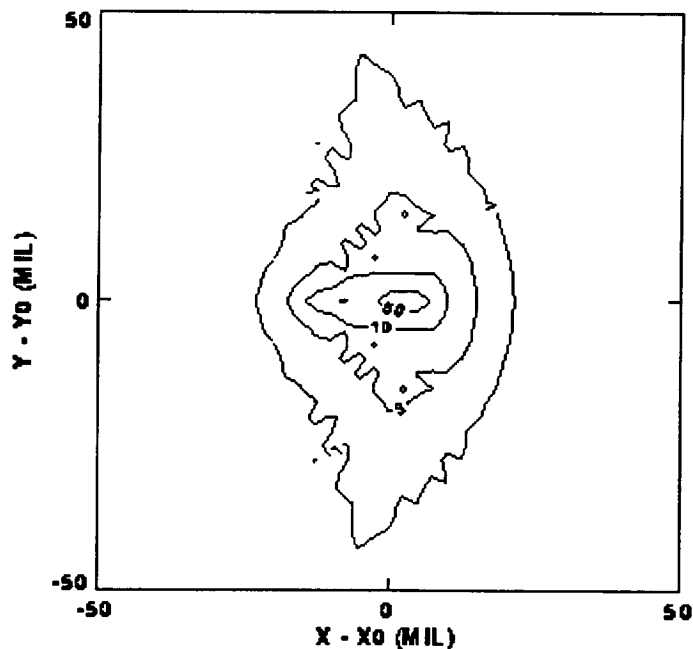


**Figure 43.** Ion-density distribution at the entrance of the exit cylinder, analogous to Fig. 37, calculated for the conditions of Fig. 42. Instead of the four separate 50% contours that appear in Fig. 37, there is a single 50% contour. The contours appear focused in the Y-direction, analogous to Fig. 38, but this is an artifact of plotting fractions of peak current density. The peak current density of this figure is more than a factor two larger than that for Figs. 37 and 38, so the 1% contour of this figure is nearly analogous to the 3% contour of Figs. 37 and 38.

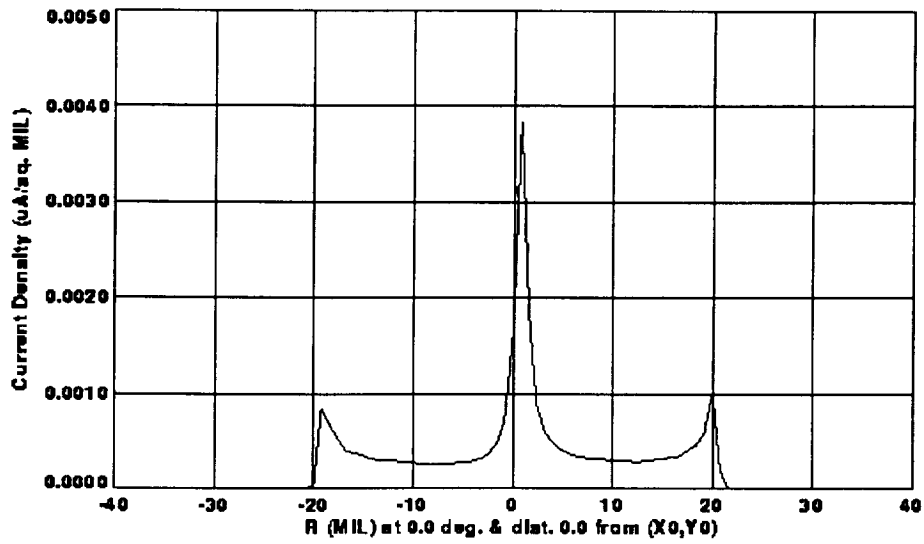


**Figure 44.** Ion-density along the X-axis in the entrance cylinder of the INMS quadrupole deflector. This distribution is from the plane at  $Z=1.71''$ , which is near the extraneous line intersecting the entrance cylinder in Fig. 35. The distribution is nearly symmetric radially, so the density along the Y-axis is similar. About 0.3 mA of the 0.5 mA ion current is concentrated in the outer ring of the distribution ( $0.0005 \text{ mA/mil}^2$  over annulus 40 mils in diameter and 5 mils wide).

## 4. The Exit Lens

The exit-lens system directs ions from the quadrupole deflector or switching lens into a single Radio Frequency quadrupole mass analyzer. The geometry of the exit-lens system (also called the nozzle) initially provided by NASA during the first quarter of the project is given in Figure 1. Preliminary calculations were done using this geometry, with estimated values for dimensions not shown in the diagram.

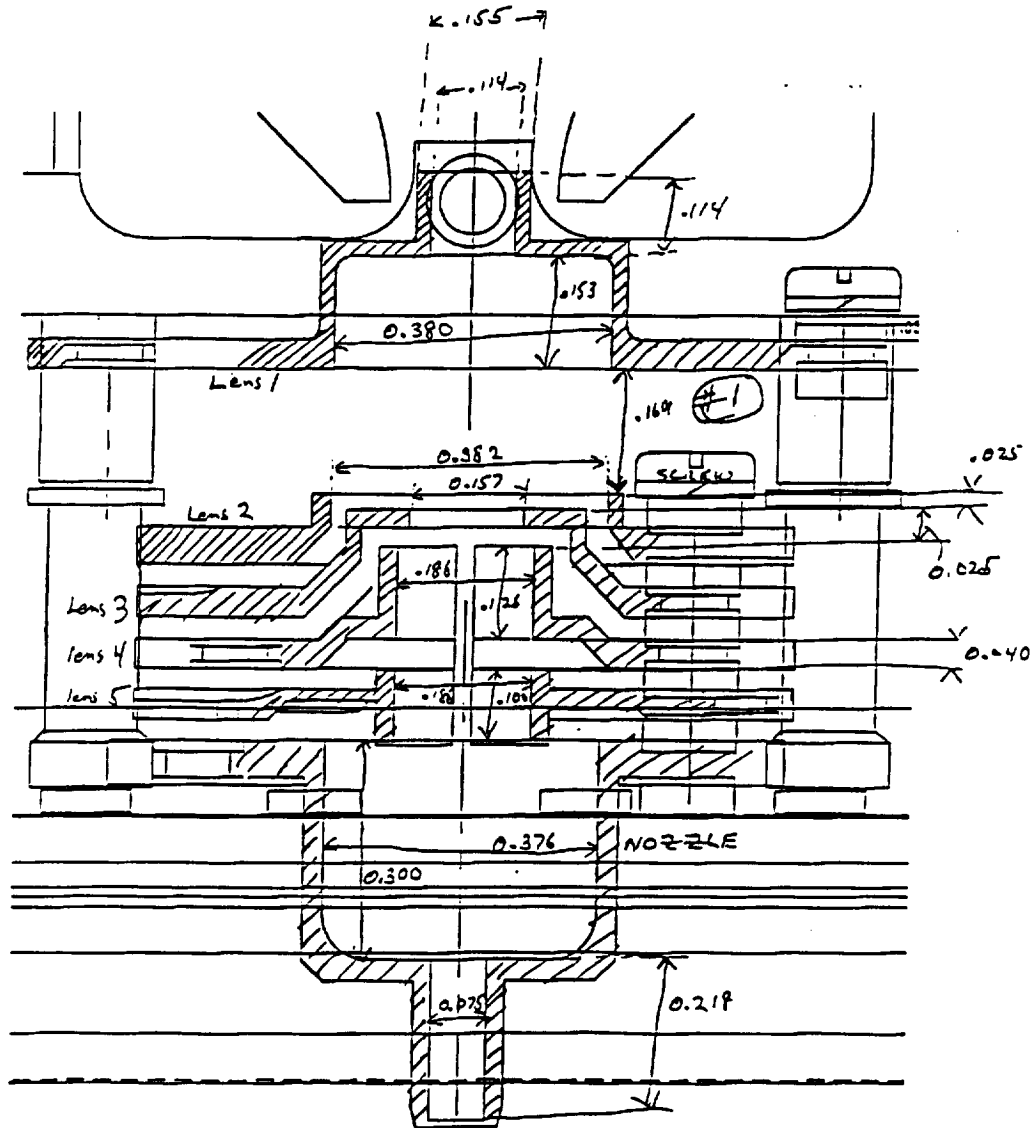


Figure 1: Geometry of the initial model of the exit lens.

Minor, and some major changes in the model were made during the course of the project as we received the geometry of an updated model and more detail, shown in Figure 2. The exit lens system consists of six electrostatic lenses (named IonLens1, IonLens2, IonLens3, IonLens4, IonLens5 and IonLens6). The cylindrical part of IonLens1, the first lens encountered by the ions exiting the quadrupole deflector, extends into the deflector. The gap between IonLens2 and IonLens3 was reduced from the initial model. IonLens3 has been practically eliminated in the INMS model; The horizontal segment of IonLens3 is left to maintain the space between IonLens2 and IonLens4 and the overall dimensions of the instrument. The BEAM3D model of the system in perspective and in cross-section is given in Figure 3. The model contains IonLens3

in its entirety, with its voltage maintained the same as that of IonLens2. IonLens4 and IonLens5 which are split lenses in the INMS model have been modeled as whole lenses. These differences, however, should not affect the ion optics of the model and the results reported here. Figures 4a-f show views of the individual lenses.

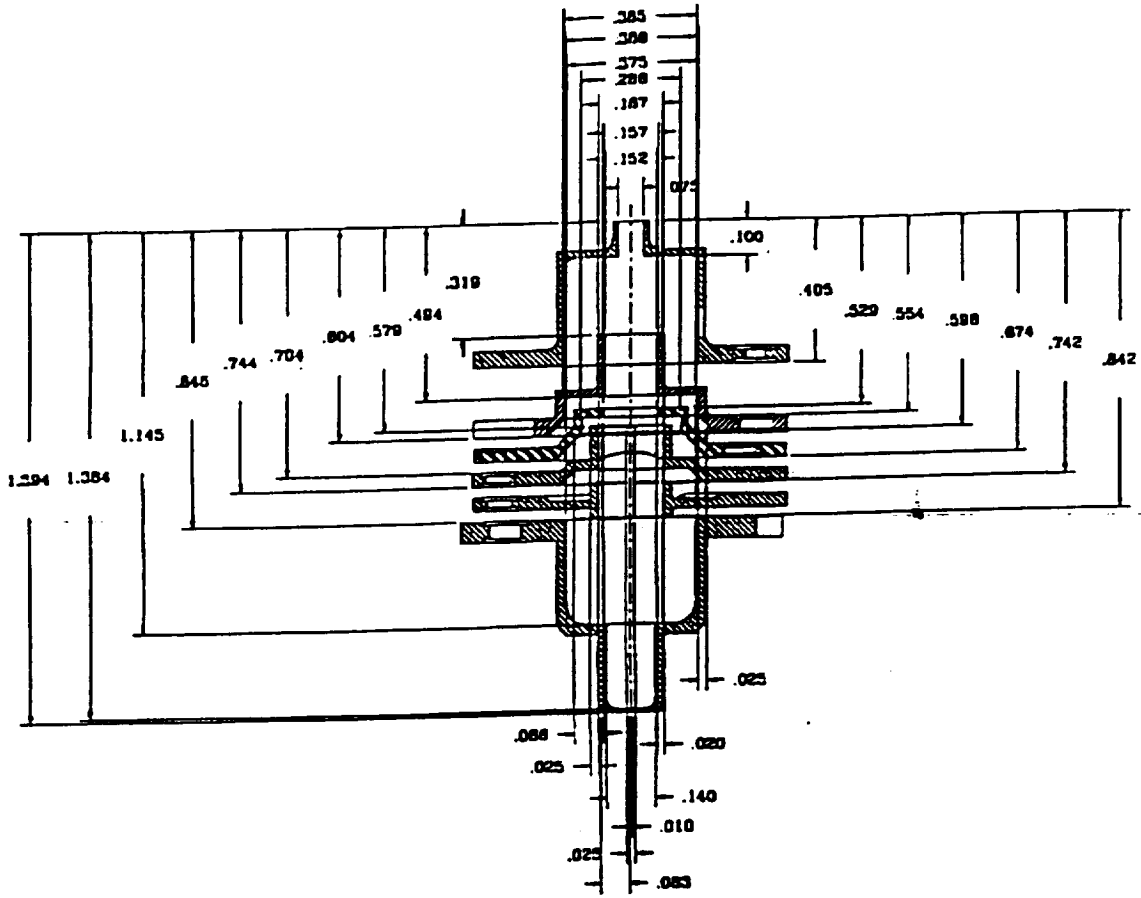
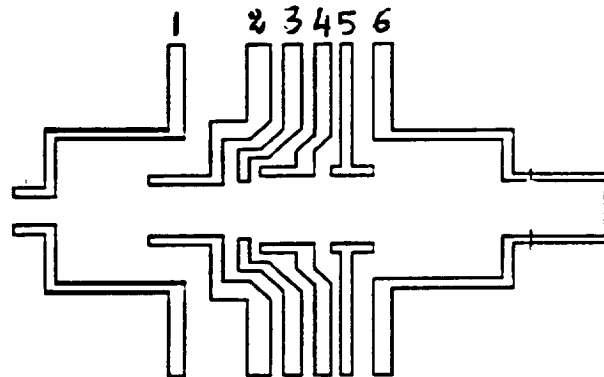
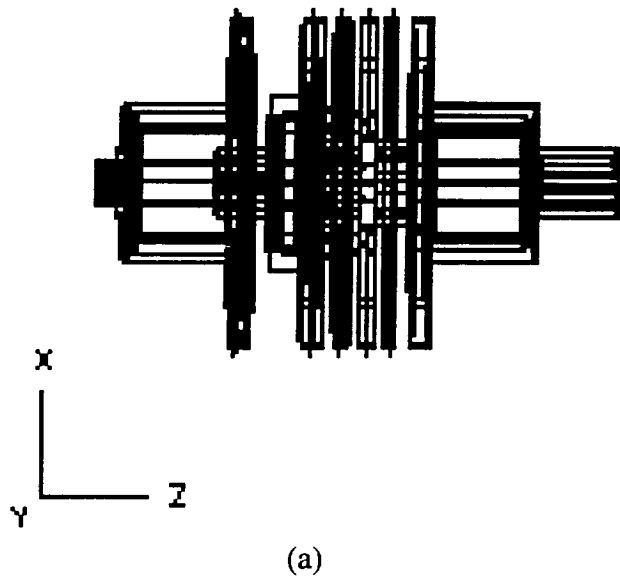
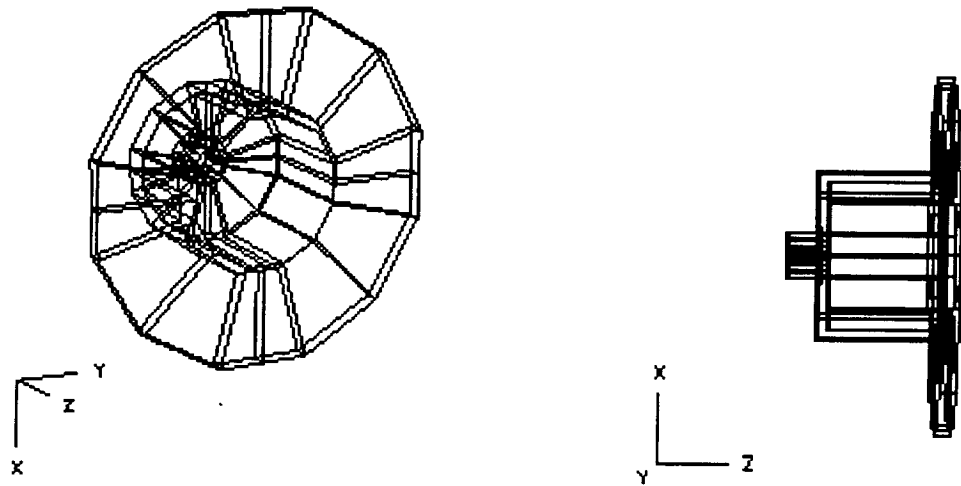


Figure 2: Geometry of the Exitlens of the INMS.



**Figure 3: (a) Perspective and (b) cross-sectional views of the Exitlens model.**



**Figure 4a: IonLens 1 of the exit lens system.**

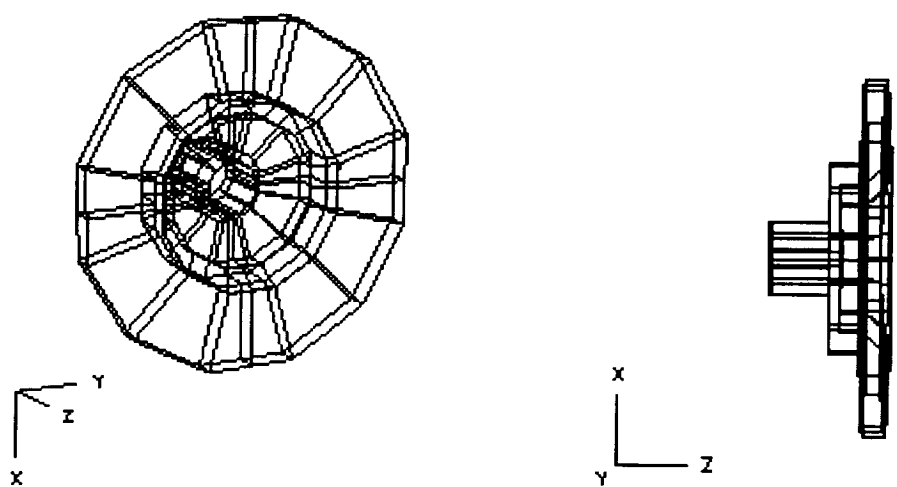


**Figure 4b: IonLens 2 of the exit lens system.**

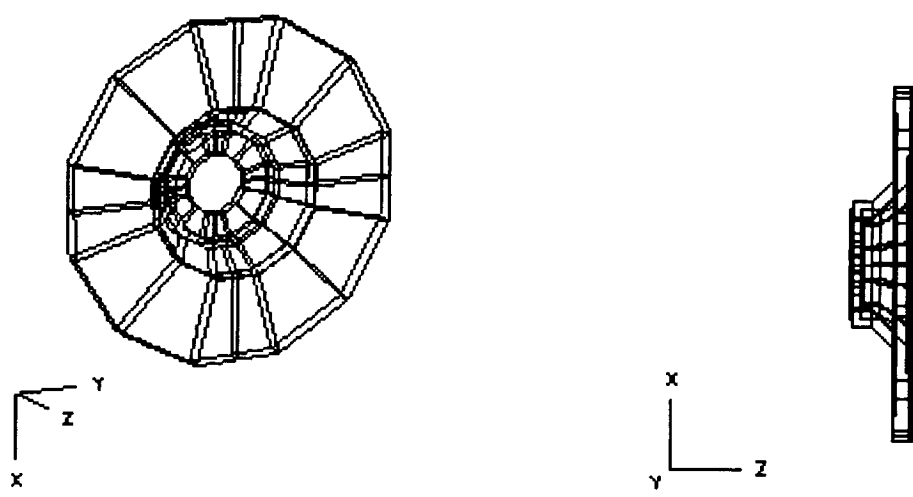


**Figure 4c: IonLens 3 of the exit lens system.**

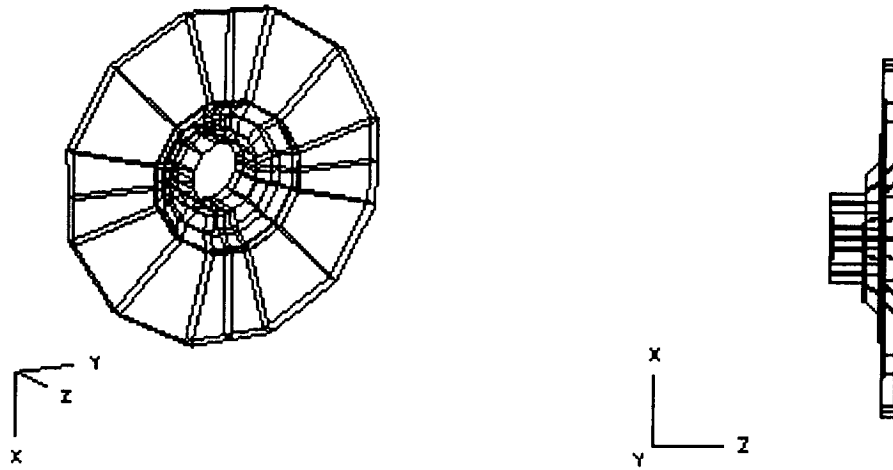


**Figure 4d: IonLens 4 of the exit lens system.**

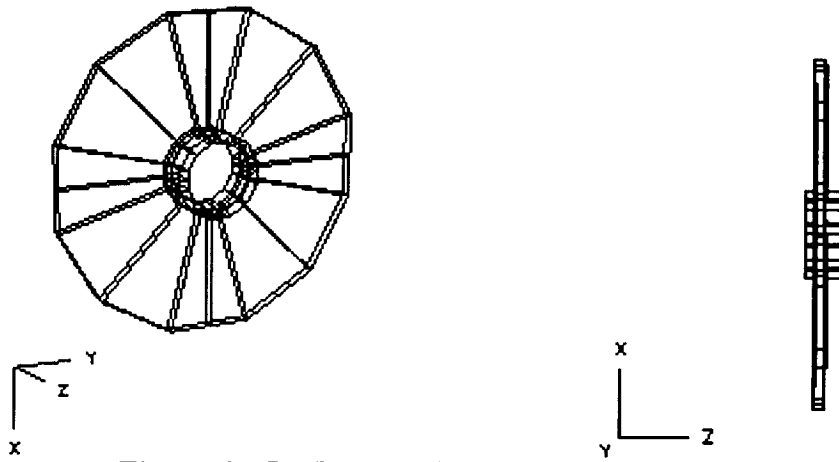


**Figure 4e: IonLens 5 of the exit lens system.**

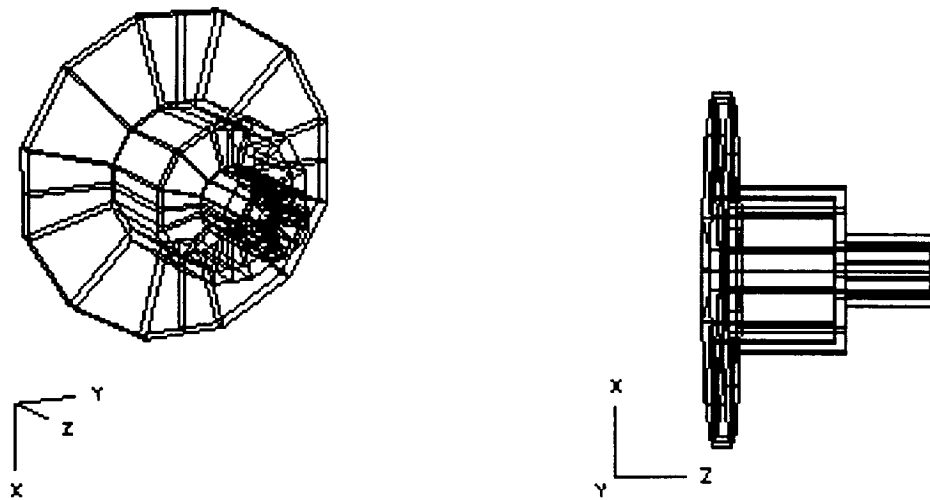


**Figure 4f: IonLens 6 of the exit lens system.**

The geometry of the assembly of the open source, the quadrupole deflector and the exitlens is shown in Figure 5. A cross section of the BEAM3D model of the same is shown in Figure 6. As described in section 3, trajectories of ions deflected by 90° in the quadrupole deflector traverse in the z direction of a flipped coordinate system and hence the axis of the exitlens system in the BEAM3D simulation is parallel to that of the open source. In reality, the axis of the exit lens system is perpendicular to that of the open source.

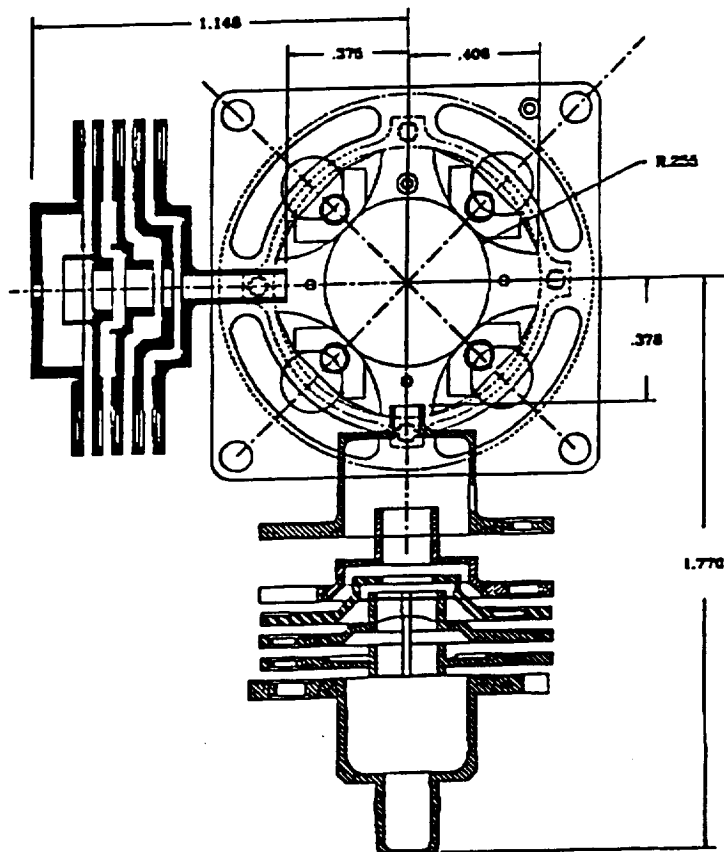


**Figure 5:** The INMS geometry of the assembly of open source, quadrupole deflector and the exitlens.

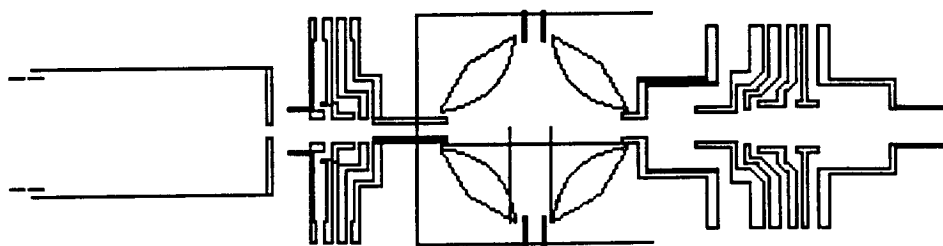


**Figure 6:** Cross section of the BEAM3D model of the open source, quadrupole deflector and the exitlens system.

## Ion optics of the INMS

The simulation of the ion optics for the INMS electrodes between the open source and the mass analyzer is illustrated in Figure 7 which shows the model with trajectories of ions with a kinetic energy of 3 eV.

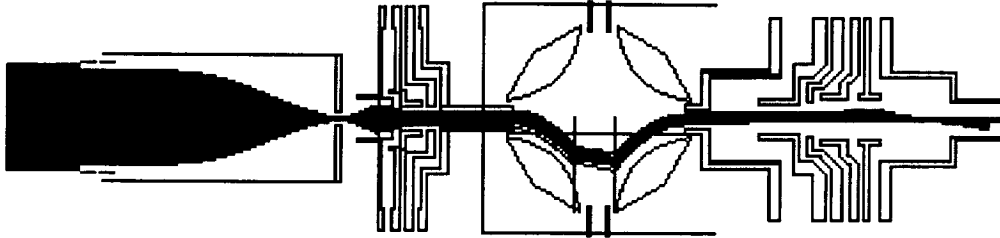
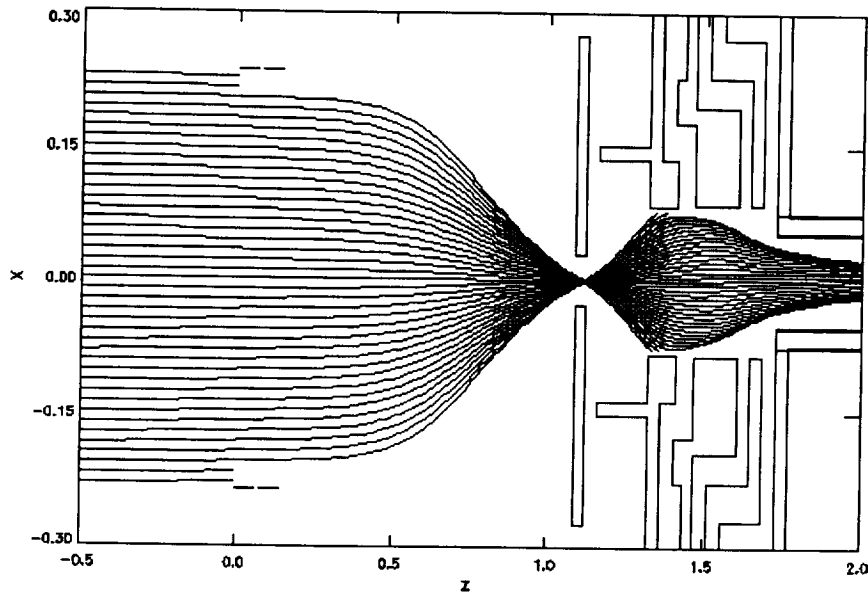


Figure 7: Trajectories of ions with energy of 3 eV.

Figures 8 and 9 show an exploded view for clarity. These figures show trajectories surrounded by outlines of the electrodes. The ions enter the open source at the left of Figure 8 and exit the last lens into the mass analyzer at the right of Figure 9. The right of Figure 8 blends into the left of Figure 9. The ions impinge on the mass analyzer at the right of Figure 8 with maximum concentration over a region about 0.030" wide in X. This region is much narrower in Y, typically 0.002", as illustrated in the YZ trajectory plot in Figure 10. Typically 60% of the incident flux is transmitted through the mass analyzer and about one-fifth of this flux is in the region of maximum concentration. Contours of this distribution are shown in Figure 11. Since the entrance aperture of the mass analyzer is 0.002" in diameter, less than 1% of the ion flux actually impinges on the aperture.

Preliminary simulations were carried out to analyze the variation of transmission with voltages on the individual electrodes of the exitlens. Results showed that

- Calculations of best focus with the penultimate electrode (IonLens5), nominally at -138 Volts, shows the Y-width of the region of high concentration is minimized for voltages near -10 Volts. The Y-width is broadened significantly for voltage changes of 20 Volts or more. The X-width is insensitive to this voltage over several hundred Volts.
- X-displacement of the high concentration region with quadrupole deflector potential is 0.006"/Volt, a low sensitivity compared to the range of these potentials for which ions are transmitted through the deflector.
- When the potential on the first high-voltage electrode (IonLens2) of the exitlens (nominally at -223 Volts) is increased to the maximum high voltage used on any electrode (-771 Volts), the high concentration region in X was narrowed by a factor near two, and the ion density increased accordingly.
- The ion optics is insensitive to the second high-voltage electrode (Ionlens3) of the exit lens (nominally at -229 Volts).



**Figure 8.** The open source and entrance lens of the INMS. Both the X and Z dimensions are in inches, so the cross-sectional (X) scale exceeds the axial (Z) scale by a factor near 2.5. Trajectories are incident from the left with 3 eV kinetic energy along the axis of the INMS. The segmented electrodes (not shown) of the open source preceding the apertured electrode focus the trajectories into the aperture. The electrodes of the entrance lens, at the right, direct the ions into a cylinder leading to the quadrupole deflector. Only trajectories in the XZ plane are shown; in the analyses over one thousand ions simulate the flux. In these calculations the open-source electrodes are grounded except for the apertured endplate at -200 Volts. The first two electrodes of the entrance lens are grounded, and the last two are at -11 and -19 Volts respectively.

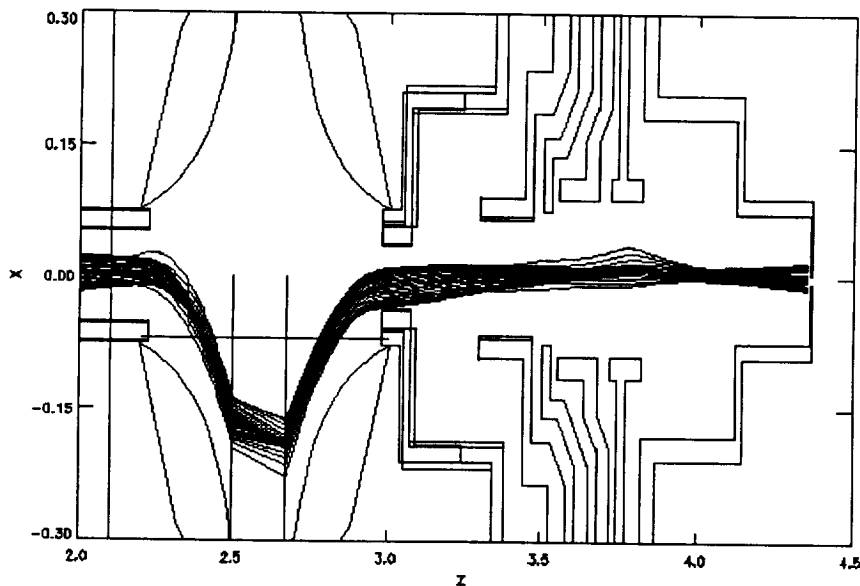


**Figure 9.** The quadrupole deflector and exit lens of the INMS. The X and Z scales are the same as in Fig. 8. Trajectories incident from the left are those on the right of Fig. 8. The quadrupole deflector is on the left. The deflector sweeps the ions through 90°; in simulation, the ion-flux on the horizontal line in the deflector is transferred to the second vertical line to enable an axial simulation. The exit lens on the right directs the ions to the mass spectrometer. Ions enter the spectrometer through the small aperture in the last electrode. In these calculations the quadrupole-deflector plates are at  $\pm 39.5$  Volts and the exit-lens electrodes are at -19, -229, -223, -771, -18, and -550 Volts respectively.

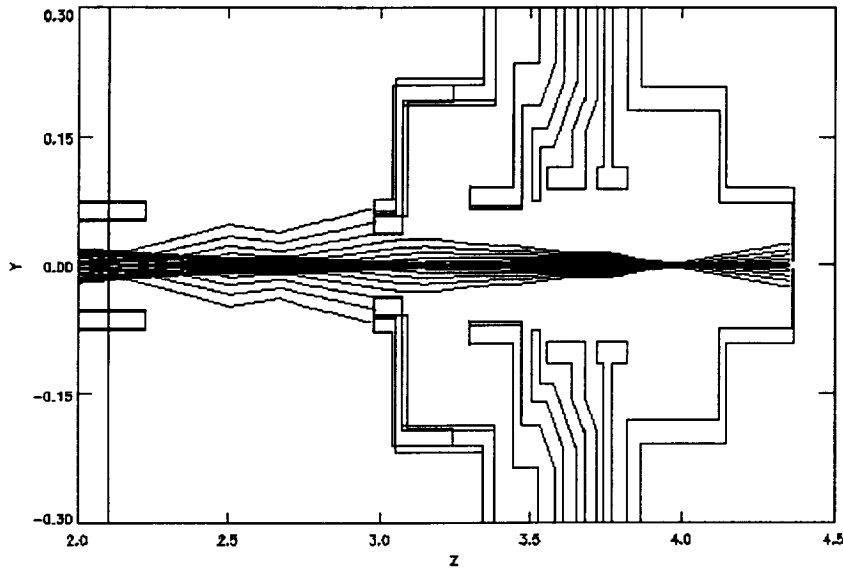


**Figure 10.** The quadrupole deflector and exit lens of the INMS in YZ cross-section. This is the axial plane perpendicular to the plane shown in Fig. 9. The portions of these trajectories preceding this region are similar to those shown in Fig. 8. In this plane the trajectory crossover in the apertured electrode of the open source is imaged in the small aperture of the spectrometer entrance.

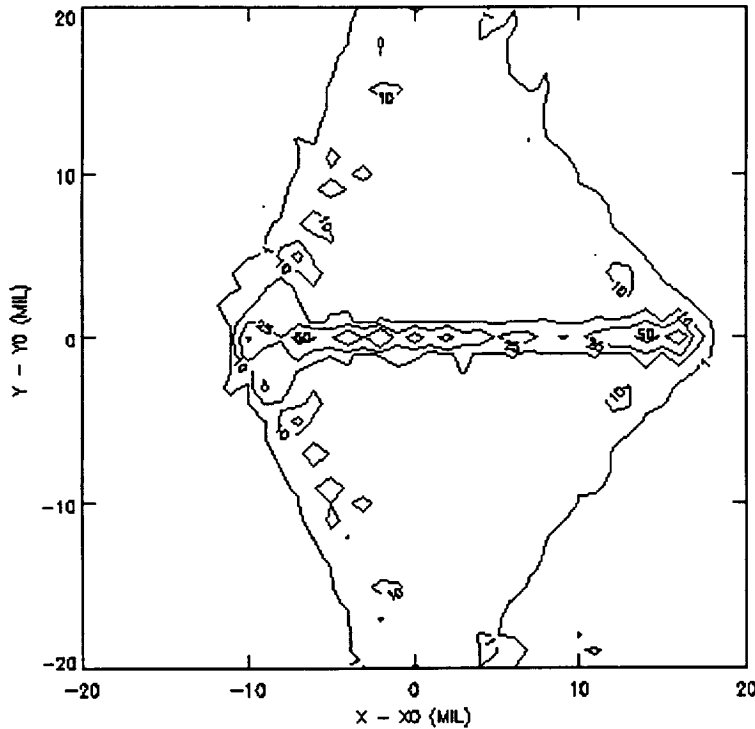


**Figure 11.** A contour plot of the ion flux at the end of the exit lens. Levels at 50, 25, 10, and 1% of peak flux intensity are shown. The maximum flux lies in a narrow band,  $\sim 2$  mils wide in Y and over 30 mils long in X. It is surrounded by an extended region of lower flux levels which fade slowly to zero. The 2-mil diameter of the entrance aperture of the mass spectrometer is very small on the scale of this plot. Even though data from 696 trajectories was used in the diagram, substantial noise remains.

Simulations were carried out to further analyze transmission through the INMS and to study ion losses at different parts of the INMS. Transmissions were calculated for selected ion energies of 0.73 and 4.08 eV, which are the spacecraft equivalent energies of  $\text{Li}^+$  (7 amu) and  $\text{K}^+$  (39 amu) ions for a satellite velocity of 4.5 km/sec. These are equivalent to simulations of 4 and 22 amu ions for a satellite velocity of 6 km/sec. For these calculations, voltages on the entrance electrodes and the ion trap segments were kept at zero. Voltages on the aperture plate (optimized for maximum transmission) for  $\text{Li}^+$  and  $\text{K}^+$  ions were -18 Volts and -180 Volts respectively. Voltages on the four open source electrodes were 0, -10, -20 and -50 Volts. Pairs of quadrupole deflector plates were maintained at -5 and -95 Volts ( $-50 \pm 45$ ) for  $\text{Li}^+$  ions and -2 and -98 ( $-50 \pm 45$ ) Volts for  $\text{K}^+$  ions. Transmission was calculated at the end of the quadrupole deflector and also at the end of the exit lens just before the aperture at various angles. Figures 12 and 13 give the variation of transmission with angle at these points for the two cases. As found earlier, while losses occur in the entrance lens, deflector and exit lens, more losses occur in the entrance lens at higher ion energies and more losses occur in the deflector at lower ion energies.

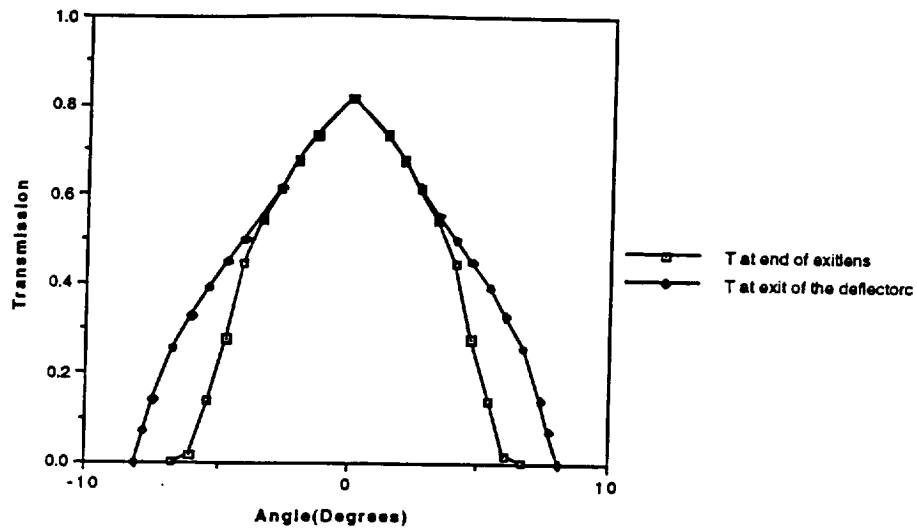


Figure 12: Variation of transmission with angle for 0.73 eV ions.

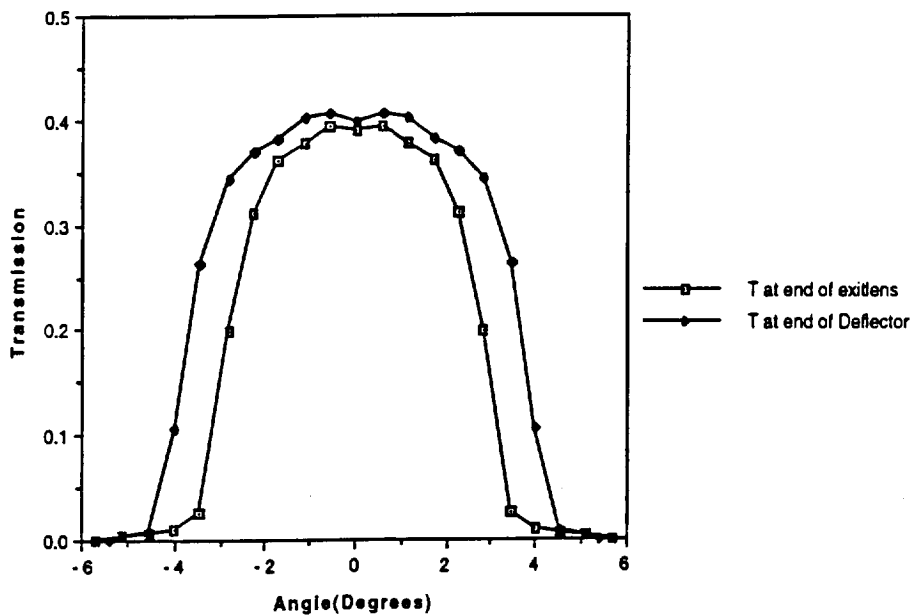


Figure 13: Variation of transmission with angle for 4.08 eV ions.

## Neutral Beams

The INMS is used to detect neutral particles entering the open source. These particles enter with a kinetic energy defined by their mass and the satellite velocity. They pass through the small aperture at the end of the open source unscattered and unaffected by potentials on the open-source electrodes. Upon entering the entrance lens, they are ionized by an electron gun, making them sensitive to the lens electrode potentials. Some of these ions are transmitted through the entrance lens, deflector and exit lens to be detected in the mass spectrometer.

The Sarnoff BEAM3D software can be used to start a beam at a transverse plane in the entrance lens. The neutral beam has a small cross-section limited by the diameter of the aperture between the source and lens. Thus the neutral beam consists of a bundle of particles with a diameter near 0.060", equal to that of the aperture. It is directed along the axis. Trajectories from a simulation of this type of a nitrogen beam are shown in Figure 14. All the ions are transmitted. Trajectories from simulations of this type for a deuterium beam and for a beam of 75 amu ions are similar to those shown in Figure 14 in that all the ions are transmitted when the quadrupole deflector potentials are adjusted.

When neutral beams are ionized in the entrance lens, both scattered and unscattered particles are ionized. Transmission of only unscattered particles is wanted. Scattered particles differ from unscattered particles only in having an energy of 0.015 eV since they are thermalized to the satellite reference frame. The simulation for scattered particles is done at the thermalized energy. The scattered particle distribution is not limited by the aperture between the source and lens, so the spatial distribution of the scattered particles is much larger. A simulation of thermalized scattered particles is shown in Figure 15. A bit more than 1% of these ions are transmitted, so even if they are 50 times more abundant than nitrogen, the nitrogen is still a factor of two more abundant at the detector. The transmission fractions in the INMS are shown in Figure 16.

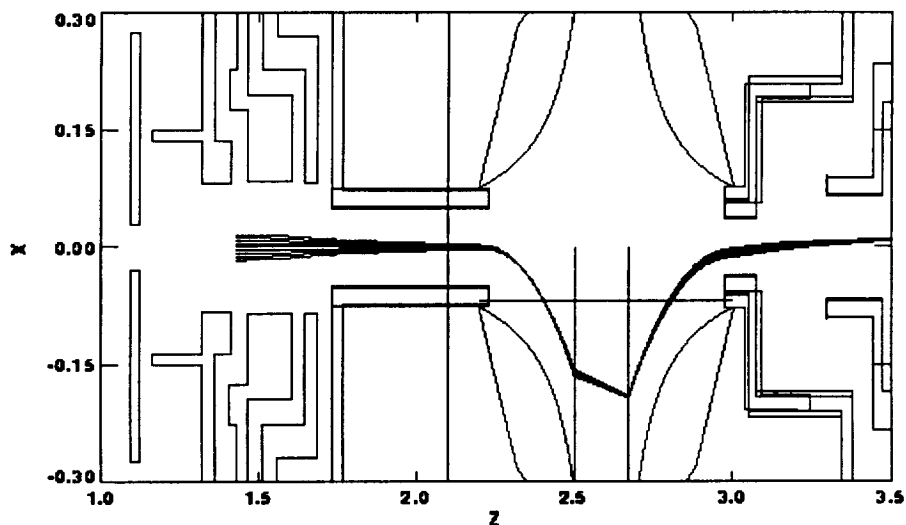


**Figure 14.** Trajectories from a neutral beam in the INMS. The neutral beam (not shown) enters the lens through the aperture at the left. These 28 amu particles have 5.224 eV of kinetic energy. It is ionized following passage through the aperture at the plane where the trajectories start. The trajectories, taken from the ionized neutral beam, are transmitted through the entrance lens, the quadrupole deflector, and into the exit lens. This neutral beam is collected with the satellite velocity vector parallel to the source axis. The apertured electrode is at -10 Volts and the two subsequent electrodes are grounded. The two electrodes preceding the quadrupole deflector are at -11 and -19 Volts respectively. The ions are positive. In these calculations the quadrupole-deflector plates are at  $\pm 35.5$  Volts and the exit-lens electrodes are at -19, -229, -223, -771, -18, and -550 Volts respectively. All the ions are transmitted, where transmission means the ions arrive at the endplane of the exit lens.

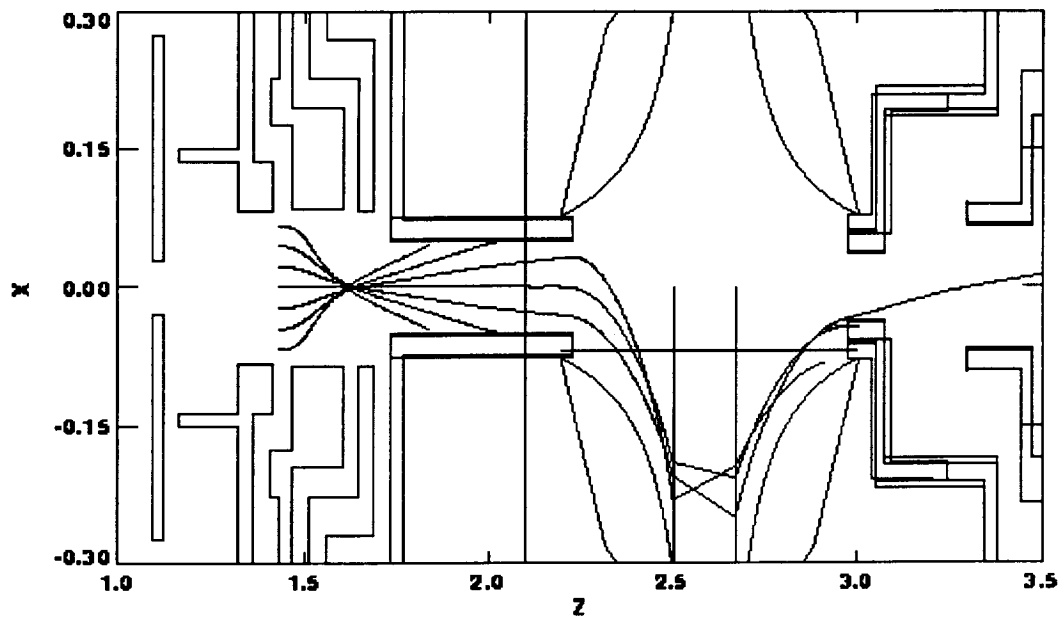


**Figure 15.** Trajectories from scattered neutral particles in the INMS. The neutral particles (not shown) enter the lens through the aperture at the left. Before or after entering, these particles collide with the walls of the source and thermalize to the reference system of the satellite. They are ionized at the plane where the trajectories start. All but 16 of the 1449 trajectories stop. The particles in this simulation have 0.015 eV kinetic energy. The electrode potentials are the same as in Fig. 14.

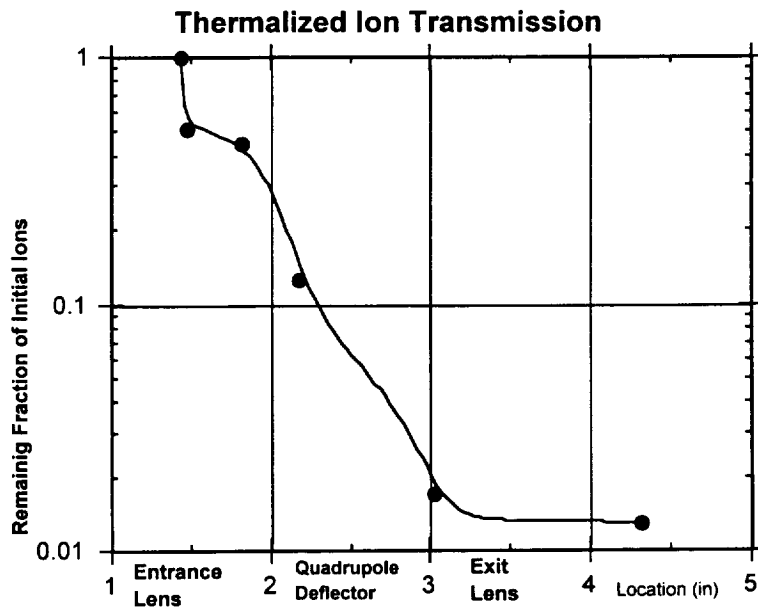


**Figure 16.** Thermalized Ion Transmission versus INMS Location for 0.015 eV ions. The locations of ion-flux loss are shown. The ions have 0.015 eV of kinetic energy in the axial direction and are drawn from a distribution of 0.015 eV thermalized ions in the radial directions. The points are (1.43, 1.0), (1.47, 0.51), (1.82, 0.45), (2.18, 0.125), (3.02, 0.017), and (4.32, 0.013).

## Comparison with Experiment

With the detailed model of the open source, the quadrupole deflector and the exit lens system in place, simulations were carried out to compare transmission through the exit lens system with experimental data. The results should qualitatively agree regarding peak shapes, positions, etc. Comparisons were made with experimental results from both the engineering model and the flight instrument.

## Comparison with Engineering Model

Ion transmission measurements were made with the engineering model (hereafter referred to as EM) of the INMS at NASA. At PES and Sarnoff simulations were done with the same voltages as were used in the measurements. Selected ion trajectories are shown in Figure 17. The ions are created by an electron gun in the central region of the open ion source, near  $Z = 1.47''$ . They have the thermal energy of the test environment, near  $kT$  for  $T \sim 300^\circ\text{K}$ . The ion type is unknown. The region of ionization was chosen to fill the cylinder of the last open-ion-source electrode, as ions from beyond this region would be lost in the cylinder.

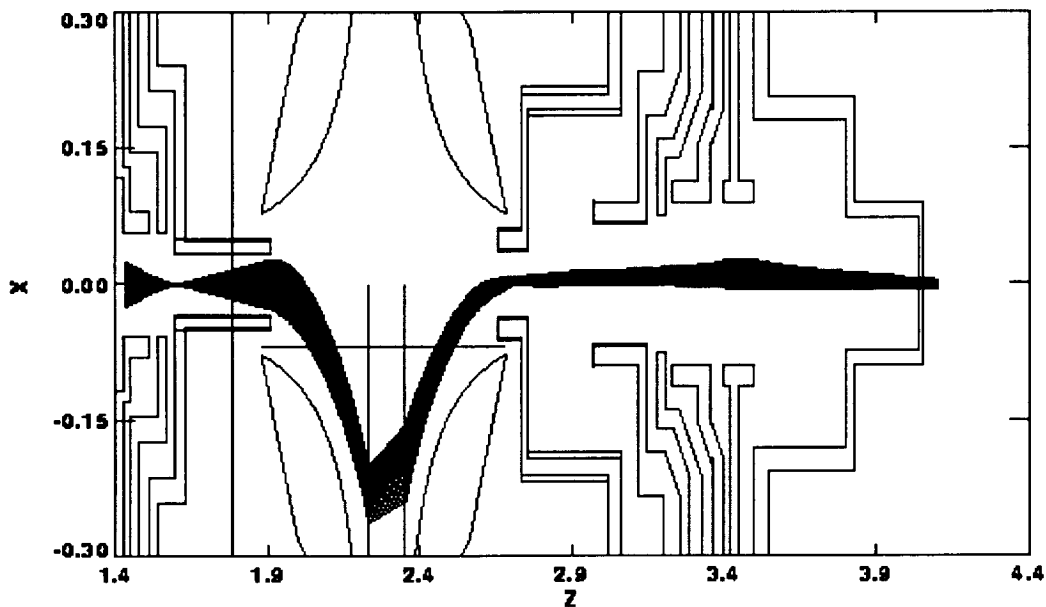


**Figure 17.** Trajectories from a thermal-ion beam in the INMS. The plane (XZ) of deflection is shown. Thermalized neutrals in the open-ion-source lens at left are ionized by an electron gun (not shown). The initial movement of the beam under the electrostatic forces leads to a crossover at the entrance to the cylinder of the last electrode of the open-ion-source lens. Beyond the crossover the ions fill the cylinder. (Because the ions fill the cylinder, it was unnecessary to consider ions from a larger ionization region than that shown at left.) The ion beam is deflected by the quadrupole to enter the ion lens at right, and, after passing through it, most of them enter the small nozzle of the last electrode of this lens. The voltages on the open-ion-source lens electrodes (13 (not shown), 14, 15, and 16) are 0.5, 0, -5, and -10 Volts respectively. The voltages on the ion-lens electrodes (1, 2, 3, 4, 5 & 6) are -10, -287, -287, -415, -74, and -482 Volts respectively. The voltages on the quad lens electrodes (QL1, QL2, QL3, and QL4) are -1.25, -1.25, -18.75, and -18.75 Volts respectively.

With the last open-ion-source electrode at -10 Volts, quad-lens grids 3 and 4 were scanned from -20 to -25 Volts (voltage QL3) to obtain the transmission curve for the INMS. These lenses are at the upper right and lower left of Fig. 17. Quad lenses 1 and 2 (upper left and lower right) were at (-20 - QL3) Volts, i. e., slightly positive. The ion transmission is obtained from the ion current exiting the ion lens at the far right of Fig. 17, near  $Z = 4.0''$ ; the transmission is the ratio of this ion current to the initial ion current at the far left of Fig. 17.

The calculated and measured transmission is shown in Figure 18. The transmission scale in Fig. 18 is that of the calculation, as the initial measured current is unknown. In Fig. 18 it is seen that the voltage of the calculated transmission peak is about 3 Volts below the measured voltage. The width of the calculated transmission is about 0.5 Volts whereas the width of the measured peak is 1.3 Volts.

The difference in the voltage of the transmission peaks is attributed to the sensitivity of centering the ion current density onto the nozzle entrance of the last ion-lens electrode. Small changes in the voltage QL3 on the quadrupole elements can significantly displace the ion current density at this entrance, as shown in Figs. 19 and 20. Other perturbations in the system are also expected to displace the ion current density at this entrance.

The calculated transmission peak is well below 10%. These transmission losses are not apparent from the trajectories shown in Fig. 17, but they are apparent from trajectories in the plane normal to that of Fig. 17, shown in Fig. 21. Following the crossover formed immediately following the ion creation, there are no focusing forces within the quadrupole deflector in the plane shown in Fig. 21. Thus, many ions do not enter the ion lens. The collimated beam formed from those that do enter is much larger than the nozzle entrance on the last electrode; so many of these ions do not enter the detector.

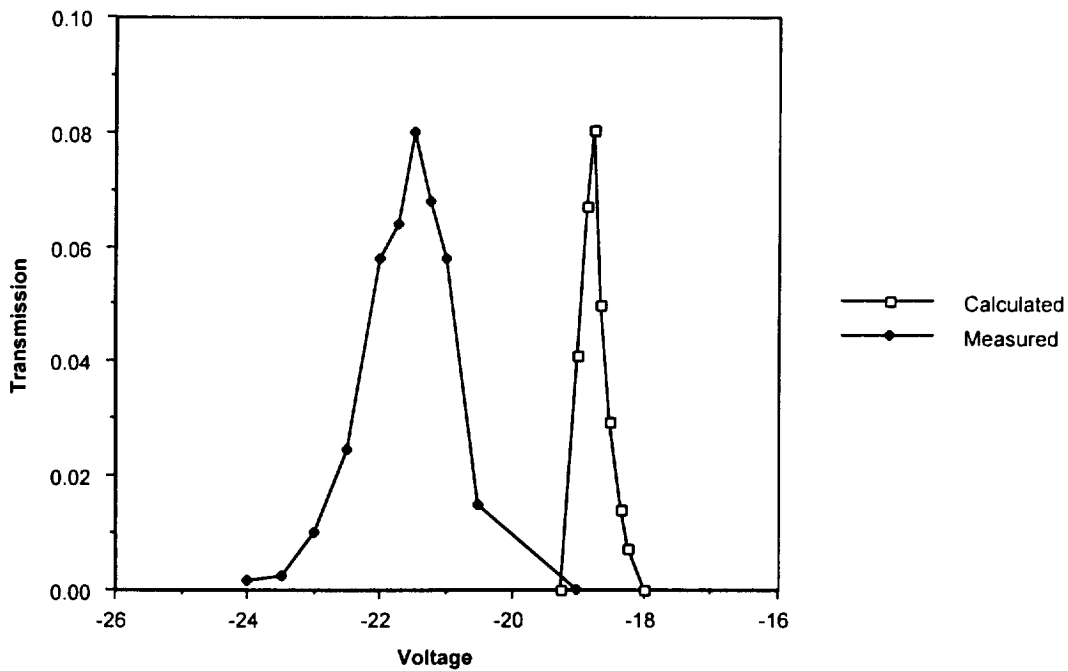


**Figure 18.** Ion transmission into the nozzle of the last ion-lens electrode shown in Fig. 17. The calculated transmission is the fraction of the number of ions in the open-ion-source that enter the nozzle. The measured transmission, from Dr. Heidi Manning of NASA, is in arbitrary units, as the initial number of ions is unknown. The voltage QL3 is described in the caption of Fig. 17, where trajectories from the calculation at QL3 = -18.75 are shown.

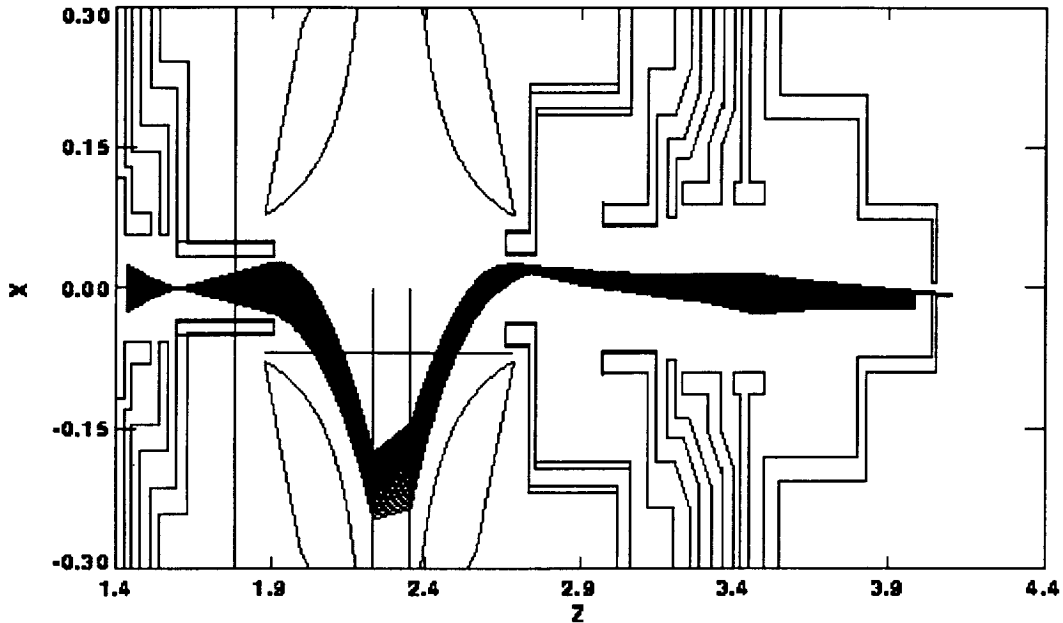


**Figure 19.** Trajectories from a thermal-ion beam in the INMS. The plane (XZ) of deflection is shown. The conditions are the same as Fig. 17, except QL1, QL2, QL3, and QL4 are changed to -1.75, -1.75, -18.25, and -18.25Volts respectively. After the ion beam passes through the ion lens, most of them miss the small nozzle of the last electrode of this lens. The calculated transmission at QL3 = -18.25 Volts in Fig. 18 is obtained from this beam.

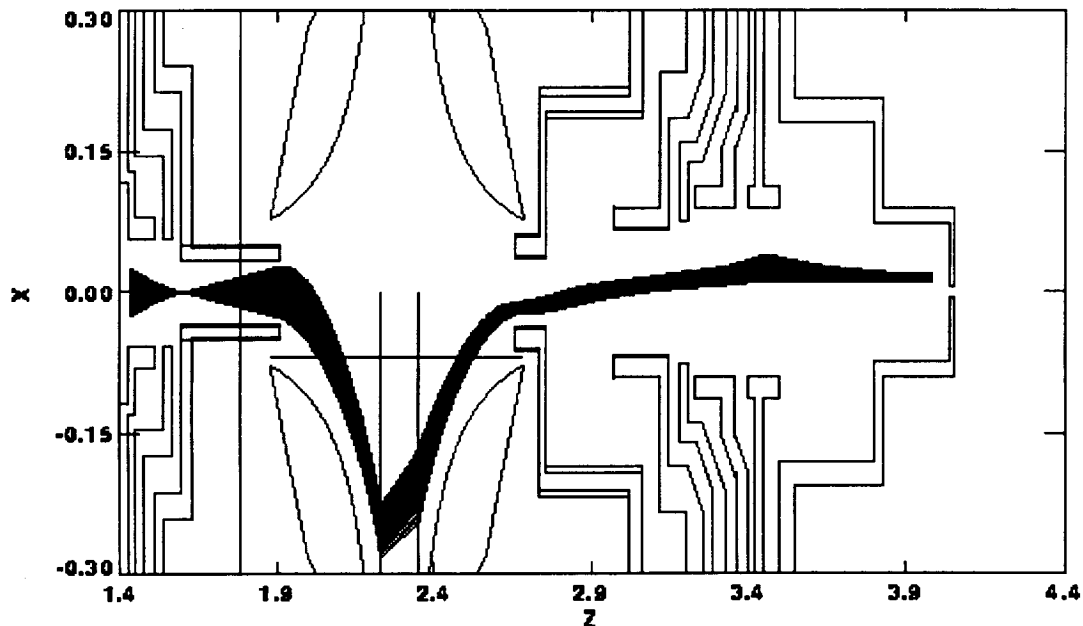


**Figure 20.** Trajectories from a thermal-ion beam in the INMS. The plane (XZ) of deflection is shown. The conditions are the same as Fig. 17, except QL1, QL2, QL3, and QL4 are changed to -0.75, -0.75, -19.25, and -19.25 Volts respectively. After the ion beam passes through the ion lens, all the trajectories shown here miss the small nozzle of the last electrode of this lens. The calculated transmission at QL3 = -19.25 Volts in Fig. 18 is obtained from this beam.

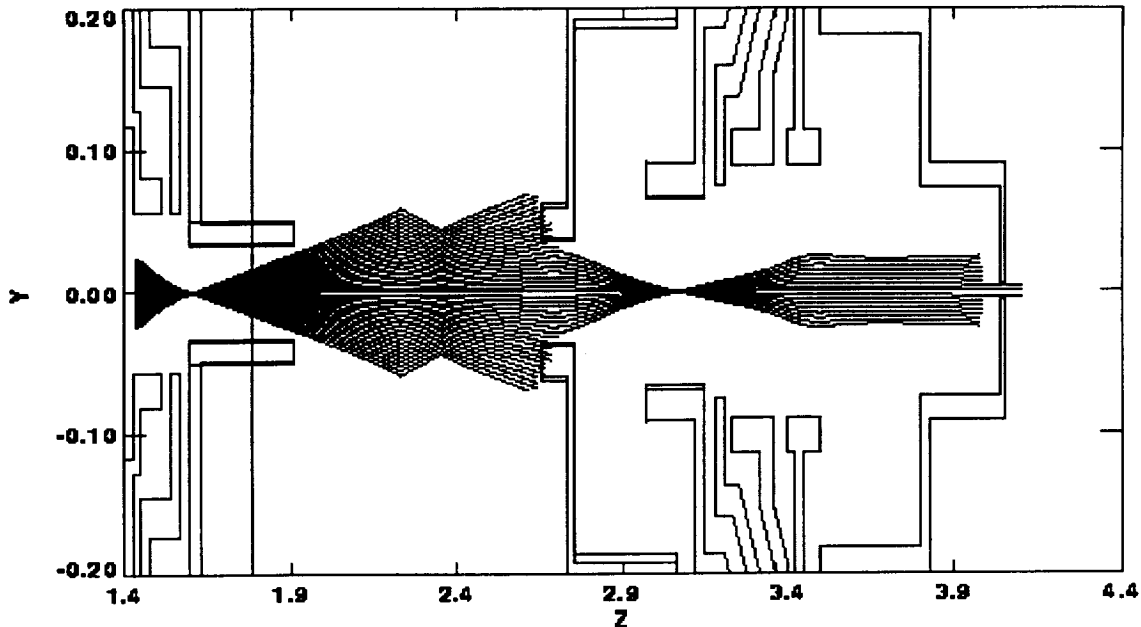


**Figure 21.** Trajectories from a thermal-ion beam in the INMS. The plane (YZ) perpendicular to deflection the deflection plane is shown. The conditions are the same as Fig. 17. Thermalized neutrals in the open-ion-source lens at left are ionized by an electron gun (not shown). The initial movement of the beam under the electrostatic forces leads to a crossover at the entrance to the cylinder of the last electrode of the open-ion-source lens. Beyond the crossover the ions fill the cylinder. The ion beam is deflected by the quadrupole to enter the ion lens at right. The zigzag is an artifact of the transfer of the beam from a horizontal plane to a vertical plane in the deflector, as shown in Fig. 17; the trajectories are nearly linear in this region. Many trajectories do not enter the ion lens. From those that do, only a few enter the small nozzle of the last electrode of this lens.

The transmission curves for calculated and experimental measurements for three more examples are shown in Figures 22, 23 and 24. These calculations and measurements were done with voltage on the quadrupole deflector entrance and exit cylinders (denoted by K) at -10, -20 and -100 Volts. . Calculated ion trajectories for these cases are shown in figures 25, 26 and 27 respectively. The peaks of the transmission curves are listed in Table 1.

**Table 1.** Transmission Peaks in INMS.

K	QL3 Voltage for Peak	
	Measured	Calculated
-10 Volts	-21.5 Volts	-18.9 Volts
-20	-41.5	-37.5
-100	-200	-185

The ions are formed in the open source lens, pass through it, the quadrupole deflector and the ion lens into a small nozzle. This nozzle is the entrance to the mass spectrometer. This system filters the ions, passing ions only when the quadrupole deflector electrode QL3 lies in a narrow voltage range, as shown in Figs. 22-24. This system actually consists of two filters, for the quadrupole deflector is a broad filter and the ion lens is a narrow filter. The ion lens is a filter because the ion beam must impinge in the small nozzle entrance, something it may not always do.

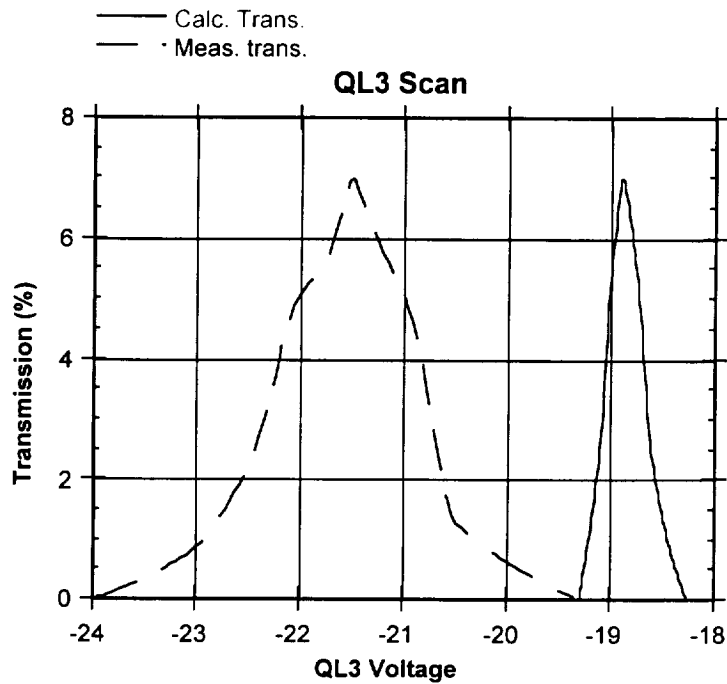


**Figure 22.** Ion transmission into the nozzle of the mass spectrometer for  $K = -10$  Volts. The calculated transmission is the fraction of the number of ions in the open-ion-source that enter the nozzle. The measured transmission is in arbitrary units, as the initial number of ions is unknown. The voltage QL3 is applied to one of the electrodes of the quadrupole deflector. The other voltages are given in the caption of Fig. 25.

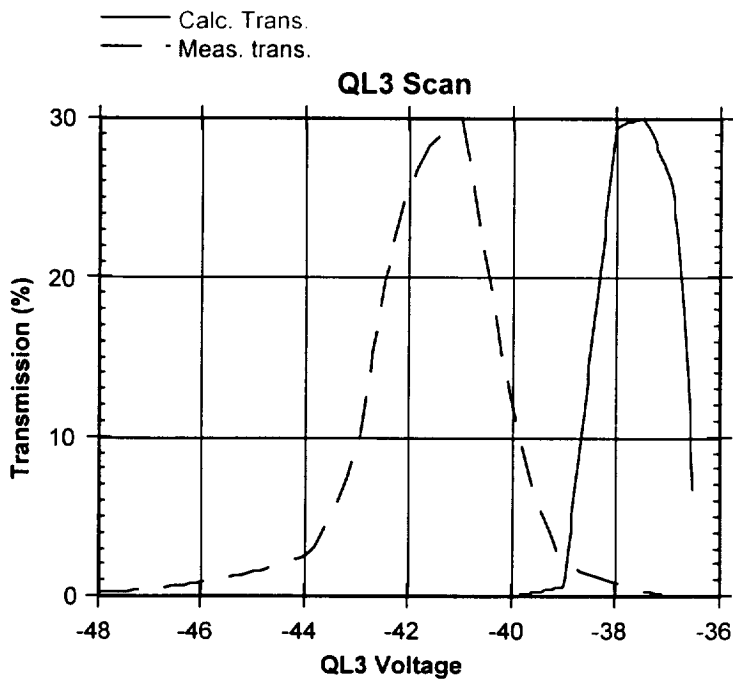


**Figure 23.** Ion transmission into the nozzle of the mass spectrometer for  $K = -20$  Volts. The voltage QL3 is applied to one of the electrodes of the quadrupole deflector. The other voltages are given in the caption of Fig. 26. The maximum transmission is several times that in Fig. 22 due to the increased focus in the ZY plane of the deflector illustrated in Fig. 29.

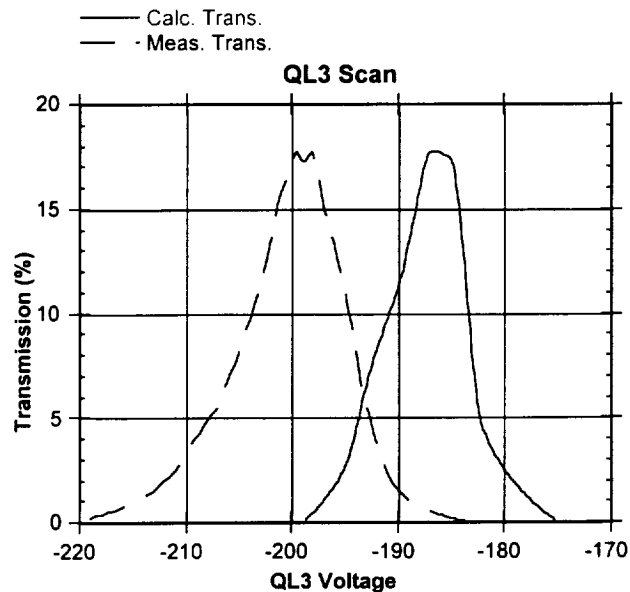


**Figure 24.** Ion transmission into the nozzle of the mass spectrometer for  $K = -100$  Volts. The voltage QL3 is applied to one of the electrodes of the quadrupole deflector. The other voltages are given in the caption of Fig. 27. The maximum transmission is twice that in Fig. 22. Unlike the larger transmission shown in Fig. 23 due to the increased focus in the ZY plane of the deflector, the transmission increase shown here is due to the displaced ion crossover in the ion lens shown in Fig. 30.

## Trajectories

Selected ion trajectories for  $K = -10$  Volts are shown in Fig. 25. The ions are created by an electron gun in the central region of the open ion source, near  $Z = 1.47''$  in Fig. 25. They have the thermal energy of the test environment, near  $kT$  for  $T \sim 300^\circ\text{K}$ . The ion type is unknown. The region of ionization was chosen to fill the cylinder of the last open-ion-source electrode, as ions from beyond this region would be lost in the cylinder.

A plot of trajectories for  $K = -20$  Volts is shown in Fig. 26. The trajectories in Figs. 25 and 26 are similar, except the initial crossover is behind the entrance cylinder in Fig. 25 and beyond the entrance cylinder in Fig. 26. The origin of this change lies not with the voltages on the entrance cylinder, but with the voltages on the electrodes before it, open-ion-source electrodes 1 and 2. These voltages are 0.5 and 0 Volts respectively in Fig. 25 and 2 and -2 Volts respectively in Fig. 26. Small voltage changes near the ion source affect the trajectories significantly. However, the transmission with QL3 voltage is not changed significantly.

The width of the beam in the ion lens of Fig. 26 is greater than the width in Fig. 25. The difference is -20 Volts on the first electrode of the ion lens (the exit cylinder of the deflector) in Fig. 26 and -10 Volts on it in Fig. 25. The lens formed by the first two ion-lens electrodes (the second electrode is always at -287 Volts) is weaker in Fig. 26 than in Fig. 25, leading to a broader beam inside ion-lens electrode 5.

A plot of trajectories for  $K = -100$  Volts is shown in Fig. 27. The lens at the entrance to the ion lens is weakened further and the beam fills much of the aperture of the fifth electrode of the ion lens. The initial cross over in the open-ion-source lens has returned to the entrance of the entrance cylinder due to the increased voltage on the entrance cylinder.

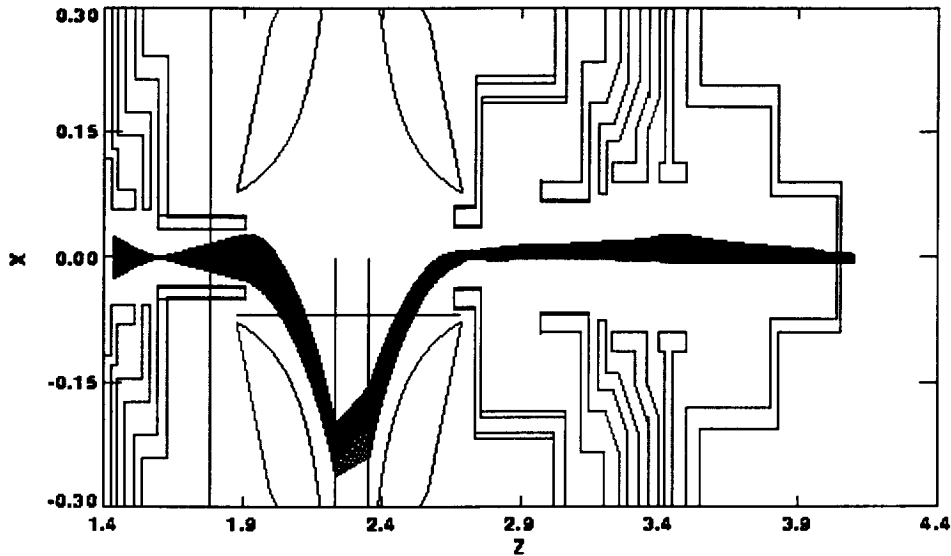


**Figure 25.** Trajectories from a thermal-ion beam in the INMS. The plane (XZ) of deflection is shown. Thermalized neutrals in the open-ion-source lens at left are ionized by an electron gun (not shown). The initial movement of the beam under the electrostatic forces leads to a crossover at the entrance to the cylinder of the last electrode of the open-ion-source lens. Beyond the crossover the ions fill the cylinder. (Because the ions fill the cylinder, it was unnecessary to consider ions from a larger ionization region than that shown at left.) The ion beam is deflected by the quadrupole to enter the ion lens at right, and, after passing through it, most of them enter the small nozzle of the last electrode of this lens. The voltages on the open-ion-source lens electrodes (1 (not shown), 2, 3, and 4) are 0.5, 0, -5, and -10 Volts respectively. The voltages on the ion-lens electrodes (1, 2, 3, 4, 5, and 6) are -10, -287, -287, -415, -74, and -482 Volts respectively. The voltages on the quad lens electrodes QL1, QL2, QL3, QL4, QL5, and QL6 are -1.25, -1.25, -18.75, -18.75 -10, and -10 Volts respectively. The calculated data point at QL3 = -18.75 Volts in Fig. 22 is taken from this calculation. For other data points QL4 = QL3 and QL1 = QL2 = -20 Volts - QL3.

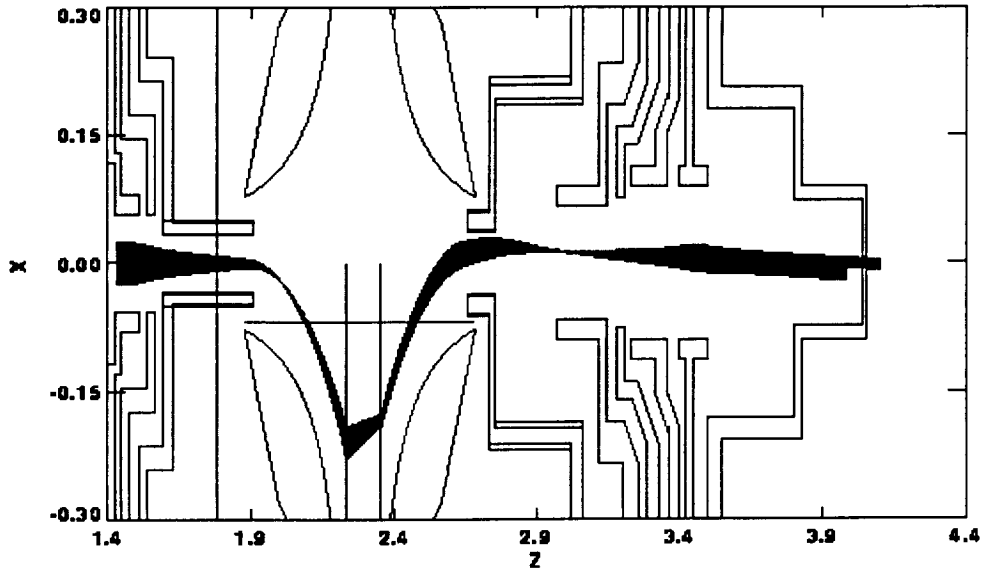


**Figure 26.** Ion trajectories for  $K = -20$  Volts in the INMS. The conditions are similar to those shown in Fig. 25 for 10-Volt ions. The termination of some trajectories near  $Z = 3.9''$  distinguishes trajectories that do not enter the mass spectrometer from those that do. The voltages on the open-ion-source lens electrodes (1 (not shown), 2, 3, and 4) are 2.0, -2, -5, and -20 Volts respectively. The voltages on the ion-lens electrodes (1, 2, 3, 4, 5, and 6) are -20, -287, -287, -415, -74, and -482 Volts respectively. The voltages on the quad lens electrodes QL1, QL2, QL3, QL4, QL5, and QL6 are -3.0, -3.0, -37.0, and -37.0, -20, and -20 Volts respectively. The calculated data point at QL3 = -37 Volts in Fig. 23 is taken from this calculation. For other data points QL4 = QL3 and QL1 = QL2 = -40 Volts - QL3. The first ion crossover is in the quadrupole deflector, well beyond the entrance cylinder. Changes of the voltages on the open-ion-source lens electrodes 1 and 2 from 2.0 and -2.0 Volts, respectively, to 0.5 and 0.0 Volts moves this crossover from beyond the entrance cylinder to its beginning, as in Fig. 25.

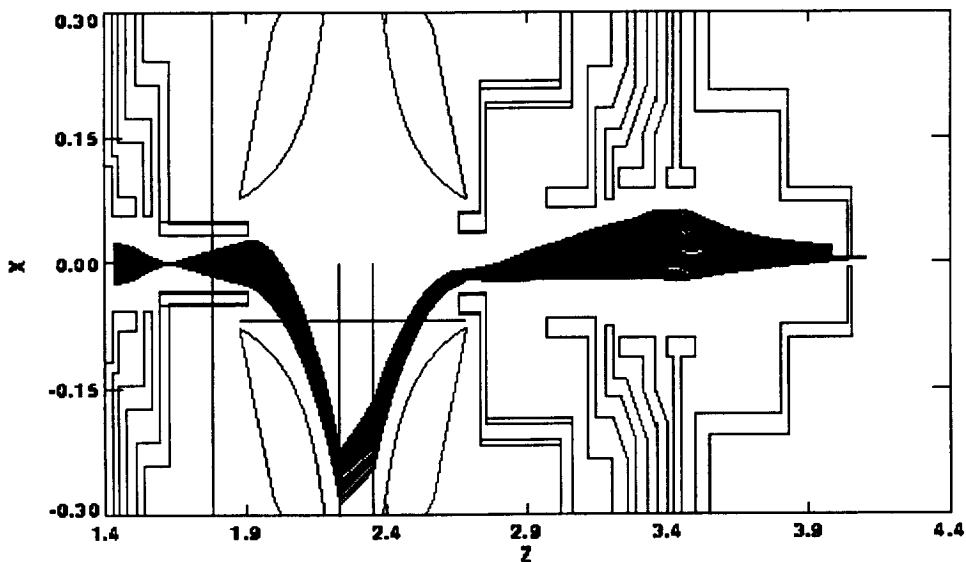


**Figure 27.** Ion trajectories for  $K = -100$  Volts in the INMS. The conditions are similar to those shown in Fig. 25 for 10-Volt ions. The voltages on the open-ion-source lens electrodes (1 (not shown), 2, 3, and 4) are 2.0, -2, -5, and -100 Volts respectively. The voltages on the ion-lens electrodes (1, 2, 3, 4, 5, and 6) are -100, -288, -288, -417 (average of 4A and 4B), -59 (average of 5A and 5B), and -484 Volts respectively. The voltages on the quad lens electrodes QL1, QL2, QL3, QL4, QL5, and QL6 are -15.0, -15.0, -185.0, and -185.0, -100, and -100 Volts respectively. The calculated data point at QL3 = -185 Volts in Fig. 24 is taken from this calculation. For other data points QL4 = QL3 and QL1 = QL2 = -200 Volts - QL3. The weak lens at the entrance of the ion lens results in a broad beam in the lens. Very few of these trajectories enter the mass spectrometer.

The trajectories plotted in Figs. 25-27 are taken from the XZ plane of the INMS, the plane of deflection. Trajectories from the YZ plane, perpendicular to this plane, are shown in Figs. 28-30 for  $K = -10, -20$  and  $-100$  Volts respectively. The ion lens get progressively weaker as the voltage on its first electrode is increased. This moves the crossover in the ion lens from near the entrance in Fig. 28 to near the exit in Fig. 30. Ion transmission is improved when this second crossover is near or on the exit.

The location of the first ion crossover has a large effect on the ion transmission of the INMS. When it is located near the beginning of the entrance cylinder of the quadrupole deflector, as in Figs. 28 and 30, the beam expands in the YZ plane and much of it is lost in the deflector. When the crossover is beyond the entrance cylinder and in the deflector, there is much less beam expansion in the YZ plane, as in Fig. 29, and more of the beam is transmitted. The location of this crossover is strongly influenced by the voltages on the open-ion-source lens, especially by the voltages on its first two electrodes.

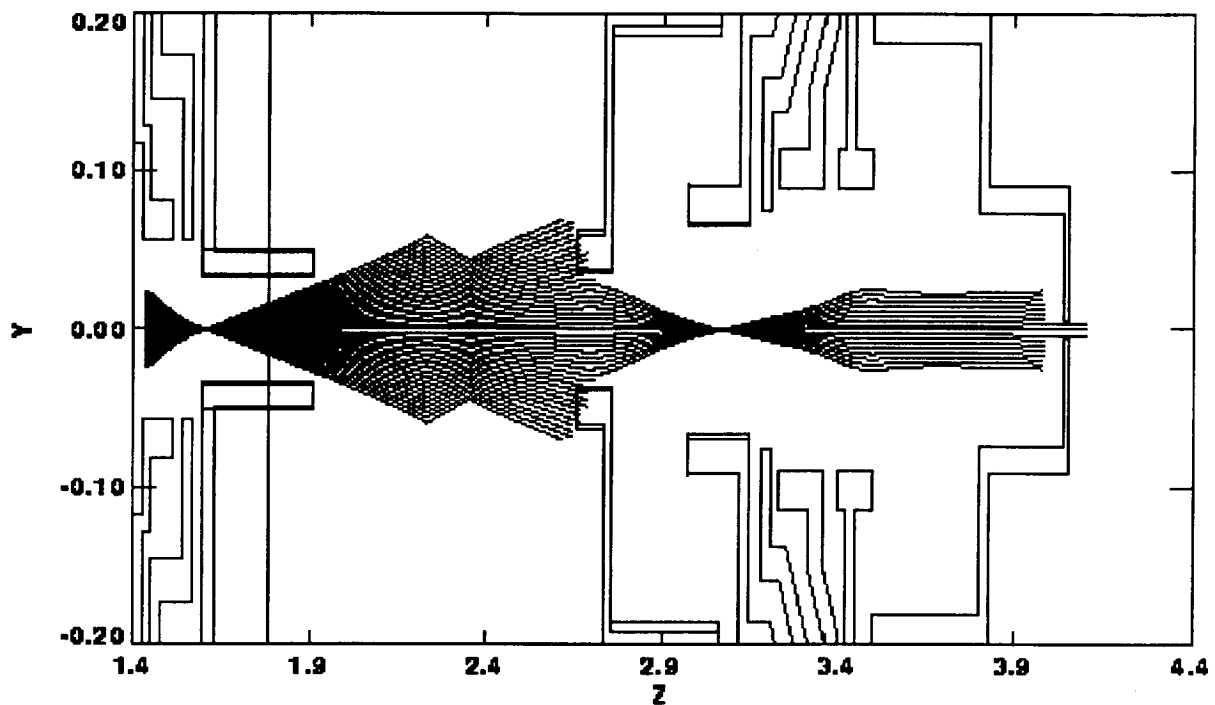


**Figure 28.** Trajectories from a thermal-ion beam in the INMS accelerated to 10 Volts. The plane (YZ) perpendicular to deflection the deflection plane is shown. The conditions are the same as Fig. 25. Thermalized neutrals in the open-ion-source lens at left are ionized by an electron gun (not shown). The initial movement of the beam under the electrostatic forces leads to a crossover at the entrance to the cylinder of the last electrode of the open-ion-source lens. Beyond the crossover the ions fill the cylinder. The ion beam is deflected by the quadrupole to enter the ion lens at right. The zigzag is an artifact of the transfer of the beam from a horizontal plane to a vertical plane in the deflector, as shown in Fig. 25; the trajectories are nearly linear in this region. Many trajectories do not enter the ion lens. From those that do, only a few enter the small nozzle of the last electrode of this lens.

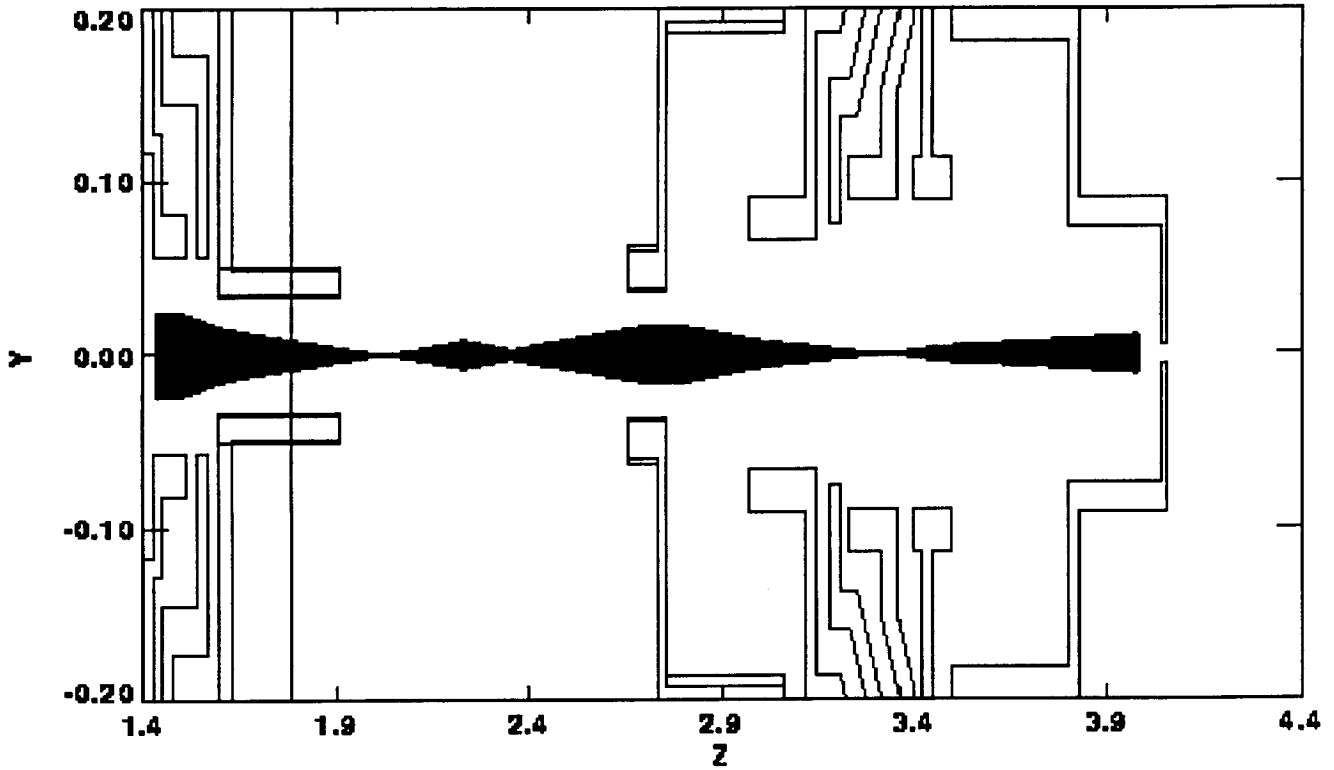


**Figure 29.** Trajectories from a thermal-ion beam in the INMS accelerated to 20 Volts. The view is similar to Fig. 28. The conditions are the same as Fig. 26. Thermalized neutrals in the open-ion-source lens at left are ionized by an electron gun (not shown). The initial movement of the beam under the electrostatic forces leads to a crossover in the deflector. The change in the voltages on the open-ion-source lens electrodes 1 (not shown) and 2 from 0.5 and 0 Volts to 2.0 and -2 Volts shifts the crossover from the before the entrance cylinder, as in Fig. 28, to beyond it. The ion beam is deflected by the quadrupole to enter the ion lens at right. The zigzag is an artifact of the transfer of the beam from a horizontal plane to a vertical plane in the deflector, as shown in Fig. 26; the trajectories are nearly linear in this region. The crossover in the ion lens is deeper into the ion lens here than in Fig. 28 because the lens formed by the first two electrodes of this lens is weaker. While all these trajectories enter the ion lens, none enter the small nozzle of the last electrode of this lens, as the trajectories originating on  $X = 0$  (at the left) end on  $X = -0.026$ " (at the right).

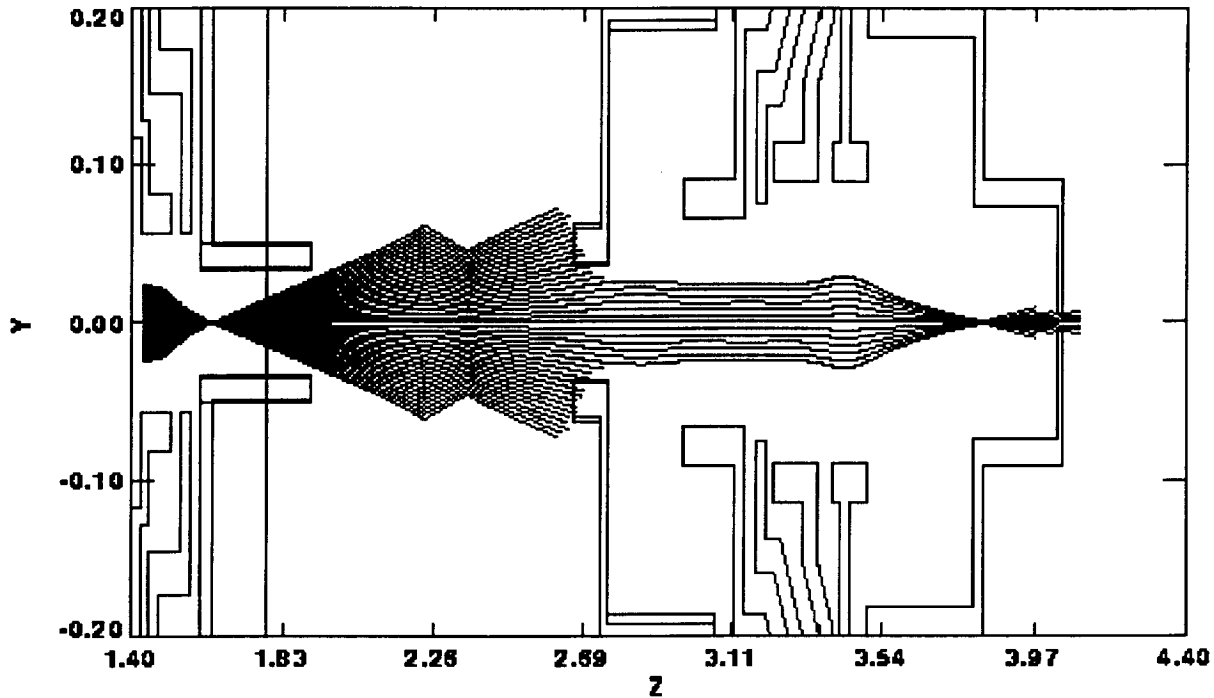


**Figure 30.** Trajectories from a thermal-ion beam in the INMS accelerated to 100 Volts. The view is similar to Figs. 28 and 29. The conditions are the same as Fig. 27. Thermalized neutrals in the open-ion-source lens at left are ionized by an electron gun (not shown). The initial movement of the beam under the electrostatic forces leads to a crossover at the entrance to the cylinder of the last electrode of the open-ion-source lens, as in Fig. 28. The ion beam is deflected by the quadrupole to enter the ion lens at right. The zigzag is an artifact of the transfer of the beam from a horizontal plane to a vertical plane in the deflector, as shown in Fig. 27; the trajectories are nearly linear in this region. The crossover in the ion lens is deeper into the ion lens here than in Figs. 28 and 29 because the lens formed by the first two electrodes of this lens is weaker. Many trajectories do not enter the ion lens. From those that do, most enter the small nozzle of the last electrode of this lens, as the crossover has been moved near its entrance.

### Misalignments and Tilts

Calculations show that misalignments of electrodes of ion-lens electrode 5, the one preceding the nozzle, deflect the ion beam with a high sensitivity. However, these misalignments cannot account for the differences shown in Table 1 because the transmission band calculated for the quadrupole deflector alone does not overlap the measured transmission. An irregularity in the open-ion-source lens or in the quadrupole deflector is required to reconcile measurement and calculation.

Misalignments of the open-ion-source lens electrodes 3 and 4 have little impact on the ion transmission. A tilt of the axis of the open-ion-source and the entrance axis of the quadrupole deflector also has little impact on the ion transmission. The irregularity must be directly associated with the quadrupole deflector.

Calculations described in section 3 for the sensitivities of transmission to misalignments of the electrodes of the quadrupole deflector indicate misalignments of the distal exit electrode (QL2) causes the largest shift in the ion transmission peak. Calculations of ion transmission in the INMS with misalignment of this electrode show no significant changes in the transmission, however. These two sets of calculations differ in that the previously reported calculations varied the beam energy whereas the deflector electrode potential is varied with constant beam energy in the present ones.

## Tolerances

Calculations for the sensitivities of transmission to changes in the parameters of the quadrupole deflector indicate the peak position is most sensitive to the lengths of the entrance and exit cylinders and to the hyperbolic parameter A of the deflector. Calculations of ion transmission in the INMS with these parameters changed show the transmission peak is sensitive to the entrance cylinder length and the parameter A, but not to the exit cylinder length.

## Entrance Cylinder

Construction irregularities from the insertion of the cylinder of the last open-ion-source electrode into the quadrupole deflector seem more likely than from a modification of the parameter A. Subsequent calculations were done with this cylinder inserted 0.050" more deeply into the deflector than specified. That is, the separation of the end of the entrance cylinder and the center of the deflector is 0.325" instead of 0.375". Ion transmission calculations for this modification of the INMS are shown in Figs. 31-33. They are analogs of Figs. 22-24. The QL3 voltage of the peak transmission is shown in Table 2. While this change does bring the QL3 values for the measured and calculated peaks closer, it does not fully reconcile measurement and calculation. Other irregularities may be present in the INMS.

**Table 2.** Transmission Peaks in INMS with Reduced Separation Between Open Source Lens and Deflector.

Ion Energy	QL3 Voltage for Peak	
	Measured	Calculated
10 Volts	-21.5 Volts	-21.1 Volts
20	-41.5	-42.3
100	-200	-214

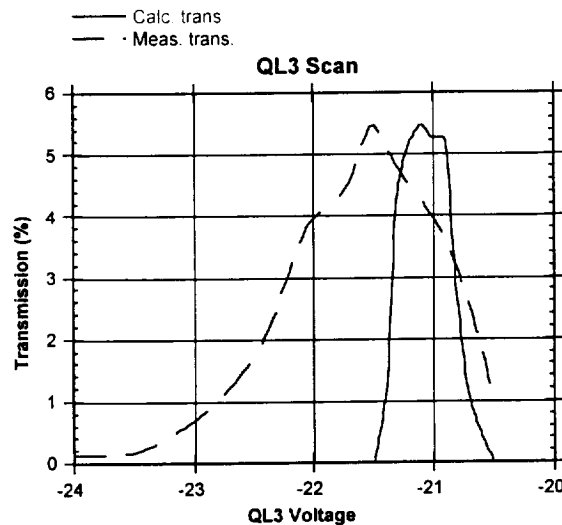


**Figure 31.** Ion transmission into the nozzle of the mass spectrometer for  $K = -10$  Volts. The entrance cylinder of the quadrupole deflector ends 0.050" closer to the center of the deflector as the spacing between the open-ion-source lens and the deflector has been reduced by this amount. Otherwise, the conditions for this data are the same as for the data shown in Fig. 22. The measured data is the same as shown in Fig. 22 except that it is recalibrated to equalize the calculated and measured transmission maxima.

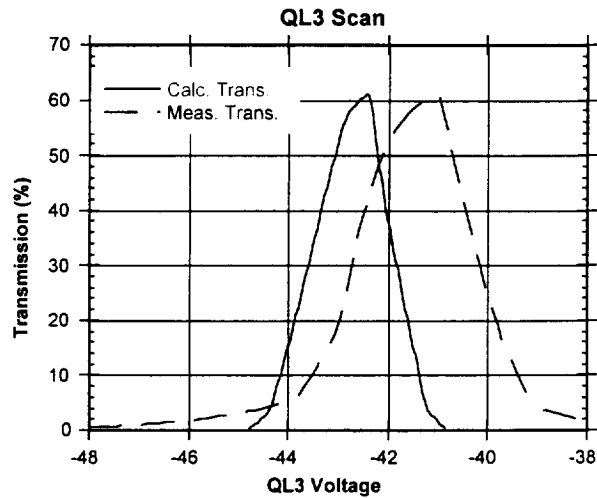


**Figure 32.** Ion transmission into the nozzle of the mass spectrometer for  $K = -20$  Volts. The entrance cylinder of the quadrupole deflector ends 0.050" closer to the center of the deflector. Otherwise, the conditions for this data are the same as for the data shown in Fig. 23. The measured data is the same as shown in Fig. 23 except that it is recalibrated to equalize the calculated and measured transmission maxima. The displaced entrance cylinder has increased the maximum transmission by nearly a factor two.

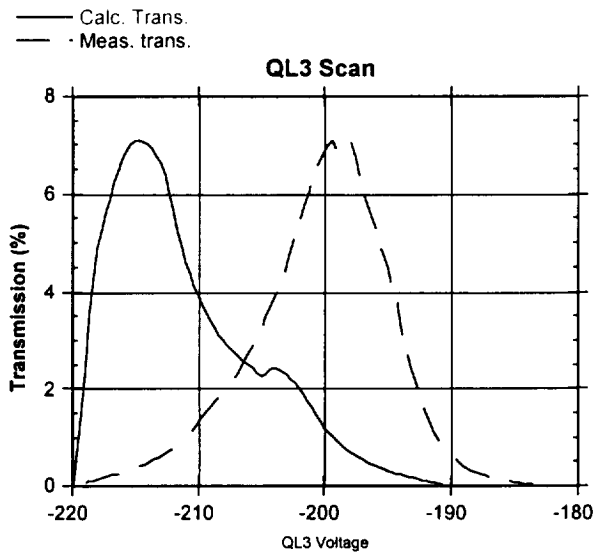


**Figure 33.** Ion transmission into the nozzle of the mass spectrometer for  $K = -100$  Volts. The entrance cylinder of the quadrupole deflector ends 0.050" closer to the center of the deflector. Otherwise, the conditions for this data are the same as for the data shown in Fig. 24. The measured data is the same as shown in Fig. 24 except that it is recalibrated to equalize the calculated and measured transmission maxima. The displaced entrance cylinder has significantly lowered the maximum transmission from that in Fig. 24 due to losses in the ion lens.

A plot of trajectories for  $K = -10$  Volts, similar to Fig. 25, for an INMS with the entrance cylinder inserted 0.050" more deeply into the quadrupole deflector is shown in Fig. 34. The ion trajectories are similar to those in Fig. 25, except for the sigmoidal behavior in the exit cylinder of the deflector. The ion beam overshoots the exit cylinder, but it is redirected back onto the ion-lens axis by the strong field between ion-lens electrodes 1 and 2.

A plot of trajectories for  $K = -20$  Volts, similar to Fig. 26, for an INMS with the entrance cylinder inserted 0.050" more deeply into the quadrupole deflector is shown in Fig. 35. The trajectories in Figs. 26 and 35 are similar.

A plot of trajectories for  $K = -100$  Volts, similar to Fig. 27, for an INMS with the entrance cylinder inserted 0.050" more deeply into the quadrupole deflector is shown in Fig. 36. The trajectories in Figs. 27 and 36 differ in the location of the beam in the ion lens. In Fig. 36 the sigmoidal trajectory behavior at the exit of the deflector causes much of the beam to be lost in the ion lens. The transmission maxima shown in Fig. 33 are much lower than those in Fig. 24 due to this loss.

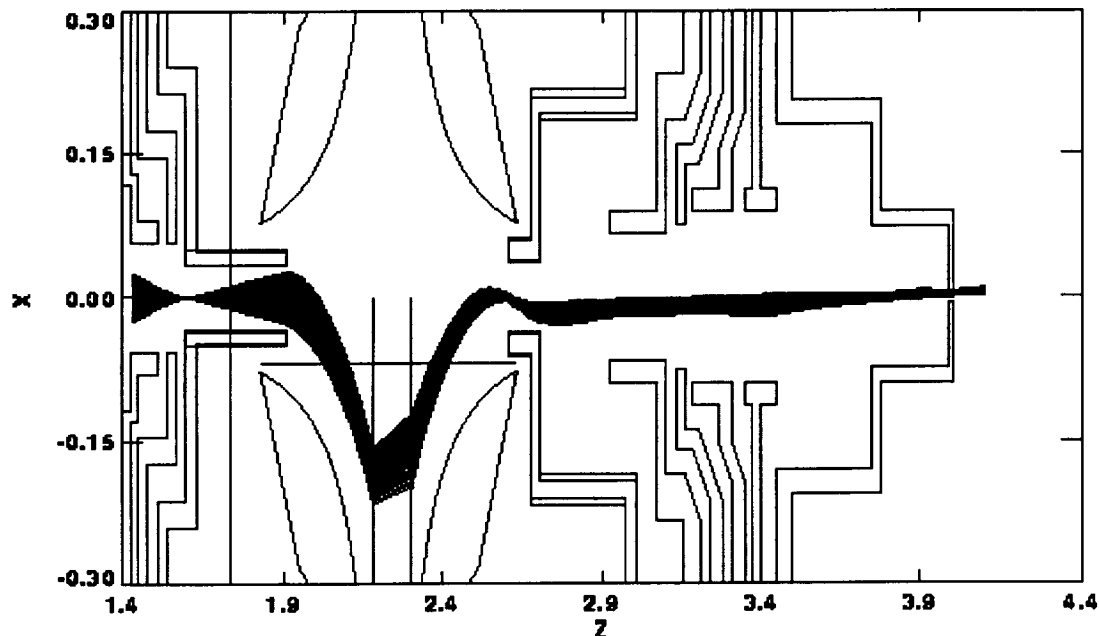


**Figure 34.** Trajectories from a thermal-ion beam in the INMS. The plane (XZ) of deflection is shown. The conditions are similar to those shown in Fig. 25 for  $K = -10$  Volts, except the entrance cylinder of the quadrupole deflector ends 0.050" closer to the center of the deflector as the spacing between the open-ion-source lens and the deflector has been reduced by this amount. The voltages on the open-ion-source lens electrodes (1 (not shown), 2, 3, and 4) are 0.5, 0, -5, and -10 Volts respectively. The voltages on the ion-lens electrodes (1, 2, 3, 4, 5, and 6) are -10, -287, -287, -415, -74, and -482 Volts respectively. The voltages on the quad lens electrodes QL1, QL2, QL3, QL4, QL5, and QL6 are 1.1, 1.1, -21.1, -21.1, -10, and -10 Volts respectively. The calculated data point at QL3 = -21.1 Volts in Fig. 31 is taken from this calculation. For other data points QL4 = QL3 and QL1 = QL2 = -20 Volts - QL3.

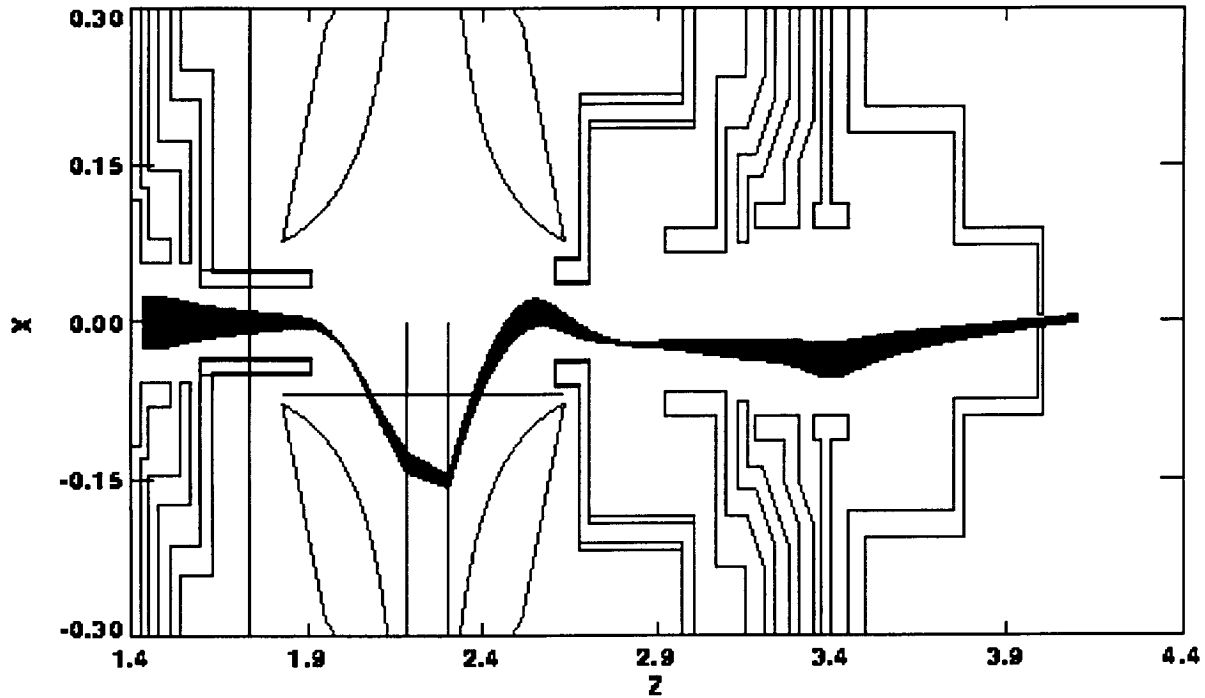


**Figure 35.** Ion trajectories in the INMS for  $K = -20$  Volts. The conditions are similar to those shown in Fig. 5 for  $K = -20$  Volts, except the entrance cylinder of the quadrupole deflector ends 0.050" closer to the center of the deflector. The voltages on the open-ion-source lens electrodes (1 (not shown), 2, 3, and 4) are 2.0, -2, -5, and -20 Volts respectively. The voltages on the ion-lens electrodes (1, 2, 3, 4, 5, and 6) are -20, -287, -287, -415, -74, and -482 Volts respectively. The voltages on the quad lens electrodes QL1, QL2, QL3, QL4, QL5, and QL6 are 2.0, 2.0, -42.0, and -42.0, -20, and -20 Volts respectively. The calculated data point at QL3 = -42 Volts in Fig. 32 is taken from this calculation. For other data points QL4 = QL3 and QL1 = QL2 = -40 Volts - QL3.

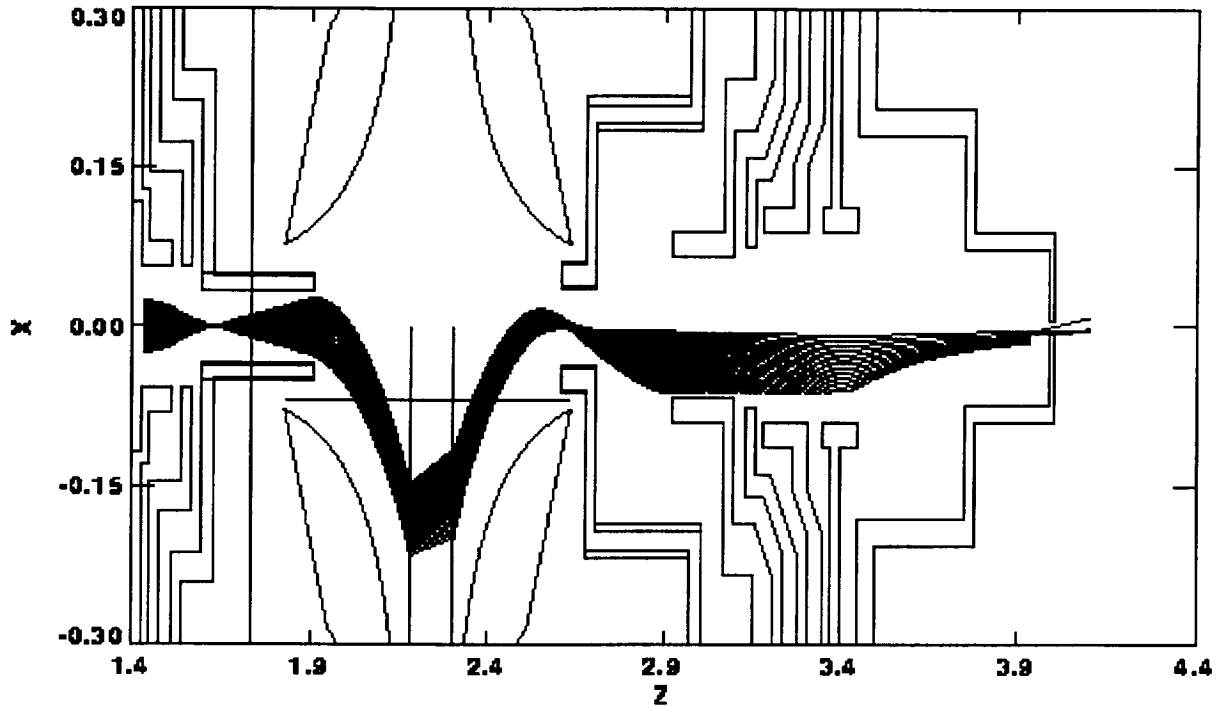


**Figure 36.** Ion trajectories in the INMS for  $K = -100$  Volts. The conditions are similar to those shown in Fig. 27 for  $K = -100$  Volts, except the entrance cylinder of the quadrupole deflector ends 0.050" closer to the center of the deflector. The voltages on the open-ion-source lens electrodes (1 (not shown), 2, 3, and 4) are 2.0, -2, -5, and -100 Volts respectively. The voltages on the ion-lens electrodes (1, 2, 3, 4, 5, and 6) are -100, -288, -288, -417 (average of 4A and 4B), -59 (average of 5A and 5B), and -484 Volts respectively. The voltages on the quad lens electrodes QL1, QL2, QL3, QL4, QL5, and QL6 are 8.0, 8.0, -208.0, and -208.0, -100, and -100 Volts respectively. The calculated data point at QL3 = -208 Volts in Fig. 33 is taken from this calculation. For other data points QL4 = QL3 and QL1 = QL2 = -200 Volts - QL3.

### The parameter A of the Hyperbolic Deflector

A modification of the parameter A could be a construction irregularity associated with assembly of the rods, as this parameter also defines the separation of the rods in the deflector. Subsequent calculations were done with this parameter increased from 0.25" to 0.28". That is, the separation of opposite rods is 0.56" instead of 0.50". Ion transmission calculations for this modification of the INMS are shown in Figs. 37-39. They are analogs of Figs. 22-24. The QL3 voltage of the peak transmission is shown in Table 3. While this change does bring the QL3 values for the measured and calculated peaks closer, it does not fully reconcile measurement and calculation. Other irregularities may be present in the INMS.

**Table 3.** Transmission Peaks in INMS with Increased Hyperbolic Parameter A.

Ion Energy	QL3 Voltage for Peak	
	Measured	Calculated
10 Volts	-21.5 Volts	-21.0 Volts
20	-41.5	-41.7
100	-200	-208

Plot of the ion trajectories with A increased from 0.25" to 0.28" are similar to Figs. 25-27, and so they are not repeated.

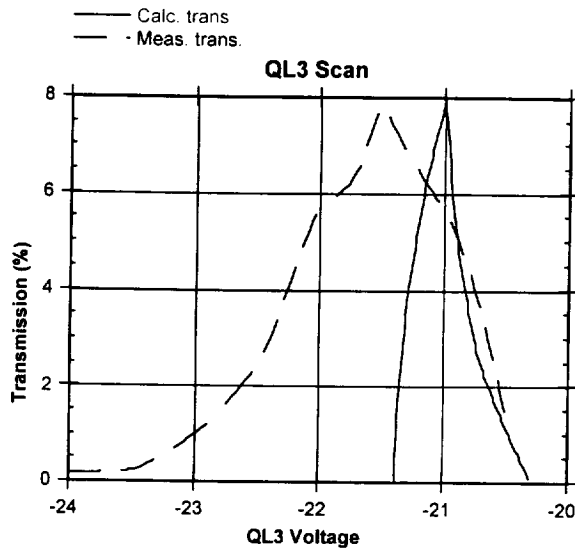


**Figure 37.** Ion transmission into the nozzle of the mass spectrometer for  $K = -10$  Volts. The hyperbolic parameter  $A$  has been increased from  $0.25''$  to  $0.28''$ . Otherwise, the conditions for this data are the same as for the data shown in Fig. 22. The measured data is the same as shown in Fig. 22 except that it is recalibrated to equalize the calculated and measured transmission maxima.

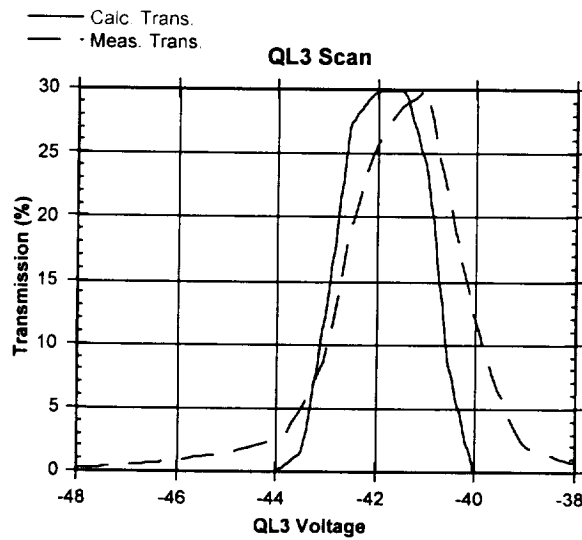


**Figure 38.** Ion transmission into the nozzle of the mass spectrometer for  $K = -20$  Volts. The hyperbolic parameter  $A$  has been increased from  $0.25''$  to  $0.28''$ . Otherwise, the conditions for this data are the same as for the data shown in Fig. 23. The measured data is the same as shown in Fig. 23 except that it is recalibrated to equalize the calculated and measured transmission maxima.

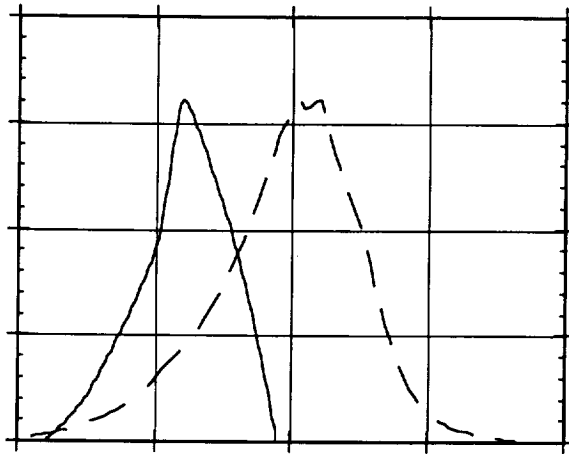


**Figure 39.** Ion transmission into the nozzle of the mass spectrometer for  $K = -100$  Volts. The hyperbolic parameter  $A$  has been increased from  $0.25''$  to  $0.28''$ . Otherwise, the conditions for this data are the same as for the data shown in Fig. 24. The measured data is the same as shown in Fig. 24 except that it is recalibrated to equalize the calculated and measured transmission maxima.

### Comparison with Flight Instrument

Comparisons were also made of the simulation results with the experimental results from the flight instrument. Six data sets, called QL3 scans, were given us for the flight instrument. Voltages used for these scans were as follows:

Open Lens 3 = -5 volts  
 Quad Lens 5 = Quad Lens 6 = 0 volts  
 IonLens 2 and 3 = -293 volts  
 IonLens 4 = -412 volts  
 IonLens5 = -57 volts  
 Open Lens 4 = IonLens 1 =  $k$  (constant varies with each scan)

The voltages for each scan are:

es121196.a01 ---  $K = -5$  volts, open lens 1 = open lens 2 = 0 volts  
 es121196.a04 ---  $K = -5$  volts, open lens 1 = open lens 2 = +2 volts  
 es121196.a13 ---  $K = -10$  volts, open lens 1 = open lens 2 = 0 volts  
 es121196.a16 ---  $K = -10$  volts, open lens 1 = open lens 2 = +2 volts  
 es121196.a19 ---  $K = -20$  volts, open lens 1 = open lens 2 = +2 volts  
 es121196.a22 ---  $K = -20$  volts, open lens 1 = open lens 2 = 0 volts

The voltage on Quad Lens 3 is varied keeping

Quad Lens 3 = Quad Lens 4  
 Quad Lens 1 = Quad Lens 2 =  $-(\text{Quad Lens 3}) + 2K$

Two of these correspond most closely to the voltages used in data sets given us for the EM. One of them, dataset es121196.a13, is shown in Fig. 40. It is analogous to Fig. 22 of EM. This figure shows calculated and measured data. The calculated and measured energies of the transmission peaks differ less (1 volt instead of 3) here compared to Fig. 22 of EM. Trajectories from the transmitted beam are similar to those shown in Figs. 25 and 28 of EM.

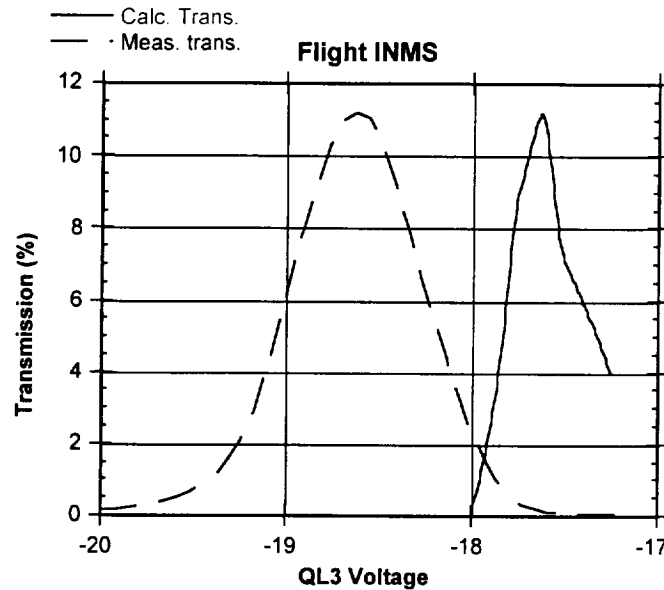


**Figure 40.** Ion transmission into the nozzle of the mass spectrometer for 10-Volt ions. The calculated transmission is the fraction of the number of ions in the open-ion-source that enter the nozzle. This figure is analogous to Fig. 22 of EM. The measured transmission, dataset es121196.a13 from NASA, is in arbitrary units, as the initial number of ions is unknown. The voltage QL3 is applied to one of the electrodes of the quadrupole deflector. The voltages on the open-ion-source lens electrodes (1, 2, 3, and 4) are 0, 0, -5, and -10 Volts respectively. The voltages on the ion-lens electrodes (1, 2, 3, 4, 5, and 6) are -10, -293, -293, -412, -57, and -500 Volts respectively. The voltages on the quad lens electrodes are  $QL4 = QL3$  and  $QL1 = QL2 = -20 \text{ Volts} - QL3$ , and  $QL5 = QL6 = 0 \text{ Volts}$ .

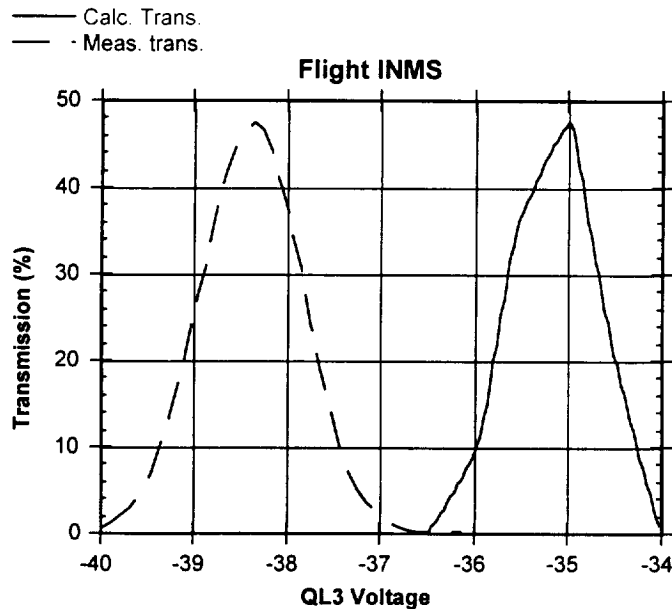


**Figure 41.** Ion transmission into the nozzle of the mass spectrometer for 20-Volt ions. The information shown in Fig. 40 for 10-Volt ions is shown here for 20-Volt ions. This figure is analogous to Fig. 23 of EM. The measured transmission is dataset es121196.a19 NASA. The voltage QL3 is applied to one of the electrodes of the quadrupole deflector. The voltages on the open-ion-source lens electrodes (1, 2, 3, and 4) are 2, 2, -5, and -20 Volts respectively. The voltages on the ion-lens electrodes (1, 2, 3, 4, 5, and 6) are -20, -293, -293, -412, -57, and -500 Volts respectively. The voltages on the quad lens electrodes are  $QL4 = QL3$  and  $QL1 = QL2 = -40 \text{ Volts} - QL3$ , and  $QL5 = QL6 = 0 \text{ Volts}$ .

The second one, dataset es121196.a19, is shown in Fig. 41. It is analogous to Fig. 23 of EM. This figure shows calculated and measured data. In both figures, the calculated transmission peak is 3 to 4 Volts below the measured one. (This difference will be discussed in connection with Fig. 44.) The peaks in Fig. 41 are shifted about 3 eV toward lower energies compared to the peaks in Fig. 23 of EM. This is attributed to the use of ground potential on the endplates of the quadrupole deflector in these measurements instead of the entrance/exit potential (K) used for the EM measurements. A calculation with the endplate potentials changed confirms this shift.

Figure 43 shows transmission curves similar to those in Fig. 40 except for voltage changes on the open-ion-source-lens electrodes 1 and 2 from 0 to 2 Volts. While the calculated transmission is changed very little, the measured transmission is shifted by about 2 Volts, so the difference between calculation and measurement is increased to 3 Volts. The calculated trajectories look more like those shown in Figs. 26 and 29 of EM. That is, the first ion crossover is deep inside the quadrupole deflector. The origin of the beam in the open-ion-source lens had to be displaced 0.08" toward the deflector to permit transmission of the beam.

The 2-Volt shift in the voltage of the measured transmission peak is clearly connected to the 2 Volt change in the voltages on open-ion-source-lens electrodes 1 and 2. Yet there is no change in the calculated transmission. As the calculation are done for thermal ions, the measurements could be selecting ions with 2 Volts of kinetic energy when 2 Volts is applied to these electrodes. A calculation with 2-Volt ions shifts the transmission peak by 2 volts to -19.5 Volts. It also moves the first ion crossover inside the open-ion-source-lens,

Figure 44 shows transmission curves similar to those in Fig. 41 except for voltage changes on the open-ion-source-lens electrodes 1 and 2 from 2 to 0 Volts. While the calculated transmission is changed very little, the measured transmission is shifted by about 2 Volts, so the difference between calculation and measurement is decreased to 1 Volt. The calculated trajectories look more like those shown in Figs. 25 and 28 of EM. That is, the first ion crossover is inside the open-ion-source-lens. By analogy to the discussion of the data in Fig. 43, the measurements shown in Fig. 41 could be selecting ions with 2 eV of kinetic energy. A calculation with 2-Volt ions shifts the calculated transmission peak in Fig. 41 to -37.0 Volts.

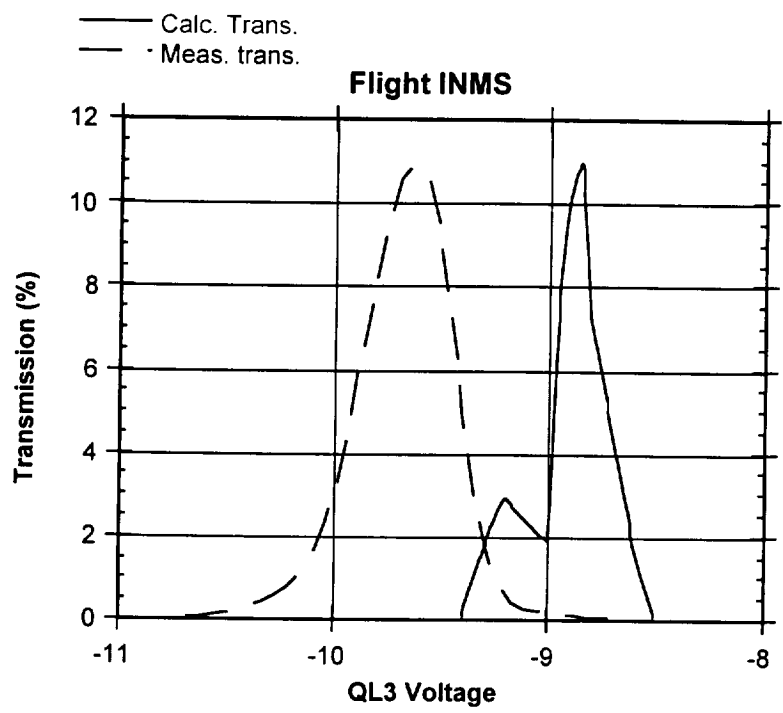


Figure 42. Ion transmission into the nozzle of the mass spectrometer for 5 Volt ions.

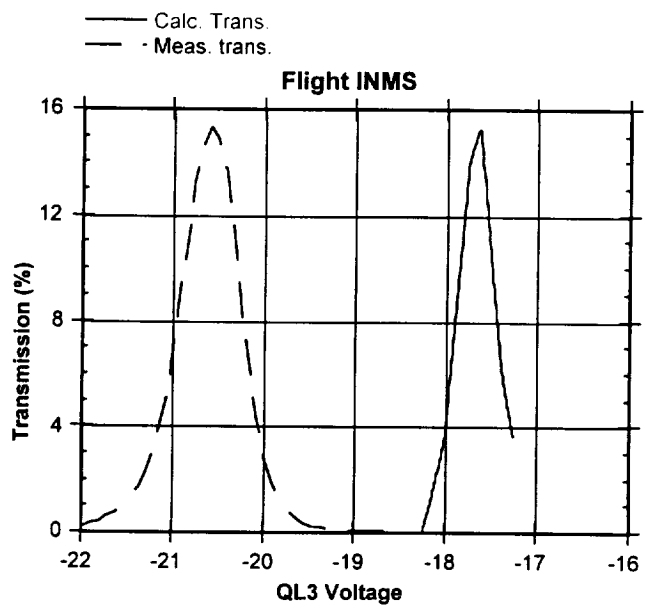
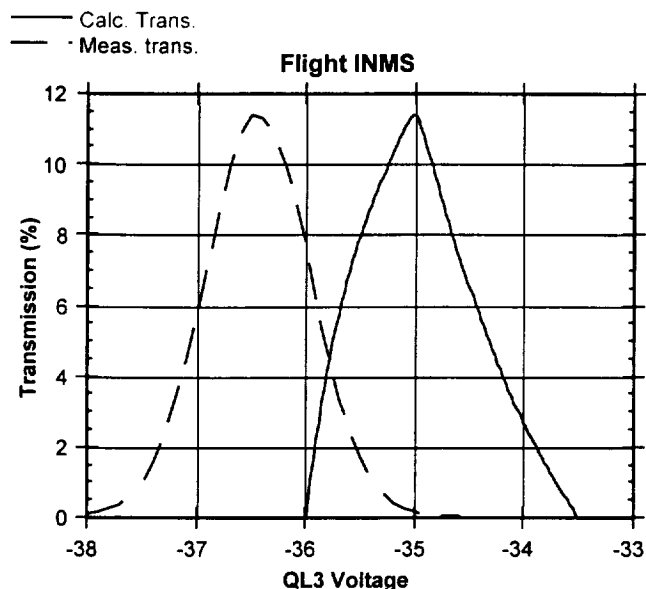


Figure 43. Ion transmission into the nozzle of the mass spectrometer for 10-Volt ions. This figure is analogous to Fig. 40, except the voltages on open-ion-source lens electrodes 1 and 2 are 2 Volts. The measured transmission, dataset es121196.a16 from NASA, is in arbitrary units, as the initial number of ions is unknown.



**Figure 44.** Ion transmission into the nozzle of the mass spectrometer for 20-Volt ions. This figure is analogous to Fig. 40, except the voltages on open-ion-source lens electrodes 1 and 2 are 0. The measured transmission, dataset es121196.a22 of NASA, is in arbitrary units, as the initial number of ions is unknown.

### Comparisons in Ion Mode

From the discrepancies between measured and calculated, it was suspected that the discrepancies might be due to the method of simulating trajectories in the neutral mode. Subsequently, many other datasets were sent from NASA, with transmissions measured for ions of selected energy. In this case, the datasets were generated in the ion mode, with ion beams of various energies from 2.8 to 20 eV introduced directly into the beam. The ions were started outside of the instrument and not created inside as was with the thermal gas. The voltages used were

Ion deflector voltages = 0 volts

Open Lens 1 and Open Lens 4 set to one of two values, -5 or -30 volts.

Open Lens 3 = -5 volts

Quad Lens 5 = Quad Lens 6 = 0 volts

IonLens 2 and 3 = -196 volts

IonLens 4 = -408 volts

IonLens5 = -44.5 volts

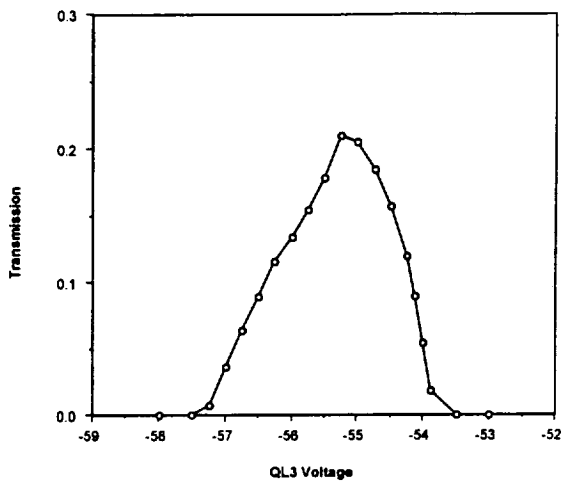
Open Lens 4 = IonLens 1 = k (constant varies with each scan)

The voltage on Quad Lens 3 is varied keeping

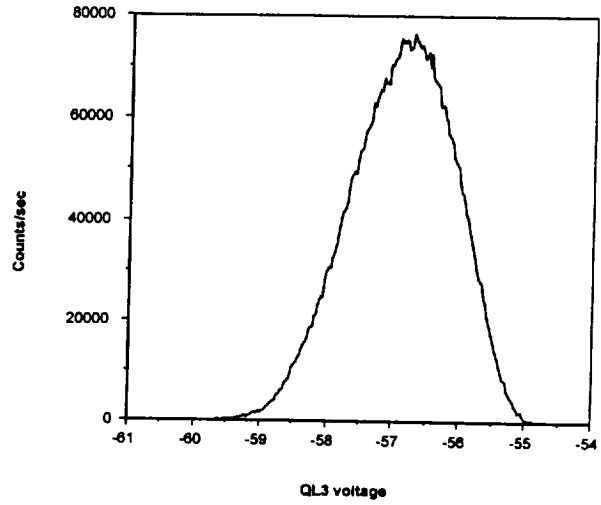
Quad Lens 3 = Quad Lens 4

Quad Lens 1 = Quad Lens 2 = -(Quad Lens 3) + 2K

Figures 45 and 46 show comparison of calculated and measured results for two datasets. The results are listed in Table 4 which gives the energy, OpenLen4 voltage, voltages for maximum transmission, the half width half maximum values for the different cases.

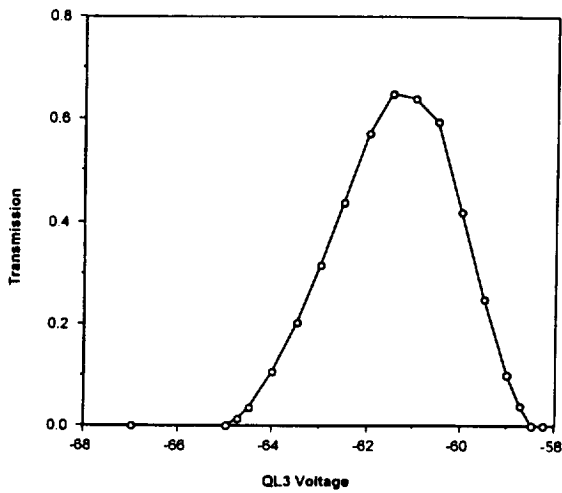


(a)

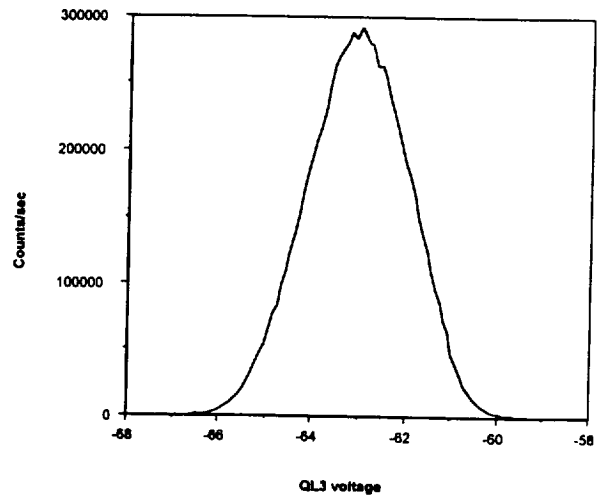


(b)

Figure 45: Dataset "es1/21/a15" (a) Calculated and (b) Measured  
Energy = 2.8 eV; Open Lens4 = -30 volts



(a)



(b)

Figure 46: Dataset "es1/21/a14" (a) Calculated and (b) Measured  
Energy = 10 eV; Open Lens4 = -30 volts

**Table 4: Experimental and calculated data for transmission in ion mode.**

Test ID	Energy	Lens4 Voltage	V at MaxT(Exp)	V at MaxT(Cal)	FWHM(Exp)	FWHM(Cal)
es1/21/a16	2.8	-5	-12.11	-11.33	1.1	0.63
es1/21/a15	2.8	-30	-56.73	-55.4	2	2.1
es1/21/a14	3.8	-5	-13.6	-12.25	0.84	0.78
es1/21/a12	3.8	-30	-55.9	-55.9	2.65	2.54
es1/21/a11	6	-5	-15.3	-14.4	0.85	1
es1/21/a10	6	-30	-59.75	-58	2.4	3.06
es1/21/a08	7.8	-30	-61.2	-59.25	2.45	3.28
es1/20/a15	10	-5	-18.65	-18	1.25	1.47
es1/20/a14	10	-30	-63.05	-61.3	2.656	3.3
es1/20/a05	12	-5	-20.7	-19.75	1.5	1.75
es1/20/a08	12	-30	-65.4	63	2.7	3.3
es1/22/a00	14.3	-30	-67	-64.5	3.1	3.56
es1/22/a01	14.5	-5	-22.7	-22	1.9	2
es1/22/a09	20.15	-5	-28.2	-26.84	2.54	1.9

Calculated magnitudes of voltage at maximum transmission are slightly lower than the experimental values in most cases listed above while the FWHM are higher. However, the agreement between calculated and experimental results is reasonably good.

## 5. The Mass Analyzer

The quadrupole mass filter of the INMS consists of four precision ground hyperbolic rods mounted in a rigid mechanical assembly. The rod spacing diameter,  $r_0$  is 0.58 cm and the rod length is 10 cm. Radio Frequency (RF) and Direct Current (DC) potentials are applied together to excite the quadrupole rods and create an electrostatic field within the quadrupole region. This dynamic field controls the transmitted mass, the resolution, and the transmission efficiency.

The BEAM3D software could not be used for the purpose of modeling the mass analyzer because the software simulates static fields and cannot simulate the dynamic electrostatic fields of the analyzer. Hence, a software called SIMION was used to model parts of the analyzer. However, to simulate the trajectories through the mass analyzer realistically, beam conditions at the exit lens or the entrance of the mass analyzer have to be simulated or the two models have to be interfaced. To overcome this problem, the exit lens system was also modeled using SIMION.

Figure 1 shows the mass analyzer modeled utilizing user programs and the workbench feature of SIMION. To facilitate ease of varying the geometry, the mass analyzer has been modeled as three different overlapping instances that are synchronized in their operation: The quadrupole lens modeled as a 3D array, the quadrupole as a mirrored 2D array, and the exit lens with a plate detector (a 3D array). The quadrupole has been modeled as four hyperbolic sections. Figure 2 shows the three parts of the mass analyzer model. Figure 3 shows the SIMION model of the Ion Lens system (exit lens system). The modeling and some simulations of the mass analyzer were carried out during the last quarter of the project. However, detailed studies of transmission through the analyzer have not been completed.

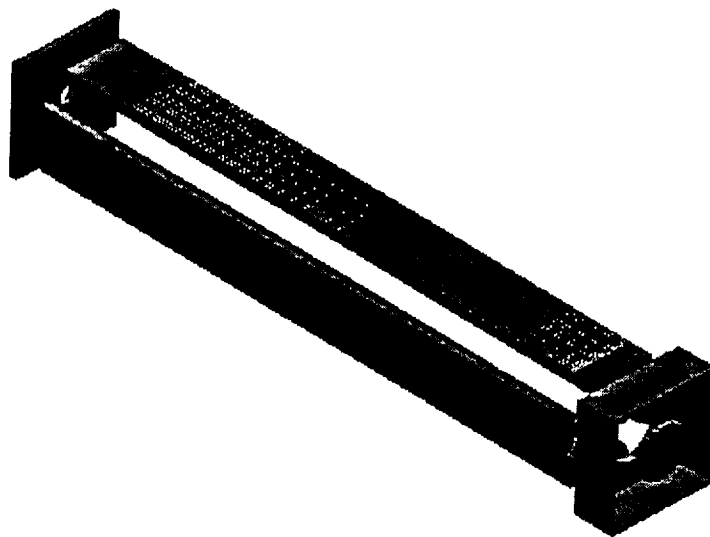
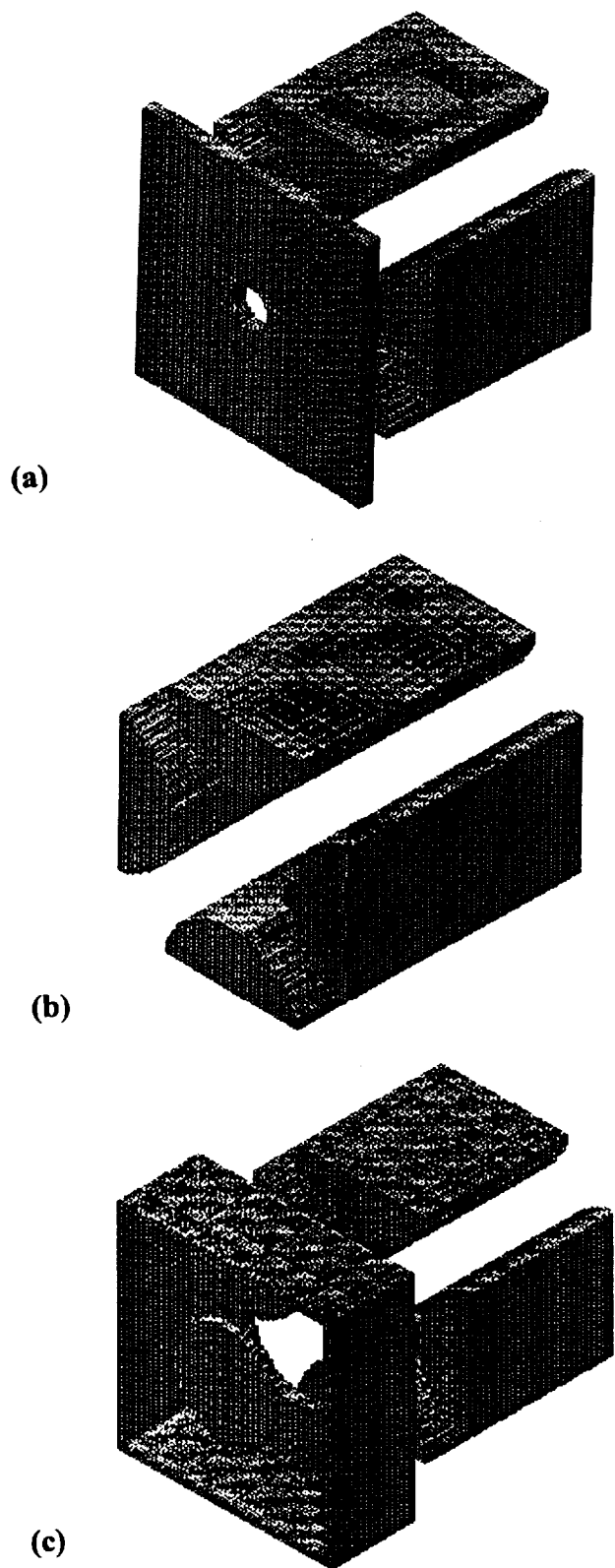


Figure 1: SIMION model of the mass analyzer.



**Figure 2:** The mass analyzer is modeled in three overlapping parts: (a) The entrance lens (b) The quadrupole and (c) The exit lens with detector.



**Figure 3:** SIMION model of the ion lens system.

PES plans to continue the SIMION simulations as part of NASA's continuing efforts to develop miniature mass spectrometer for use in space research. PES is a participant in a coordinated project of the Planetary Instrument Definition and Development Program (PIDDP) led by Dr. Paul Mahaffy of NASA's Goddard Space Flight Center.

As part of the program, PES will develop detailed model of the mass analyzer with the dimensions provided by NASA. This model will serve as a benchmark for our efforts to miniaturize the analyzer and the Ion Lens system and also improve performance. Simulations will be carried out with smaller quadrupoles and Ion Lenses of varied size, geometry and configurations to help in the design of a smaller instrument. Analyses will be carried out to study peak shapes, resolution and sensitivity. Simulation of the ion optics of the mass spectrometer will be used to design the ion lens system, quadrupole and the detector geometry. Each of these parts will be designed individually and placed on the ion optics workbench of SIMION. Very accurate simulations can be carried out by this method, since it permits different number of grid points per unit area in different sections, allowing for higher accuracy where needed.

## 6. Miniaturization of the Instrument

The simulations described in the earlier sections shed light on the possible ways of reducing the size and weight of the INMS sensor without degrading the performance of the mass spectrometer.

Reduction in size can be achieved by reducing the dimensions of the electrodes or completely eliminating the electrodes, which are not absolutely essential for performance. Some reduction in weight is automatically achieved by reduction in the dimensions of the sensor. Small reductions in the radii of the electrodes or the spacing between them can result in significant reduction in weight. This is because major contribution to the weight of the sensor comes from the metallic parts that hold the electrodes together and the housing of the sensor. Reduction in weight is also achieved by the use of lighter weight material for the electrodes.

### Reduction in Dimensions

Simulations were carried out with a general reduction by 10% in all the geometrical parameters of the open source electrodes, keeping the aperture radii and the spacing between electrodes unchanged. As is to be expected, preliminary calculations with example simulations did not show significant differences from the results that have been discussed. A general reduction should however be viewed with caution since in many instances, it may not be possible in practice. Further calculations would be necessary to investigate the practicality of these reductions.

Simulations with reduced length of the cylindrical part of the extractor electrode (Lens 4) of the open lens (described in Section 2) indicated that performance transmission improved with reduction in the length of this part. This will also reduce the overall length of the sensor.

Analysis of the sensitivity of transmission to the geometrical parameters of the quadrupole deflector (described in Section 3) showed that there is improvement in transmission with reduced separation between the endcaps. Further simulations have to be carried out to find the limits on this reduction before there is a degradation of performance. A reduction in separation would result in a reduction in the overall size of the sensor.

In adapting an older design of the INMS for the Cassini mission, one of the lenses in the exit lens system, Lens 3, was redesigned. The horizontal part was removed, and the vertical part was retained to hold it in place, without changing the locations of the other lenses in the system. This resulted in the overall dimensions of the same being unchanged. The voltage on the Lens 3 was maintained at the same voltage as Lens 4. In effect, Lens 4 and the remaining part of Lens 3 together function as a single unit. In an attempt to reduce the size and weight, simulations were

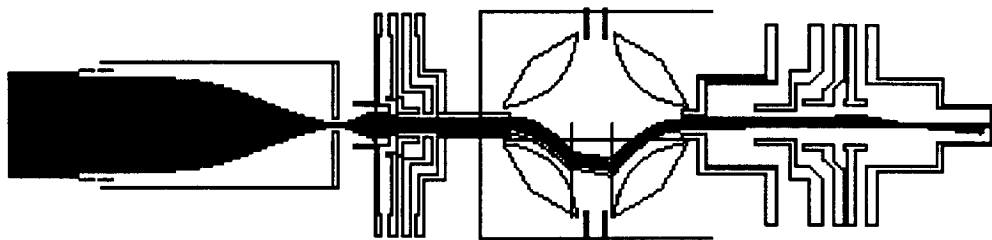


Figure 1: Ion trajectories through the model with IonLens 3 removed.

carried out with Lens 3 removed in its entirety and Lens 4 moved closer to Lens 2 to close the gap (Figure 1). Simulations for 28 amu ions with this model showed transmission with the new model was not significantly different (it was very slightly higher) than that with the old model. Simulations show that IonLens 3 can be completely removed with no loss in transmission. Further simulations are to be carried out to study the possibility of eliminating or reducing the dimensions of other electrodes.

A significant reduction in size can be achieved by reducing the length of the quadrupole in the mass analyzer since it reduces the overall dimension of the sensor. As mentioned earlier, PES is a participant in NASA's ongoing efforts to miniaturize the instrument and continues to carry out simulations to design a smaller mass analyzer. Using the current model as the benchmark, simulations will be carried out with shorter quadrupoles. Simulation of the ion optics of the mass spectrometer will be used to design the ion lens system, quadrupole and the detector geometry. Each of these parts will be designed individually and placed on the ion optics workbench of SIMION. Very accurate simulations can be carried out by this method, since it permits different number of grid points per unit area in different sections, allowing for higher accuracy where needed.

## Reduction in Weight

As part of the effort to investigate ways of reducing the weight and size of the INMS sensor, a study of some ceramic materials was undertaken to identify possible candidates for use in certain parts of the proposed lighter-weight, more compact model. The findings would also help PES in the development of a lighter model of the GC-MS to be commercialized in Phase III.

Ceramic materials are being used increasingly in biomedical, high vacuum, environmental, aerospace and other applications. They are high-strength, lightweight materials with high electrical and thermal insulation properties. Our study included a wide range of ceramic materials including alumina-based ceramics and glass ceramics.

Table 1: Physical properties of some ceramic materials.

PROPERTY	UNITS	ALUMINUM SILICATE	MACOR <sup>®</sup>	SCG	BORON NITRIDE +		
		M120F		COMPOSITE	HBN	HBR	HBC
COLOR		TAN TO PINK	WHITE	BLACK/GREEN	WHITE	WHITE	WHITE
DENSITY	G/CC	2.3	2.52	1.86	2.10	2.00	1.90
POROSITY	% WATER ABSORPTION	3	0	15	7	11	13
FLEXURAL STR.	KPSI	9	13	5	13	8	3
COMPRESSIVE STR.	KPSI	40	50	14	16	10	6
HARDNESS	KNOOP	500	250	-	19	26	16
THERMAL COND.	W/M <sup>°</sup> K	1.3		40	59	55	28
	W/M <sup>°</sup> C		1.46				
COEFFICIENT OF LINEAR THERMAL EXPANSION	25 <sup>°</sup> TO 300 <sup>°</sup> C	3.3	9.3	2.2			
	25 <sup>°</sup> TO 1500 <sup>°</sup> C				4	4	.4
	(X10 <sup>-6</sup> )						
MAXIMUM USE TEMP.	°C	1150	1000	400	550-850	850	850
VACUUM ATMOSPHERE	°C	-		1800	550-1600	1150-1600	2000-3000
DIELECTRIC STR.	VOLTS/MIL	100	1000	-			
	V/MMX10 <sup>3</sup>				53	53	54
VOLUME RESISTIVITY	OHM-CM 25 C	>10 <sup>14</sup>	>10 <sup>16</sup>		>10 <sup>15</sup>	>10 <sup>15</sup>	>10 <sup>15</sup>
DIELECTRIC CONSTANT	1 MHZ 25 <sup>°</sup> C	5.3		-	4.2	4.1	4.1
	1 KHZ 25 <sup>°</sup> C	-	6.03		-		
LOSS FACTOR	1 MHZ 25 <sup>°</sup> C	.053		-	<.0002	<.0002	<.0002
	1 KHZ 25 <sup>°</sup> C		.0047		-		

Table 1 gives the physical properties of a number of ceramic materials. Most alumina-based ceramics have low density, but have high porosity and therefore, they may not be the best candidates for high vacuum applications. They are normally hard to machine because of their brittleness. Glass ceramics on the other hand, have low density and zero porosity, making them good materials for high vacuum applications. They are also highly machinable. Glass ceramic is a polycrystalline solid prepared by controlled crystallization of glass. The crystallization is accomplished when a suitably constituted glass is subjected to a regulated heat treatment schedule that results in the formation and growth of crystalline structures within the glass. Glass ceramics are distinct from traditional ceramics in that the crystalline material component is produced from within the parent glass material instead of being introduced in the already crystalline form when the material is compounded. They are distinct from the amorphous glasses in that they contain crystalline structures.

MACOR, a glass ceramic developed by Corning, is a very good candidate for many mass spectroscopic applications. It is a white, odorless, porcelain-like (in appearance) material composed of approximately 55% fluorphlogopite mica and 45% borosilicate glass. MACOR's highly interlocked microstructure is the key to its machinability. Figure 2 shows the magnified picture of MACOR's microstructure. During machining, the interlocking intersections of the randomly oriented crystals that, in effect, stops the micro cracks from propagating through the matrix outside the local cutting area. Since the fracture is localized, MACOR glass ceramic does not sacrifice the strength or hardness for the sake of its machinability. Its unique microstructure makes it dimensionally very stable under irradiation, making it highly suitable for aerospace and nuclear industries.

MACOR is being used increasingly in many applications including mass spectrometry. Its low density (2.52 g/cc) as compared to other metals and its capability of being machined into complicated shapes and precision parts with ordinary metal working tools, quickly and inexpensively, makes it highly suitable for these applications.



Figure 2: Microstructure of MACOR MGC 5000X magnification.

Table 2 gives the material properties of MACOR and Figure 3 depicts some of its physical characteristics. MACOR has a continuous use temperature of 800°C and a peak temperature of 1000°C. Its coefficient of thermal expansion readily matches most metals and sealing glasses. Unlike most ductile materials, it does not deform. It is an excellent insulator at high voltages, various frequencies and high temperatures. It has superior gas and vacuum even at elevated temperatures and is highly recommended for use in vacuum systems as feed through lines, thermocouple insulators, and in other applications requiring electrical and thermal insulators. In addition, because of the glass-ceramic nature of MACOR, it has zero porosity, making it a good material for high-vacuum applications.

MACOR can also be joined or sealed to both itself and to other materials with vacuum tight seals. This eliminates the need for screws, nuts, etc., which could introduce misalignments and also add to the weight. Like many ceramics, MACOR can be thick film metallized using metal inks, or thin film metallized by sputtering to produce high quality metallized components with outstanding electrical characteristics.

MACOR has been used in many parts of a mass spectrometer built at the David Sarnoff Research Center and PES proposes to do the same for the proposed miniature model. Major manufacturers such as Hewlett Packard, FINNEGAN MAT, Extrel and Vestec are already using MACOR for similar applications. Some of the companies we have contacted and received information from are WESGO/DURAMIC in New Jersey, Coors Ceramic Company in Colorado, Ceramic Products Inc. in NJ, and Scientific Instrument Services in NJ. These companies supply a number of mass spectrometer parts and also offer customized precision machine services.

We also studied another class of materials, namely the polyimide resins. Of these, VESPEL, a family of polyimides developed by Dupont is being increasingly used in engineering designs that require parts that are smaller, lighter and capable of performing over a wide temperature range. One of the SP series from this family, namely SP-1, is an unfilled resin grade, which provides the maximum physical strength, elongation and toughness and best electrical and thermal insulation properties. Others in the series, graphitized to different extents, are also widely used for specific applications. These materials are recommended for GC-MS applications for injection port liner seals, insulators, washers, ferrules, etc.

Table 2: Material Properties of MACOR

### I. Thermal

	SI/Metric	English	
Coefficient of Expansion			
	-200- 25°C	74x10 <sup>-7</sup> /°C	41x10 <sup>-7</sup> /°F
	25-300°C	93x10 <sup>-7</sup> /°C	52x10 <sup>-7</sup> /°F
	25-600°C	114x10 <sup>-7</sup> /°C	63x10 <sup>-7</sup> /°F
	25-800°C	126x10 <sup>-7</sup> /°C	70x10 <sup>-7</sup> /°F
Specific Heat, 25°C	.79 KJ /kg°C	0.19 Btu/lb°F	
Thermal Conductivity, 25°C	1.46 W/m°C	10.16 $\frac{\text{Btu in}}{\text{hr ft}^2\text{°F}}$	
Thermal Diffusivity, 25°C	7.3x10 <sup>-7</sup> m <sup>2</sup> /s	0.028 ft <sup>2</sup> /hr	
Continuous Operating Temperature	800°C	1472°F	
Maximum No Load Temperature	1000°C	1832°F	

### III. Electrical

	SI/Metric	English	
Dielectric Constant, 25°C			
	1 KHz	6.03	6.03
	8.5 GHz	5.67	5.67
Loss Tangent, 25°C			
	1 KHz	4.7x10 <sup>-3</sup>	4.7x10 <sup>-3</sup>
	8.5 GHz	7.1x10 <sup>-3</sup>	7.1x10 <sup>-3</sup>
Dielectric Strength, AC or DC (at .01" thickness, 25°C)	40 KV/mm	1000V/mil	
DC Volume Resistivity, 25°C	>10 <sup>16</sup> ohm-cm	>10 <sup>16</sup> ohm-cm	

### II. Mechanical

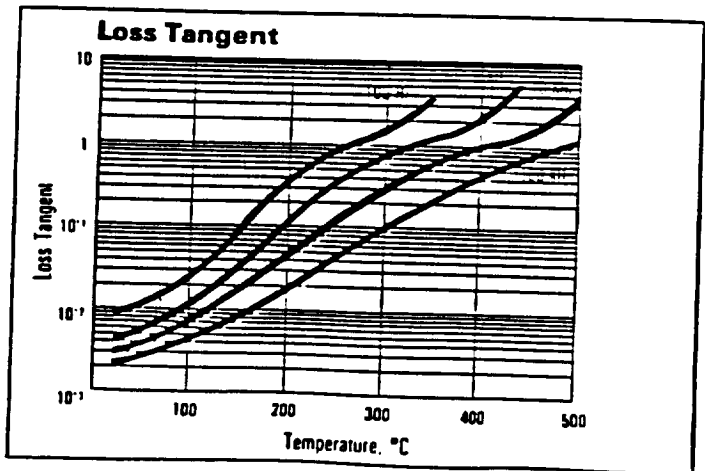
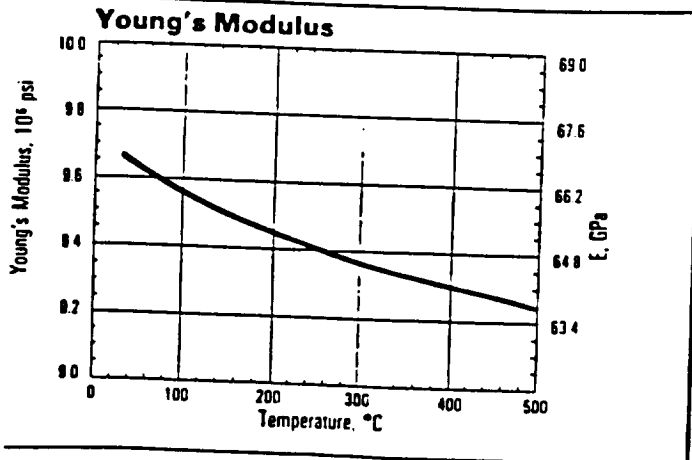
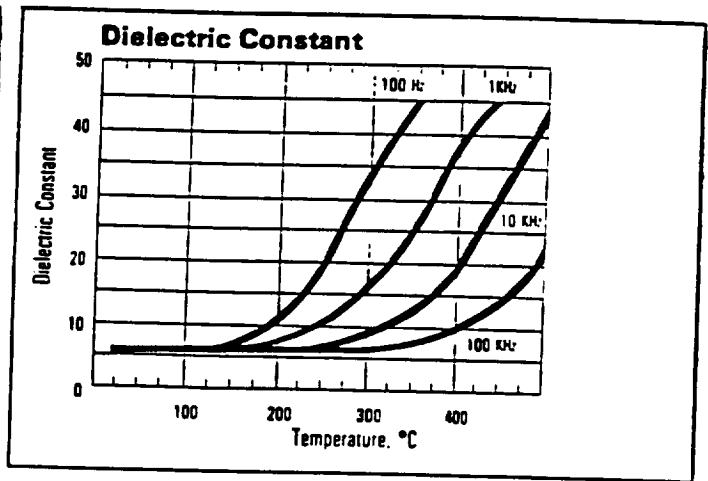
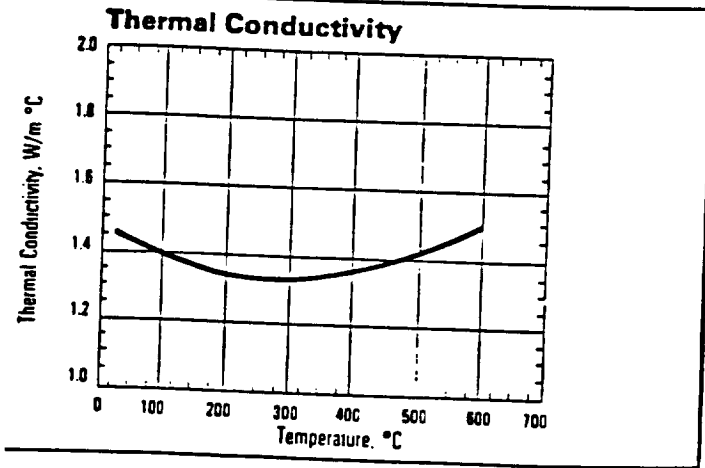
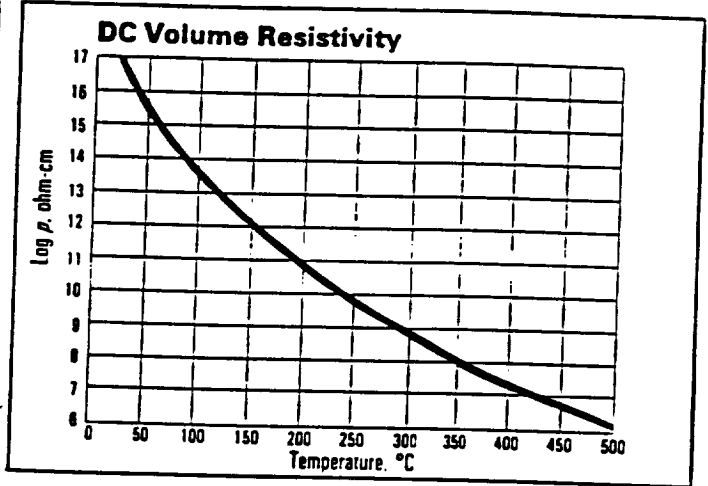
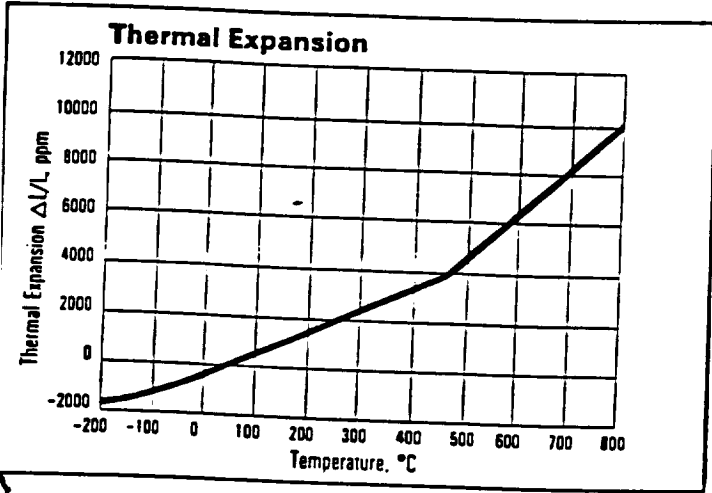
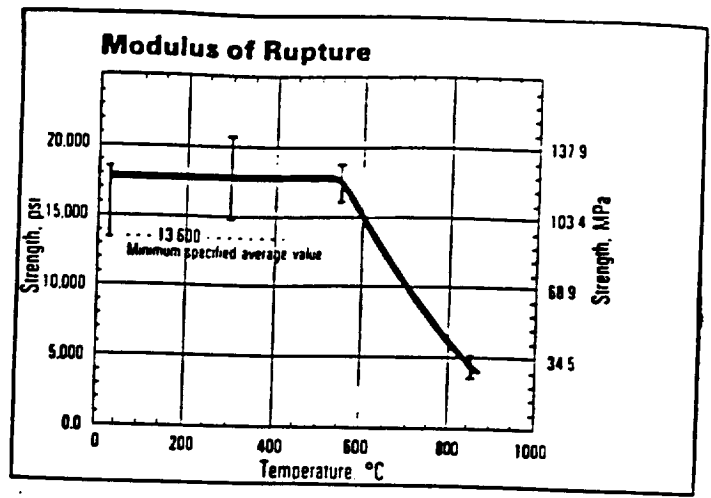
	SI/Metric	English
Density	2.52 g/cm <sup>3</sup>	157 lbs/ft <sup>3</sup>
Porosity	0%	0%
Young's Modulus, 25°C (Modulus of Elasticity)	66.9 GPa	9.7x10 <sup>6</sup> psi
Poisson's Ratio	0.29	0.29
Shear Modulus, 25°C	25.5 GPa	3.7x10 <sup>6</sup> psi
Hardness, Knoop 100g Rockwell A	250	250
	48	48
Modulus of Rupture, 25°C (Flexural Strength)	94 MPa	13,600 psi (minimum specified average value)
Compressive Strength	345 MPa	50,000 psi
Fracture Toughness	1.53 MPa m <sup>0.5</sup>	1,390 psi in <sup>0.5</sup>

### IV. Chemical

Solution	Tests			Results
	pH	Time	Temp.	Weight Loss (mg/cm <sup>2</sup> ) Gravimetric
5% HCL (Hydrochloric Acid)	0.1	24 hrs.	95°C	~ 100
0.002 N HNO <sub>3</sub> (Nitric Acid)	2.8	24 hrs.	95°C	~ 0.6
0.1 N NaHCO <sub>3</sub> (Sodium Bicarbonate)	8.4	24 hrs.	95°C	~ 0.3
0.02 N Na <sub>2</sub> CO <sub>3</sub> (Sodium Carbonate)	10.9	6 hrs.	95°C	~ 0.1
5% NaOH (Sodium Hydroxide)	13.2	6 hrs.	95°C	~ 10
<b>Resistance to water over time</b>				
H <sub>2</sub> O	7.6	1 day*	95°C	0.01
		3 days*	95°C	0.07
		7 days*	95°C	9.4
		3 days**	95°C	0.06
		6 days**	95°C	0.11

\*Water not freshened daily  
\*\*Water freshened daily

**Figure 3**  
Physical Characteristics of MACOR



## 6. Portable Gas Chromatograph – Mass Spectrometer System

A project to design and build a prototype portable Gas Chromatograph-Mass Spectrometer (GC-MS) was undertaken in Phase II, with plans to develop a commercial product in Phase III. GC-MS not only offer a much wider range of chemicals and biochemical agents for analysis, but also offer a much greater sensitivity than most other analytical techniques such as FTIR, Raman spectroscopy and tunable diode laser spectroscopy. For example, tunable diode laser spectrometers are normally limited in detecting only one chemical per diode laser. The development of a portable GC-MS was undertaken because although GC-MS are an extremely powerful tool for identifying and analyzing chemical and biological agents including environmental contaminants, existing GC-MS systems are too large and heavy to be suitable for field applications.

The goal for Phase II was to build a working prototype with design modifications to reduce the weight and size and improve resolution and sensitivity. Further reduction in size and weight and the addition of many other features to develop a high performance GC-MS would be undertaken in Phase III. The development will result in a low-weight, highly sensitive, field portable GC-MS that can be used as a powerful tool for identifying and analyzing chemical and biological agents, including environmental contaminants.

The proposed GC-MS system is shown in Figure 1. Its design is based on the small GC-MS technology developed by Lawrence Livermore Laboratories (LLNL) and the bench top GC-MS developed by Hewlett-Packard.

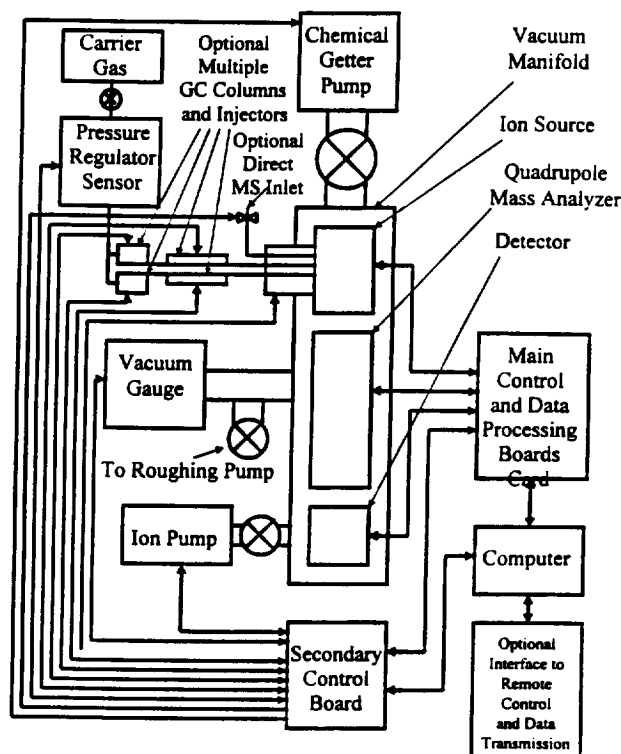


Figure 1: Schematic diagram of the proposed GC-MS system.

With limited funding in Phase II, a preliminary working prototype of significantly reduced size and weight from the original models was designed and built with plans to introduce more features, improve sensitivity and further reduce weight and size in Phase III.

Reduction in size and weight and improvements in resolution and sensitivity were mainly achieved by

- Employment of a miniature chemical getter pump (~1 lb.) and a miniature ion pump (~ 1 lb.) as opposed to the commonly used diffusion pump or turbo molecular pump systems (15-20 lb. or more). Chemical getter pumps have high pumping capacity for chemically active gases like H<sub>2</sub>, O<sub>2</sub>, N<sub>2</sub>, CO<sub>2</sub>, H<sub>2</sub>O, etc., whereas ion pumps are especially good for pumping chemically inactive noble gases. A lighter vacuum chamber has been designed for further weight reduction and will be built in Phase III.
- Employment of HP's state of the art monolithic quadrupole mass selector HP 5972. The monolithic quartz quadrupole (~ 6 in. long with 1 in<sup>2</sup> cross section), not only has less weight, but also has better thermal stability than the metallic ones. This resulted in significant increase in sensitivity and resolution.
- Implementation of direct sample injection to the mass spectrometer for significantly faster data analysis of gaseous samples and lower power consumption.

The current model of the GC-MS, which weighs about 50 pounds, has the following characteristics:

◇ **Mass Spectrometer:**

◇ Mass Analyzer	Quadrupole mass filter
◇ Mass Range:	2 - 700 amu
◇ Resolution ( $\Delta m$ ):	$\pm 0.3$ amu
◇ Sensitivity:	1 ppm (1ng/ $\mu$ L) to 1 ppb (1pg/ $\mu$ L)
◇ Typical Sample Injection:	1 $\mu$ L or less
◇ Ionization Source:	70 eV electron impact

◇ **Gas Chromatograph:**

- ◇ Column temperature programmable from room temperature to 300°C
- ◇ Column temperature slew rate linear 10°C/min or better
- ◇ Low carrier gas flow rate (typical 0.06  $\mu$ L/min)
- ◇ HP-5 column (100  $\mu$ m i.d. x 10 m long)

◇ **Injector:**

- ◇ Temperature programmable from room temperature to 300°C
- ◇ Accept liquid injections
- ◇ Programmable split ratio

◇ **Carrier Gas Supply:**

- ◇ Hydrogen - Input pressure in the order of 4-5 PSIG

◇ **Vacuum Level:**

- ◇ Better than  $10^{-4}$   $\tau$  during sample analysis.

◇ **Data Collection System:**

◇ Dynamic range:  $10^5$ , Resolution: 16 bits, Scan rate: < 1 sec.

◇ **Operator Interface:**

◇ Graphics display, Keyboard and Mouse.

◇ **Size, Weight and Power Consumption:**

◇ Size: approximately 10"x20"x25"

◇ Weight: about 50 lbs (compared to Bruker Instruments: 240 lbs and Viking: 125 lbs)

◇ Power consumption: 265 W (compared to Viking: 1 kW)

Figures P1 – P6 showing major parts of the GC-MS system and an inventory of parts with their weights and sizes are given at the end of this section.

**Sensitivity of GC-MS**

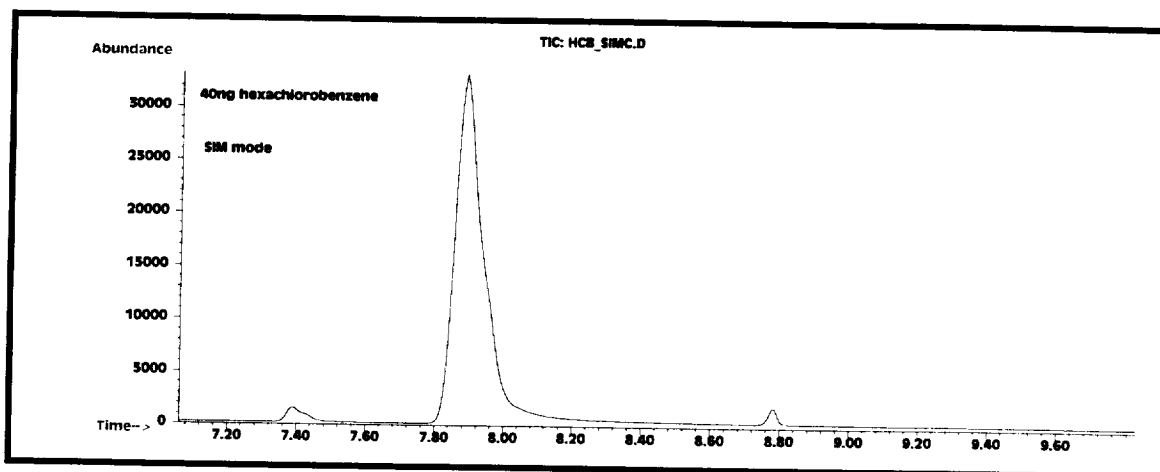
To test the sensitivity of the mass spectrometer as well as the efficiency of the GC column for separations, a variety of samples were tested at varying concentrations. Hexachlorobenzene was injected at concentrations of 40 ng, 20pg and 200 fg in order to monitor the relative sensitivity of the mass spectrometer. For pure samples the SIM mode was the preferred method of detection that allowed for highest sensitivity. Table 1 gives the experimental instrument settings utilized for hexachlorobenzene. GC spectral peaks in Figures 2a, 3a and 4a indicate that the mass spectrometer is sensitive to sample concentrations varying from the nanogram to the femtogram range. Figures 2b, 3b and 4b depict the resolved mass spectrometer peak components and their relative abundance.

In order to test the efficiency of the Gas Chromatograph column for separations, a solution comprised of a mixture of three components was used. The Extracted Ion mode of separation was used for detection of the unknown mixture. Figure 5 shows the resolved GC spectral peaks for the three components for an injected volume of 20ng. Figures 6a-c show the mass spectrometer resolution for the three unknown peaks as well as their identification through a library search of relevant spectra.

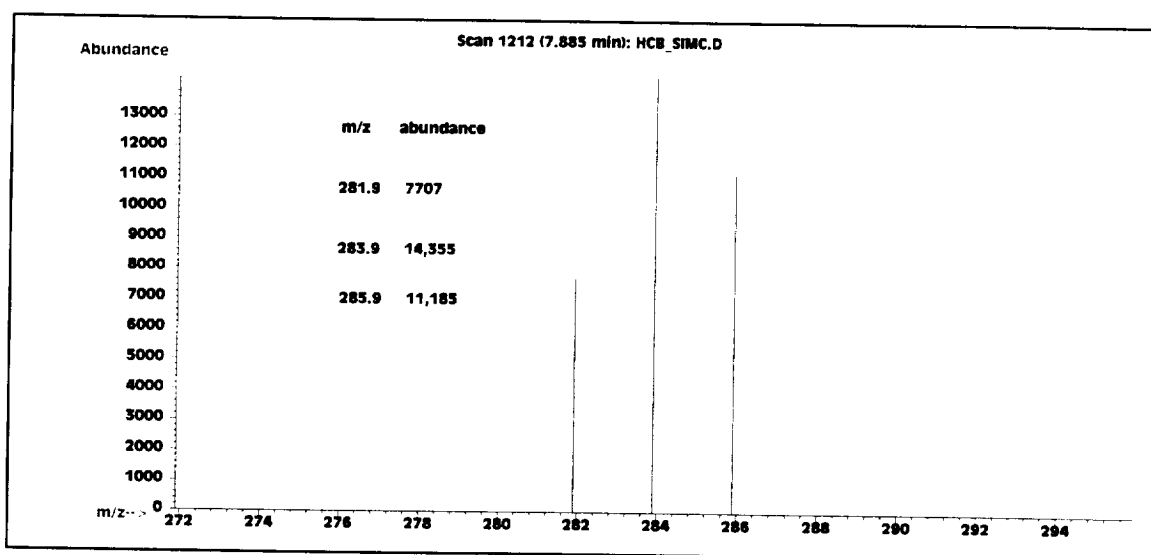
These sample experimental findings illustrate the high level of sensitivity and separation efficiency of the portable GC-MS instrument.

**Table 1**

Experimental Settings	Value
Inject. Port T	280°C
MSD Interf T	280°C
Initial Oven T	70°C
Oven T Incr	15-20°C/minute
Column P	5 psi
Solvent	isooctane
Sample	hexachlorobenzene
Inject volume	2 µL
Threshold	0
EM Setting	+400V rel to tune
A/D samples	2 <sup>3</sup> (1.7 scans/sec)

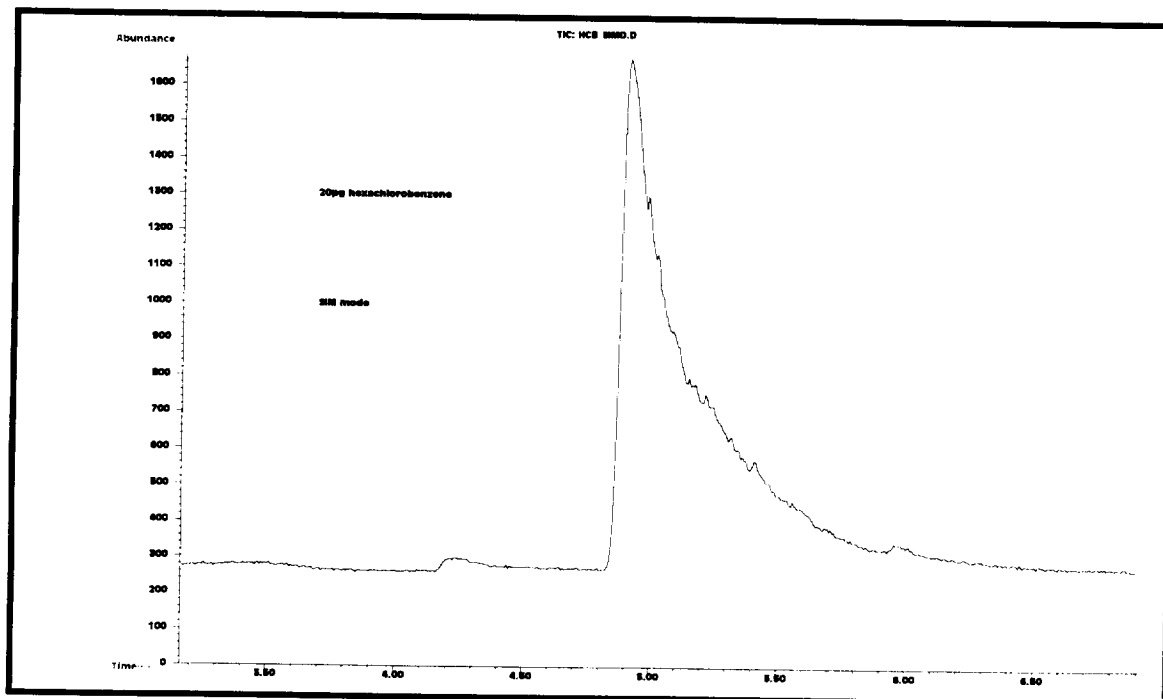


(a)

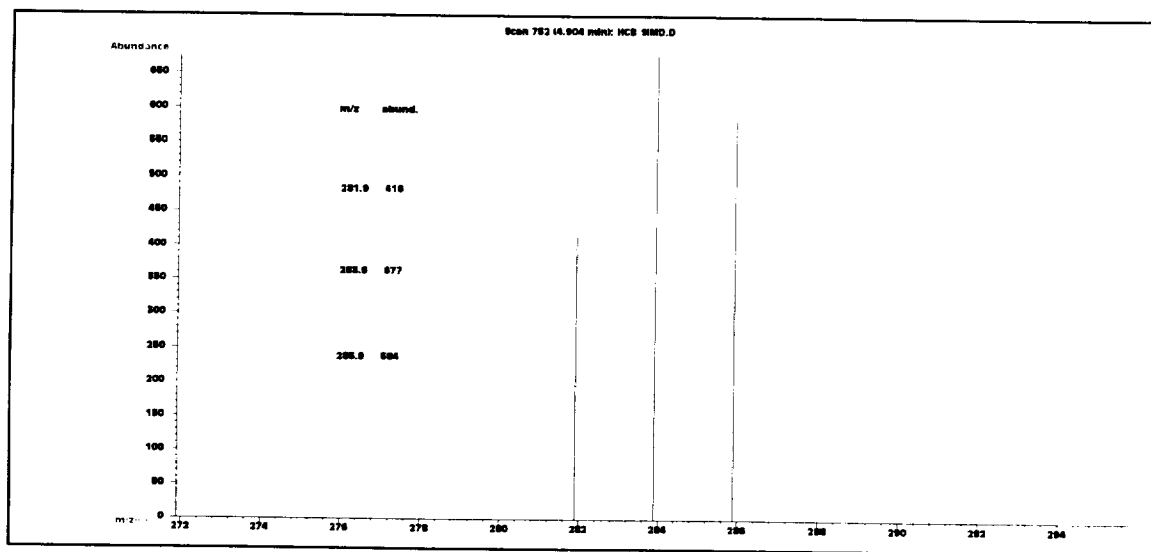


(b)

**Figure 2:** MS/GC Spectra for Hexachlorobenzene in SIM mode. (a) GC Spectral peaks for 40ng Hexachlorobenzene. This is a plot of the relative peak abundance versus retention time. (b) Corresponding Mass Spectrometer peaks for hexachlorobenzene. At a retention time of 7.9 minutes, the peak can be resolved into three mass components.

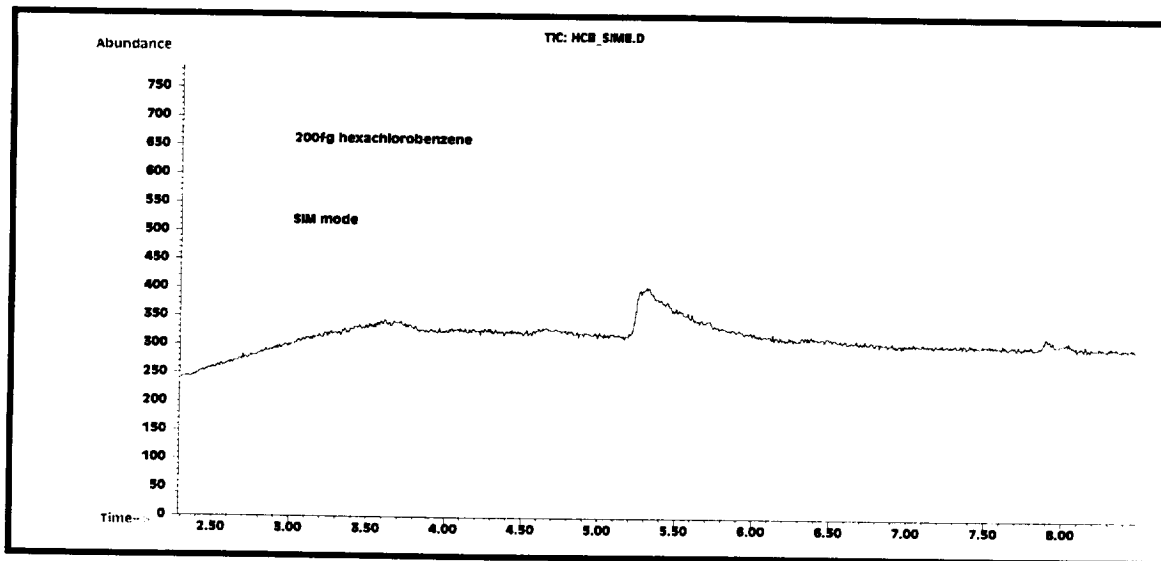


(a)

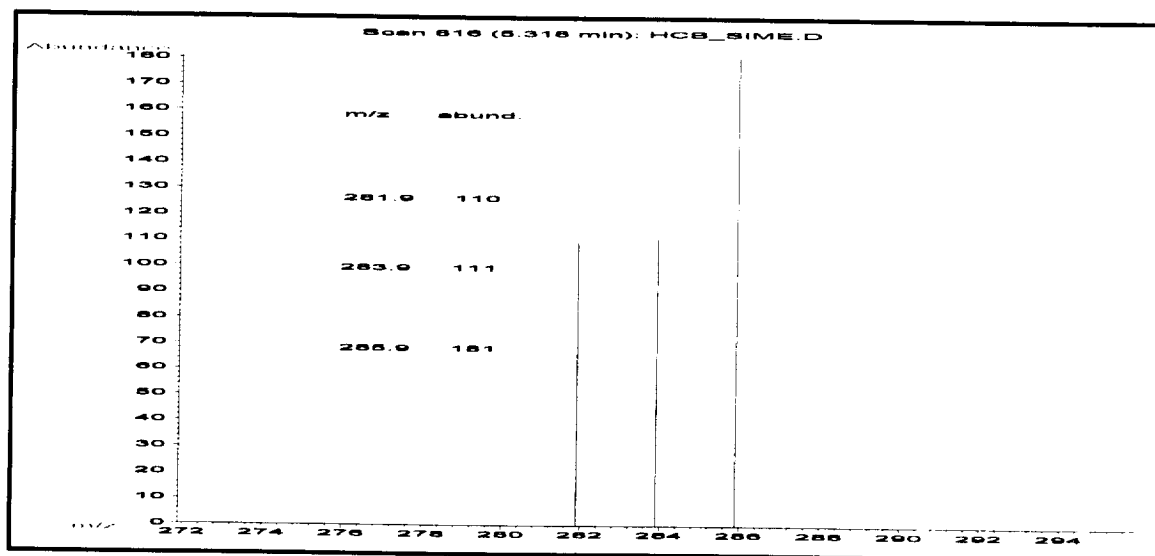


(b)

**Figure 3: MS/GC Spectra for Hexachlorobenzene in SIM mode. (a) GC Spectral peaks for 20pg Hexachlorobenzene. This is a plot of the relative peak abundance versus retention time. (b) Corresponding Mass Spectrometer peaks for hexachlorobenzene. At a retention time of 4.9 minutes, the peak can be resolved into three mass components as indicated.**



(a)



(b)

**Figure 4:** MS/GC Spectra for Hexachlorobenzene in SIM mode. (a) GC Spectral peaks for 200fg Hexachlorobenzene. This is a plot of the relative peak abundance versus retention time. (b) Corresponding Mass Spectrometer peaks for hexachlorobenzene. At a retention time of 5.3 minutes, the peak can be resolved into three mass components as indicated.

Experimental Settings	Value
Inject. Port T	150°C
MSD Interf T	156°C
Initial Oven T	67°C
Oven T Incr	15-20°C/minute
Column P	6 psi
Solvent	isooctane
Sample	mixture of 3 compounds
Inject volume	2 $\mu$ L
Threshold	0
EM Setting	+400V rel to tune
A/D samples	2 <sup>3</sup> (1.7 scans/sec)

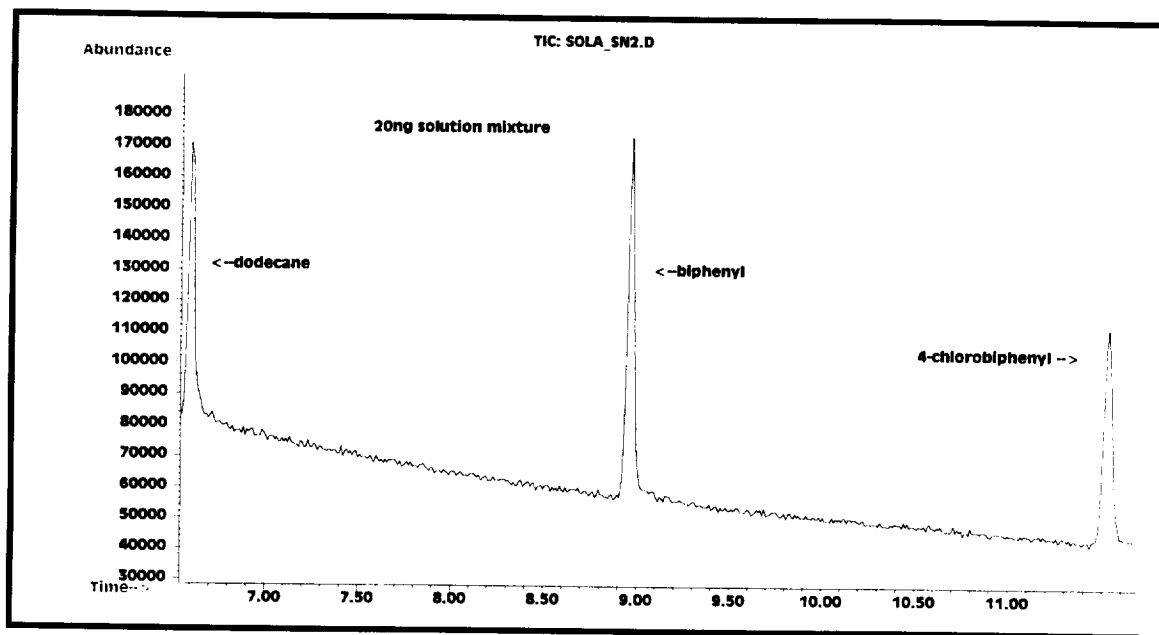
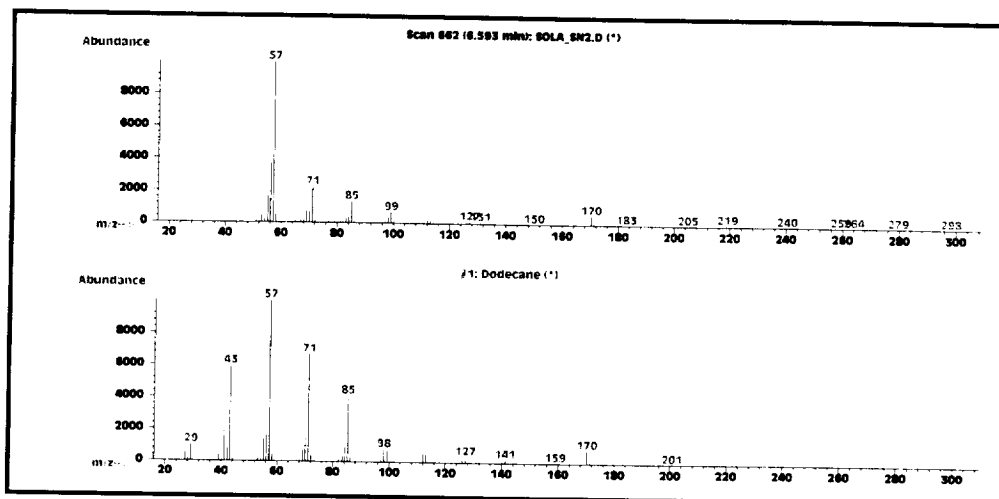
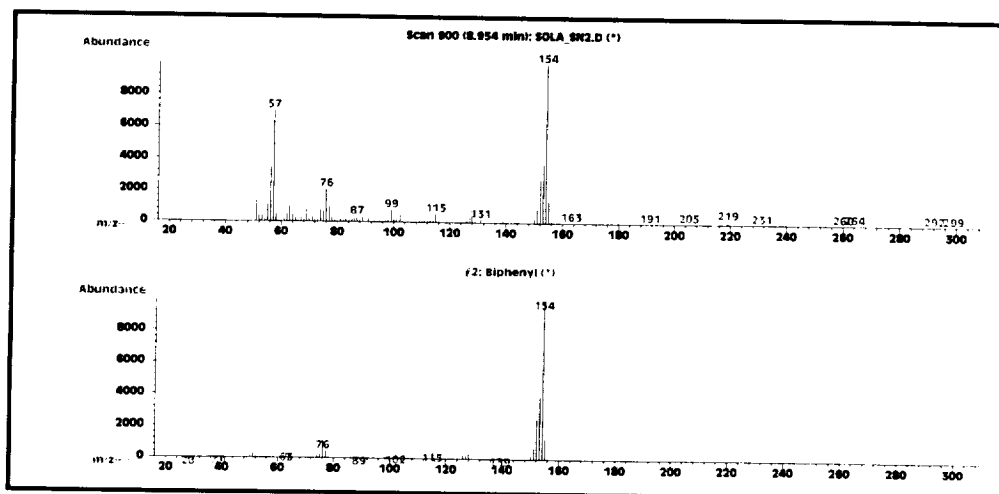


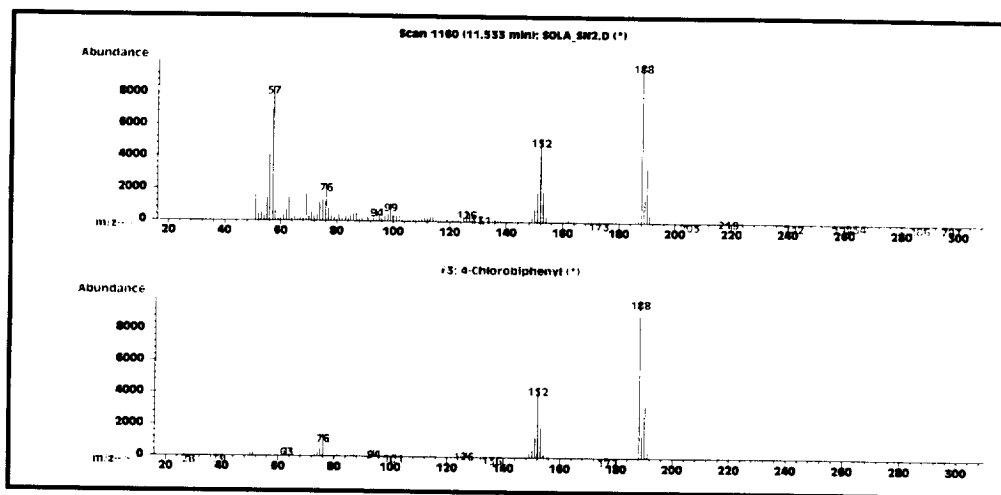
Figure 5: MS/GC Spectra in Extracted Ion SCAN mode for a 20 ng mixture of three components (dodecane, biphenyl, and 4-chlorobiphenyl) showing their relative peak abundance versus retention time.



(a)



(b)

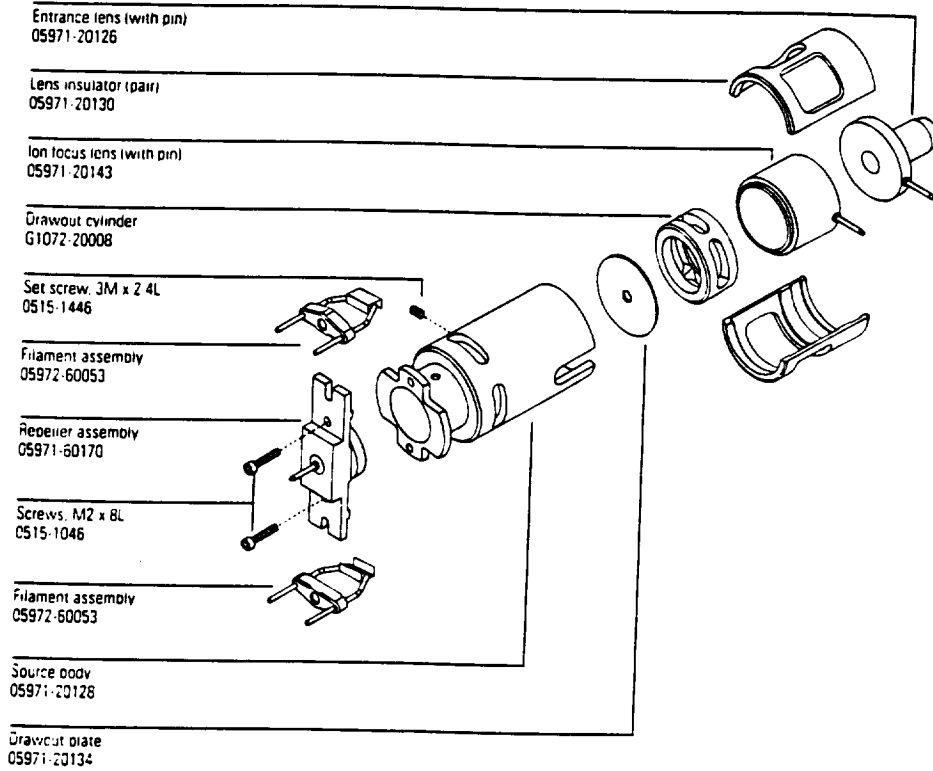


(c)

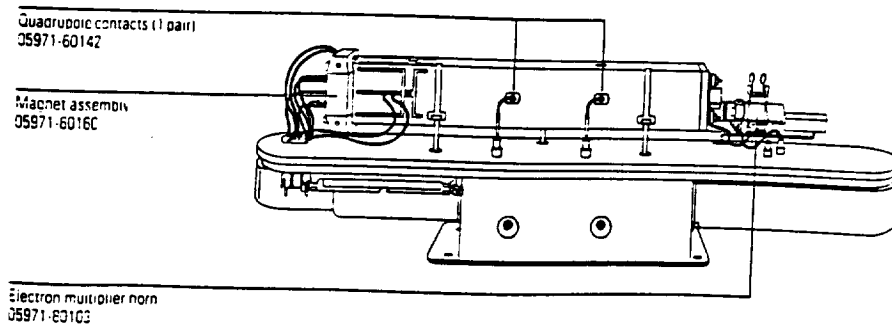
Figure 6: Library search spectral peak matches. The library search of spectra correlated the unknown peaks in Figure 5 with those of three components in the mixture. Shown are the mass spectrometer peaks for (a) dodecane, retention time 6.59 min; (b) biphenyl, retention time 8.95 min. and (c) 4-chlorobiphenyl, retention time 11.53 min.

# Major Parts of the GC-MS

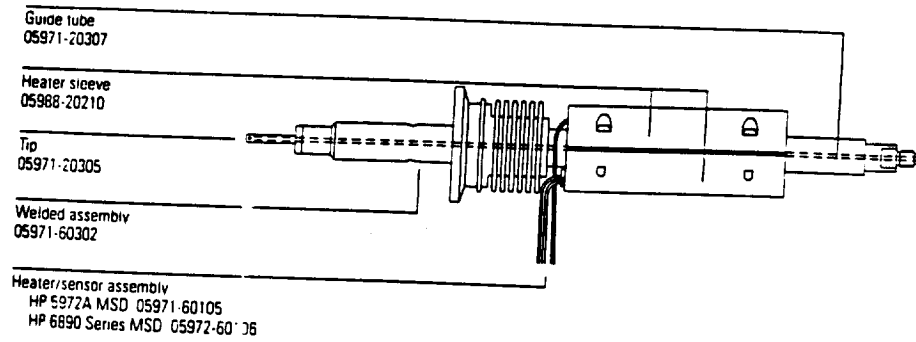
## P1 Ion Source



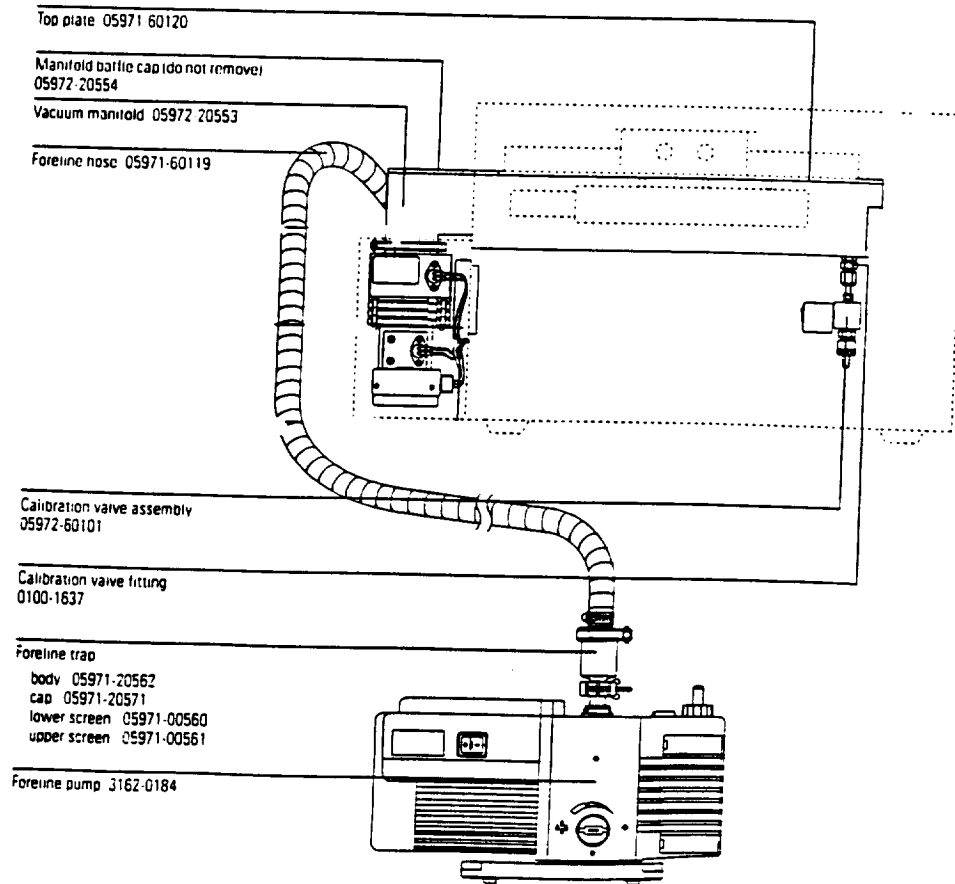
## P2 Analyzer



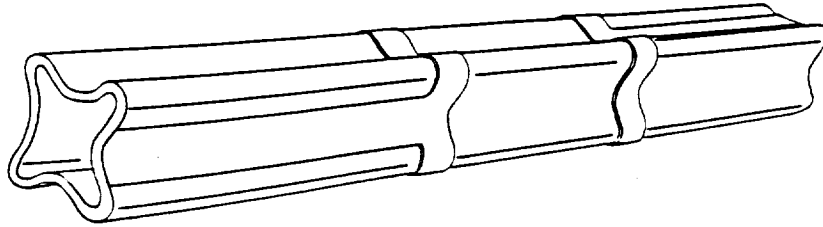
### P3 GC Interphase



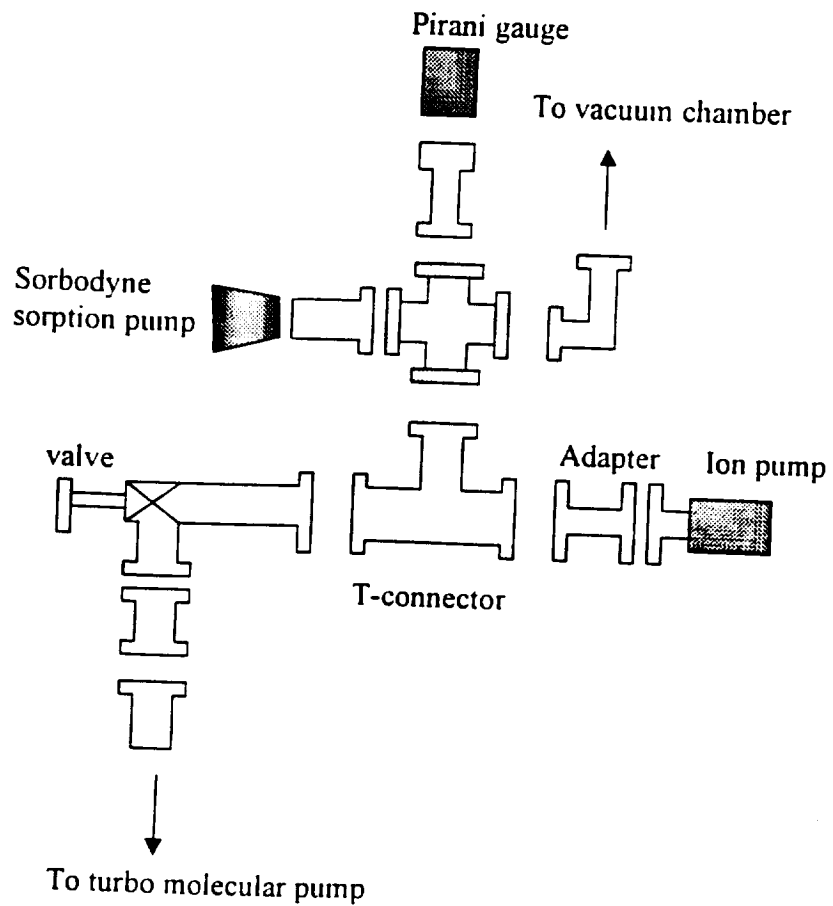
### P4 Vacuum System



## P5 Quadropole



## P6 Vacuum System Plumbing



## Inventory of GC-MS parts

Instrument: HP5972A&HP6890 MS & GC						
Inventory and weights/sizes of selected parts						
<i>material: SS=stainless steel; AL=aluminum; AU=gold plated; CU=copper</i>						
Mass Spectrometer Components	volume(cm <sup>3</sup> )	$\rho$ (g/cm <sup>3</sup> )	weight	material	dimensions	P/N
<b>ion source</b>						
drawout cyinder		7.9		SS		G1072-20008
drawout plate		7.9		SS		05971-20134
entrance lens		7.9		SS		05971-20126
filament assembly				tungsten		05972-60053
ion focus lens		7.9		SS		05971-20143
lens insulator				plastic		05971-20130
repeller assembly		7.9		SS		05971-60170
source body		7.9		SS		05971-20126
<b>total ion source</b>	<b>11</b>	<b>7.9</b>	<b>86.2g</b>			
<b>magnet assembly</b>						
quadrupole contacts		8.96		CU	1.2X1.2X2.5cm	05971-60160
radiator	18.3	2.7	49.3g	AL	2.5X4X3.5cm(-0.5mm thic	05971-60142
quadrupole mass filter	49.7			quartz	16X3.5X3.5cm(-2mmthick)	05971-20120
<b>electron multiplier</b>						
electron multiplier horn	7.1	7.9	55.8g	SS	8X5X8cm	05971-80102
<b>total weight of components</b>			<b>191.3g</b>			
<b>Mass Spectrometer Mounting Assembly</b>						
top plate	108.6	7.9	857.8g	SS		05971-60120
top board			726g			05971-69001
RF amplifier						
DC amplifiers						
High voltage supply						
Thermcouple amplifier						
Alternate filament relay						
Feedthrough connections						
<b>total weight of mounting assembly</b>			<b>1583.8g</b>			
<b>Vacuum System Components</b>						
foreline pump*						3162-0184
foreline trap*	197.8	7.9		SS	L=7cm;r=3cm	refer to manual
foreline hose*	1246			plastic	L=155cm;r=1.6cm	05971-60119
pirani vacuum gauge			90g	AlMgSi		TPR 250
calibration valve assembly	60.5	8.75		brass	5.5cmX5.5cmX1cm	05972-60101
calibration valve fitting	12.6	2.7		AL	d=4cm,h=1cm	0100-1637
manifold O-ring			72.6g	rubber	d1=8.5cm;d2=39cm	05971-40100
O-ring assembly			4.53g	rubber	d=2cm	0100-1183
Coseal (GC interface)			2.72g	rubber	d~3cm	0100-1597
NW40/NW50 conical reducer						8102-027
CF275						8111-041
cold cathode gauge			907.2g			
ion pump			1020.6g			
CF133			397g			
CF275/CF133 Conflat O-length reducer			1077.3g			8411-002
CF275-4 way cross			3.16g			8404-002
CF275-manual valve			3.5g			3300-006
NW40			394.6g			8111-041
CF275-manual valve w/ metal seal bonnett			1757.7g			3300-036
sorbodnye sorption pump			907.2g			SBD-20Hz
NW40						8025-036
sorption pump						
NW50			510.3g			8041-111
<b>GC Interface Components</b>						
guide tube	6.2	7.9	12.2g	SS	d=1.5cm,L=3.5cm,2mm thick	05971-20307

heater sleeve		81.4	2.7	23.7g	AL	d=3.6cm,L=8cm,2mm thick	05988-20210
tip (gold plated)				19.39	AU		05971-20305
welded assembly				2.7	AL		05971-60302
heater sensor assembly					cords		05971-60105
nut				7.9	SS		
conditioned ferrule					graphite		0100-0691
GC interface							
GC interface socket				8.75	27.2g	brass	05971-20133
<b>total weight of interface components</b>				<b>63.1g</b>			
<b>Splitless Inlet Components</b>							
	volume(cm <sup>3</sup> )	$\rho$ (g/cm <sup>3</sup> )	weight	material	dimensions	P/N	
septum retainer nut		7.9		SS		18740-60835	
septum				rubber		5181-1263	
split insert weldment w/ tubing		2.7		AL		19251-60575	
liner seals				rubber	r=1.25cm;L=2.5cm	5180-4182	
<b>total volume of injection port</b>	12.26						
liner	0.25			quartz glass	id~2mm	5181-8818	
shell weldment	15.7	2.7	42.4	AL	6.5X5.0X4.0cm(-1mmthick)	refer to manual	
retaining nut		7.9		SS		19251-20620	
seal		19.39		AU		18740-20885	
washer		2.7		AL		5061-5869	
reducing nut		7.9		SS		18740-20800	
insulation						19243-00065	
lower insulation						19243-00060	
lower insulation cover		2.7		AL		19243-00070	
column ferrule				graphite		5080-8853	
column nut		7.9		SS		5020-8292	
septum				rubber		5181-1263	
<b>total volume of inlet components</b>	15.1				r=1cm;L=4.8cm		
capillary column	0.08			fused Si	ID=0.1mm;L=10m	19091S-002	
<b>total volume of inlet components</b>	<b>43.4</b>						
<b>Other Components</b>							
	volume(cm <sup>3</sup> )	$\rho$ (g/cm <sup>3</sup> )	weight	material	dimensions	P/N	
capillary column holder		7.9	623.7g	SS	d=17.4cm;L=1.5cm		
heater*			1800g	ceramic	4.4HX5.8WX7.3D(in.)	6795-200	
turbomolecular drag pump*			3600g			THP 062	
pressure regulator		7.9	1814g	SS	14X14X7 (cm)	refer to manual	
circuit board			997.9g		25cmX41.5cm	05990-69406	
<b>total weight of other components**</b>			<b>3435.6g</b>			05972-69020	
<b>Notes:</b>							
*** denotes components that will not be utilized in portable MS/GC system							
**** denotes total weight of components in portable GC/MS system							

## 8. Phase III Plan

In Phase III, PES plans to commercialize the Gas Chromatograph – Mass Spectrometer built in Phase II. PES will be collaborating with Extrel to package and market the system.

The development effort will be continued in Phase III. Further miniaturization and increase in sensitivity will be achieved by following means:

- ◇ The monolithic quadrupole mass selector HP 5973 will be used to improve sensitivity.
- ◇ The vacuum system of the GC-MS will be further improved by replacing the prevailing cast or machined aluminum vacuum chamber with a newly designed thin wall stainless steel vacuum chamber and the use of copper (or silver plated copper) gaskets to replace the prevailing elastomer O-rings. With the improved vacuum performance, miniature pumps with less power consumption can be used.
- ◇ The GC heating, cooling and temperature control system will be improved. A miniature GC oven will be designed which will not only reduce the weight, size and power consumption, but also shorten the time of data collection cycle.
- ◇ Direct mass spectrometer injection port will be designed and a differential pump used for improved vacuum.
- ◇ Allow multiple GC columns to be fed to the mass spectrometer for faster data analysis of wider ranges of chemicals and biochemicals without changing the GC columns.
- ◇ In order to implement automated data collection/identification, wireless data transmission and remote control, PES has developed a generic tele-maintenance system for remote control and data acquisition through regular phone lines; patent pending). This will be incorporated into the GC-MS system in Phase III. Furthermore, the GC-MS will be designed to be operable with batteries or solar panels, taking advantage of the recent development of high energy density (280 Wh/L and 125 Wh/Kg) rechargeable Li/Li<sub>x</sub>MnO<sub>2</sub> batteries.

When the development is complete, the GC-MS will have a resolution of 0.3 amu and sensitivity better than 1 ppm (full scan) and ~1 ppb (selected ion monitoring). The system will fit in a 9.5"x18"x27" brief case.

While the above GC-MS system will serve as a field portable unit for many applications such as environmental detection, PES plans to continue its efforts to design and build a miniature mass spectrometer for space applications. A miniature mass analyzer will be designed using a much smaller (about 2") quadrupole. Highly accurate simulations will be carried out to aid in the design process.

## INMS Parameters

Simulation of the INMS ion optics requires input of the grid dimensions. The INMS grids have complex structures, so many parameters are needed to describe the grid. There are many grids, so a multitude of parameters is needed for the simulation. The format for entering parameters into the simulation is not generally the format given in the NASA Engineering Specifications. The multitude of parameters combined with different presentation formats will result in discrepancies between simulation and measurement unless great care is taken.

As a first step toward a firmer relation between the Specifications and the simulations, both sets of parameters have been mapped onto diagrams of the INMS. These maps are shown in Figs. 1-14 for the entrance lens and in Figs. 15-31 for the exit lens. These figures are colorized to distinguish the simulation parameters (in red) and the NASA Specifications (in blue). Dimensions in black are not well defined by the Specifications.

Several figures are needed for most grids, as placement of all the parameters on a figure leads to indecipherable clutter. The specifications for each grid of the entrance lens (Figs. 2-12) and for the nozzle (Figs. 28-30) begin at the front outside corner and proceed counterclockwise around the cross-section. The specifications for each grid of the exit lens (Figs. 14-27) begin near the axis and proceed radially outward. A new figure is introduced when the figure becomes too busy. Three figures are needed for most grids. The List of Figures provides a guide to the parameters on each figure.

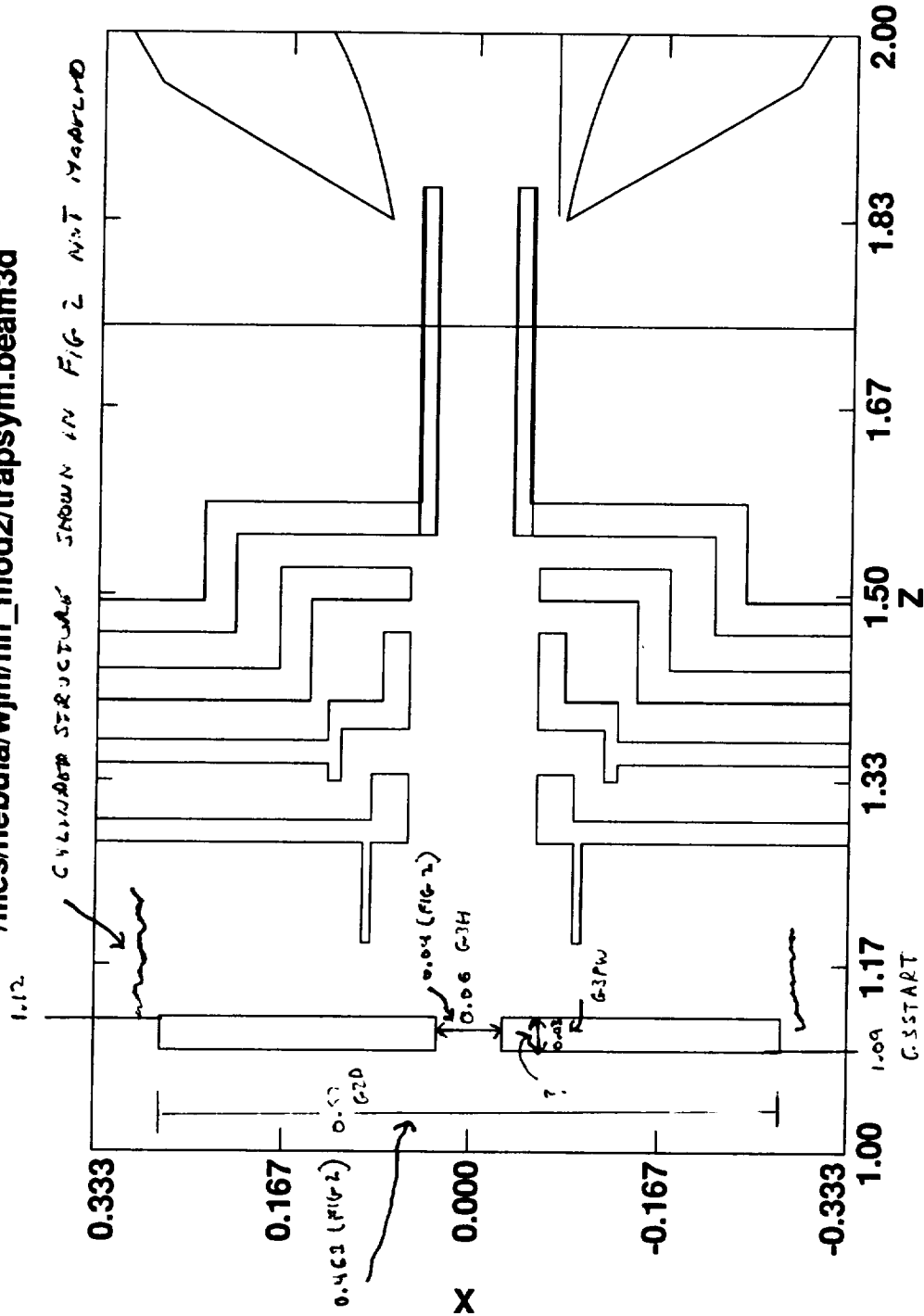
## LIST OF FIGURES

### Figure

1. Open Source Aperture Electrode.
2. Entrance Lens, Grid 1, Front Corner to Inside Entrance Cylinder.
3. Entrance Lens, Grid 1, Entrance Cylinder to Outside Exit Cylinder.
4. Entrance Lens, Grid 1, Exit Cylinder to Rear Corner.
5. Entrance Lens, Grid 2, Front Corner to Inside Entrance Cylinder.
6. Entrance Lens, Grid 2, Entrance Cylinder to End of Exit Cylinder.
7. Entrance Lens, Grid 2, Exit Cylinder to Rear Corner.
8. Entrance Lens, Grid 3, Front Corner to Inside Aperture.
9. Entrance Lens, Grid 3, Aperture to Rear Surface.
10. Entrance Lens, Grid 3, Rear Surface to Rear Corner.
11. Entrance Lens, Grid 4, Front Corner to Inside Cylinder.
12. Entrance Lens, Grid 4, Cylinder to Rear Corner.
13. Cylindrical Surface for Mapping Potentials in Simulation.
14. Exit Lens, Grid 1, Small Cylinder.
15. Exit Lens, Grid 1, Large Cylinder.
16. Exit Lens, Grid 1, Additional Parameters.
17. Exit Lens, Grid 2, Small Cylinder.
18. Exit Lens, Grid 2, Large Cylinder.
19. Exit Lens, Grid 2, Bevel.
20. Exit Lens, Grid 3, Aperture.
21. Exit Lens, Grid 3, Cylinder.
22. Exit Lens, Grid 3, Bevel.
23. Exit Lens, Grid 4, Cylinder.
24. Exit Lens, Grid 4, Bevel.
25. Exit Lens, Grid 4, Additional Parameters.
26. Exit Lens, Grid 5, Radial Parameters.
27. Exit Lens, Grid 5, Axial Parameters.
28. Nozzle, Front Corner to Inside Large Cylinder.
29. Nozzle, Large Cylinder to Exit Aperture.
30. Nozzle, Exit Aperture to Rear Corner.
31. Cylindrical Surface for Mapping Potentials in Simulation.

ZX

Data created on 04/30/96 at 09:28:47 in file  
/files/nebula/wjm/fin\_mod2/trapsym.beam3d



Unit of measure is the IN

RED INDICATES CURRENT LADS Model dimensions  
BLUE INDICATES DIMENSIONS FROM NASA diagrams  
BLACK INDICATES QUESTIONABLE dimension

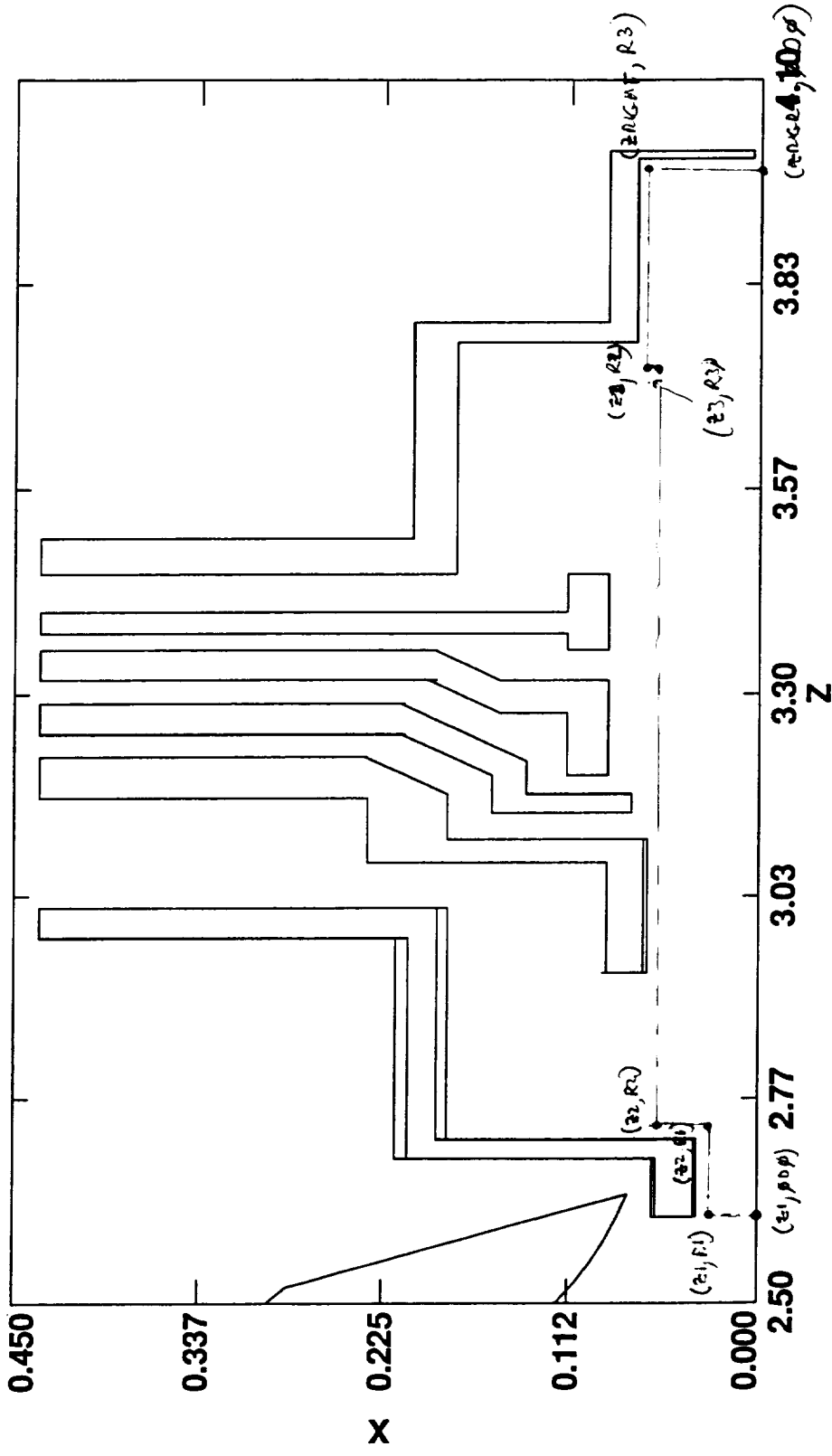
04/30/96 10:58



EXIT LENS POTMAP

ZX

Data created on 04/30/96 at 09:28:47 in file  
/files/nebula/wjm/fln\_mod2/trapsym.beam3d



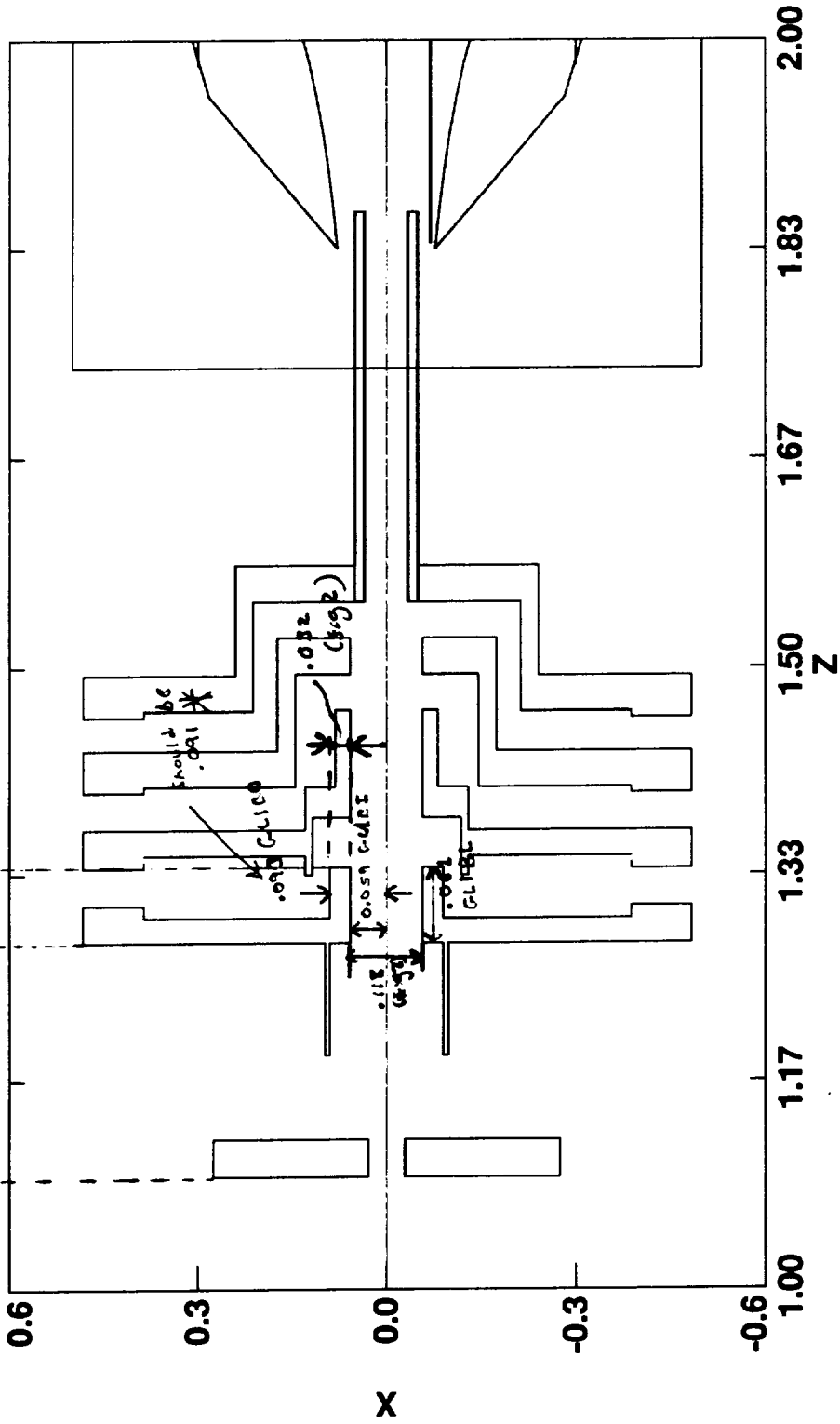
Unit of measure is the IN

05/08/96 10:51

ZX  
 .249  
 (FIG. 2)

Data created on 04/30/96 at 09:28:47 in file  
 /files/nebula/wjm/fin\_mod2/trapsym.beam3d

.198  
 (FIG. 2)

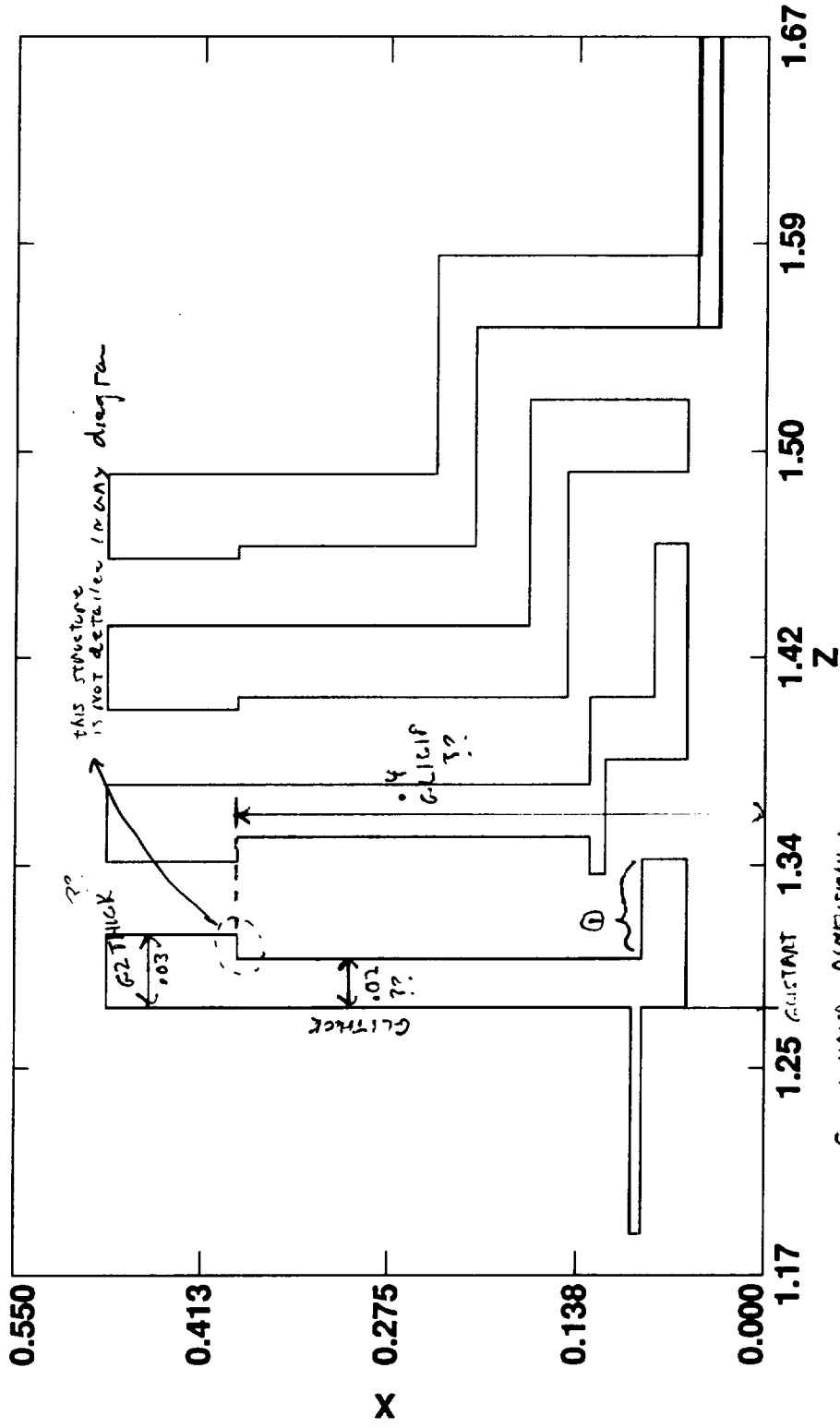


RED INDICATES CURRENT LADS MODEL DIMENSIONS  
 BLUE INDICATES DIMENSIONS FROM NASA DIAGRAMS  
 BLACK INDICATES QUESTIONSABLE DIMENSIONS 04/30/96 13:44

Unit of measure is the IN

ZX

Data created on 04/30/96 at 09:28:47 in file  
/files/nebula/wjm/flin\_mod2/trapsym.beam3d



① CIRCULAR DIMENSION  
RELATIVE TO LENS THICKNESS

RED INDICATES CURRENT CADS MODEL DIMENSIONS

BLUE INDICATES DIMENSIONS FROM NASA 04/30/96 15:37  
diagrams

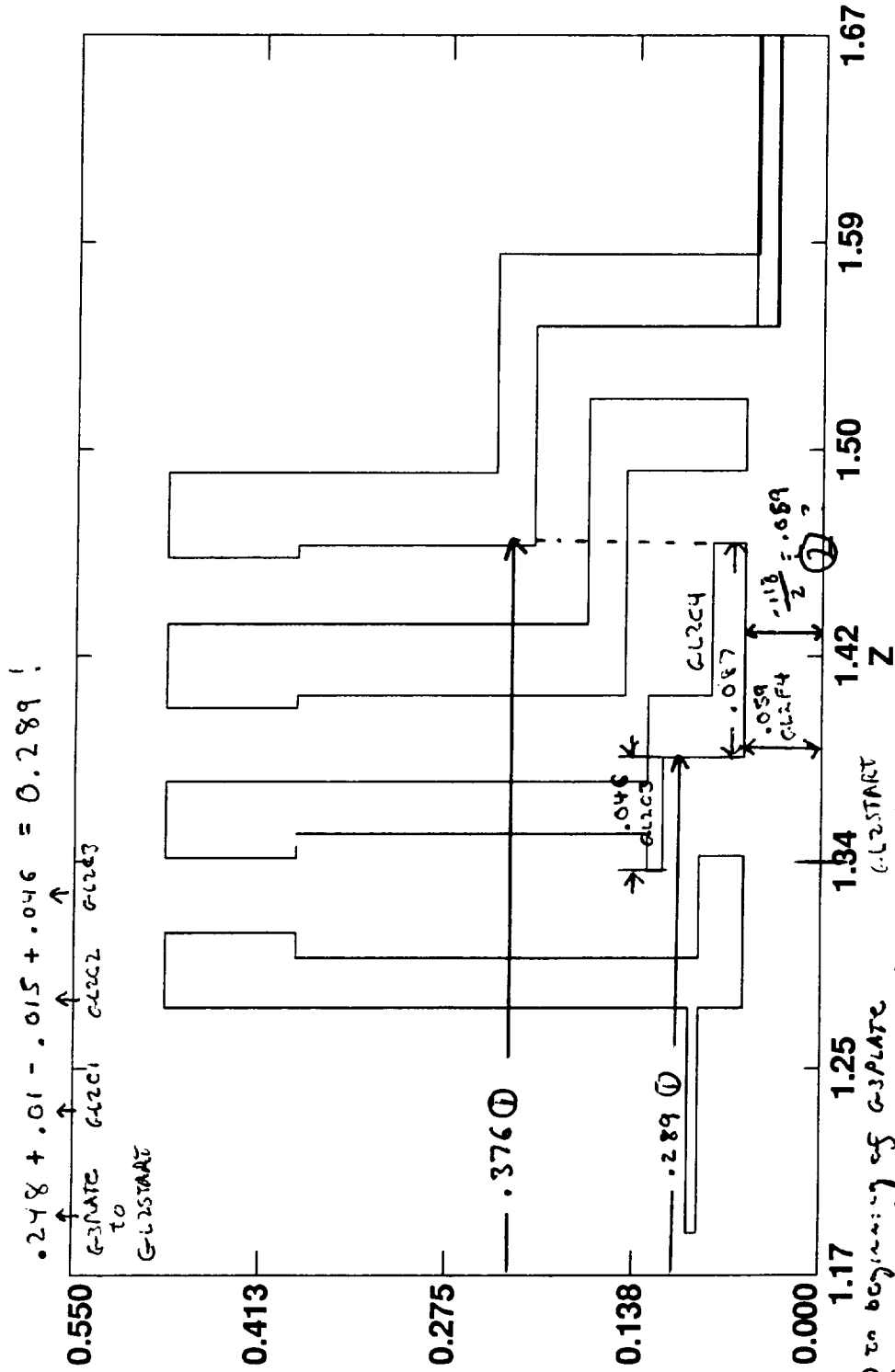
BLACK INDICATES QUESTIONABLE DIMENSIONS

Unit of measure is the IN



ZX

Data created on 04/30/96 at 09:28:47 in file /files/nebula/wjm/fin\_mod2/trapsym.beam3d



① to beginning of G-3PLATE  
 ② FIG 2 refers to an inner diameter of .117 BUT IT IS POSSIBLE TO DETERMINE WHAT THIS REFERS TO.

RED INDICATES CURRENT LADS MODEL  
 BLUE INDICATES DIMENSIONS FROM NASA DRAWING (FIG 2)  
 BLACK INDICATES QUESTIONABLE DIMENSION

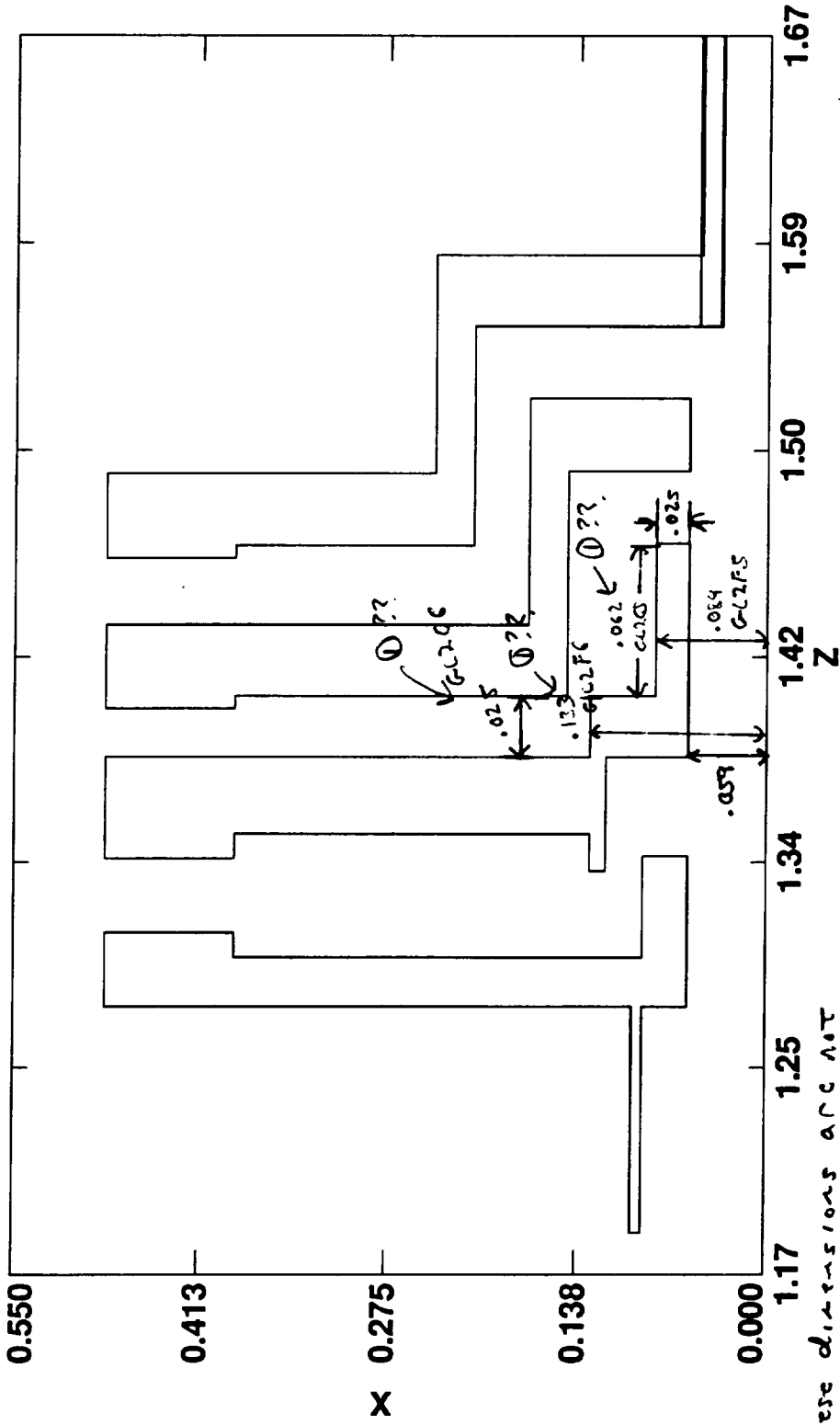
Unit of measure is the IN

04/30/96 15:37

5-2-96

ZX

Data created on 04/30/96 at 09:28:47 in file /files/nebula/wjm/fin\_mod2/trapsym.beam3d



① these dimensions are NOT SPECIFIED

RED INDICATES CURRENT LABS MODEL DIMENSIONS  
BLUE INDICATES DIMENSIONS FROM NASA DIAGRAMS  
BLACK INDICATES QUESTIONABLE DIMENSIONS

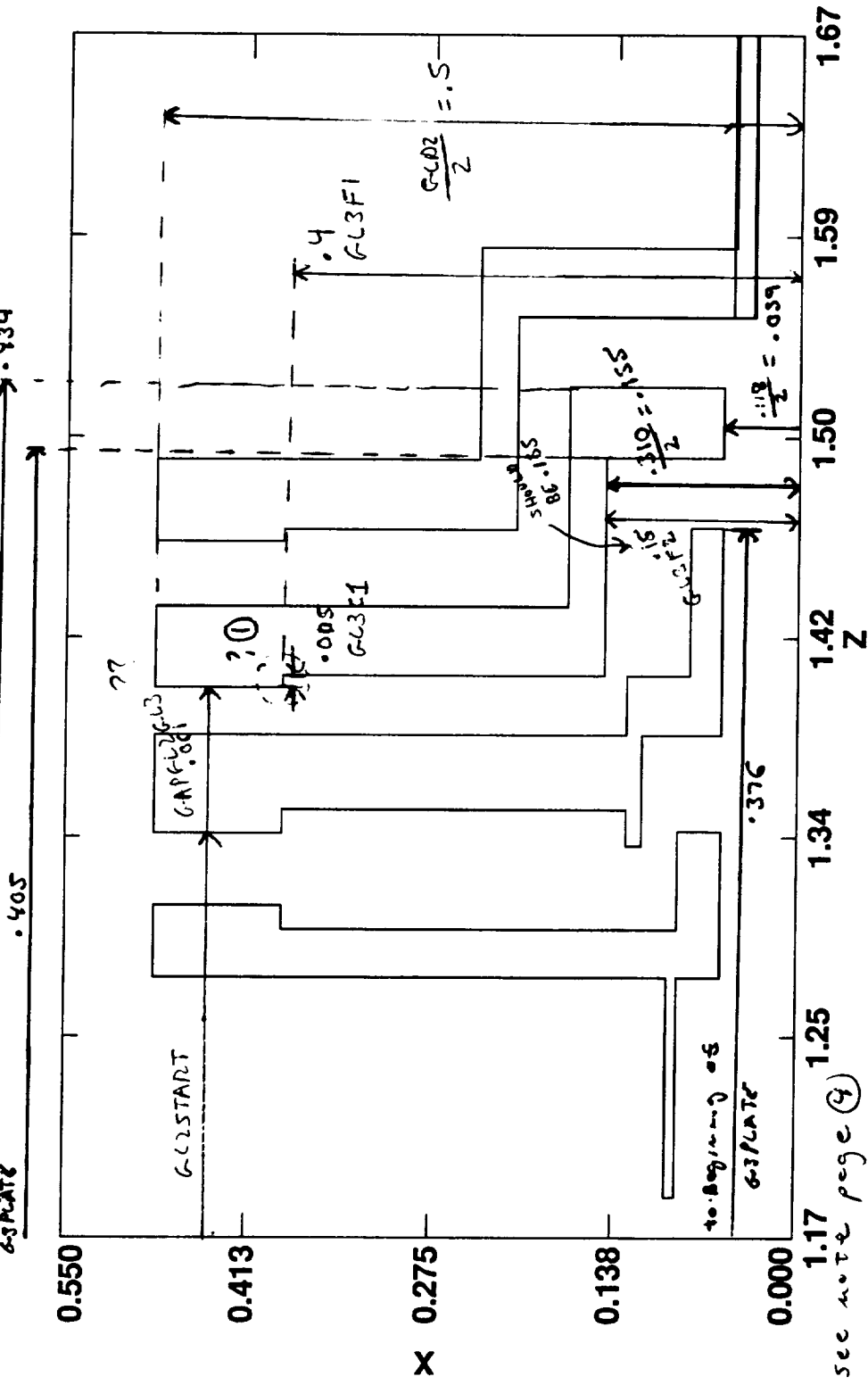
Unit of measure is the IN

05/02/96 09:44

ZX

Data created on 04/30/96 at 09:28:47 in file  
/files/nebula/wjm/fin/mod2/trapsym.beam3d  
→ .434

to beginning of  
G3PLATE



RED INDICATES CURRENT LEADS FROM DIRECTION  
BLUE INDICATES DIMENSION FROM NASA DIAGRAM (FIG 2)  
BLACK INDICATES QUESTIONABLE DIMENSION

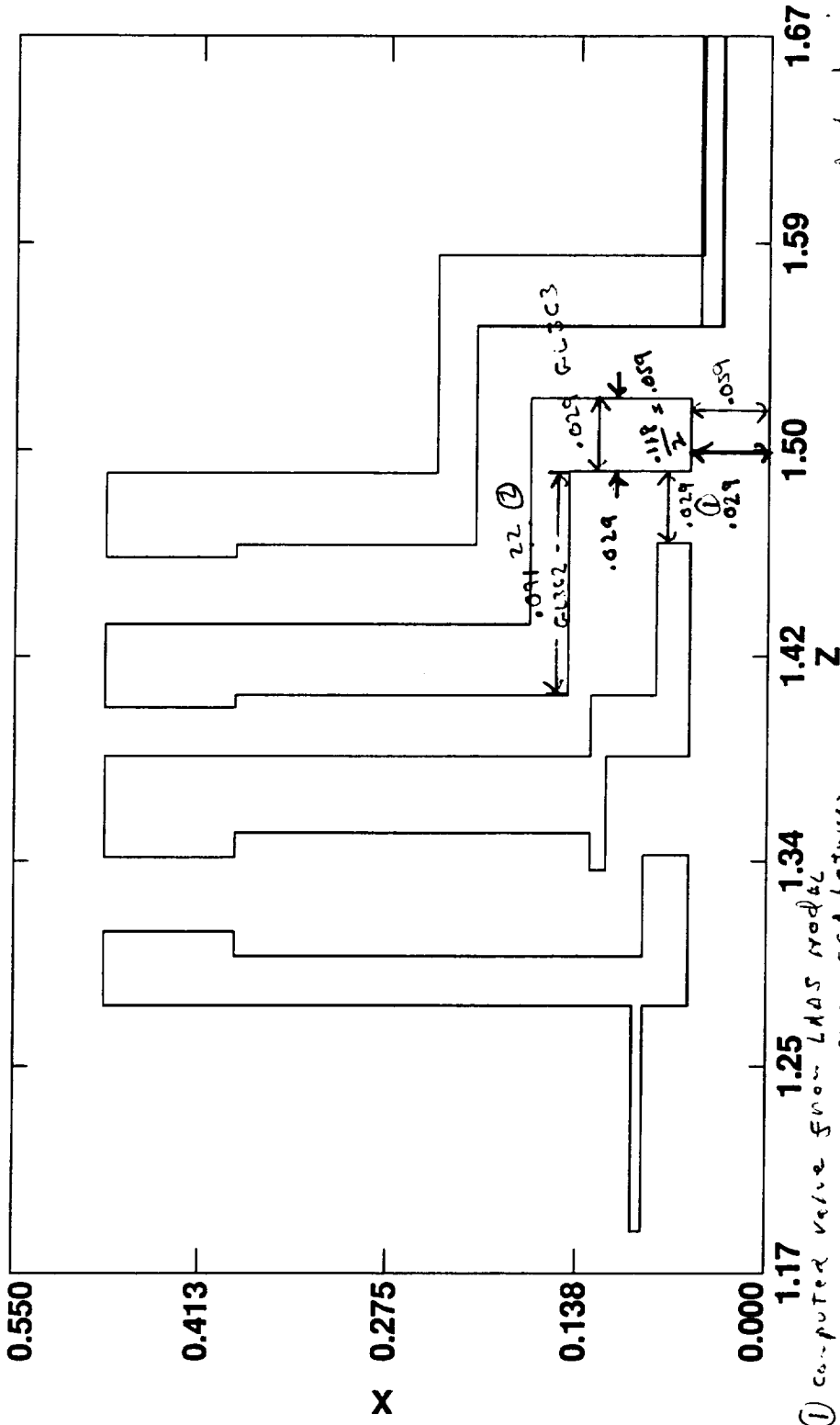
① see note page 4

Unit of measure is the IN

05/02/96 09:44

ZX

Data created on 04/30/96 at 09:28:47 in file  
/files/nebula/wjm/fin\_mod2/trapsym.beam3d



- ① computed value from LADS model
- ② dimension chosen for propagation between  
GL2 & GL3

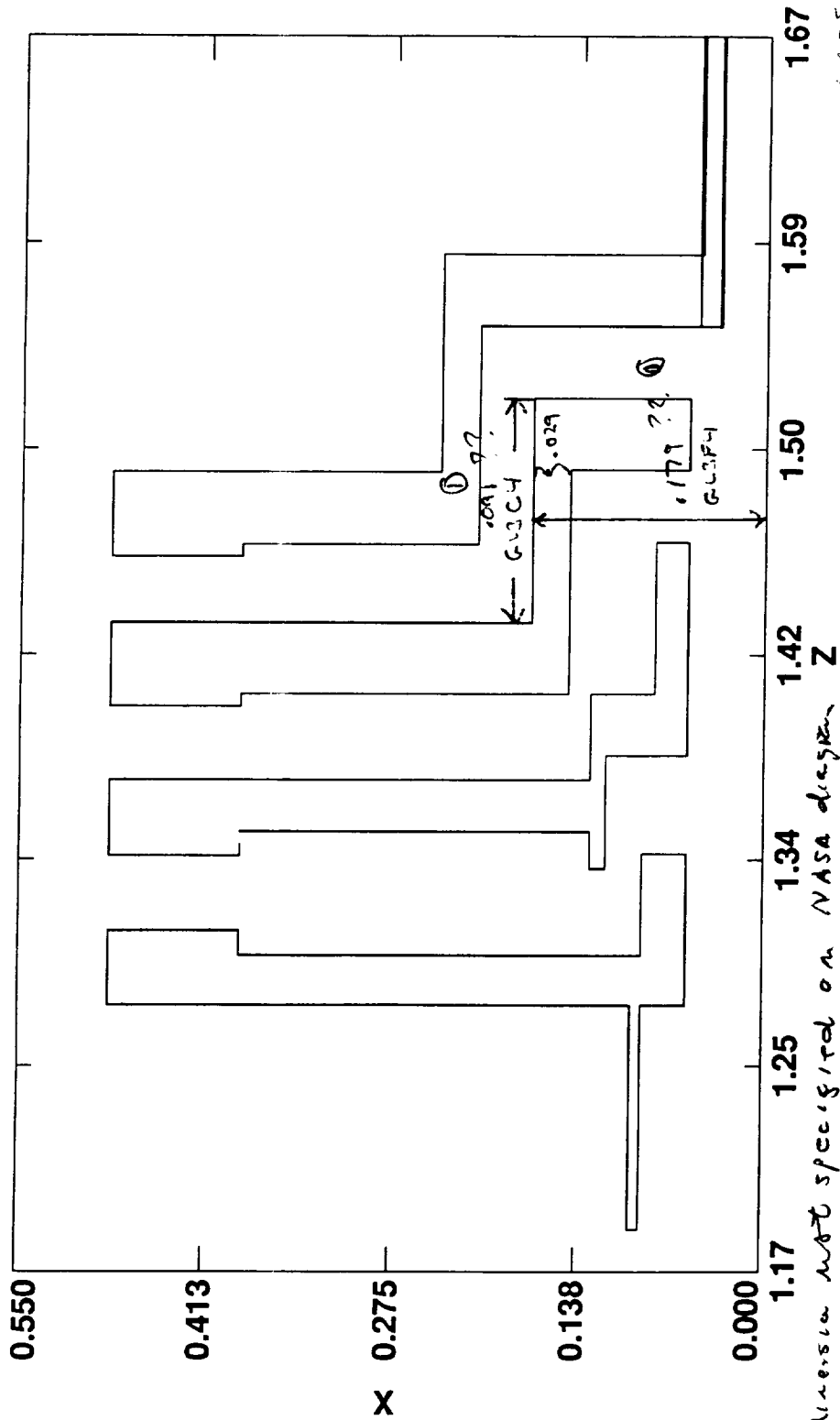
RGB INDICATES CURRENT CADS MODEL DIMENSION  
BLUE INDICATES DIFFUSION FROM NASA DIAGRAM (FIG 2)  
BLACK INDICATES QUESTIONABLE DIMENSION

Unit of measure is the IN

05/02/96 09:44

Data created on 04/30/96 at 09:28:47 in file  
 /files/nebula/wjm/fin\_mod2/trapsym.beam3d

ZX



RED INDICATES CURRENT CASE NUMBER  
 DIMENSION

BLUE INDICATES DIMENSIONS FROM  
 NASA DIAGRAM (FIG 2)

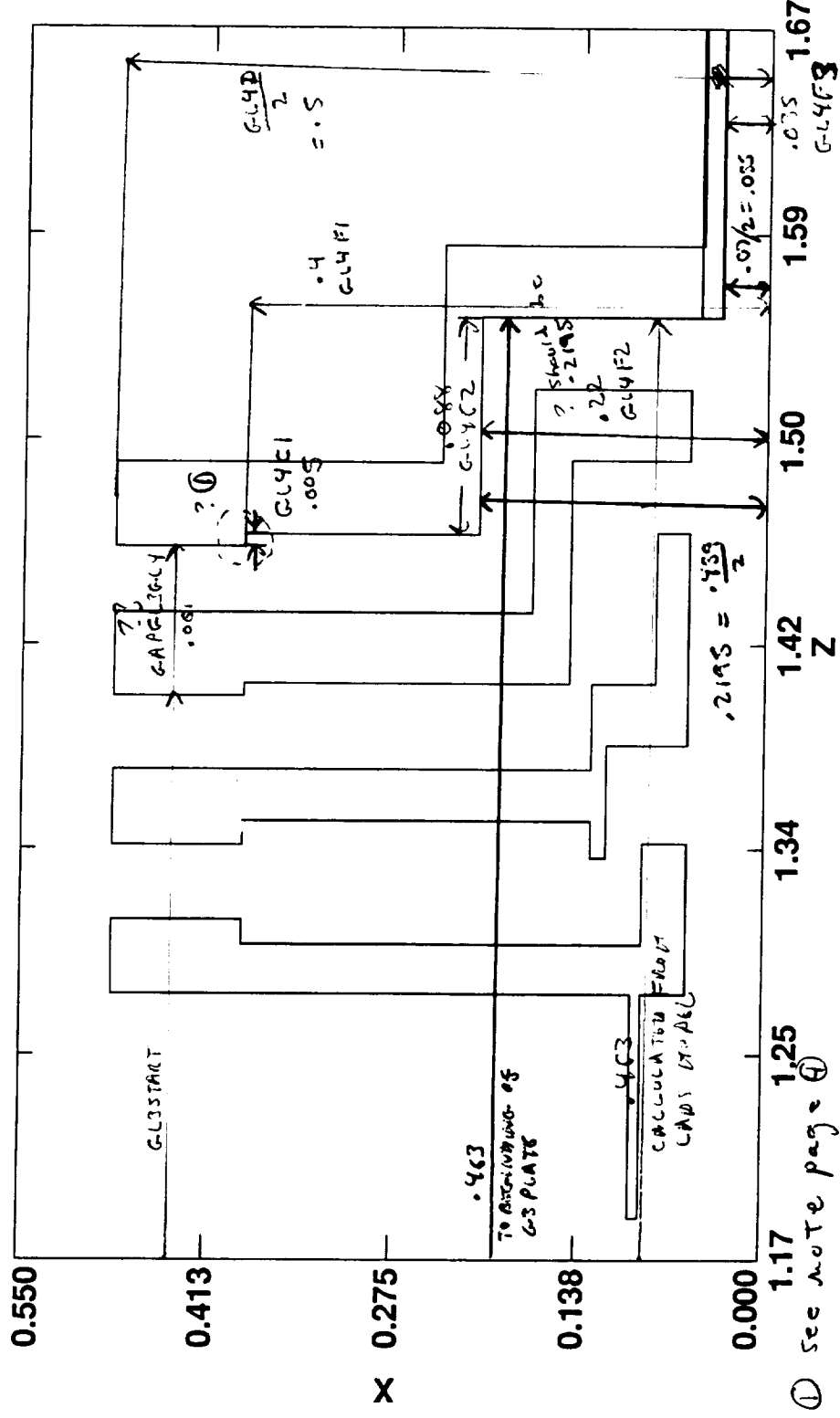
BLACK INDICATES QUESTIONABLE DIMENSION

Unit of measure is the IN

04/30/96 15:37

G-44(1)  
ZX

Data created on 04/30/96 at 09:28:47 in file  
/files/nebula/wjm/fin\_mod2/trapsym.beam3d



Red indicates dimensions from current CAD model  
Blue indicates dimensions from NISA diagram  
Black indicates question marks or dimensions

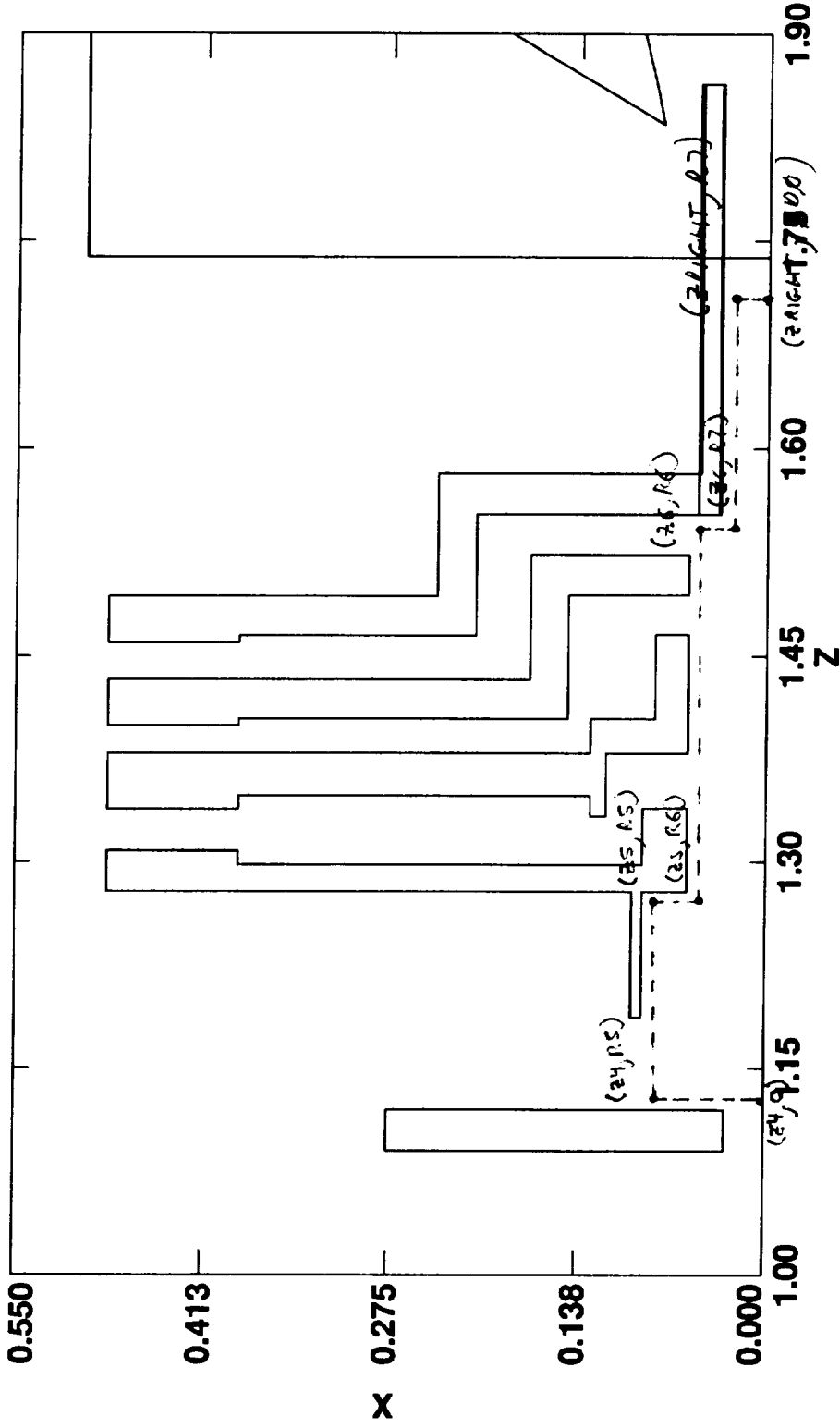
Unit of measure is the IN

04/30/96 15:37



ZX

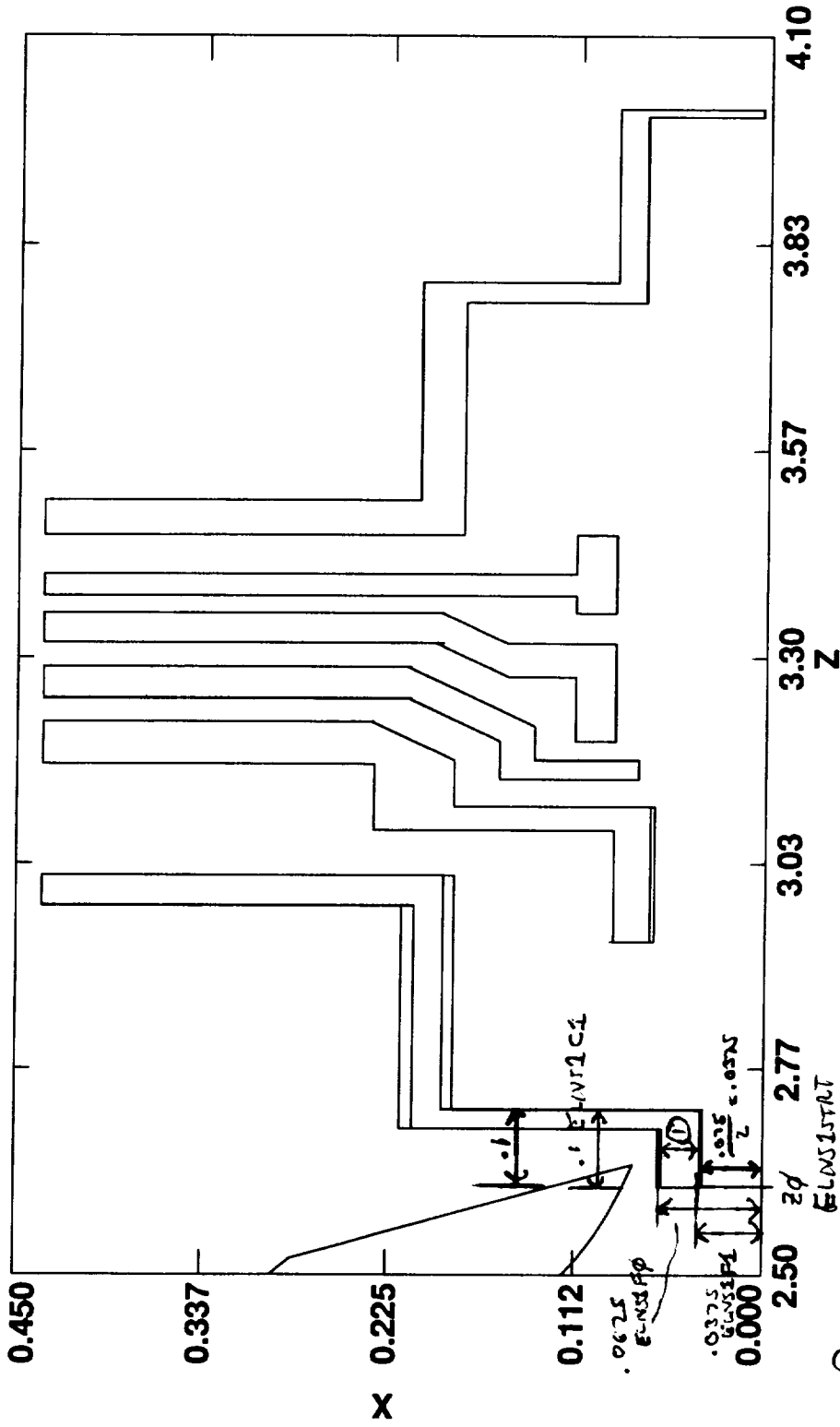
Data created on 04/30/96 at 09:28:47 in file  
/files/nebula/wjm/fin\_mod2/trapsym.beam3d



Unit of measure is the IN

EXLNS1 (j)  
ZX

Data created on 04/30/96 at 09:28:47 in file  
/files/nebula/wjm/fin\_mod2/trapsym.beam3d



① ASSUME EXLNS1 THICKNESS OF .025

RED INDICATES CURRENT CAS MODEL DIMENSIONS  
BLUE INDICATES DIMENSIONS FROM WASA DIAGRAM (FIG 3)  
BLACK INDICATES QUARTER DIMENSION

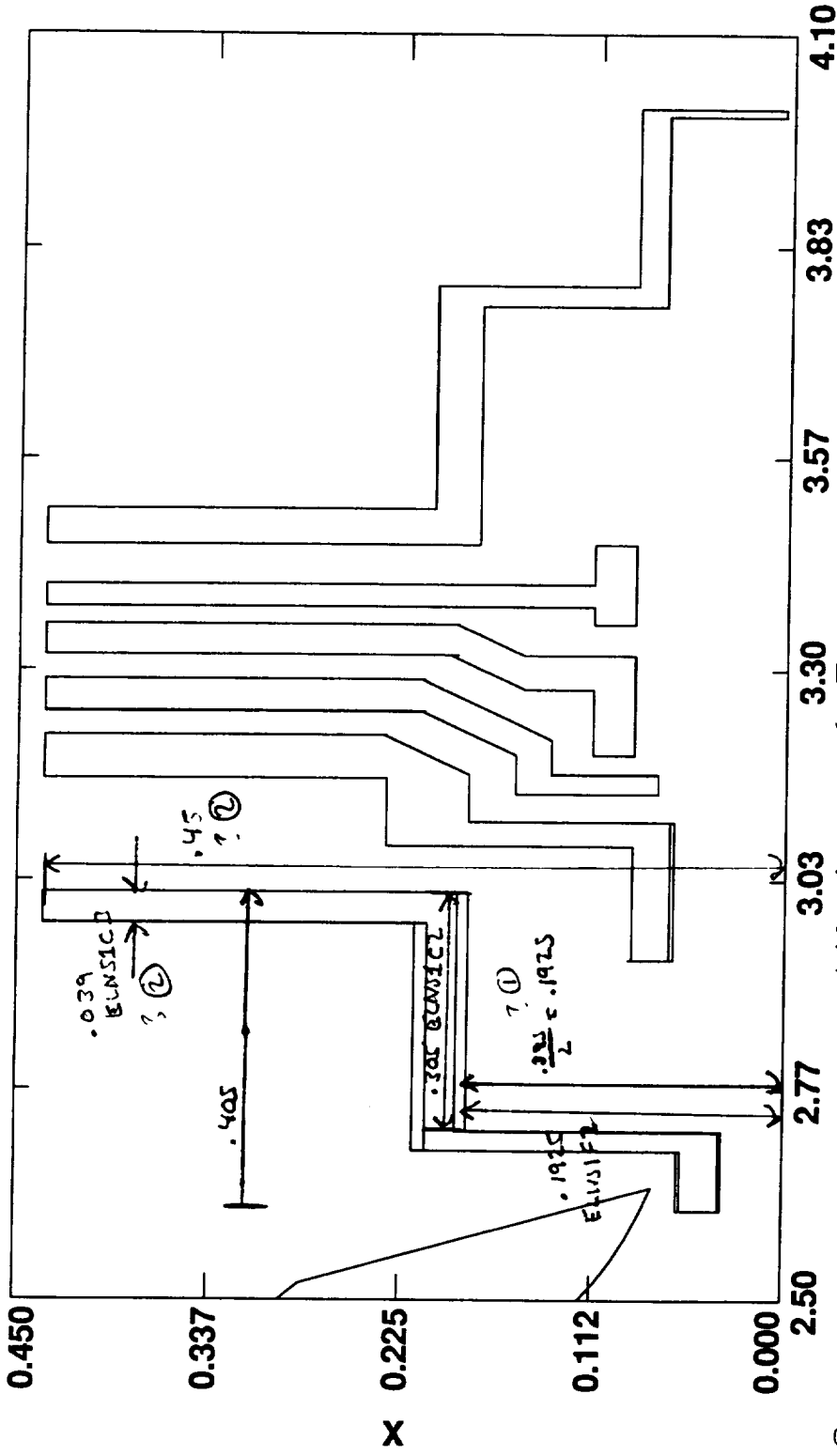
Unit of measure is the IN

05/03/96 11:14

EXCNSI(2)

ZX

Data created on 04/30/96 at 09:28:47 in file  
/files/nebula/wjm/fin\_mod2/trapsym.beam3d



- ① OVERLAPPING DIMENSIONS ON NASA DIAGRAM (FIG-3)
- ② NO CORRESPONDING DIMENSION ON NASA (FIG-3) DRAWING

Unit of measure is the IN

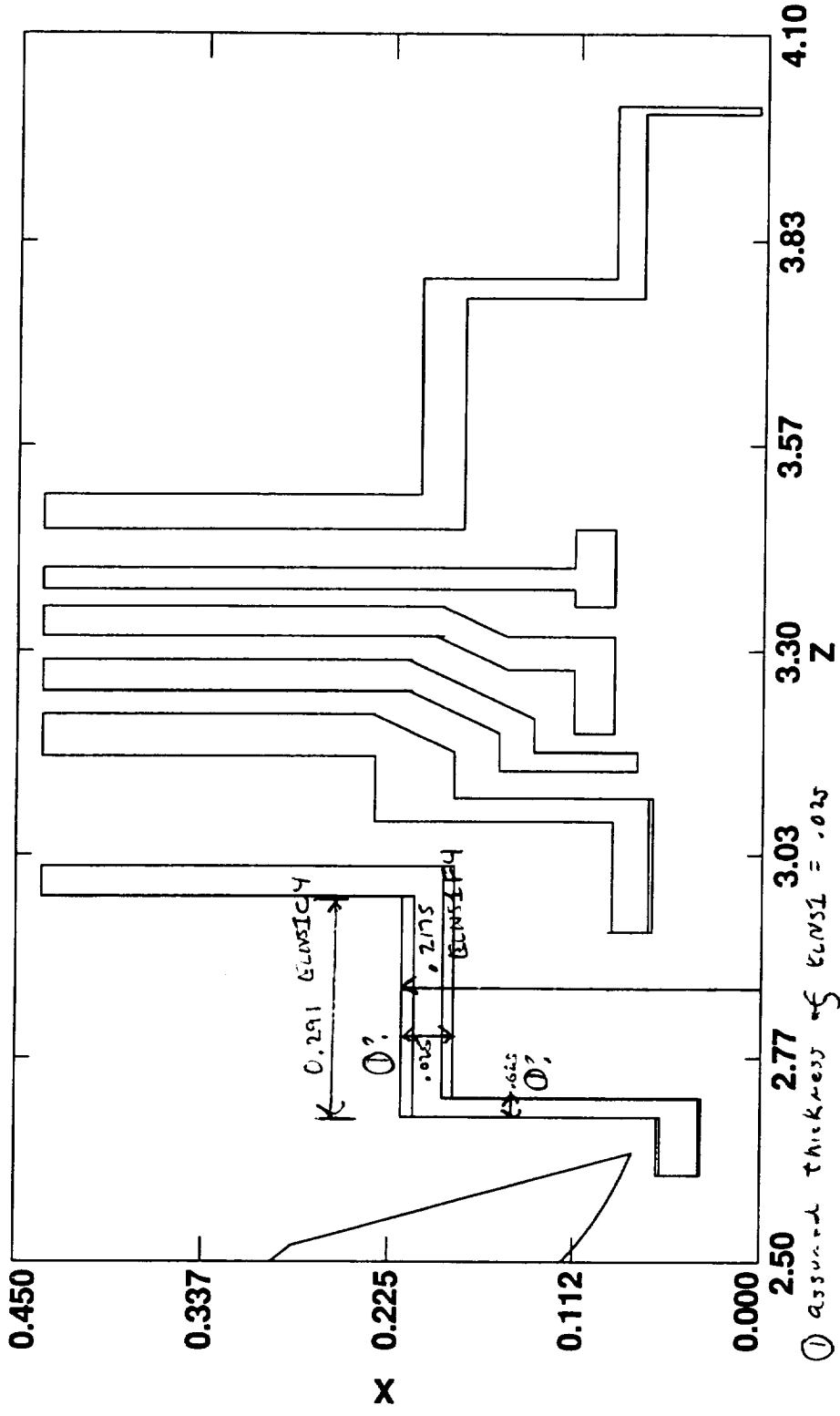
RED INDICATES CURRENT CADS MODEL DIMENSION (FIG-3)  
BLUE INDICATES DIMENSION FROM NASA DIAGRAM (FIG-3)  
BLACK INDICATES QUESTIONABLE DIMENSION

05/03/96 11:14

ELNS1 (3)

ZX

Data created on 04/30/96 at 09:28:47 in file  
/files/nebula/wjm/fin\_mod2/trapsym.beam3d



RED INDICATES CURRENT LADS MODEL DIMENSIONS  
BLUE INDICATES ALIGNMENT FROM WISA DRAWING (FIG. 3)  
BLACK INDICATES QUESTIONABLE DIMENSION

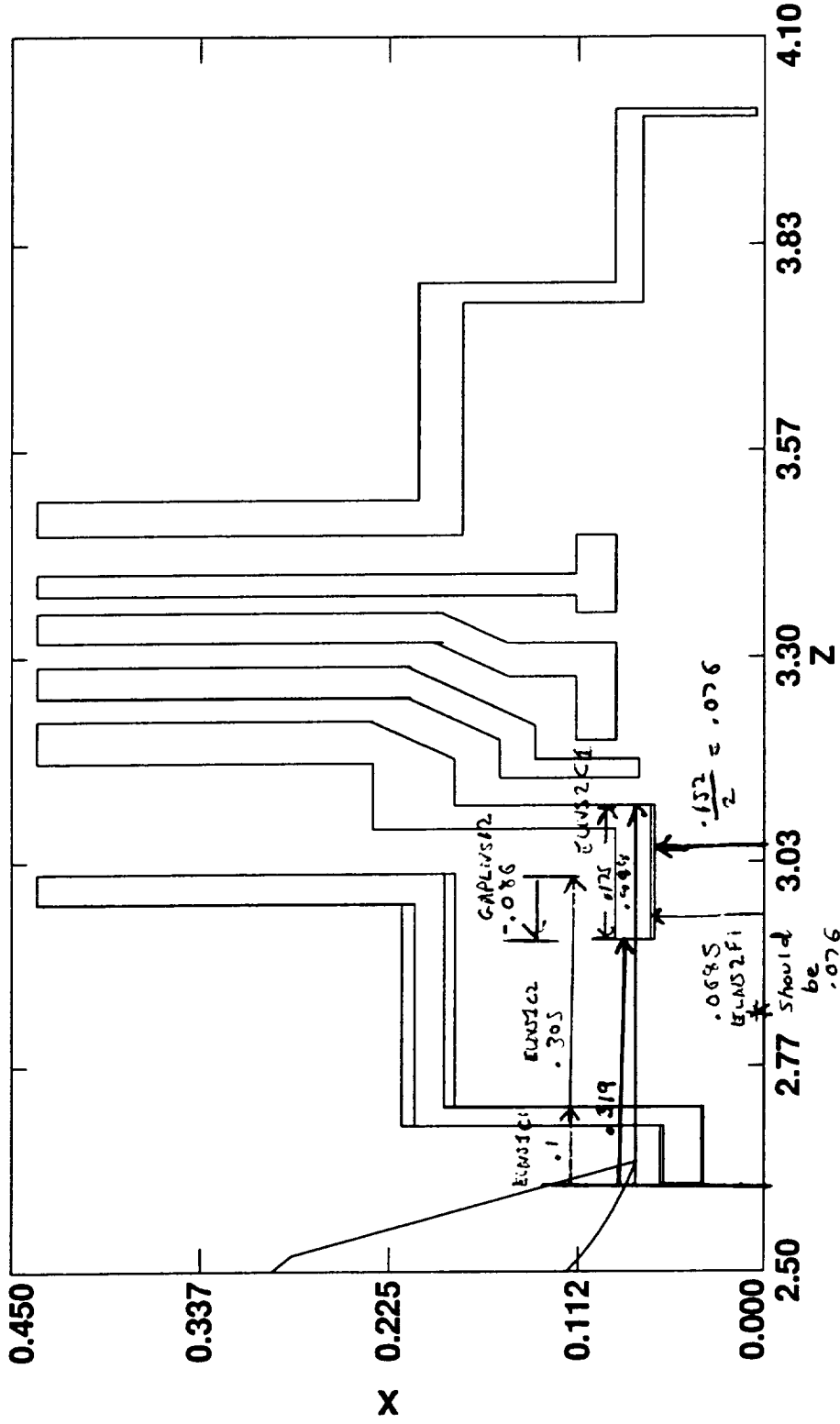
Unit of measure is the IN

05/03/96 11:14

EXLMS2 (1)

ZX

Data created on 04/30/96 at 09:28:47 in file  
/files/nebula/wjm/fin\_mod2/trapsym.beam3d

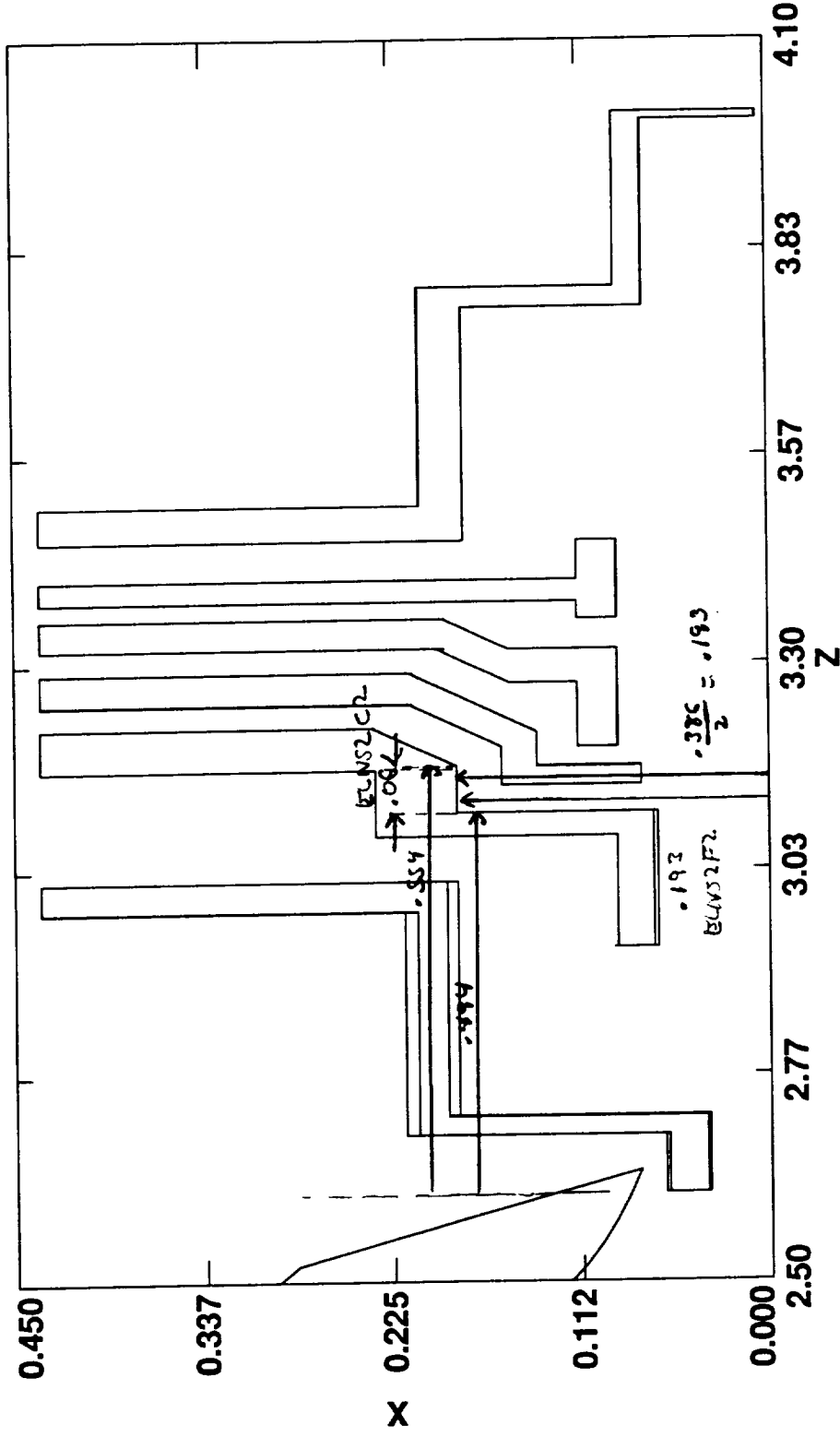


RED INDICATES CURRENT IADS MODEL DIMENSION  
BLUE INDICATES DIMENSION FROM NASA DIAGRAM (FIG 3)  
BLACK INDICATES QUESTIONABLE DIMENSION 05/03/96 11:14

Unit of measure is the IN

EX LENS2 (2)  
ZX

Data created on 04/30/96 at 09:28:47 in file  
/files/nebula/wjm/fin\_mod2/trapsym.beam3d

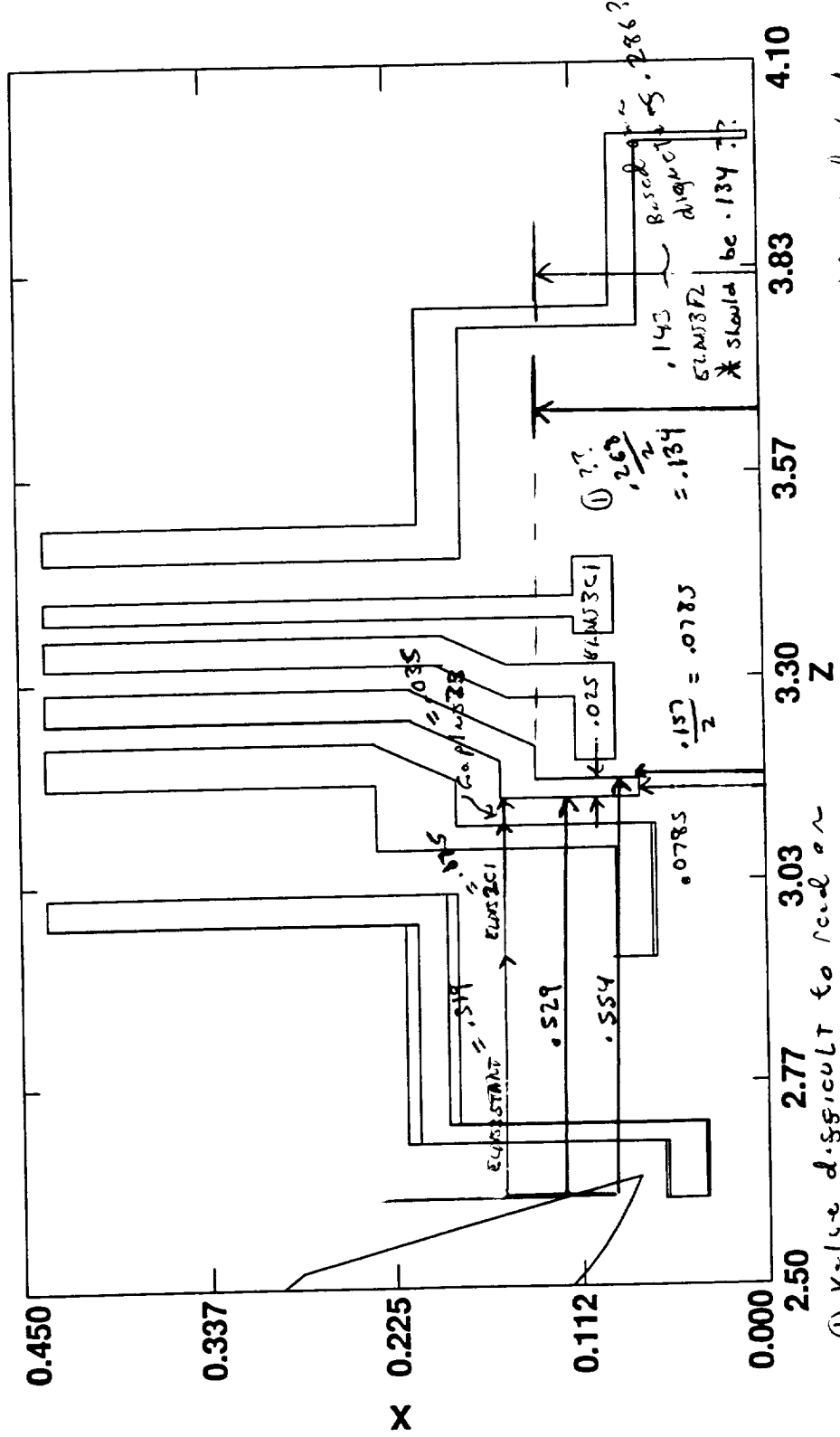


RED INDICATES CURRENT LAD5 Model dimensions  
BLUE INDICATES DIMENSION FROM NARA DIAGRAM (FIG 3)  
BLACK INDICATES QUOTEABLE dimension

Unit of measure is the IN



Data created on 04/30/96 at 09:28:47 in file /files/nebula/wjm/fin\_mod2/trapsym.beam3d



RED INDICATES CURRENT CAD'S MODEL DIMENSION  
 BLUE INDICATES DIMENSION FROM NASA DIAGRAM (FIG 3)  
 BLACK INDICATES QUESTIONABLE DIMENSION 05/03/96 11:14

① Value difficult to read on FIG 3

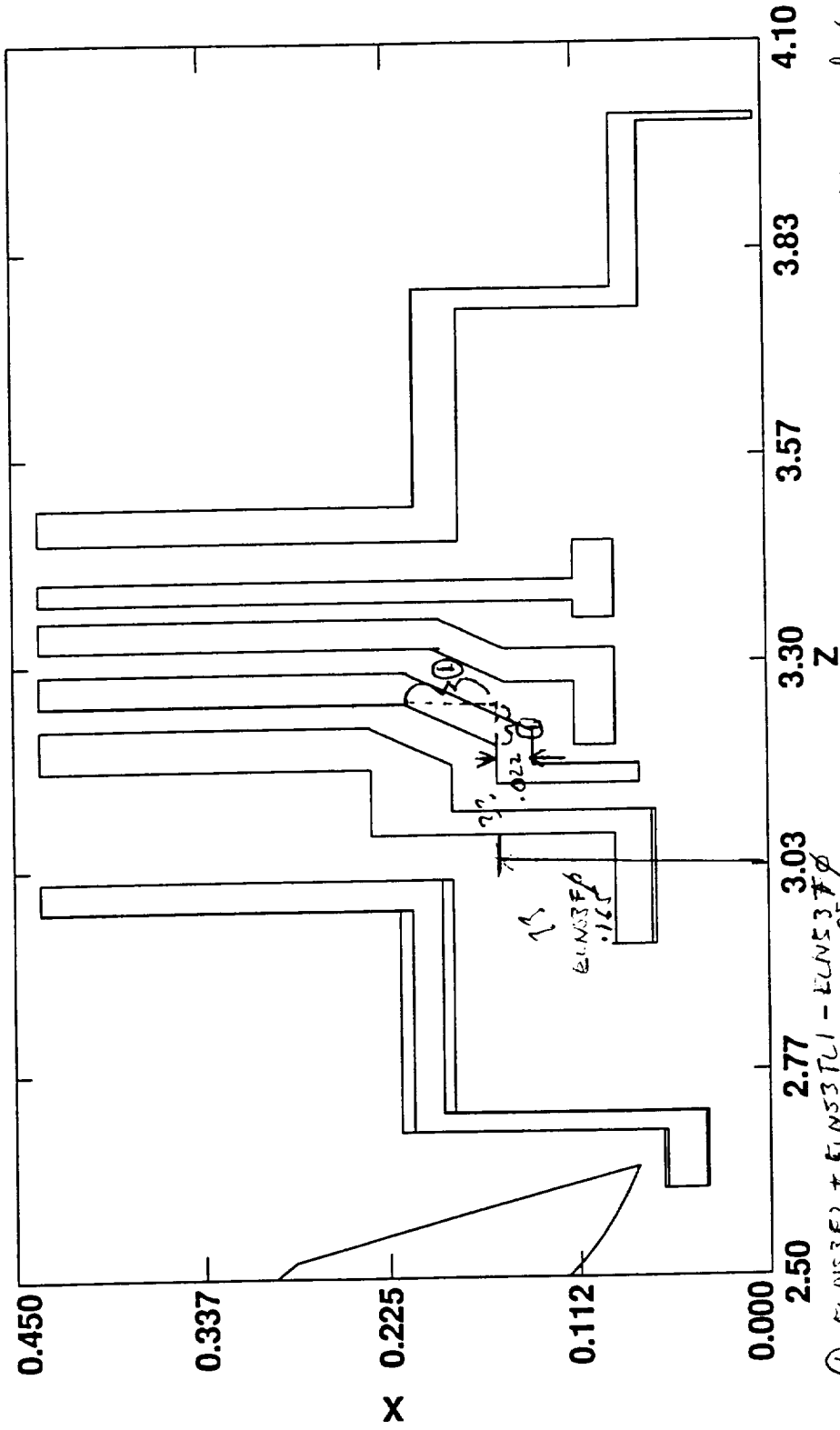
Unit of measure is the IN



EXLAMS 3 (3)

ZX

Data created on 04/30/96 at 09:28:47 in file  
/files/nebula/wjm/fin\_mod2/trapsym.beam3d



①  $EUN3F2 + EUN3T1 - EUN3FF$   
 $.143 + .071 - .165$   
 $= .055$

RED INDICATES CURRENT CADS Model dimension  
 BLUE INDICATES DIMENSION FROM NASA diagram (Fig 3)  
 BLACK INDICATES Questionable dimension

05/03/96 11:14

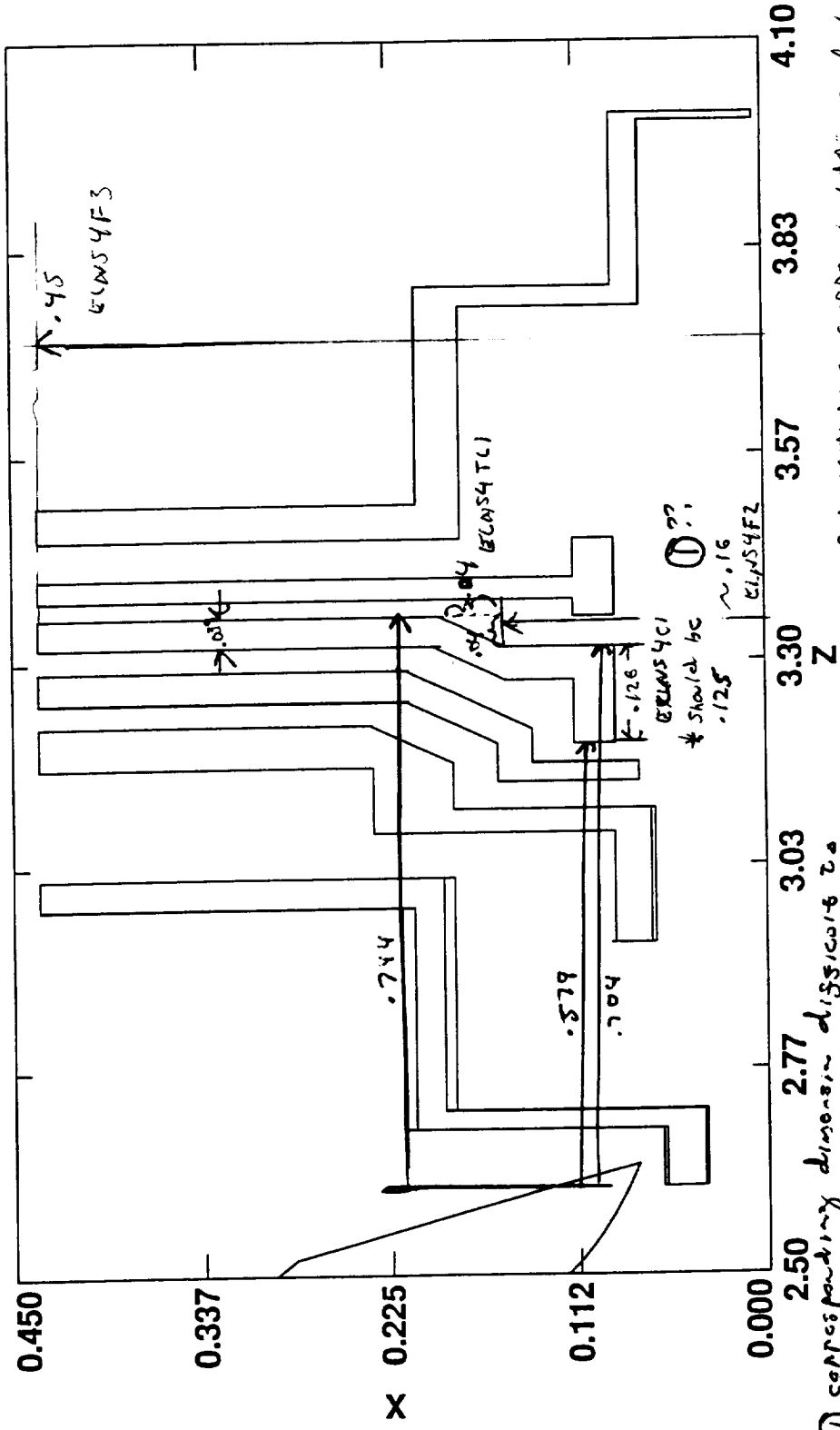
Unit of measure is the IN



EXCIVSY(2)

ZX

Data created on 04/30/96 at 09:28:47 in file  
/files/nebula/wjm/fin\_mod2/trapsym.beam3d



① corresponding dimension dissiolate 2.0  
 determine for Fig 3 may be  
 .0133 + .016 = .1795

RED INDICATES CURRENT CADS Model dimensioning  
 BLUE INDICATES dimension from MSA drawing (Fig 3)

05/03/96 11:14

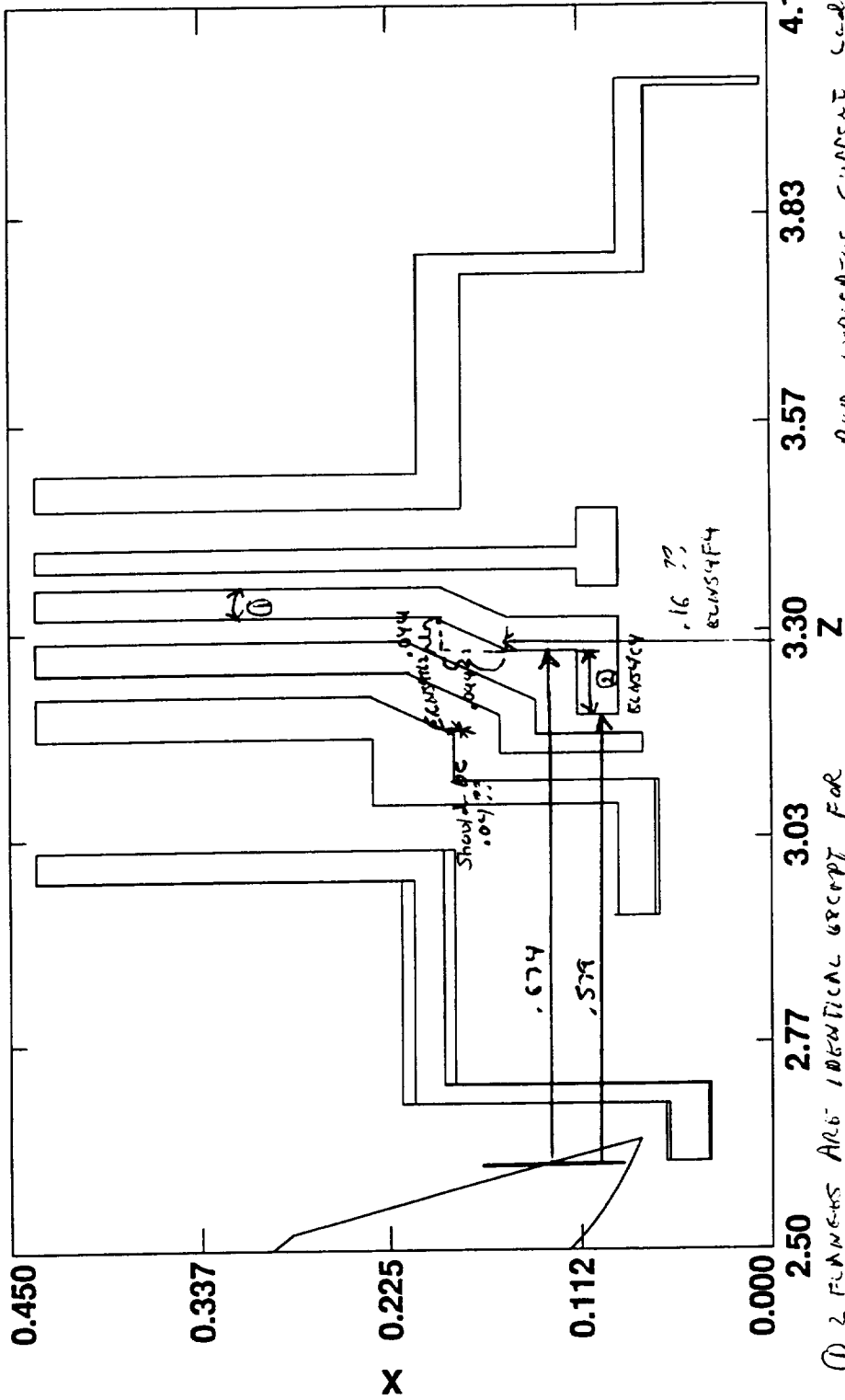
Unit of measure is the IN

BLACK INDICATES questionable dimension

EXCNSY(3)

ZX

Data created on 04/30/96 at 09:28:47 in file  
/files/nebula/wjm/fin\_mod2/trapsym.beam3d



- ① 2 FLANGES ARE IDENTICAL EXCEPT FOR Z POSITION
- ②  $.125 + .04 - .039 - .044 = .083$   
\* Should be .095

Unit of measure is the IN

RED INDICATES CURRENT LEADS MADE/DIMENSION  
BLUE INDICATES DIMENSION FROM NASA DRAWING (FIG 3)

05/03/96 11:14

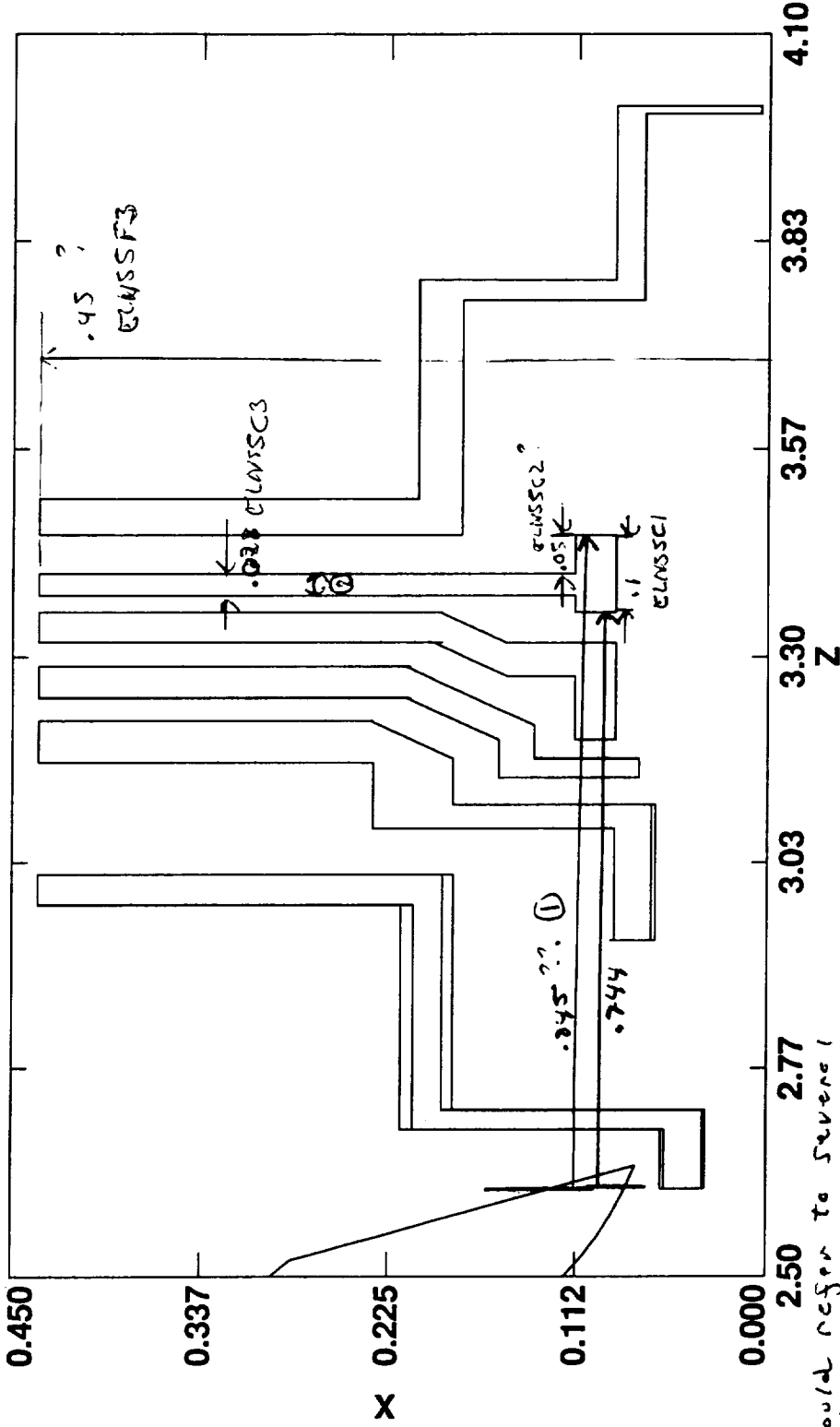
BLACK INDICATES QUESTIONABLE DIMENSION



EXLNS5(2)

ZX

Data created on 04/30/96 at 09:28:47 in file  
/files/nebula/wjm/fin\_mod2/trapsym.beam3d



① could refer to several dimensions

② DIMENSIONS ARE IDENTICAL EXCEPT FOR Z POSITION

Unit of measure is the IN

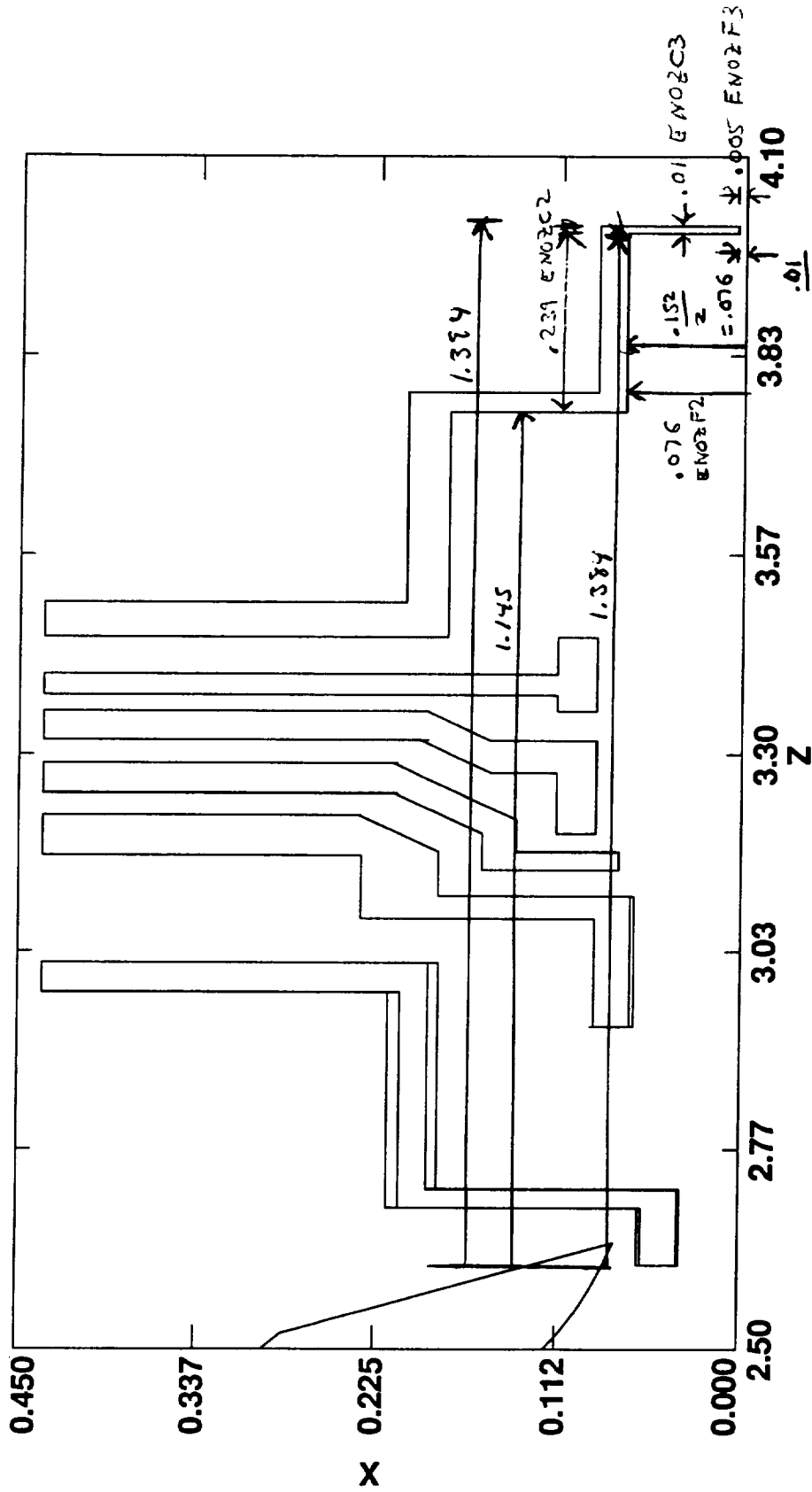
RGB INDICATES CURRENT CADS MODEL DIMENSION  
BLUE INDICATES DIMENSION FROM NASA DIAGRAM (FIG 5) 05/08/96 10:51

BLACK INDICATES QUESTIONABLE DIMENSION



ENOFZLG (2)  
ZX

Data created on 04/30/96 at 09:28:47 in file  
/files/nebula/wjm/fin\_mod2/trapsym.beam3d



RED INDICATES CURRENT LADS MODEL  
DIMENSION

BLUE INDICATES DIMENSIONS FROM NASA DATA  
(07103)

BLACK INDICATES QUESTIONABLE DIMENSIONS

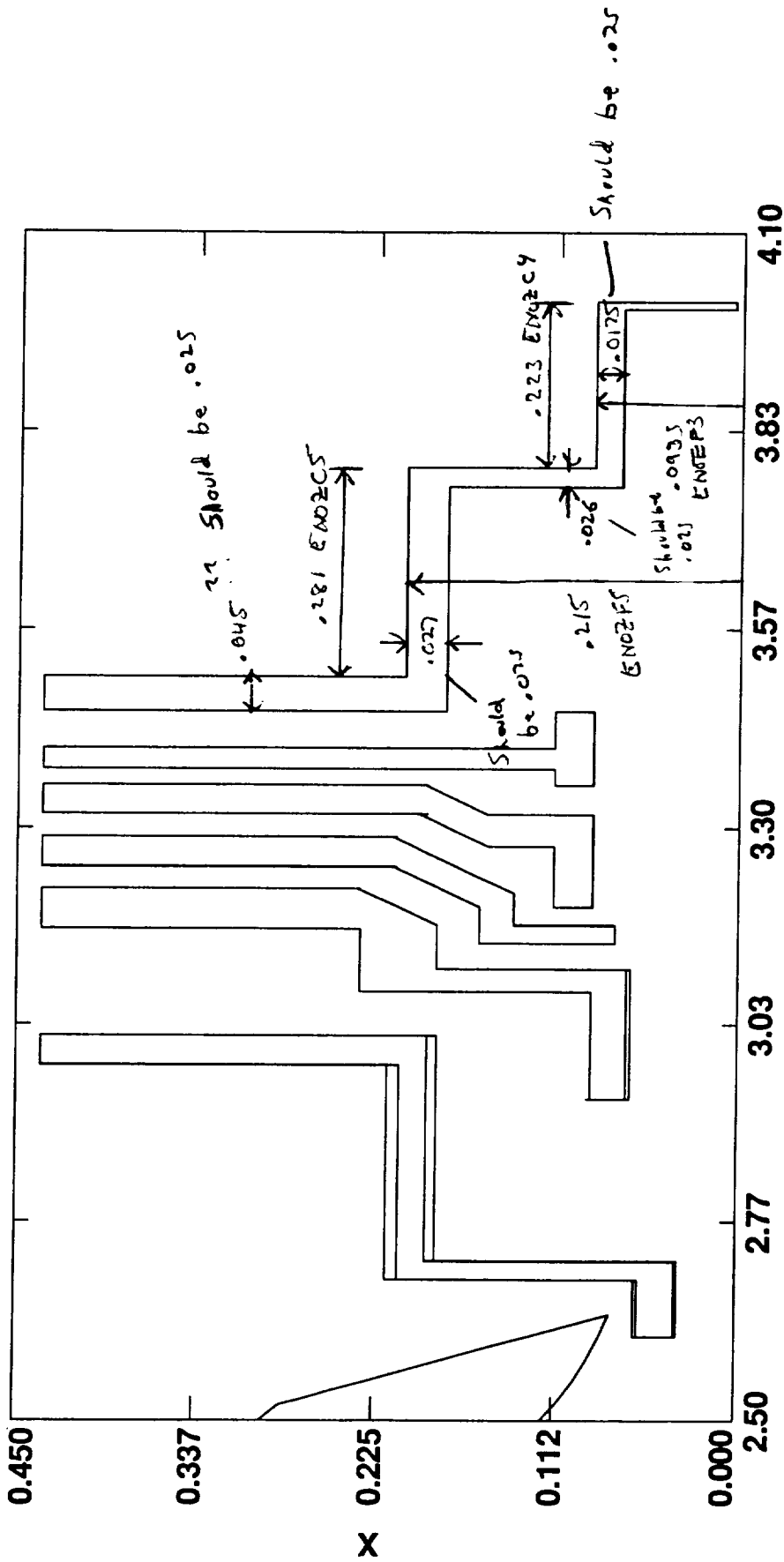
Unit of measure is the IN

05/08/96 10:51

EMOZELV (3)

ZX

Data created on 04/30/96 at 09:28:47 in file  
/files/nebula/wjm/fin\_mod2/trapsym.beam3d



RED INDICATES CURRENT CADDS MODEL DIMENSION  
 BLUE INDICATES DIMENSION FROM NASA DIAGRAM (FIG 3)

Unit of measure is the IN

BLACK INDICATES QUESTIONABLE DIMENSION

05/08/96 10:51

# REPORT DOCUMENTATION PAGE

Form Approved  
OMB No. 0704-

The reporting burden for this collection of information is estimated to average 1 hour per response, including the time for reviewing instructions, searching existing data sources, gathering and maintaining the data needed, and completing and reviewing the collection of information. Send comments regarding this burden estimate or any other aspect of the collection of information, including suggestions for reducing this burden, to Washington Headquarters Services, Directorate for Information Operations and Reports, 1215 Jefferson Davis Highway, Suite 1204, Arlington VA 22202-4302, and to the Office of Management and Budget, Paperwork Reduction Project (0704-0188), Washington, DC 20503

AGENCY USE ONLY (Leave Blank)		2. REPORT DATE 7/11/97	3. REPORT TYPE AND DATES COVERED Final Report (Jan 12, 1995 - July 11, 1997)	
TITLE AND SUBTITLE Design of An Improved Ion Neutral Mass Spectrometer for NASA Applications.			8. FUNDING NUMBERS NAS5 - 32823	
AUTHOR(S) Viji K. Swaminathan, Roger C. Alig				
PERFORMING ORGANIZATION NAME(S) AND ADDRESS(ES) Princeton Electronic Systems P. O. Box 8627 Princeton, NJ 08543-8627			8. PERFORMING ORGANIZATION REPORT NUMBER PES/NASA -95- 1	
SPONSORING/MONITORING AGENCY NAME(S) AND ADDRESS(ES) NASA/Goddard Space Flight Center Engineering Procurement Office Greenbelt, MD 20771			10. SPONSORING/MONITORING AGENCY REPORT NUMBER	
. SUPPLEMENTARY NOTES				
a. DISTRIBUTION/AVAILABILITY STATEMENT			12. DISTRIBUTION CODE	
. ABSTRACT (Maximum 200 words) The ion optics of NASA's Ion Neutral Mass Spectrometer (INMS) sensor was simulated with three dimensional models of the open source, the quadrupole deflector, the exit lens system and the quadrupole mass analyzer to design more compact models with lower weight. Comparison of calculated transmission with experimental results shows good agreement. Transmission analyses with varying geometrical parameters and voltages throw light on possible ways of reducing the size of the sensor. Trajectories of ions of mass 1-99 amu were simulated to analyze and optimize transmission. Analysis of open source transmission with varying angle of attack shows that the angular acceptance can be considerably increased by programming the voltages on the ion trap/collimator. Analysis of transmission sensitivity to voltages and misalignments of the quadrupole deflector rods indicate that increased transmission is possible with a geometrically asymmetrical deflector and a deflector can be designed with much lower sensitivities of transmission. Bringing the disks closer together can decrease the size of the quadrupole deflector and also increase transmission. The exit lens system can be redesigned to be smaller by eliminating at least one electrode entirely without loss of transmission. Ceramic materials were investigated to find suitable candidates for use in the construction of lighter weight mass spectrometer. A high-sensitivity, high-resolution portable gas chromatograph mass spectrometer with a mass range of 2-700 amu has been built and will be commercialized in Phase III.				
. SUBJECT TERMS			15. NUMBER OF PAGES 152	
			16. PRICE CODE	
SECURITY CLASSIFICATION OF REPORT Unclassified	18. SECURITY CLASSIFICATION OF THIS PAGE Unclassified	19. SECURITY CLASSIFICATION OF ABSTRACT Unclassified	20. LIMITATION OF ABSTRACT 200 words	